INTERNATIONAL DOCTORAL
SCHOOL OF THE USC

Cristian
Suárez Oubiña

PhD Thesis

Advanced analytical methodologies for characterizing inorganic nanoparticles and assessing their impact on the aquaculture sector

Santiago de Compostela, 2023

Doctoral Programme in Chemical Science and Technology

TESIS DE DOCTORADO

ADVANCED ANALYTICAL METHODOLOGIES FOR CHARACTERIZING INORGANIC NANOPARTICLES AND ASSESSING THEIR IMPACT ON THE AQUACULTURE SECTOR

Cristian Suárez Oubiña

ESCUELA DE DOCTORADO INTERNACIONAL DE LA UNIVERSIDAD DE SANTIAGO DE COMPOSTELA

PROGRAMA DE DOCTORADO EN CIENCIA Y TECNOLOGÍA QUÍMICA

SANTIAGO DE COMPOSTELA

2023

DECLARACIÓN DEL AUTOR DE LA TESIS

D. **CRISTIAN SUÁREZ OUBIÑA**

Título de la tesis: **Advanced analytical methodologies for characterizing inorganic nanoparticles and assessing their impact on the aquaculture sector**

presento mi tesis, siguiendo el procedimiento adecuado al reglamento y declaro que:

1) La tesis abarca los resultados de la elaboración de mi trabajo.

2) De ser el caso, en la tesis se hace referencia a las colaboraciones que tuvo este trabajo.

3) Confirmo que la tesis no incurre en ningún tipo de plagio de otros autores ni de trabajos presentados por mí para la obtención de otros títulos.

4) La tesis es la versión definitiva presentada para su defensa y coincide la versión impresa con la presentada en formato electrónico.

y me comprometo a presentar el compromiso documental de supervisión en el caso que el original no esté depositado en la escuela.

Santiago de Compostela, 24 de abril de 2023

AUTORIZACIÓN DEL DIRECTOR/TUTOR DE LA TESIS

Advanced analytical methodologies for characterizing inorganic nanoparticles and assessing their impact on the aquaculture sector

D. Antonio Moreda Piñeiro

Dª. Pilar Bermejo Barrera

INFORMAN:

Que la presente tesis, se corresponde con el trabajo realizado por D. Cristian Suárez Oubiña, bajo nuestra dirección/tutorización, y autorizamos su presentación considerando que reúne los requisitos exigidos en el Reglamento de Estudios de Doctorado de la USC y que, como directores de esta, no incurre en las causas de abstención establecidas en la Ley 40/2015.

De acuerdo con lo indicado en el Reglamento de Estudios de Doctorado, declara también que la presente tesis doctoral es idónea para ser defendida en base a la modalidad de Monográfica con reproducción de publicaciones, en los que la participación del doctorando fue decisiva para su elaboración y que se ajustan al Plan de Investigación.

Santiago de Compostela, 24 de abril de 2023

"And once the storm is over, you won't remember how you made it through, how you managed to survive. You won't even be sure, whether the storm is really over. But one thing is certain. When you come out of the storm, you won't be the same person who walked in. That's what this storm's all about."

Haruki Murakami in *Kafka on the Shore*

"Genius is 1% talent and 99% hard work."

Albert Einstein

FUNDING

- Xunta de Galicia (Development of a Strategic Grouping in Materials-AEMAT, reference ED431E2018/08).
- Xunta de Galicia (Grupo de Referencia Competitiva, reference ED431C2018/19).
- Ministerio de Economía, Industria y Competitividad (project INNOVANANO, reference RT2018-099222-B-100).
- Ministerio de Economía, Industria y Competitividad (project FOODNANORISK, reference PID2021-125276NB-I00).
- European Union – Interreg POCTEP (project ACUINANO, reference 07-12-ACUINANO_1_E).

ACKNOWLEDGEMENTS

Al volver la vista hacia atrás cuatro años, es increíble darse cuenta de lo mucho que ha cambiado todo, y cuánto he cambiado yo. Cuatro años después, hoy ha llegado el momento de poner el punto y final a una etapa. Un camino lleno de momentos maravillosos (y no tan maravillosos), un camino lleno de pasión, un camino lleno de luchas y de perseverancia, un camino que me ha cambiado la vida. Es tremendamente difícil lo que supone condensar en unos pocos párrafos la gratitud que siento hacia todas las personas que me han ayudado a lo largo de este viaje.

En primer lugar, quiero dar las gracias a todos mis compañeros del grupo GETEE, con los que he compartido tantas y tantas horas. Ha sido realmente un orgullo formar parte de un equipo como vosotros, con un entorno de trabajo tan agradable, lleno de cariño, amabilidad y por supuesto profesionalidad. Gracias a Mari Carmen y a Raquel por haber sido las primeras personas en recibirme al grupo de investigación en aquellas prácticas externas del grado, y haberme hecho sentir tan cómodo, integrado y valorado desde el primer día que puse un pie en vuestros laboratorios. Gracias a Elena por tu amabilidad y cercanía en todo momento. Gracias a Manolo por tu serenidad y el buen humor y energía que transmites siempre. Gracias a Paloma por tu enorme ayuda en el laboratorio, tus consejos, tu sinceridad y tus críticas, siempre constructivas, que son las que valen la pena de verdad. También gracias a Mari por tu energía positiva, y gracias a Mónica por tu ayuda todos estos años, resolverme dudas de administración y portándote tan bien siempre conmigo.

Por supuesto, gracias a mis compañeros de laboratorio: Ana, Juanjo e Iván. Gracias por vuestro apoyo, por los consejos, y por los momentos compartidos a lo largo de todos estos años. Os deseo la mejor de las suertes, estoy convencido de que os irá increíble ahora y siempre. Gracias también a todos mis anteriores compañeros en el pasado que me han ayudado tanto durante todos estos años. Gracias a Iria por tu amabilidad infinita. Gracias a Kolita y Thilini por haber sido personas tan maravillosas conmigo.

Gracias a todos los compañeros y miembros del grupo LIDSA, por vuestro afecto y ayuda siempre que la he necesitado. Gracias a Ali, a María Celeiro, a Lúa, a todos. Gracias a María Llompart por interesarte por mí, además de las buenas y cariñosas palabras que has tenido siempre para mí. Y gracias especialmente a Dani, gracias por ser un gran amigo, por ofrecerme tu ayuda y apoyo siempre que puedes, por todas las charlas y risas que hemos tenido en los pasillos del departamento.

Gracias también a Mónica Quarato, por todos los momentos y risas compartidas que fueron muchísimas en tus meses de estancia en Santiago y en todas las veces que hemos coincidido. Gracias también a Alex, por ser tan amable durante tus meses de estancia, aunque te estuvieras peleando meses con el equipo de single-cell, las risas y lamentos que hemos compartido tampoco las olvido. Tampoco quiero olvidarme de Laura del Instituto de Investigación Sanitaria de Santiago de Compostela por tu paciencia y amabilidad, y del personal del Instituto de Cerámica de Galicia, especialmente de Rubén, de Mónica y de Mar por el apoyo y cariño que me mostraron los meses que estuve allí.

Grazie all'altra mia famiglia italiana del Dipartimento di Chimica dell'Università degli Studi di Bari Aldo Moro. Sono davvero grato per tutto l'amore e la gentilezza che ho ricevuto fin dal primo giorno. Grazie a tutti i miei colleghi. Grazie a Chinzia, a Cristina Filosa, a Tiziana, a tutti. E naturalmente, grazie mille alle professoresse Anna Rosa Mangone e Lorena Gianossa per avermi accettato nel vostro gruppo. Grazie per la fiducia e l'affetto che avete riposto in me fin dal primo momento, è stato un vero piacere aver condiviso questi tre mesi in un gruppo di ricerca come il vostro. Thanks also to the Greek girls, thanks to Natalia, Elpida, and Rea for all the moments we spent together during those months in Bari. Σας ευχαριστώ πολύ για όλα κορίτσια, είστε καταπληκτικές. Per tutto questo, un pezzo del mio cuore rimarrà per sempre a Bari, grazie mille.

Gracias a mi familia, por haberme apoyado en todas las etapas de mi vida desde niño y haber estado a mi lado y al lado de mis padres siempre.

Gracias a mis amigos, por ser unas personas tan maravillosas y por haberme ayudado siempre que lo he necesitado, por haberos preocupado por mí o por alegraros incluso más que yo de mis propias alegrías, gracias por todo. Gracias a Sheila, a Stella, a Pablo, a Rafa, a Noe, a Ana, a Andrea, y en definitiva, gracias a todas las personas que me queréis, me apoyáis y que hacéis de mí una mejor persona y más feliz.

Un agradecimiento especial a mis directores de tesis. Gracias a Pilar por aceptarme en el grupo y por la confianza depositada en mí para hacer esta tesis doctoral, estoy realmente agradecido de la oportunidad que me disteis. Y gracias a Antonio, gracias por todo. Por muchas líneas que escriba es imposible describir la gratitud que siento por toda la confianza que depositaste en mí. Gracias por haberme apoyado en todos los momentos, en los buenos, y en los no tan buenos. Gracias por compartir todos tus conocimientos y contagiar tu pasión por lo que haces como si fuera tu primer día. Gracias por haberme dado la oportunidad de realizar la tesis en un proyecto tan atractivo y completo como ha sido éste, aprendiendo infinidad de técnicas y metodologías. Estos años han sido un privilegio para mí, y yo he intentado devolver toda esa confianza dando lo mejor de mí con trabajo, dedicación y pasión. Espero haber estado a la altura de las expectativas.

Y por último, gracias a mis padres. Gracias por todo. Gracias por haber luchado todos los días de vuestra vida por mi bienestar, mi educación y mi salud. Gracias por haberme dado el mejor entorno que un bebé, un niño, un adolescente, un chico y un hombre haya podido tener nunca. Gracias por vuestro apoyo y amor incondicional. Gracias por enseñarme a valorar las cosas, por enseñarme a luchar para conseguirlas, porque al final el esfuerzo sí que tiene su recompensa. No ha sido un camino sencillo, pero lo hemos conseguido. Todo lo que soy es gracias a vosotros, y esta tesis doctoral es, sin duda, para vosotros. Esta tesis doctoral es para ti, Mamá. Esta tesis doctoral es para ti, Papá.

GRACIAS.

Cristian

Santiago de Compostela, 2023.

INDEX

INDEX

ABBREVIATIONS

A

AF4: Asymmetric Flow Field-Flow Fractionation

AF4-ICP-MS: Asymmetric Flow Field-Flow Fractionation–Inductively Coupled Plasma Mass Spectrometry

AFM: Atomic Force Microscopy

AgNPs: silver nanoparticles

AuNPs: gold NPs

C

CETGA: Galician Aquaculture Technology Centre

CIIMAR: Interdisciplinary Centre for Marine and Environmental Research

CLP: Classification, Labelling, and Packaging

COVID: Corona Virus Disease

CuNPs: copper NPs

CuONPs: copper oxide NPs

D

DMEM: Dulbecco´s Modified Eagle Medium

DMSO: Dimethyl Sulfoxide

DLS: Dynamic Light Scattering

DRC: Dynamic Reaction Cell

E

EC: European Comission

ECHA: European Chemicals Agency

ECJ: European Court of Justice

EDX: Energy-Dispersive X-ray

EFSA: European Food Safety Authority

ELS: Electrophoretic Light Scattering

EU: European Union

F

FAO: Food and Agriculture Organization of the United Nations

FBS: Fetal Bovine Serum

FDA: Food and Drug Administration

FEAP: Federation of European Aquaculture Producers

FFF: Field-Flow Fractionation

H

HBSS: Hanks`Balanced Salt Solution

HDC: Hydrodynamic Chromatography

I

ICP-MS: Inductively Coupled Plasma Mass Spectrometry

ICP-OES: Inductively Coupled Plasma Optical Emission Spectrometry

INL: International Nanotechnology Iberian Laboratory

IS: Internal Standard

ISO: International Organization for Standarization

K

KED: Kinetic Energy Discrimination

L

LA-ICP-MS: Laser Ablation Inductively Coupled Plasma Mass Spectrometry

LIBS: Laser-Induced Breakdown Spectroscopy

LOD: Limit Of Detection

LOQ: Limit Of Quantification

M

MALDI-TOF: Matrix-Assisted Laser Desorption-Ionization Time Of Flight

MALS: Multi Angle Light Scattering

MNPs: Metallic nanoparticles

m/z: mass-to-charge ratio

N

NMs: nanomaterials

NOM: Natural Organic Matter

NPs: nanoparticles

NTA: Nanoparticle Tracking Analysis

P

PBS: Phosphate-Buffered Saline

PVP: Polyvinyl-Pyrrolidone

Q

QDs: Quantum Dots

R

RCF: Relative Centrifugal Field

REACH: Registration, Evaluation, Authorization, and Restriction of Chemicals

ROS: Reactive Oxygen Species

RPq: Rejection Parameter q

RSD: Relative Standard Deviation

S

SC-ICP-MS: Single Cell Inductively Coupled Plasma Mass Spectrometry

SD: Standard Deviation

Sd-FFF: Sedimentation Field-Flow Fractionation

SeNPs: selenium NPs

SEC: Size Exclusion Chromatography

SEM: Scanning Electron Microscopy

SF-ICP-MS: Sector Field Inductively Coupled Plasma Mass Spectrometry

SIMS: Secondary Ion Mass Spectrometry

SP-ICP-MS: Single Particle Inductively Coupled Plasma Mass Spectrometry

STD: Standard

T

TE: Transport Efficiency

TeNPs: tellurium NPs

TEM: Transmission Electron Microscopy

TiO_2NPs: titanium dioxide nanoparticles

U

UN: United Nations

UV: UltraViolet

UV-VIS: UltraViolet-Visible

X

XPS: X-ray Photoelectron spectroscopy

XRD: X-Ray Diffraction spectroscopy

XRF: X-Ray Fluorescence spectroscopy

Z

ZnONPs: zinc oxide nanoparticle

ABSTRACT

This doctoral thesis focuses on the development of novel analytical methods for the study of inorganic nanoparticles (NPs). The proposed research presents a serious challenge for the enhancement of the detection and characterization of NPs through the use of analytical tools with immense potential, such as reaction gases for interferences removal in inductively coupled plasma – mass spectrometry (ICP-MS), single particle detection (spICP-MS), single cell detection (scICP-MS), and imaging (NPs distribution in tissues) by laser ablation ICP-MS (LA-ICP-MS). All these nanometrological tools have been focused on cultured fish/shellfish products to assess information regarding the potential risk of NPs in the aquaculture industry. In recent decades, nanomaterials (NMs) and nanotechnology have brought about a revolution at the scientific and industrial level, involving applications in several fields such as chemistry, biology, and medicine, among others.

This thesis focuses mostly on silver and titanium dioxide nanoparticles (Ag NPs and TiO_2 NPs). These NPs are nowadays widely used and concerns about their potential impact on the environment, mainly the marine environment, and humans has been raised. Since the lack of toxicological assessments and the absence of robust and reliable nanometrological platforms for NPs characterization, the potential risk of NPs remains uncertain. Some of these questions are addressed in this PhD thesis by developing several analytical procedures for the assessment of the influence of Ag NPs and TiO_2 NPs on aquaculture species such as sea bass (*Dicentrarchus labrax*), sea bream (*Sparus aurata*), and clams (*Ruditapes philippinarum*), three of the most important cultured species worldwide.

Aquaculture is the cultivation of aquatic organisms under controlled circumstances for human consumption. Aquaculture's primary responsibility is to efficiently supplement conventional capture fisheries and to satisfy future food demands from the population and fish consumption increase. Currently, cultured seafood account for more than fifty percent of the fish and aquatic food consumed worldwide. Additionally, the aquaculture sector must promote sustainable aquaculture production and guarantee food safety

for consumers, meanwhile confronting obstacles such as the emergence of novel diseases, climate change, and antibiotic misuse. Although aquaculture is undoubtedly expanding, the development in the European Union (EU) member states has been rather gradual; as a result, the European Commission (EC) established a strategy to promote aquaculture. Member states are highly qualified and equipped with adequate technological resources and technical expertise to promote this sector in an ecologically friendly and sustainable manner. Besides, the EU's strict regulations requirements assure the safety of seafood for consumers.

In terms of aquaculture output, Spain leads the EU due to its advantageous geographical location and environment. Spanish aquaculture production is diversified, with sea bass, sea bream, rainbow trout, turbot, and mussels as dominating species. Particularly, Galicia stands out as an aquaculture power in Spain, leading the production of turbot and mussels. Galicia is an ideal territory for the promotion of this sort of activity due to its location, geographical and climatic qualities, and more than 1,500 kilometres of coastline.

In view of the significant rise in the use of NMs and the aquaculture industry, it is essential to examine the impact that the discharge of these materials may have on the marine environment and the potential effects on cultured species. Consequently, this influence is the core of this doctoral thesis, which provides to the scientific community information and advanced methodologies from several perspectives. Inorganic nanoparticles are fundamentally unstable and, if released into the environment, are susceptible to a wide range of physical, chemical, and biological processes that depend not only on the NPs' properties, but also on the aquatic ambient conditions. Multiple types of NPs have been proven to have harmful impacts on a variety of marine organisms, including bacteria, algae, molluscs, and fish. In addition, it is well recognized that the primary mechanisms of toxicity by NPs are ion release, reactive oxygen species (ROS) formation, and physical stress related to the size, shape, and surface properties of NPs. In addition to the difficulties inherent to NPs as a result of their changing and complex behaviour, there is a lack of a standardised regulatory framework for their usage and reliable

information on their toxicological consequences. In response to the demand for reliable studies and information and to promote aquaculture, the EU has supported several research projects to ensure food safety and aquaculture products of high quality.

Even though spICP-MS is regarded as the most dominant and widely used technique for the analysis of NPs, the use of complementary methodologies that enhance and fortify spICP-MS data is needed. In the different chapters of this doctoral dissertation, these new advanced procedures will be discussed from numerous perspectives. Isobaric spectral interferences are one of the most significant constraints of ICP-MS (and spICP-MS). This limitation can be overcome by employing the Dynamic Reaction Cell (DRC) technology described in this project for dissolved analytes (chapter 1) and NPs of different nature (chapter 2), which involves the use of a reaction gas to remove interferences or move the analytes to interference-free regions (on-mass and mass-shift modes). In these chapters, ammonia (NH_3) is used as a reaction gas, and it offers high selectivity because of the several ammonia-based adducts or ion products that allow measurements at mass-to-charge ratios (m/z) without interference. By other side, the quantitative analysis of trace elements and NPs in single biological cells is playing an increasingly important role. Single cell-ICP-MS has emerged as one of the most promising developing approaches for addressing these issues, as it allows lower detection limits, reveals cell heterogeneity, and distinguishes single cells. Thus, chapter 3 summarises the development of novel approaches for assessing the association of NPs in cells from certain organs of aquaculture species and derive findings of significant importance to support and complement data from other investigations developed in the current PhD Thesis.

Bioaccumulation studies were conducted on clam, sea bass and sea bream species in chapter 4 to observe the impact and effects of Ag NPs and TiO_2 NPs of different sizes under several exposure times and NPs concentrations. In addition, the influence of various cooking techniques was investigated, and data on bioavailability was obtained. Some patterns were identified throughout the aquaculture cycle and linked to NPs exposure, where Ag NPs underwent ionisation

processes and TiO_2 NPs were found to be aggregated. Various sample pretreatments, such as enzymatic hydrolysis for NPs isolation and microwave assisted acid digestion for total element determination were used. In addition, *in-vitro* procedures such as bioaccessibility and cellular transport using a Caco-2 model were applied to obtain information regarding human bioavailability of NPs after cultured fish/shellfish consumption. At this point, the effect of culinary procedures was also tested for a more reliable risk assessment in humans.

A completely different approach is the creation of elemental biodistribution images in tissues, studies that have aroused great interest in the scientific community in recent years. Despite the outstanding capabilities, LA-ICP-MS is restricted by several factors, the most significant the lack of adequate reference materials which hampers quantitative analysis and imaging studies. The use of laboratory-produced standards derived from porcine gelatine has allowed this barrier to be overcome, and the use of LA-ICP-MS as nanometrological tool, which is uncommon for NPs assessment, has been described in chapter 5.

This Doctoral thesis is divided into five chapters which are titled as follows: *Exploiting dynamic reaction cell technology for removal of spectral interferences in the assessment of Ag, Cu, Ti, and Zn by inductively coupled plasma mass spectrometry* (chapter 1); *Single-particle inductively coupled plasma mass spectrometry using ammonia reaction gas as a reliable and free-interference determination of metallic NPs* (chapter 2); *Single-cell-ICP-MS for studying the association of inorganic nanoparticles with cell lines derived from aquaculture species* (chapter 3); *Bioaccumulation and human risk assessment of inorganic nanoparticles in aquaculture species* (chapter 4); and *Quantitative imaging in fish tissues exposed to titanium dioxide nanoparticles by laser ablation-inductively coupled plasma-mass spectrometry* (chapter 5). Each chapter is briefly described in this section including the motivation for the research, the results gathered, and the major drawn conclusions.

Chapter 1: Exploiting dynamic reaction cell technology for removal of spectral interferences in the assessment of Ag, Cu, Ti, and Zn by inductively coupled plasma mass spectrometry.

Ammonia as a reaction gas has been investigated for the determination of Ti, Zn, Cu, and Ag by ICP-MS. Dynamic reaction cell was proved to overcome spectral interferences from complex matrices when assessing elements such as Cu, Ti, and Zn. On-mass and mass-shift (Ti-, Cu-, Zn-, and Ag- based ammonia clusters) working modes using ammonia as a reaction gas were evaluated and compared to the conventional or "vented" mode analysis. The on-mass approach takes advantage of collisional focusing phenomena because of ion confinement (longer travelling path in the ion guide) caused by energy losses from successive collisions in the cell. Moreover, the operating conditions of the DRC were adjusted by altering the ammonia gas flow rate and rejection parameter q (RPq). Optimised conditions were applied to demonstrate the effectiveness of either on-mass or mass-shift strategies for removing Ca and P interferences at concentrations up to 50 mg L^{-1}. Finally, the sensitivity of all measurement modes was investigated, and improved detection limits (at values of a few ng L^{-1}) were achieved.

Chapter 2: Single-particle inductively coupled plasma mass spectrometry using ammonia reaction gas as a reliable and free-interference determination of metallic NPs.

Since the significant increase and the potential threats of NPs in the environment, highly efficient analytical strategies are required for monitoring and characterizing these new pollutants. Despite spICP-MS is the most promising method for determining NPs, problems derived from spectral interferences caused by isobaric isotopes or polyatomic species can be found for certain elements. There are a variety of options to overcome these drawbacks, but DRC technology offers the most promising outcomes. Regarding NPs, there are only few applications of DRC technology to date, as the behaviour of NPs in the cell is considerably different from that of dissolved analytes, mainly due to a larger ion-explosion than that occurred for dissolved ionic analytes. In addition, among the investigated reaction gases,

ammonia has an unpredictable reactivity, as it offers the benefit of producing multiple adducts or ion products and, thus, higher selectivity in ICP-MS/MS for interferences removal by on-mass and mass-shift approaches. Therefore, in chapter 2, DRC-based spICP-MS methods using ammonia as a reaction gas (on-mass or mass-shift approaches) were developed to determine TiO_2 NPs, copper oxide NPs (CuO NPs), copper NPs (Cu NPs), and zinc oxide NPs (ZnO NPs) (ZnO NPs). Extensive research was conducted on the effects of ammonia flow rate and dwell time on the peak width (transient NP signal in spICP-MS). The impact of the NPs' size and composition was also studied. The on-mass and mass-shift procedures have been found to be effective for evaluating Cu NPs and CuO NPs (original mass-to-charge ratio of 63 and the $Cu(NH_3)_2$ ion product). However, the on-mass mode was preferred for evaluating ZnO NPs (original mass-to-charge ratio of 64 using a gas flow of 0.25 mL min^{-1}). Furthermore, the mass-shift method was the most effective approach to face Ti interferences in TiO_2 NPs measurements (mass-to-charge ratio of 131 for $Ti(NH)(NH_3)_4$ at 0.75 mL min^{-1}).

Chapter 3. Single-cell-ICP-MS for studying the association of inorganic nanoparticles with cell lines derived from aquaculture species.

Large-scale manufacturing, discharge, and potential risks associated with inorganic NPs demand data to evaluate the potential damage of these new pollutants, specifically data addressing uptake of inorganic NPs in marine organisms and its consequences at the biological level. *In-vitro* experiments for evaluating NPs absorption by cells are attractive in light of these toxicity studies, but no agreement procedure is available for elucidating NPs association/internalization with/in cells. A new field of research has been opened up thanks to scICP-MS, which enables the ultra-low level quantification of dissolved metals and inorganic NPs in single cells by operating at a minimal sample uptake rate and distinguishing between individual cells in a close native cell-state. Thus, the third chapter deals with the evaluation of TiO_2 NPs and Ag NPs associated and/or internalised in cell lines from aquaculture species such as sea bass, sea bream, and

clams by scICP-MS. High dissolving background, peak coincidence between multiple cells, and spectral interferences are all factors that have been considered throughout the optimization studies. Dwell times of 50 µs for Ag NPs and 100 µs for TiO_2 NPs were shown to be optimal. By implementing DRC technology with a flow rate of 0.75 mL min^{-1} of NH_3 and monitoring the $^{48}Ti(NH)(NH_3)_4$ adduct (m/z = 131), free-interference Ti measurements have been obtained. The effect of other factors on scICP-MS precision, including washing cycles and cells concentration, was also thoroughly examined. Limits of detection of attograms per cell were reached (5.0±1.4 for Ag and 95±11 for Ti measurements. The developed method was applied to kidney cells from sea bass and sea bream, as well as for mantle cells from clam, and data have revealed that the degree of association/internalisation of NPs in cells was significantly influenced by the nanoparticle size distribution, the TiO_2 NPs or Ag NPs concentration, and the cultured species under study.

Chapter 4. Bioaccumulation and human risk assessment of inorganic nanoparticles in aquaculture species.

To obtain studies evaluating the potential toxicity of inorganic NPs and their impact on the marine environment, reliable nanotoxicological studies are essential for a better understanding of the impact of NPs on marine organisms. Unfortunately, this task is complex since the properties of NPs in the aquatic environment vary, and the true effects of their presence are yet unclear and difficult to study. In addition, several NPs characteristics must be considered since they have a considerable impact on the toxicity of NPs. The fourth chapter of this PhD thesis deals with the potential bioaccumulation of Ag NPs and TiO_2 NPs in cultured species (sea bass, sea bream and clams), as well as the potential risk for human after cultured fish/shellfish consumption (human bioavailability). Several NPs sizes and concentrations, and exposure times were studied, and information regarding target organs in fish for NPs bioaccumulation was obtained. Several patterns were identified after exposure assays, and Ag NPs were found to be ionised and TiO_2 NPs

aggregated. In addition, information on safety of cultured fish/shellfish was assessed by human bioavailability trials (*in vitro* bioaccessibility and *in vitro* Caco-2 cellular transport). The assessment of Ag NPs and TiO_2 NPs was performed by spICP-MS methodologies proposed in chapter 2.

Chapter 5. Quantitative imaging in fish tissues exposed to titanium dioxide nanoparticles by laser ablation-inductively coupled plasma-mass spectrometry.

The knowledge of NPs behaviour in biological systems and in the environment requires the development of reliable and efficient analytical methodologies. Elemental biodistribution studies in biological tissues can help to address biological challenges regarding toxicity. This area could complement well-established techniques such as spICP-MS by providing essential information on the bioaccumulation of metals in a wide variety of soft tissues. Even though this type of study is becoming increasingly popular in cell lines, and tissues from tumours and some other organs, published papers focused on NPs are scarce. Biological tissue imaging/elemental bioimaging can be performed by LA-ICP-MS and the fifth chapter of this doctoral thesis describes the sample pre-treatment processes for preparing biological tissues and matrix standards, as well as for imaging by LA-ICP-MS. Laboratory-made porcine gelatin standards produced not only qualitative but also quantitative images, demonstrating competent and reliable capabilities for imaging studies. High-speed scanning and low laser fluency allowed sensitive and quantitative bioimaging studies with high spatial resolution. Imaging datasets of tissues from unexposed and TiO_2 NPs exposed aquaculture species were obtained and compared. The data collected were used to locate prominent areas of TiO_2 NPs, as well as to better understanding of the distribution pattern. These initial findings proved the potential of LA-ICP-MS imaging studies to provide crucial information on the distribution of NPs in fish tissues.

I. INTRODUCTION

1. NANOMATERIALS AND INORGANIC NANOPARTICLES

1.1 Background and fundamental concepts

The American physicist Richard Feynman, Nobel Prize laureate in 1965, introduced the ideas that would become the foundation of nanotechnology in a conference titled "Plenty of Room at the Bottom" delivered in the meeting of the American Physical Society in December 1959. Feynman is commonly considered as the father of nanotechnology [1], despite his talk went unnoticed for several years and his paper in the journal Engineering and Science was only cited seven times during the following twenty years. The lecture's title, "Plenty of Room at the Bottom" suggested that things could be made much, much smaller than they were and still work, so it was time to see how small we could make them. In this conference given more than 60 years ago, Feynman was already persuaded of the immense possibilities that existed if scientific community could operate on a tiny scale: "In the year 2000, when they look back at this age, they will wonder why it was not until the year 1960 that anybody began seriously to move in this direction"; "I can hardly doubt that when we have some control of the arrangement of things on a small scale we will get an enormously greater range of possible properties that substances can have, and of different things that we can do" [2].

Nanomaterials (NMs) and nanotechnology have radically changed the scientific scenario during the past decades. Several disciplines, such as physics, chemistry, engineering, mechanics, and medicine [3], stand to benefit greatly from this new technological development. These changes are considered as a new industrial revolution. Nanoscience is the study of the characteristics and manipulation of materials with at least one dimension between 1 to 100 nanometers (10^{-9} metres), or, in other words, materials consisting of a few hundred or thousands of atoms organised in a certain manner. On the other hand, nanotechnology is defined as "the design, characterization, production and application of structures, devices and systems by

controlling shape and size at the nanoscale" [4]. Regarding the term "nanomaterials", scientists have not agreed on a specific definition. The International Organization for Standardization (ISO) has described nanomaterial as a "material with any external nanoscale dimension or having internal nanoscale surface structure" [5]. The Food and Drug Administration (FDA) also refers to NMs as "materials that have at least one dimension in the range of approximately 1 to 100 nm and exhibit dimension dependent phenomena" [6].

In 2011, the European Commission (EC) released the Recommendation 2011/696/EU [7], which contained one of the most well-established definitions for NMs. Conversely, this concept was recently modified and revised in the EC Recommendation 2022/C229/01 of 10 June 2022 [8]. Thus, the term "nanomaterials" embraces all the materials specified by the EC today as: "a natural, incidental or manufactured material consisting of solid particles that are present, either on their own or as identifiable constituent particles in aggregates or agglomerates, and where 50 % or more of these particles in the number-based size distribution fulfil at least one of the following conditions:

a) one or more external dimensions of the particle are in the size range 1 nm to 100 nm;

b) the particle has an elongated shape, such as a rod, fibre or tube, where two external dimensions are smaller than 1 nm and the other dimension is larger than 100 nm;

c) the particle has a plate-like shape, where one external dimension is smaller than 1 nm and the other dimensions are larger than 100 nm."

Therefore, the original definition of NM described in the Recommendation 2011/696/EU, underwent three key modifications in the current EC Recommendation 2022/C229/01 of 10 June 2022: the dimensional requirements of NMs have been presented and distinguished from other entities; NMs are restricted to solid particles only, excluding liquid particles in emulsions or gaseous particles; and finally, "contains" has been replaced by "consists of" in the definition, so that the term now refers to a material by itself, not to ingredients or parts of other materials. Also, it is important to emphasize the

following definitions clearly associated to NMs [8]: (a) "particle" means a minute piece of matter with defined physical boundaries; single molecules are not considered 'particles'; (b) "aggregate" means a particle comprising of strongly bound or fused particles; and (c) "agglomerate" means a collection of weakly bound particles or aggregates where the resulting external surface area is similar to the sum of the surface areas of the individual components.

There is a common misconception that NMs, and mainly inorganic nanoparticles (NPs), are materials that emerged at the end of the 20th century from a laboratory. Volcanic ash, sea spray, fine sand, and organic matter are examples of incidental by-products of natural processes that have historically and now contributed to their presence of NMs in the environment [9,10]. Nevertheless, it is also true that scientists and engineers did not create methods capable of comprehending, controlling, and harnessing the vast potential of these surprising and outstanding materials until the end of the 20th century. Since the first explorations about NMs and NPs, the scientific community interest on NMs has increased very fast as shown in **Figure 1**. The research publications represent applications in a variety of scientific disciplines such as chemistry, biology, physics, and medicine, among others.

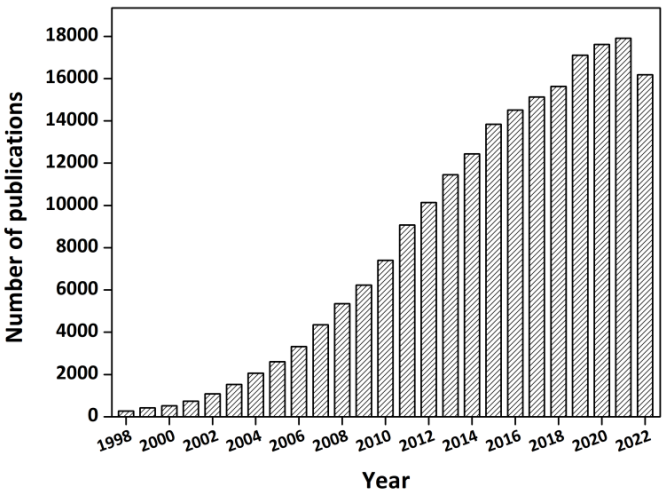

Figure 1. Number of publications per year on inorganic nanoparticles. (Source: Web of Science)

To better understanding the qualities and possible applications of NMs and NPs, they require to be categorised. Despite their wide variety, NMs are often classified according to one of three factors: where they originated, how many nanoscale dimensions they possess, or their chemical composition. Considering their origin, there are three distinct sorts of NMs. First, there are "NMs of natural origin" which are created by natural occurrences and processes such sandstorms, forest fires, volcanic ash, and marine aerosols, as previously mentioned [9]. The second category consist of “incidental NMs,” which is of anthropogenic origin but are formed accidentally by combustion processes or material wear and tear, among other sources. The third category, “engineered NMs” is corresponded to those NMs and/or NPs manufactured or synthesised purposely in the laboratory.

Considering the number of dimensions at the nanoscale, up to three types can be distinguished: one-dimensional NMs, such as nanotubes, polymeric nanofibers or nanorods; two-dimensional NMs, such as monolayers or polymeric films; and, finally, when the three dimensions are within the nanoscale, they are referred as nanoparticles.

The nanomaterial composition is the final, and probably the most prevalent and identification category. In this scenario, there are two primary categories: organic and inorganic NMs. Carbon atoms are the only component of organic NMs implying several entities such as fullerenes, dendrimers, and liposomes. Inorganic NMs provide a broad range of entities that can be separated into two subgroups: quantum dots (QDs) and inorganic nanoparticles (NPs) in which metallic nanoparticles (such as Ag NPs and Au NPs) and nanoparticles from metal oxides and hydroxides (such as CuO NPs, TiO_2 NPs, and ZnO NPs, among other) are included.

Quantum dots are semiconducting NPs that are often made of sulphides, selenides, and tellurides of Zn, Cd, or Hg. Due to their size, a quantum confinement effect is obtained, which is responsible of the exceptional optoelectric properties (high fluorescence quantum yield, broad absorption bands, narrow and symmetric emission spectra, and high photostability) of these NMs [11,12]. Regarding NPs, their size and structure endow them with unique features that their bulk

counterparts above this tiny scale lack [13]. **Figure 2** shows a comparison of the size of NPs with other entities from nanoscale to macro-scale.

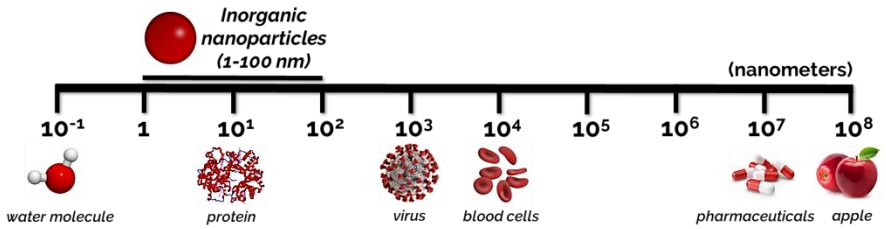

Figure 2. Comparative size scale from nanoscale to macro-scale.

1.2 Outstanding properties and applications

Nanotechnology is currently present in a variety of applications in industry, science, and technology. Nanomaterials are used in industrial sectors as pharmaceuticals, food, textiles, cosmetics, electronics, medicine, the production of renewable energies, as well as environmental applications [3]. Nanoscale materials are of great interest since their physicochemical, electrical, and optical properties are vastly different from those bulk materials [13,14]. One of the most significant distinctions between a bulk material and its nano-sized equivalent is the higher surface area to mass ratio of the nano-sized material, which results in enhanced reactivity [15]. The optical, magnetic, and electrical characteristics of NMs differ from those at the micrometre scale due to electronic confinement that causes quantum effects to predominate when the dimensions fall below nanometer-scale [15]. Furthermore, excellent antibacterial, antifungal, and antimicrobial capabilities, as well as the capacity of several NPs to absorb ultraviolet (UV) radiation, are several of the most common commercial applications of NMs today [3]. Therefore, NMs are present in many household products (sunscreens, cosmetics, fabrics, foodstuff, computers, sport equipment, etc.) [16].

Certain physicochemical properties that severely influence their behaviour or may contribute to their toxicity deverse our attention. These properties include NPs size or size distribution, shape, aggregation and agglomeration state, chemical composition, surface

area, charge, among others [10,17,18]. In addition, the Z-potential is a frequently used as a measurement for estimating the stability of particles in solution and their susceptibility to be dispersed, agglomerated, or settled, and it relies on the charge of the particles and the medium's parameters (pH and ionic strength) [19]. Among the vast diversity of NPs, Ag NPs and TiO_2 NPs stand out from the other ones because of their several applications. However, there are various further NPs with interesting uses that deserve important attention. Gold NPs have been extensively studied and their use in mainly focused on biomedicine for developing diagnostic and/or visualisation techniques, and also as carriers for therapeutic drugs transfer to target organs [20,21]. SiO_2 NPs are one of the most commonly used NMs worldwide in terms of mass manufacturing [16], whereas CeO_2 NPs are frequently used as catalysts or catalyst supports in the automobile sector [22]. Due to the photo-oxidizing and photocatalytic characteristics, ZnO NPs are used as an antibacterial agent [23] and as a UV radiation blocker in sunscreens [24].

Particularly interesting and innovative physicochemical capabilities of Ag NPs include excellent electrical and thermal conductivity and catalytic potential. Based on the StatNano database, **Figure 3** [16] provides an overview of the most prominent implementations of Ag NPs in society today. The most widespread application is mostly due to the excellent antibacterial properties [25]. Coating and surface charge of Ag NPs also contribute to their antibacterial effectiveness [26,27]. Currently, the exact mechanism by which Ag NPs display their antibacterial action remains uncertain. Because of their antimicrobial qualities, their uses reach several industries, such as the textile industry, medical equipment, wastewater treatment [28], and surface nano-coatings during the pandemia derived from Corona Virus disease (COVID-19) [29]. In addition, Ag NPs are often used as contrast agents, in cosmetics formulations, and for preparing biological and chemical sensors [28].

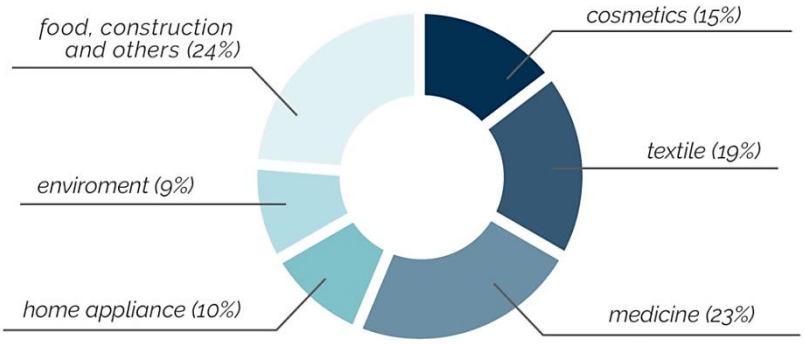

Figure 3. Applications of silver nanoparticles.
(Source: StatNano, 2021. Nanotechnology Products Database (NPD))

The most prominent areas of use of TiO_2 NPs are displaced in **Figure 4**. Titanium dioxide was originally employed as a pigment because it provides whiteness and opacity owing to reflection and no absorption of visible light. The bulk material is applied to a variety of goods, including coating materials, foodstuff, inks, and toothpaste, among others. TiO_2 NPs are also utilised as an antibacterial agent due to their photo-oxidant and photo-catalytic qualities [30]. The use as antimicrobial agent is due to the production of ROS after UV light exposure because [31]. This process also allows TiO_2 NPs to be an efficient UV light-blocking agent. The antibacterial mechanisms of TiO_2 NPs and Ag NPs are still unknown. Moreover, the size and shape of the NPs, as well as the presence of other elements in doped composites, affects and also can enhance the catalytic and photocatalytic activity [30]. TiO_2 NPs has several remarkable usages in the field of electronics, including the manufacturing of sensors and solar cells, photo-catalytic degradation of contaminants [32], and nano-coating of surfaces with self-cleaning characteristics during the COVID-19 emergency [29].

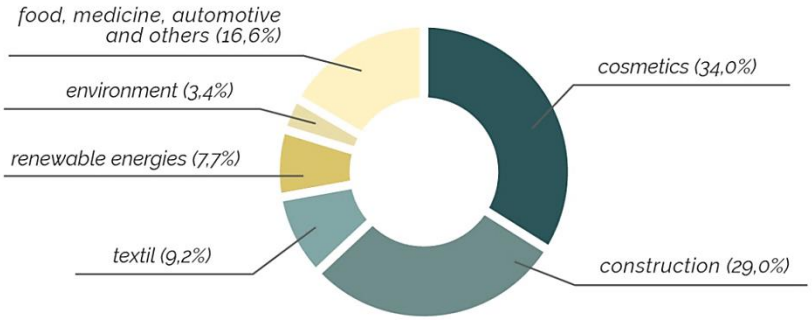

Figure 4. Applications of titanium dioxide nanoparticles. (Source: StatNano, 2022. Nanotechnology Products Database (NPD))

The additive E-171, which contains a substantial portion of TiO_2 NPs, is frequently used in the food industry to make food more aesthetically appealing or to colour foodstuff as a whitening and opacifying chemical. Even though there is substantial discussion about the use or restriction of this food ingredient [33]. Despite the fact that a rule banning the manufacturing or importation of E171-containing foods into the EU came into force in August 2022, the European Court of Justice (ECJ) annulled the European Commission's regulation in November 2022, and it is uncertain what will occur in the coming months and years. Additionally, health safety officials in the United States, Canada, and the United Kingdom authorised its use as a food additive in early 2022.

1.3 Emerging pollutants and problems

Because of their outstanding physicochemical properties and the widespread use of NMs, especially NPs, concerns about the potential toxicity due to NMs releasing into the environment and, consequently, the risk to humans and the marine ecosystem have been raised [34,35]. The potential risk of NPs exposure is still unknown due to the lack of toxicological evidence. Official government authorities have proposed regulations to control the use and labeling of NPs, while companies throughout the world exploit their innovative features and exploring different uses [10]. Because of their high surface reactivity, NPs have a significant role in environmental processes [36]. Nanoparticles' degree of toxicity can be influenced by a important number of factors:

chemical composition, size, surface coating or modification, and other physical and chemical properties [10,17,18].

To evaluate the environmental risk associated by these new emerging pollutants in terms of uptake and biological impact, toxicity studies must be conducted. Unfortunately, because the characteristics of NPs in the aquatic environment vary, the real impact of their presence in the aquatic environment is still unclear and difficult to investigate [37], just as NPs are often found in low concentrations in the marine environment. Therefore, the development of powerful and reliable nanometrological platforms is required for the monitoring, determination, and characterization of NPs in marine organisms. Current NPs determination methodologies include techniques such as UV-Visible spectroscopy, Dynamic Light Scattering (DLS), X-ray diffraction (XRD), and a variety of microscopy techniques. Inductively coupled plasma mass spectrometry (ICP-MS) based technologies, involving single-particle (spICP-MS), Dynamic-Reaction-Cell (DRC) technology, single-cell (scICP-MS) and laser ablation (LA-ICP-MS), could be the most promising ones. All these approaches provide the analyst a description of the NP's physicochemical attributes by different approaches.

2. AQUACULTURE: GLOBAL STATUS AND FUTURE PERSPECTIVES

2.1 Background and importance of aquaculture

Aquaculture is the cultivation of aquatic organisms under controlled conditions, primarily for human consumption. It is a concept connected to agriculture in which fish are used instead of plants or animals. Aquaculture is also known as fish cultivation and is practiced around the world in different environments/facilities: freshwater ponds, rivers, and even on land in tanks, among others. Food and Agriculture Organization of the United Nations (FAO), founded in 1945, is one of the largest specialized agencies of the United Nations, and define aquaculture as follows: "Aquaculture is the farming of aquatic organisms, including fish, molluscs, crustaceans and aquatic plants. Farming implies some form of intervention in the rearing process to enhance production, such as regular stocking, feeding, protection from predators, etc." In addition, aquaculture is a crucial basis of the FAO's Blue Transformation plan [38], which aims to increase the role of aquatic foods in feeding the Earth planet through climate and environmentally-friendly policies and practices, as well as technical advancements. In regard with the period from 1990 and 2020 the aquaculture had experienced a growth over 600%, with an average growth rate of 6.7% [39,40].

Despite the stagnation of catch fisheries output since the late 1980s and the rising demand for fish and fishery products, aquaculture has been the driving force behind the enormous expansion of the worldwide supply as it is illustrated in **Figure 5**. Oceans' natural productivity is currently considered as ended, since they can no longer naturally meet the demand for seafood and the yearly capture of edible marine protein has surpassed the highest rate. Aquaculture is the method for closing the seafood supply gap. The primary responsibility of aquaculture is to efficiently complement wild-caught fish options to increase the amount of seafood available worldwide.

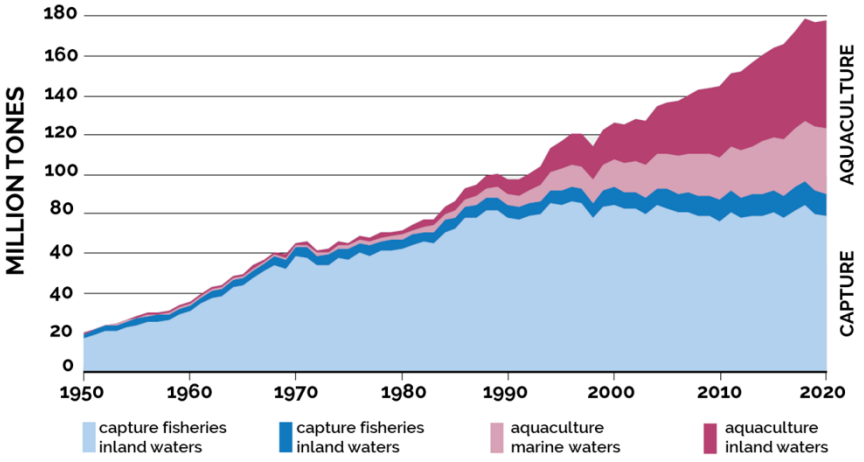

Figure 5. World captures fisheries and aquaculture production. Data from the FAO report 2022 [39].

Aquaculture is frequently the major source of many edible aquatic creatures, such as Atlantic salmon, sea bass, and warm-water prawns. **Figure 6** shows the world aquaculture production based on the type of species in agreement with the Spanish Business Association of Aquaculture (APROMAR) [41]. Nowadays, the goal is to increase global aquaculture output by up to 40% from 2020 to 2030 in a sustainable manner in order to meet the rising demand for aquatic food while creating employment and ensuring incomes [39]. Because of overfishing of our seas and other natural resources raises annually, new seafood sources are required to feed the world's expanding population, since as reported by the United Nations (UN) 10 billion people is expected to inhabit the planet by 2050 [42]. The answer for future generations to have access to healthy and ecologically friendly protein sources is to raise fish ethically and sustainably.

Aquaculture is not only essential, but also a sustainable alternative for consumers when compared to other forms of farmed protein. Compared to chicken, pig, and beef, fish and, especially seafood, retains more protein than any other dietary items [43]. In addition, aquaculture also offers lower environmentally impacts when producing edible animal protein, and emitts less greenhouse emissions

than other agricultural practices [44,45]. Therefore, aquaculture has the potential to improve the health of our planet and the health of our population, and it must be developed as an environmentally friendly and socially responsible activity, also considering food safety and animal welfare [39,46,47].

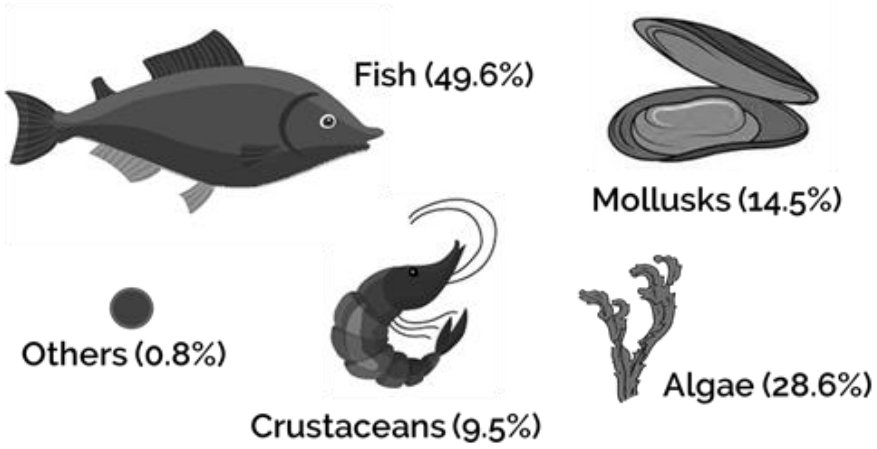

Figure 6. Distribution percentage of aquaculture production (t) in 2020 by group [41].

2.2 Status-quo: Europe, Spain, and Galicia

2.2.1 Europe

Today, the aquaculture industry provides more than 50% of the fish and aquatic foods consumed by humans, and this expansion is paralleled by a plateau in the volume of fish from traditional capture fisheries, as is illustrated in **Figure 5**. In contrast, aquaculture in the EU is facing stagnation and the rate of growth of fish farming in EU states has been extremely sluggished since 2000. In fact, aquaculture has expanded by only 1.1% annually compared to 4.3% overall during the past decade. In 2019, EU aquaculture production accounted for less than 2% of global production and only 10% of all seafood consumed in the EU [41].

Despite these facts, Europe boasts 55,000 kilometres of coastline, the second-longest in the world behind Canada, as well as favourable environmental, physical, and oceanic conditions for

aquaculture. In addition, Europe's aquaculture industry has proved to has the expertise, experience, and technical resources to be environmentally sustainable, commercially viable, and socially responsible, with secure and high-quality employment. According to the most recent data, Europe's aquaculture production accounts for 2.7% of the global total [41] as showed in **Figure 7**. Norway is the clear leader in aquaculture production in Europe, followed by Turkey according to Federation of European Aquaculture Producers (FEAP). The majority of Norwegian production is committed to intensive Atlantic salmon farming, which is the most important activity and accounts for more than 80% of the country's overall aquaculture output. Also on the entire European continent, the aquaculture production of two species, sea bass and sea bream, stands out with 298,083 tonnes and 321,911 tonnes in 2021, respectively. In general, EU aquaculture production in 2020 was 1,094,315 tonnes (552,625 tonnes of fish).

Aquaculture in the EU took place mainly in marine waters (72.6%), whereas 27.4% is produced in freshwaters. Regarding farmed species, the main farmed fish species produced in EU was rainbow trout (183,506 tonnes in 2020), followed by sea bream (93,131 tonnes) and sea bass (81,369 tonnes) also in 2020 [39]. In addition to the excellent environmental conditions of EU for fish/shellfish farming, EU states are leaders in technology and research, and have well-trained human resources. Another positive aspect is the high regulatory standards that EU has put in place to ensure food safety from aquaculture products as well as ensuring a scrupulous respect for the environment. This feature can be also considered a disadvantage for the progress of aquaculture, because a demanding legal regulatory framework can increase the production costs because of the environmental constraints [41].

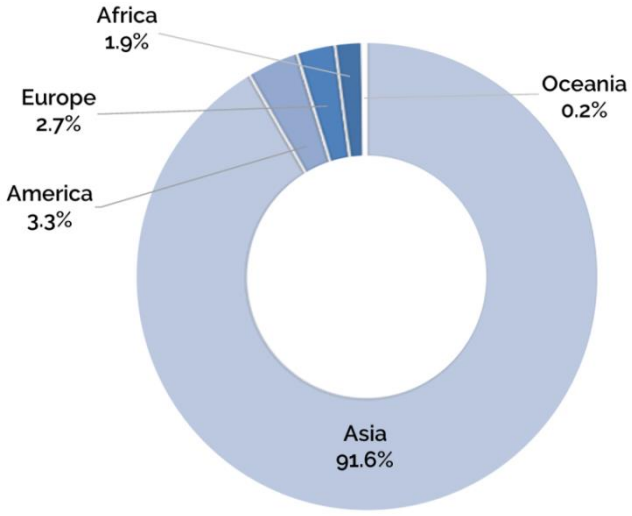

Figure 7. Distribution of aquaculture production by continent. Data from the APROMAR report [41].

2.2.2 Spain

Spain is a country with a long fishing tradition and a significant culture of fish consumption. The geographical position and peninsular layout (also two archipelagos) make Spain to be a country with a favourable environment for aquaculture practices. In addition to the large coastline (more than 8,000 kilometres), Spain has numerous water resources such as nine major rivers, lakes, reservoirs, and minor rivers. The range of conditions across the country has allowed for the existence of a wide variety of species and implies a significant opportunity for the expansion of aquaculture production of fish, mollusks, crustaceans, and even algae. Spain leads the EU in terms of aquaculture fish captures (more than 5,000 aquaculture facilities in operation and production) and accounts for 25.3% of the EU total in 2020 with 276,571 tonnes. Considering the production value, APROMAR has stated that Spain is the second producer in EU after France (525.8 million euros, 15.6% of the total). In 2021, the aquaculture harvest in Spain would amount to 327,309 tonnes with a first sale value of 629,0 million euros. The 327,309 tonnes may be split down primarily into four species, with mussels (255,303 tonnes)

as a leader species, followed by sea bass, rainbow trout, and sea bream [41].

Marine fish farming in Spain reached 58,761 tonnes in 2021, and the sea bream harvest represented 9,632 tonnes. Valencian Community was the leader in cultured sea bream (5,486 tonnes, 57% of the total). Regarding sea bass harvest from aquaculture facilities, a total of 23,924 tonnes were produced in 2021 being Andalusia the leader with 7,365 tonnes (31% of the total). Other species such as rainbow trout had significant productions (15,357 tonnes) as well as turbot and sole, both leaded by Galicia (7,629 and 1,027 tonnes, respectively) [41,48]. Consequently, numerous areas can be distinguished within the Spanish territory: the Northwest Zone for the production of mussels, clams, and turbot (Galicia as the main producing region); the Continental Zone (trout and sturgeon production); the Mediterranean Zone for the production of sea bream, sea bass, and corvina; the South Atlantic Zone for the production of sea bream and sea bass; and the Canary Islands Zone for the production of sea bream and sea bass.

In addition to the aquaculture productivity, Spanish scientists have published more than 150 aquaculture-related articles every year, more than those published by other European reserachers. Therefore, scientific literature regarding aquaculture by Spanish researchers ranked fifth globally in the amount of scientific articles published in aquaculture in 2021 [49].

2.2.3 Galicia

Galicia is a perfect place for the development of aquaculture activities due to the geographical and climatic characteristics, such as more than 1,500 kilometres of coastline (Galician Community is surrounded by the Atlantic Ocean and the Cantabrian Sea), and the abundance freshwater resources. In addition, Galicia has a long tradition in fishing and seafood is the basic foodstuff of the referred "Atlantic Diet". The first mussel farm in Galicia was established in 1945, and currently there are more than 3,300 mussel farms that produce more than 250,000 tonnes of shellfish annually [48,50], making Galicia the world leader in the production of this specie.

Galicia is also a leader in the production and marketing of turbot (Galician fish farms generate 95% of the farmed turbot and sole sold in Spain and 85% of the farmed turbot and sole sold in Europe). In addition to these two species, there is significant outputs of slender clam, fine clam, and Japanese clam; also cockles, curly oysters, flat oysters, scallops, and rainbow trout; and several red, green, and brown seaweed species (see **Table 1**).

Aquaculture in Galicia has significant scientific research support with specialised institutes funded by the regional sdministration, and outstanding technology which contribute to high-impact scientific initiatives that allow a sustainable development of aquaculture activities. Consequently, the need for boost aquaculture production to satisfy global demand represents an opportunity for the Galician community which will require a constant investment and technological development for improving the production and for investigating new marine species.

Table 1. Main species of Galician aquaculture production in 2021: weight and value. [50]

Species	Weight (tones)	Production value (€)
Seaweed (total)	2.7	14600
Japanese clams	1458.6	16,742900
Mussels	251202.2	139,204800
Oyster	933.3	2,930000
Cockles	836.4	4,329400
Turbots	7629.7	56,212400
Sole	649.0	7,278200
All species	262997.8	233,151000

2.3 Sustainability, challenges and future vision

As has been mentioned, the international community faces the tremendous issue of maintaining an adequate supply of food and nutrients for a growing population while assuring sustainable economic, social, and environmental growth by 2050, when the global population is projected to reach over 10 billion [42]. Currently, around

17% of the world's animal protein consumption is derived from fish [39], and the development of the aquaculture sector would face the challenge of the future animal protein requirements.

The FAO is pushing a plan known as “Blue Transformation”, which is a concerted effort to secure and maximise the contribution of aquatic food systems (both from marine and inland waters) to food safety, nutrition, and affordable and nutritious meals for all population. Blue transformation explores sustainable aquaculture, minimising the impact on the environment and the lives of people throughout the world [39]. Blue Transformation defines three main objectives, as follows:

- “Sustainable aquaculture expansion and intensification – to support global food security targets and satisfy global demand for nutritious aquatic food and equitable distribution of the benefits.”
- “Effective management of all fisheries – to deliver healthy stocks and secure livelihoods.”
- “Upgraded value chains – to ensure the social, economic and environmental viability of aquatic food systems, and secure nutritional outcomes.”

To achieve these objectives, one of the greatest challenges currently facing aquaculture is the production of fish fed with sustainable and safe diets that allow normal development and growth of fish in captivity [40,51]. Moreover, aquaculture sector must ensure food safety for the consumer, despite numerous obstacles: new pathogens, climate change, and misuse of antimicrobials [51]. In order to remove the use of unsustainable sources, new ingredients must be developed, where prebiotics and probiotics constitute two attractive areas of investigation. When administered in active form, these chemicals positively modify the gut microbiome, imparting immunocompetence against pathogenic organisms, providing a substantial contribution to sustainability, and the reducement of therapeutic quantities [51]. In many aquaculture systems, the use of chemicals intended to prevent and treat diseases, including antimicrobials, has grown widespread. The overuse of antimicrobials

in aquaculture is problematic since can contribute to the creation and spread of antimicrobial-resistant genes and bacteria [52].

Moreover, there is a huge concern because climate change may become the greatest challenge to guarantee the maintenance and expansion of sustainable aquaculture worldwide [53–55]. Climate change has a double negative impact on fisheries and aquaculture, impacting both the availability of fishery resources and the productivity of aquaculture. This new reality necessitates a greater capacity to adapt to consequences such as: reduction of resources in traditional fishing areas; changes in the composition of catches; reconversion to be able to fish new species; increased occurrence of meteorological phenomena; and the emergence of new diseases and new pathogens with greater virulence associated with extreme climates. Toxic algal blooms are rising in frequency, volume, duration, geographical spread, and species composition on a global scale, mostly due to human activities. Their effects on output vary substantially based on species-specific effects [40,54].

In response to all of these issues to control biological and climatic risks and promote sustainable aquaculture production, recirculating aquaculture systems and offshore aquaculture have the greatest potential to overcome the challenges mentioned [56,57]. Recirculating aquaculture systems are designed to control all environmental aspects of production through continuous filtration, treatment, and reuse of water, thereby increasing operational efficiency and reducing risks associated with pathogens, parasites, and pests, as well as climate change [51]. However, these systems are constrained by high energy needs, high manufacturing prices, and waste disposal issues. On the other hand, offshore aquaculture in deep water and oceanic waters is a very appealing resource because it is designed to produce large volumes of fish while minimising land constraints due to competition with animal production and limiting environmental impact in freshwater and along the coast. To minimise conflicts with other marine uses and to guarantee adequate dilution of trash, however, judicious placement is essential [51,56]. Regarding the installation of enormous underwater cages, Norway and China currently lead the way in offshore fish farming [58,59].

Concurrently with the development of these strategies, public and private rules and standards must be established for aquaculture systems in order to enhance the environmental and social performance of aquaculture practices and technology. Nevertheless, the inconsistent execution of government laws has resulted in regional differences in output, development, and design of aquaculture systems. While governments in many Asian nations have promoted the rise of aquaculture, in other places, like EU and the United States, aquaculture growth have been restricted [60].

3. NANOTOXICITY: POTENTIAL HAZARDS TO THE ENVIRONMENT

3.1 Raising concerns and singular behaviour

Since the rapid growth and potential impact of nanotechnology, raising concerns regarding NMs releasing into the environment, and consequently, the potential risk to humans and ecosystem, have been generated. In order to evaluate the environmental risk associated by these novel pollutants, in terms of uptake and biological impact, data are required from toxicity studies. Aquatic environment and aquatic life are also exposed to NMs which could affect marine organisms by different mechanisims. However, the concentrations of metals and NPs at background levels in the natural environment are quite low, far from the high doses required for acute toxicity testing.

Unfortunately, because NPs vary their characteristics in the aquatic environment, the true impacts of their presence in the aquatic environment are yet unknown and difficult to study [37,61,62]. Nanoparticles are inherently unstable, and are susceptible to undergo physical, chemical, and biological processes once released in the environment (**Figure 8**). Several factors that might affect the toxicity from NPs (and also regulate environmental transformations) include the chemical composition, size, form, surface coating or modification, solubility characteristics, and other physical and chemical features [63].

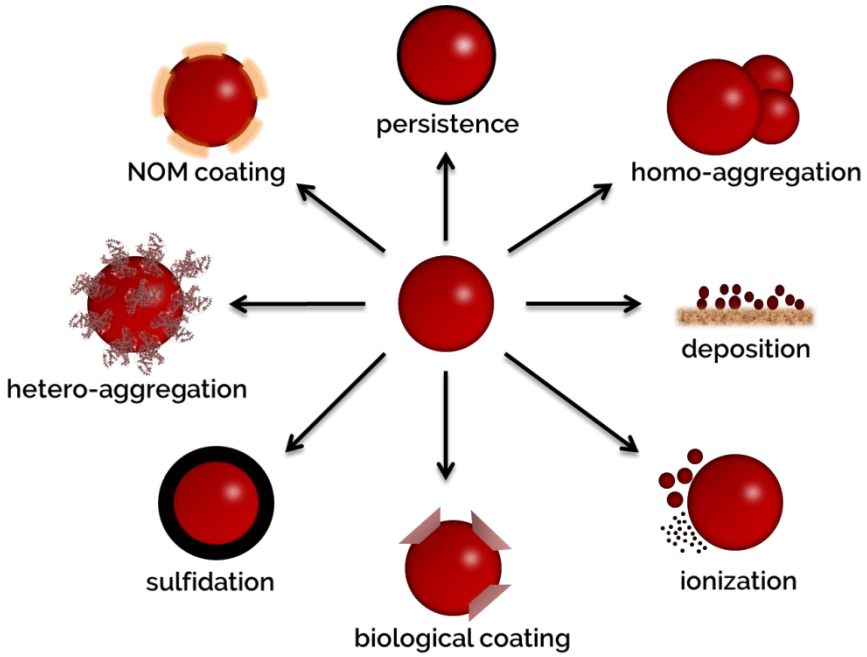

Figure 8. Schematic overview displaying the main physical, biological and chemical transformations of nanoparticles in the aquatic environment [61,62].

The behaviour of the NPs depends not only on the properties of the NPs but also on the aquatic environmental conditions, and the type and composition of the water. Nanoparticles in natural waters are often coated by natural organic matter (NOM), which is thought to have a stabilizing effect via charge repulsion (produced by carboxylic acid functional groups) and steric interactions inhibits aggregation [64]. Surface charge and reactivity is also a crucial phenomena due to affect NPs stability and aggregation as well as interactions with other substances and pollutants [64]. Agglomeration and sedimentation are the most relevant physicochemical processes affecting TiO_2 NPs in seawater, whereas ionization is the main phenomenea for Ag NPs under environmental conditions.

Therefore, nanotoxicity studies (nanotoxicology) pursue better understanding and knowledge about the potential threats caused by

NPs in the different ecosystems, aquatic organisms, and also in human health. Due to their ability to bind or interact with biological components as well as the alteration of their surface properties, these studies present several obstacles [61,62]. Disruption of membrane integrity, protein destabilization and oxidation, nucleic acid damage, ROS generation, and toxic and harmful compounds releasing are potential toxicological pathways caused by NPs exposure [65,66]. Many of the harmful activities arise from the production of free radicals by NPs. When the NPs are irradiated with light, often UV, the absorption of a photon with energy larger than or equal to their band gap occurs and an electron jumps from the valence band to the empty conduction band resulting in the production of an electron-hole pair and ROS. Different oxygen species have been recognized to originate ROS ($^{\cdot}O_2^-$, $^{\cdot}OH$, and H_2O_2) [67].

Nanoparticles may be taken up by cells through a variety of mechanisms, although endocytosis predominates because to their tiny size. Exposure to NPs causes modifications in organelles including mitochondrial malfunction, endoplasmic reticulum stress, and lysosomal rupture. Nanoparticles have the potential to trigger cell death, reduce cellular metabolic activity, and change cell function and appearance [66]. In addition, NPs may cause direct or indirect damage to extracellular membranes and intracellular membranes of the nucleus, mitochondria, and lysosomes, affecting their structure, shape, and stability. Also, NPs can cause the formation of membrane holes. The interaction that may take place between NPs and cellular membranes are strongly connected to NPs characteristics such as size, surface charge, and concentration [65,66].

The primary routes of NP entrance into the human body are ingestion, inhalation, and skin penetration [68]. Regarding Ag NPs and TiO_2 NPs, humans could become exposed through inhalation, ingestion, and skin penetration cause of broad use water disinfectants, sunscreens, food additives, textiles, and paints [68]. Due to the

prevalence of NPs in food, the vast absorption area, and the relatively rapid translocation rate, oral absorption is the most significant route of entry for NPs into the human body [69]. Transcellular and paracellular transporters could enable ingested NPs to cross the epithelium, reach the blood stream, and potentially reach different organs [70]. The digestion process can affect the physicochemical characteristics of NPs, mainly by dissolution or aggregation, and it may alter NPs toxicity. Therefore, different toxicity studies must be conducted to better understanding how NPs can bioaccumulate in marine products and consequently affect to human health once seafood are ingested.

3.2 Marine environment and toxicity studies

Nanoparticles can reach the marine environment from several sources, including industrial discharges, wastewater treatment, and atmospheric deposition. Once in marine systems, NPs are subjected to a highly dynamic environment and may experience a variety of reactions and transformations that alter their physicochemical characteristics [37]. These processes involve redox reactions, NPs ionisation, aggregates/agglomerates formation, and interactions with other surrounding chemicals [61,62]. As stated in the preceding section, the behaviour of NPs in the marine environment is dependent on their physicochemical qualities and environmental conditions [61,62].

The existence of NPs in nature may result in harmful impacts, and they may undergo bioaccumulation, biomagnification, and biotransformation. Bioaccumulation can be defined as the build-up of chemicals, usually harmful, in the body of an organism, from different exposure sources (mainly water, air or diet) that are not metabolized or excreted, and consequently accumulate over time. Biomagnification is the increase in the concentration of these toxic chemicals in the food chain, whereas biotransformation is described as the bioactivation process that may produce reactive and more hazardous metabolites or

compounds. In view of the mentioned NPs toxicity, two additional terms—bioavailability and bio-accessibility—gain considerable importance. Bioavailability refers to the fraction of a compound that can be taken up by the body, entering in the circulation system and being able to have an active effect. Finally, an additional term, less extended, is bioaccesibility which refers to the fraction of a compound that is released from the food matrix in the gastrointestinal tract and consequently, is available for absorption. The information acquired from toxicity studies (focused on bioaccumulation, bio-accessibility, and bioavailability) enables for the evaluation of the environmental risk posed by these pollutants, as well as the effects on different aquaculture species under varied exposure scenarios.

The research of the possible toxicity of NPs to humans is a difficult attempt that focuses predominantly on the impact of exposure to these substances in cell lines, called *in-vitro* studies. *In-vitro* tests are designed to replicate the mechanical and physiological parameters (enzyme and salt content, pH, temperature, residence time) of every stage of the gastrointestinal digestion process to assess the NPs activity after intake [71]. To establish the bio-accessibility of NPs, they should undergo a simulated digestion process emulating human gastrointestinal digestion in the stomach and small and large intestines. The complexity and heterogeneity of the investigations makes it difficult to reach feasible conclusions on the toxicity of NPs: different cell lines or tissues examined, exposure conditions, and NP attributes (composition, size, concentration, and chemical coatings among others).

Several types of NPs have demonstrated hazardous impacts on different marine organisms, including bacteria, algae, molluscs, and fish. Chemical toxicity induced by ion release or ROS generation and physical stress owing to the size, shape, and surface features of NPs are believed to be the primary mechanisms involved for NP toxicity, despite their dependency on environmental conditions and the studied

species [72,73]. Important parameters as form, surface coating, and ionic solutes' release of harmful ions must be considered when evaluating the toxicity of NPs in fish [18,63]. For instance, the toxicity of TiO_2 NPs increases with particle size and in the presence of humic acid and other pollutants. In addition, the animal lethality increases under light exposure due to the phototoxic effects and free radical generation. There are disagreements over whether or not bigger particles are more hazardous than tiny ones as there are researches with contradictory results [63]. In addition, as previously stated, the concentrations of NPs used in the toxicity studies carried out are always far greater than those found in the natural environment.

Due to their small size and rapid development, zebrafish embryos are frequently used for the study of NPs toxicity in marine organisms [63]. Also, these organisms provide other favourable characteristics such as high fecundity, embryo transparency, and short reproduction time. In addition, some studies have been conducted on the organs from fish exhibiting potential toxicity and effective bioaccumulation after NPs exposure, including species such as rainbow trout [74], goldfish [75,76], and aforementioned zebrafish [63,77]. According to several studies, the most impacted organs in fish species include the gills, gut, liver, and brain. In addition to the production of novel enzymes engaged in antioxidant defences, oxidative stress is a proposed cause of NPs' fish toxicity. This effect is most commonly associated with dissolved metals, although it also occurs after NPs exposure [78]. Major toxicity processes are regulated directly or indirectly by the formation of reactive oxygen species, and consequently, free radicals. As it is displayed in **Figure 9**, these ROS can emerge the antioxidant defence system, lipid peroxidation, protein denaturation, mitochondrial dysfunction, and DNA damage [65].

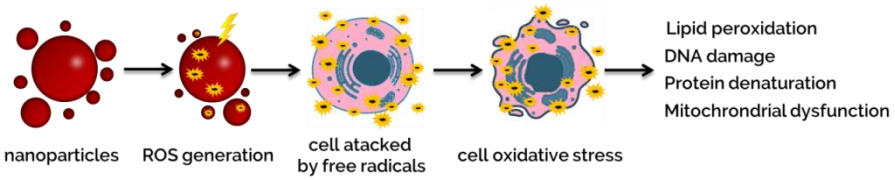

Figure 9. Toxicity effects induced by the NPs generation of reactive oxygen species (ROS) [65].

3.3 Current legislation and safety questioning

Unfortunately, there is no standardised regulatory framework governing the usage of NMs in the food industry. The complexity of NMs, the diverse characteristics and applications, and the absence of reliable information on their toxicological effects, leads to be difficult the establismnet of an uniform and globally harmonized agreement [79,80]. The objective of Regulation (EC) No 178/2002 is to provide a common basis for management action plan to products at national and EU level, enabling the unrestricted movement of products between European states, focus on ensuring a high level of safety for human and animal health, and protect consumer interests through actions along the food production chain. To this objective, the applied regulations are based on scientific evidence and a thorough risk evaluation conducted by independent authorities as the European Food Safety Authority (EFSA), which is responsible for supplying scientific and technical information, providing conclusions, and addressing to food safety emergencies. Moreover, EFSA aims to harmonise assessment criteria for NMs and to simplify the data exchange and available information. Concerning this, EFSA is continuously publishing and updating recommendations as follows: “Guidance for risk assessment of the application of nanomaterials to be applied in the food and feed chain: human and animal health” [81].

On the other hand, the European Chemicals Agency (ECHA) is responsible for Registration, Evaluation, Authorization, and Restriction of Chemicals (REACH) and Classification, Labeling, and Packaging (CLP) responsibilities. ECHA has additionally produced “Guidance on Information Requirements and Chemical Safety

Assessment." EU legislation is the most rigorous and restrictive compared to the regulations of non-EU governments. In spite of the aforementioned challenges, there are numerous rules referring to the use of NMs in several application areas, including product labelling ((EU) No 1169/2011), food packaging ((EU) No 10/2011 and (EC) 450/2009), and the use of additives ((EC) 1333/2008) where NMs must be registered in the EU before use.

Concerning the presence of NPs in foodstuff, the occurrence and use of E-171 food additive must be noted. E-171 incorporates a significant amount of TiO_2 NPs and is commonly used to make food more aesthetically appealing or to colour food as a bleaching and opacifying chemical. Several food categories, including candy products and sweets, fine baked products, different sauces, snacks, and milk could contribute to dietary exposure to E-171 additive [33]. In 2016 EFSA concluded that E-171 was not a threat to consumer health. By contrast, some years later, in May 2021, EFSA experts report that genotoxicity (potential of a chemical to damage DNA) cannot be ruled out for titanium dioxide and a safe daily consumption limit for the dietary E-171 additive could not be established. Finally, the use of titanium dioxide (E-171) as a food additive was banned in the EU as of 7th February 2022 in compliance with Commission Regulation (EU) 2022/63. Despite the regulation prohibiting the manufacturing or import of food containing E-171 in the EU came into force in August 2022, the ECJ annulled the EC regulation in November 2022. In addition, early in 2022, health authorities in the United States, Canada, and United Kingdom authorised the use of E-171 as a food additive.

One of the main responsibilities of the EU regarding food safety is to ensure food safety by providing sustainable and high-quality aquaculture products on the European market. In recent years, the EC has funded a significant number of research projects aimed at enhancing aquaculture from several approaches, namely animal welfare, sustainability, and food safety. Concerning the impact that NPs have on the aquaculture sector, NANOCULTURE and

ACUINANO projects funded by European INTERREG programmes have intended to increase the knowledge, risk assessment, and management of the environmental presence of Ag NPs and TiO_2 NPs in aquaculture products (clams, mussels, sea bass, sea bream, turbot, and seaweed). In addition, food safety of cultured products was verified, and their influence on human consumption was evaluated. These research project have involved many institutions as the International Nanotechnology Iberian Laboratory (INL) placed in Braga (Portugal), the Interdisciplinary Centre for Marine and Environmental Research (CIMAR) placed in Porto (Portugal), the Indigo Rock Marine Research Station located in Cork (Ireland), the Galician Aquaculture Cluster (CETGA), and Galician universities (University of Santiago de Compostela (USC) and University of Vigo (UVIGO)).

4. ADVANCED ANALYTICAL METHODOLOGIES

Inductively coupled plasma mass spectrometry is one of the most powerful and versatile techniques for trace and ultra-trace multielemental analysis. ICP-MS strengths include fast multi-elemental analysis, excellent sensitivity, a broad analytical working range, isotopic information, and accurate determination in a huge variety of matrices. Moreover, ICP-MS can be easily coupled to diverse sample introduction systems. Samples are introduced into the ICP-MS equipment using a nebuliser system, which consists of a nebuliser and a spray chamber that generates a polydisperse droplet aerosol. Once the droplets are in the plasma source, the solvent evaporates, forming solid particles from which the elements in those vaporized particles are further ionized. Ions are pulled through the interface into the mass spectrometer, where they are separated and identified based on their mass-to-charge ratio (m/z). As a result, the mass of element entering the plasma per unit time and traveling to the detector as ions can be assumed to be constant, resulting in a stable signal during the reading period. In contrast, if the sample contains NPs, the element is no longer homogeneously distributed, but rather appears as distinct clusters of atoms that require a new analytical approach, as explained in the following sections. This thesis is focused on the development and application of novel approaches employing ICP-MS in various working modes such as dynamic reaction cell (DRC) technology, single particle-ICP-MS (spICP-MS), single cell–ICP-MS (scICP-MS) and laser ablation–ICP-MS (LA-ICP-MS).

4.1 DRC Technology

Despite its many benefits, ICP-MS has some disadvantages as the incidence of spectral and non-spectral interferences. These interferences can emerge from the plasma gas, the sample matrix, and the solvent solution. They produce polyatomic species with the same

mass-to-charge ratio (m/z) as the analyte. Several approaches for overcoming the limitations derived from ICP-MS interferences have been developed, including cold plasma conditions, mathematical correction equations, sector-field ICP-MS (SF-ICP-MS), and collision/reaction cell technologies [82–85]. In regard with collision/reaction cells, interferences can be eliminated by selective reactivity of the analyte and/or interfering ion with a reactive gas or by collision of the ions with a non-reactive gas (often He) in conjunction with Kinetic Energy Discrimination (KED). DRC technology involves a quadrupole enclosed in a reaction chamber between the ionic lens system and the analyzer quadrupole, as it is displayed in **Figure 10**. The cell is filled with a reactive gas which interacts with the ion beam through a variety of ion-molecule reaction processes, enabling interferences to be removed or analytes to be shifted to m/z free-interference regions. The use of DRC technology requires the evaluation of the reaction gas flow rate and the ion guide dynamic bandpass involving Mathieu parameter values (RPq and RPa values), also known as rejection parameters, which are described as a stabilised mass bandpass regulating the low mass and high mass cut-off limits, respectively [86].

Several studies have outlined two available strategies for DRC technology: on-mass mode, which operates with the elemental mass-to-charge ratio; and the mass-shift approach, which operates with the mass-to-charge ratio shifted to a different region of the mass spectra monitoring the formed ion products [87]. Usually, the mass-shift work-mode is more advantageous than the on-mass approach for eliminating interferences. Nevertheless, sensitivity and stability of the measurements are also factors to consider, and they may lead to consider on-mass approaches as the most appropriate strategy in some cases. Lower reaction gas flows are used in the on-mass mode and a collisional focusing effect is observed as a consequence of ion confinement (longer path in the ion guide) due to energy losses from multiple collisions in the cell, which increases the instrumental response and contributes to detection limits improvements [88,89].

Various reaction gases, including H_2, CH_4, O_2, CH_3F, and NH_3, can be used in DRC technology. According to the research literature,

the reaction gas O_2 has a high and predictable reactivity [90,91], while H_2 is utilised specifically to eliminate Ar interferences [92]. Alternatively, the NH_3 reaction gas exhibits a high and also less predictable reactivity [87]. The uncontrolled production of ammonia clusters or ion products is advantageous compared to other reaction gases that permit interferences to be overcome. Lower reaction efficiency (in comparison to O_2) is compensated by high selectivity by generating several adducts or ion-products moving the analysis to the m/z without interferences. The use of reaction gases in spICP-MS (determination of NPs) is scarcer than in ICP-MS (determination of dissolved or ionic analytes) as the NPs behaviour in the cell differs significantly from that of dissolved analytes due to the different structure, size, and properties of the nanoparticulate forms. Despite this fact, the scientific literature reported the application of O_2, H_2, NH_3, and CH_3F as reaction gases in the assessment of several NPs [88,93,94].

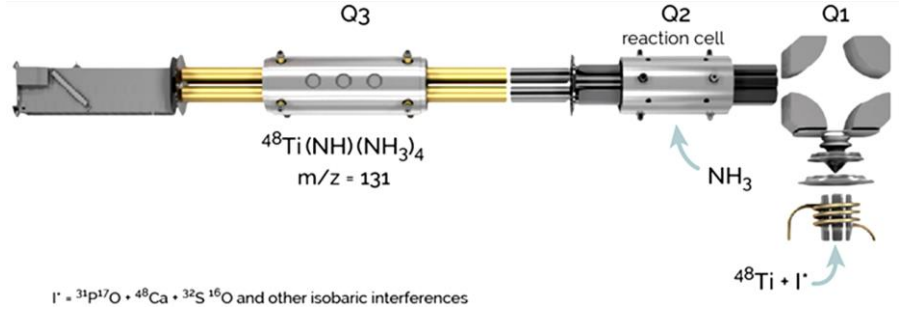

Figure 10. Schematic view of the DRC technology and application to Ti free-interference determination using ammonia as a reaction gas.

4.2 Single-particle

Inductively coupled plasma mass spectrometry in single particle detection mode (spICP-MS) has attracted a significant increase in interest in order to complement other available techniques for the NPs determinations [95]. Degueldre and Favarger reported the first study on spICP-MS in 2003 that was focused on colloids [96]. spICP-MS can precisely detect the mass and number concentration of individual NPs (particles L^{-1}) as well as the dissolved content levels in the

background, obtaining information at very low concentration levels (ng L^{-1} ranges). Moreover, the equipment is also capable to measure the average particle mass/size, and particle mass/size dispersion [97].

Depending on whether the analyte is dissolved or particulate in the sample solution, the analyte's behaviour is completely different in the plasma once is injected. Dissolved species are distributed uniformly throughout the solution and the signal received remains constant during the acquisition or scan time. Alternatively, if this solution contains NPs in suspension, the NPs will not be uniformly distributed, but will be collected in groups of atoms, and their ionisation in the plasma could produce a burst of ions that will be recorded by the spectrometer as pulses or events [98]. Due to the background caused by the dissolved species, NPs ionisation or polyatomic species in the plasma or sample matrix, each sibgle particle may then be recorded as a discrete event on a continuous baseline [97]. In this sense, the number of pulses or events registered is proportional to the number of particles contained in the sample and so provides information on the particle concentration. By other side, the pulse intensity is proportional to the mass of the analyte. If the nanoparticle's chemical composition, shape, and density are specified, this intensity recorded can reveal information about its size. External calibration procedures can also be used to quantify the dissolved content from the background intensity.

The dwell time (suitable adjustment of the detector event detection time) and an appropriate low enough sample concentration for achieving NPs to reach the detector individually are critical steps to overcome the major weakness in the calculations of this method: partial measurement counting (due to too short dwell times) or double counting of particle events (too long dwell time or high sample concentration). The high data acquisition frequency is directly governed by the dwell time but in recent years it has been feasible to reduce dwell times from milliseconds to microseconds [97]. These improvements essentially allow working with higher concentrations of NPs without signal overlap, making the analysis significantly more accurate and obtaining detection limits that are less affected by the background signal. After the signals have been processed, a set of

mathematical equations must be used for NPs assessment in terms of both number concentration and size.

Based on the theoretical principles of the spICP-MS technology described by Degueldre and Favarger [96,99,100], and consolidated by Laborda [98,101,102], these mathematical equations were derived in the equations illustrated in this section. As stated previously, the number of detected events (n_p) within a given acquisition time (t_i) is proportional to the number concentration of particles (C_p), assuming each detected event corresponds to a single particle, according to the **Equation I.1**, where n_{neb} is the nebulisation/atomisation efficiency, and Q_{sam} is the sample introduction flow rate.

$$n_p = n_{neb} \times Q_{sam} \times t_i \times C_p \quad (\mathbf{Eq.I.1})$$

Alternatively, the intensity of each event (I_p) is proportional to the number of atoms per particle and thus to the element mass per particle (m_p) as it is illustrated in the **Equation I.2**, where $K_{ICP\text{-}MS}$ is the detection efficiency defined as the ratio of the number of ions detected to the number of atoms introduced in the ICP-MS; and K_M is related to the atomic abundance of the monitored isotope and the atomic mass of the element (M_m).

$$I_p = K_{ICP-MS} \times K_M \times m_p \quad (\mathbf{Eq.I.2})$$

In the case of spherical NPs with a homogenous composition, it is also possible to compute the particle size given the particle's mass, if the composition, shape, and density are specified, using the **Equation I.3**. In this equation d represents the diameter, ρ is the density, and XP is the mass percentage of the element in the particle.

$$I_p = 16 \times \pi \times X_p \times K_{ICP-MS} \times K_M \times d^3 \quad (\mathbf{Eq.I.3})$$

Finally, mass detectability must be specified by assessing the lowest NP size capable to be detected (the height of the pulse with the least intensity discriminated from the baseline or background). Using the 3σ criteria, where σ is the standard deviation of the continuous

background signal, the equation **Equation I.4** can be applied to determine the size detection limit (LOD_{size}) as follows:

$$LOD_{size} = \left(\frac{18\,\sigma}{\pi \times X_p \times K_{ICP-MS} \times K_M} \right)^{1/3} \quad (\mathbf{Eq.\,I.\,4})$$

4.3 Single-cell

In-vitro tests can give substantial information on the internalisation capability of NPs or dissolved metals in cells, as well as on the possible hazards and risks of NPs in the environment. Trace element quantification in individual cells remains an analytical challenge due to the difficulties of this type of study and the lack of methodologies to address this issue. ICP-MS has frequently been utilised for quantitative investigations of cellular uptake of NPs and other trace elements by determining the total content following acid digestion of the pellet. Nevertheless, this type of experiment does not account for the variability that may occur between individual cells in the uptake of analytes, as it is assumed that all cells take up and accumulate these components in a same manner. Most of traditional approaches for measuring the element and/or NPs contents in cells require a procedure including lysis, extraction, and digestion stages [103,104].

Single cell-ICP-MS (scICP-MS) has become one of the most promising emerging techniques for quantitative study of trace elements and NPs in single cells. This technology provides high-quality qualities such as the analysis close to the native state of the cell, ability to distinguish single cells, ultrasensitivity of attograms per cell levels and minimal sample uptake of 10 µL min^{-1} [105,106]. Furthermore, the innovative Asperon™ chamber, displayed in **Figure 11** incorporates tangential Ar gas flow to prevent cell damage, collision, or deposition on the walls.

Like the spICP-MS, a suspension of cells is nebulised using a specific scICP-MS introduction system. Consequently, once each cell enters the plasma, the released elements are ionised, and the subsequent ionic burst of intrinsic elements is identified by ICP-MS

using the same approach of data acquisition as described in the previous section. In scICP-MS analysis, each cell is considered to be a separate entity that produces its own ion burst [105]. Similar to spICP-MS where the intensity of the events are proportional to the mass of the particle and the frequency of the pulses to the number of particles in the sample, in scICP-MS the intensity of the events provides information on the mass of the analyte inside (associated) a single cells, whereas the number of events is proportional to the number of cells that have accumulated the analyte under investigation [107]. Cellular constituents such as phosphorus, magnesium, and manganese can be monitored as cell population indicators [108,109].

The introduction of cells into the plasma is one of the major barriers in scICP-MS. Conventional cyclonic spray chambers typically remove cells that range in size from 1-100 µm. To overcome this barrier, PerkinElmer designed the novel Asperon™ introduction system which enables the entrance of micron-sized entities. Moreover, as previously stated, the Asperon™ spray chamber design as well as the flow patterns specifically positioned, provide a tangential inert gas flow that prevents cell contact and deposition on the walls [105].

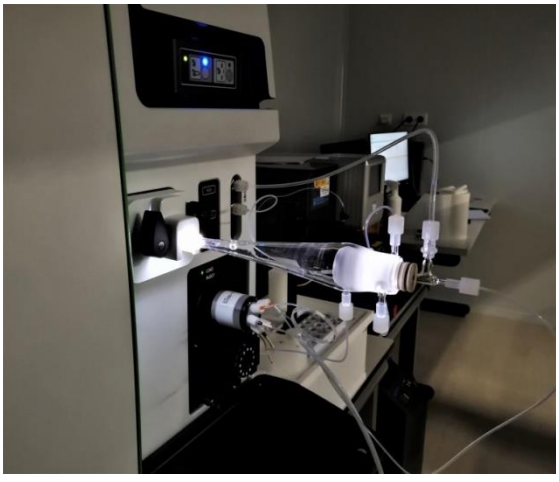

Figure 11. Single-cell-ICP-MS introduction system: innovative Asperon™ Spray chamber.

Cells isolation from the culture medium followed by re-suspension in isotonic solutions are needed to avoid the measurement of the ionic forms of the elements (or NPs) in the culture solution, and also to dimisnish the presence o matrix (culture medium) constituents [105]. This step could help to avoid high dissolved backgrounds, interferences, and extra particles from masking the signal generated by individual cells. Similarly to spICP-MS, diluted cell suspensions are required to minimize the detection of multiple events in a single pulse, ensuring that every pulse corresponds to a single cell [108].

Current studies exploiting scICP-MS for the assessment of trace elements at the level of individual cells are still scarce. However, this technique has been used in several studies on cellular bioavailability [107], as well as elements in cancer cells [108], bacterial cells [110], and algae [111]. The technique is therefore expected to be a powerful technology for several applications such as metal toxicity and environmental studies, and assays for assessing drugs effectiveness.

4.4 Laser Ablation

Elemental biodistribution (imaging) in biological tissues has emerged as a useful technique to support toxicity studies. Nanomaterials, particularly inorganic NPs, are emerging pollutants whose potential influence on the marine environment demands the development of novel monitoring and control strategies. Therefore, laser ablation–ICP-MS (LA-ICP-MS) imaging studies (example of elemental biodistribution of Pt in **Figure 12** [112]) could be a breakthrough aiming the visualisation of metal distribution, and hence, to obtain qualitative and quantitative data derived from NPs analysis.

Numerous analytical techniques have attracted great interest for biological tissue imaging and elemental bioimaging [113–115], but are generally challenging to implement due to expensive equipment or laborious sample preparation. LA-ICP-MS is widely used in tissue imaging as it provides high quality features, such as relatively low cost, small amount of sample, wide dynamic range, multi-element

detection, less incidence of spectral interferences, high spatial resolution, and simple sample preparation [116]. In addition, high sensitivity is reached at μg g^{-1} or ng g^{-1} levels [117,118]. The basis of this technique is the use of high-powered lasers to ablate the surface of a solid sample arranged in an ablation cell in an inert atmosphere at atmospheric pressure. The area impacted by the laser becomes an aerosol of the vapour phase constituents and the ablated material is transported by an inert gas flow (Ar or He) to the ICP-MS torch, where it is then atomised and ionised to perform a conventional ICP-MS analysis.

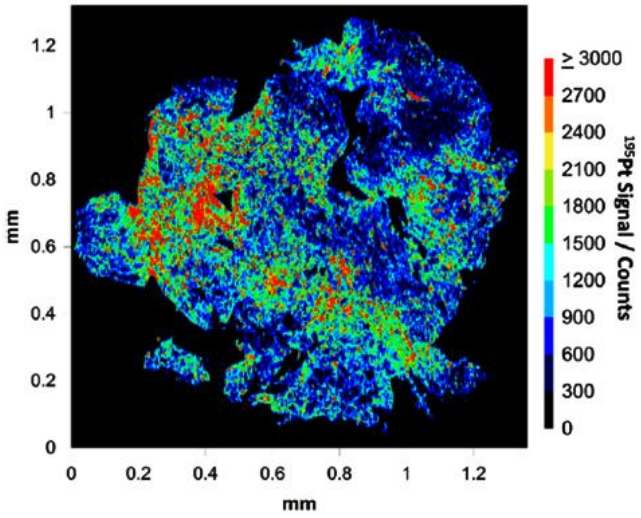

Figure 12. LA-ICP-MS imaging studies: spatial biodistribution of Pt in cisplatin-treated tumour [112]**.**

Despite its remarkable capabilities, LA-ICP-MS is limited by a number of basic factors [116]. The most significant constraint is a process known as elemental fractionation, which occurs when the abundances of the measured ions are not entirely representative of the original sample's composition. This phenomenon can occur at various stages of laser ablation [119]. Elemental fractionation could occur throughout aerosol production due to the preferred ablation of more

volatile constituents of the sample. Elemental fractionation might also occur during the transport of the aerosol from the ablation chamber to the ICP torch if particles of different sizes are involved, and also if a portion of the solid aerosol is deposited in the tube used for transport. In addition, changes in ICP-MS atomisation and ionisation may potentially contribute to elemental fractionation. Another significant constraint is the variation in the interaction between the laser beam and the sample surface depending on the characteristics of various matrices, which could produce variations in the amount of ablated analyte per pulse [116]. These matrix effects usually require a careful optimisation of the laser ablation parameters. In addition, if the standards and samples have different chemical matrices, the plasma ionisation efficiency and, thus, the instrumental response may vary during quantification, and the term for this phenomenon is referred as mass loading effect [120].

The absence of appropriate reference materials or standard matrix-matched materials complicates LA-ICP-MS quantitative analysis and imaging studies. Nowadays, there is still disagreement on establishing a universal calibration protocol for efficient quantifications [116,121]. Frequently, internal standards (IS) are utilised to compensate for variations in the ablation process, aerosol transport, and possible instrumental drift. The selected IS should behave similarly to the analyte during the operation and be distributed uniformly within the sample. The most common IS is ^{13}C; however other options have been based on using ^{32}S [122], ^{115}In [123], and ^{44}Ca [124]. In addition to the use of the adequate IS, an appropriate quantification approach is needed. Some strategies have been found to be efficient for quantitative analysis [125,126], and laboratory-produced standards derived from gelatinous substances (mainly porcine gelatin standards) are gradually becoming more widespread in order to be applied for soft tissues analysis [127,128].

As previously stated, LA-ICP-MS has experienced a significant increase in the number of analytical publications for trace and isotope analysis. Bioimaging LA-ICP-MS applications can also be found mainly focused on cells [129], and tissues from tumours [112] and several organs [130,131]. In regard with the analysis and bioimaging of NPs, some studies were also conducted by using LA-ICP-MS for characterizing Au NPs in biomaterials, evaluate the uptake in macrophages of Ag NPs or to assess the effect derived from TiO_2 NPs exposure in the reproductive toxicity of Cd. [132–134].

4.5 Complementary techniques

Due to the vast number of qualitative and quantitative properties that must be assessed to identify, characterise, and measure NPs, a combination of complementary analytical methods is required [135,136]. Electron microscopy methods (mainly Transmission Electron Microscopy (TEM)) are the most prevalent for the characterization of NPs because they provide the visualisation of their metallic core and the acquisition of data on their size, shape, and aggregation state [136] (**Figure 13** shows a TEM high resolution image for 100 nm Ag NPs standard). Moreover, TEM can be hyphenated with spectroscopic techniques such as Energy Dispersive X-ray Spectroscopy (EDXS), and the hyphenated technique allows the determination of the nanoparticle's elemental composition. Other important electron microscopy methods are Scanning Electron Microscopy (SEM) and Atomic Force Microscopy (AFM).

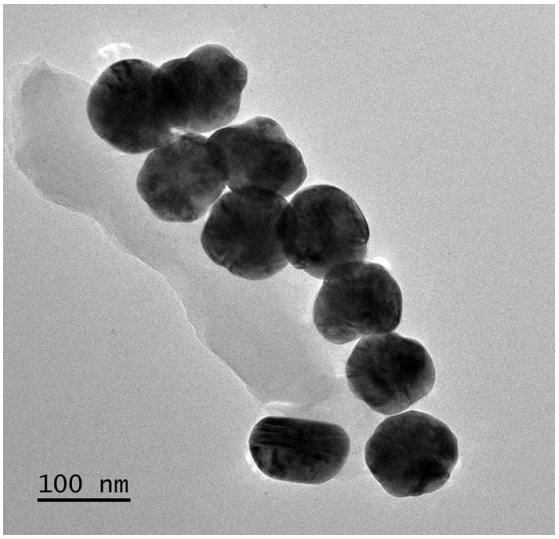

Figure 13. TEM image obtained from Ag NPs standard of 100 nm.

By visualising the position of internalised NPs in cells, as well as changes in the NPs or morphological alterations induced in the cells, TEM is also a highly valuable technique for determining potential interaction and toxicity processes [136]. By contrast, drawbacks are relatyed to the long sample preparation (clean-up procedures when dealing with complex samples) and analysis times, the high cost of the instrumentation, the need for a high concentration of NPs, and the need for several number images to obtain a representative analysis.

X-Ray Diffraction (XRD) and EDXS allow determining the elemental composition of NMs, and XRD gives information regarding the crystalline phases, the shape, and the average size. In this methodology, the X-ray beam collides on the NPs at a certain angle (θ), and diffracted X-rays are produced and collected at a second angle (2θ) depending on the distance between the planes that comprise the crystalline structure of the nanomaterial [137].

Light scattering methods, give information on the physico-chemical properties of the scattered NPs, such as their hydrodynamic

diameter and zeta potential. The most prevalent light scattering methods are Dynamic Light Scattering (DLS) and Electrophoretic Light Scattering (ELS). DLS is the most popular approach for measuring the hydrodynamic diameter of dispersed NPs, which requires knowing not only the size of the metallic core, but also the size of the electrical double layer that develops surrounding the particle due to its suspension (see **Figure 14**). The zeta potential reveals the surface charge of a particle and the degree of aggregation of particles in suspension, providing information on the level of repulsion or attraction between them [136].

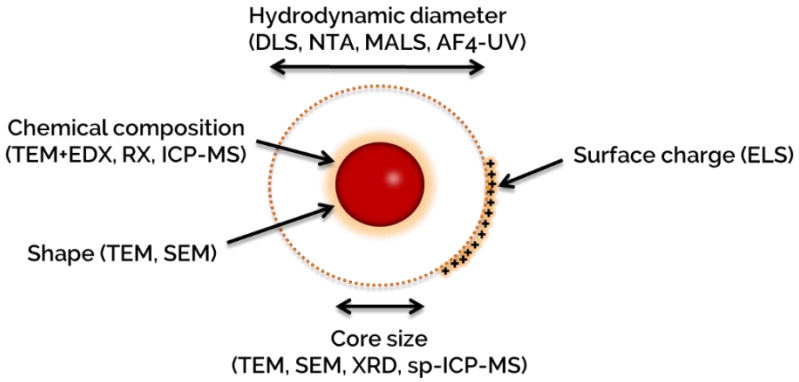

Figure 14. Analytical information provided by the most important methodologies for the characterization of inorganic NPs as individual entities [135,136].

In addition, NPs have been characterised using both chromatographic and non-chromatographic separation techniques. Hydrodynamic chromatography (HDC) is the most often employed chromatographic technique followed by size-exclusion chromatography (SEC). By contrast, Field Flow Fractionation (FFF) is a family of non-chromatographic techniques based on the application of an external field perpendicular to a laminar flow. The separation occurs when the applied field generates a sufficient mobility difference between NPs in the sample travelling toward the channel outlet. Regarding the

separation and analysis of NPs, Asymmetric-FFF (AF4) is the most popular technique to date. In AF4, the applied external field is a secondary flow, referred to as cross-flow that flows perpendicularly to the conducting flow of the system, which runs in a laminar regime (laminar flow) through the separation channel. Thus, particles that enter this laminar flow are pulled by the external field (cross-flow) to the base of the separation channel or accumulation wall, where they travel in the opposite direction of the applied field [136,138]. Therefore, their separation is a result of the equilibrium between the force of the external field and the opposing force produced by the particles propelled by the conducting flow, as it forces the NPs to be retained for a certain period depending on the particle size.

As conclussion, a combination of complementary analytical methods is required for a full characterisation of NPs (characteristics displayed in **Figure 14** and **Figure 15**) [135,136].

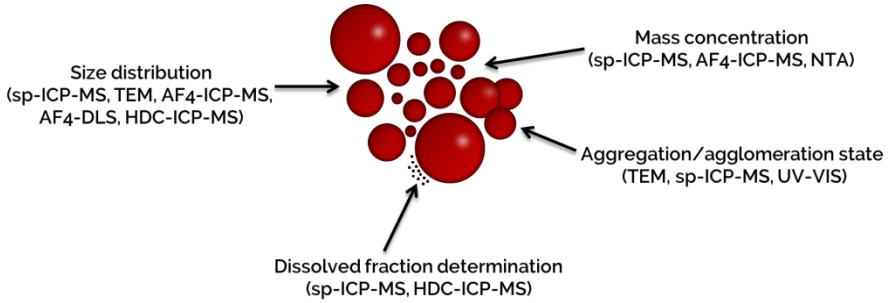

Figure 15. Analytical information provided by the most important methodologies for the characterization of inorganic NPs all-inclusive [135,136]**.**

REFERENCES

[1] “Plenty of room” revisited, Nat. Nanotechnol. 4 (2009) 781. https://doi.org/10.1038/nnano.2009.356.

[2] W.G. Eberhard, W.T. Wcislo, Plenty of room at the bottom?, Am. Sci. 100 (2012) 226–233. https://doi.org/10.1511/2012.96.226.

[3] A. López-Serrano, R.M. Olivas, J.S. Landaluze, C. Cámara, Nanoparticles: A global vision. Characterization, separation, and quantification methods. Potential environmental and health impact, Anal. Methods. 6 (2014) 38–56. https://doi.org/10.1039/c3ay40517f.

[4] Scientific Committee on Emerging and Newly Identified Health Risks (SCENIHR). Modified opinion (after public consultation) on the appropriateness of existing methodologies to assess the potential risks associated with engineered and adventitious products, . http://ec.europa.eu/health/ph_risk/documents/synth_report.pdfStakeholdercomments:http://ec.europa.eu/health/ph_risk/documents/stakeholder_comments.zip (accessed February 22, 2023).

[5] ISO/TS 80004-1:2015, Nanotechnologies – Vocabulary – Part 1: Core Terms. International Organization for Standardization. https://www.iso.org/obp/ui/#iso:std:iso:ts:80004:-1:ed-2:v1:en (accessed February 23, 2023).

[6] Considering whether an FDA-Regulated product involves the application of nanotechnology | FDA. https://www.fda.gov/regulatory-information/search-fda-guidance-documents/considering-whether-fda-regulated-product-involves-application-nanotechnology (accessed February 23, 2023).

[7] Commission Recommendation of 18 October 2011 on the definition of nanomaterial (2011/696/EU), Official Journal of the European Union, L275 (20 October 2011) 38–40.

[8] Commission Recommendation of 14 June 2021 on the definition of nanomaterial (2022/C229/01), Official Journal of the European Union, C229 (14 June 2021) 1–5.

[9] Institute of Medicine. Implications of Nanotechnology for Environmental Health Research. Washington, DC: The National Academies Press. https://doi.org/10.17226/11248.

[10] J. Jeevanandam, A. Barhoum, Y.S. Chan, A. Dufresne, M.K. Danquah, Review on nanoparticles and nanostructured materials: History, sources, toxicity and regulations, Beilstein J. Nanotechnol. 9 (2018) 1050–1074. https://doi.org/10.3762/bjnano.9.98.

[11] I.L. Medintz, H.T. Uyeda, E.R. Goldman, H. Mattoussi, Quantum dot bioconjugates for imaging, labelling and sensing, Nat. Mater. 4 (2005) 435–446. https://doi.org/10.1038/nmat1390.

[12] J.M. Costa-Fernández, R. Pereiro, A. Sanz-Medel, The use of luminescent quantum dots for optical sensing, TrAC - Trends Anal. Chem. 25 (2006) 207–218. https://doi.org/10.1016/j.trac.2005.07.008.

[13] N.S. Wigginton, K.L. Haus, M.F. Hochella, Aquatic environmental nanoparticles, J. Environ. Monit. 9 (2007) 1306–1316. https://doi.org/10.1039/b712709j.

[14] M.F. Hochella, S.K. Lower, P.A. Maurice, R.L. Penn, N. Sahai, D.L. Sparks, B.S. Twining, nanominerals, mineral nanoparticles, and earth systems, Science. 319 (2008) 1631–1635. https://doi.org/10.1126/science.1141134.

[15] F.C. Adams, C. Barbante, Nanoscience, nanotechnology and spectrometry, Spectrochim. Acta - Part B At. Spectrosc. 86 (2013) 3–13. https://doi.org/10.1016/j.sab.2013.04.008.

[16] Nanotechnology Products Database | STATNANO. https://product.statnano.com/ (accessed December 27, 2022).

[17] X. Liu, E. Dumitrescu, A. Kumar, D. Austin, D. Goia, K.N. Wallace, S. Andreescu, Differential lethal and sublethal effects in embryonic zebrafish exposed to different sizes of silver nanoparticles, Environ. Pollut. 248 (2019) 627–634. https://doi.org/10.1016/j.envpol.2019.02.085.

[18] L. Truong, T. Zaikova, B.L. Baldock, M. Balik-Meisner, K. To,

D.M. Reif, Z.C. Kennedy, J.E. Hutchison, R.L. Tanguay, Systematic determination of the relationship between nanoparticle core diameter and toxicity for a series of structurally analogous gold nanoparticles in zebrafish, Nanotoxicology. 13 (2019) 879–893. https://doi.org/10.1080/17435390.2019.1592259.

[19] K. Luyts, D. Napierska, B. Nemery, P.H.M. Hoet, How physico-chemical characteristics of nanoparticles cause their toxicity: complex and unresolved interrelations, Environ. Sci. Process. Impacts. 15 (2012) 23–38. https://doi.org/10.1039/c2em30237c.

[20] K.F. Chu, D.E. Dupuy, Thermal ablation of tumours: biological mechanisms and advances in therapy, Nat. Rev. Cancer. 14 (2014) 199–208. https://doi.org/10.1038/nrc3672.

[21] L. Dykman, N. Khlebtsov, Gold nanoparticles in biomedical applications: recent advances and perspectives, Chem. Soc. Rev. 41 (2012) 2256–2282. https://doi.org/10.1039/c1cs15166e.

[22] J.G. Dale, S.S. Cox, M.E. Vance, L.C. Marr, M.F. Hochella, Transformation of cerium oxide nanoparticles from a diesel fuel additive during combustion in a diesel engine, Environ. Sci. Technol. 51 (2017) 1973–1980. https://doi.org/https://pubs.acs.org/doi/abs/10.1021/acs.est.6b03173.

[23] M.T. Islam, A. Dominguez, B. Alvarado-Tenorio, R.A. Bernal, M.O. Montes, J.C. Noveron, Sucrose-mediated fast synthesis of zinc oxide nanoparticles for the photocatalytic degradation of organic pollutants in water, ACS Omega. 4 (2019) 6560–6572. https://doi.org/10.1021/acsomega.9b00023.

[24] S. Nafisi, H.I. Maibach, Nanotechnology in cosmetics, Cosmet. Sci. Technol. (2017) 337–361. https://doi.org/10.1016/B978-0-12-802005-0.00022-7.

[25] J. Helmlinger, C. Sengstock, C. Groß-Heitfeld, C. Mayer, T.A. Schildhauer, M. Epple, Silver nanoparticles with different size and shape: equal cytotoxicity, but different antibacterial effects, RSC Adv. 6 (2016) 18490–18501. https://doi.org/10.1039/c5ra27836h.

[26] A.M. El Badawy, R.G. Silva, B. Morris, K.G. Scheckel, M.T. Suidan, T.M. Tolaymat, Surface charge-dependent toxicity of silver nanoparticles, Environ. Sci. Technol. 45 (2011) 283–287. https://doi.org/10.1021/es1034188

[27] C.C.S. Batista, L.J.C. Albuquerque, I. De Araujo, B.L. Albuquerque, F.D. Da Silva, F.C. Giacomelli, Antimicrobial activity of nano-sized silver colloids stabilized by nitrogen-containing polymers: the key influence of the polymer capping, RSC Adv. 8 (2018) 10873–10882. https://doi.org/10.1039/c7ra13597a.

[28] Q.H. Tran, V.Q. Nguyen, A.T. Le, Silver nanoparticles: Synthesis, properties, toxicology, applications and perspectives, Adv. Nat. Sci. Nanosci. Nanotechnol. 4 (2013). https://doi.org/10.1088/2043-6262/4/3/033001.

[29] A.K. Singh, Nanostructured coatings based on metallic nanoparticles as viral entry inhibitor to combat covid-19, Sustain. Mater. Technol. 35 (2023) e00544. https://doi.org/10.1016/j.susmat.2022.e00544.

[30] Y. Nam, J.H. Lim, K.C. Ko, J.Y. Lee, Photocatalytic activity of TiO2 nanoparticles: a theoretical aspect, J. Mater. Chem. A. 7 (2019) 13833–13859. https://doi.org/10.1039/c9ta03385h.

[31] A. Raghunath, E. Perumal, Metal oxide nanoparticles as antimicrobial agents: a promise for the future, Int. J. Antimicrob. Agents. 49 (2017) 137–152. https://doi.org/10.1016/j.ijantimicag.2016.11.011.

[32] M. Tayyab Noman, M. Azeem Ashraf, A. Ali, Synthesis and applications of nano-TiO2 : a review, Environ. Sci. Pollut. Res. 26 (2014) 3262–3291. https://doi.org/10.1007/s11356-018-3884-z.

[33] M. Younes, G. Aquilina, L. Castle, K.H. Engel, P. Fowler, M.J. Frutos Fernandez, P. Fürst, U. Gundert-Remy, R. Gürtler, T. Husøy, M. Manco, W. Mennes, P. Moldeus, S. Passamonti, R. Shah, I. Waalkens-Berendsen, D. Wölfle, E. Corsini, F. Cubadda, D. De Groot, R. FitzGerald, S. Gunnare, A.C. Gutleb, J. Mast, A. Mortensen,

A. Oomen, A. Piersma, V. Plichta, B. Ulbrich, H. Van Loveren, D. Benford, M. Bignami, C. Bolognesi, R. Crebelli, M. Dusinska, F. Marcon, E. Nielsen, J. Schlatter, C. Vleminckx, S. Barmaz, M. Carfí, C. Civitella, A. Giarola, A.M. Rincon, R. Serafimova, C. Smeraldi, J. Tarazona, A. Tard, M. Wright, Safety assessment of titanium dioxide (E171) as a food additive, EFSA J. 19 (2021). https://doi.org/10.2903/j.efsa.2021.6585.

[34] M. Karimi, R. Sadeghi, J. Kokini, Human exposure to nanoparticles through trophic transfer and the biosafety concerns that nanoparticle-contaminated foods pose to consumers, Trends Food Sci. Technol. 75 (2018) 129–145. https://doi.org/10.1016/j.tifs.2018.03.012.

[35] A.R. Ribeiro, P.E. Leite, P. Falagan-Lotsch, F. Benetti, C. Micheletti, H.C. Budtz, N.R. Jacobsen, P.N. Lisboa-Filho, L.A. Rocha, D. Kühnel, D. Hristozov, J.M. Granjeiro, Challenges on the toxicological predictions of engineered nanoparticles, NanoImpact. 8 (2017) 59–72. https://doi.org/10.1016/j.impact.2017.07.006.

[36] J.R. Lead, K.J. Wilkinson, Aquatic colloids and nanoparticles: Current knowledge and future trends, Environ. Chem. 3 (2006) 159–171. https://doi.org/10.1071/en06025.

[37] G.C. Renzi M, Ecotoxicity of Nanoparticles in Aquatic Environments: A review based on multivariate statistics of meta-data, J. Environ. Anal. Chem. 2 (2015) 2–7. https://doi.org/10.4172/2380-2391.

[38] FAO. 2022. Blue Transformation - Roadmap 2022–2030: A vision for FAO's work on aquatic food systems. Rome. https://doi.org/10.4060/cc0459en.

[39] FAO. 2022. The state of world fisheries and aquaculture 2022. Towards blue transformation. Rome, FAO. https://doi.org/10.4060/cc0463en.

[40] R.L. Naylor, R.W. Hardy, A.H. Buschmann, S.R. Bush, L. Cao, D.H. Klinger, D.C. Little, J. Lubchenco, S.E. Shumway, M. Troell, A

20-year retrospective review of global aquaculture, Nature. 591 (2021) 551–563. https://doi.org/10.1038/s41586-021-03308-6.

[41] APROMAR, La acuicultura en España, (2022). https://apromar.es/wp-content/uploads/2022/10/La_acuicultura_Espana_2022_v3_APROMAR.pdf (accessed October 15, 2022).

[42] United Nations, United Nations Department of Economic and Social Affairs, Population Division (2022). World Population Prospects 2022: Summary of results. 2022. https://www.un.org/development/desa/pd/sites/www.un.org.development.desa.pd/files/wpp2022_summary_of_results.pdf.

[43] Global Seafood Alliance - Building trust in seafood. https://www.globalseafood.org/blog/what-is-aquaculture-why-do-we-need-it/ (accessed December 19, 2022).

[44] R. Hilborn, J. Banobi, S.J. Hall, T. Pucylowski, T.E. Walsworth, The environmental cost of animal source foods, Front. Ecol. Environ. 16 (2018) 329–335. https://doi.org/10.1002/fee.1822.

[45] R.R. Gentry, H.K. Alleway, M.J. Bishop, C.L. Gillies, T. Waters, R. Jones, Exploring the potential for marine aquaculture to contribute to ecosystem services, Rev. Aquac. 12 (2020) 499–512. https://doi.org/10.1111/raq.12328.

[46] F.M. and N.A. Stuart Bunting, Alexandra Pounds, Anton Immink, Simao Zacarias, Paul Bulcock, The Road to Sustainable Aquaculture: On current knowledge and priorities for responsible growth. World Economic Forum. Cologny, Switzerland. 121p, (2022).

[47] H.K. Alleway, C.L. Gillies, M.J. Bishop, R.R. Gentry, S.J. Theuerkauf, R. Jones, The ecosystem services of marine aquaculture: valuing benefits to people and nature, Bioscience. 69 (2018) 59–68. https://doi.org/10.1093/biosci/biy137.

[48] Ministerio de Agricultura, Pesca y Alimentación. Estadísticas pesqueras. Producción en acuicultura, (2021). https://www.mapa.gob.es/es/pesca/temas/acuicultura/produccion-de-

acuicultura/default.aspx (accessed December 3, 2022).

[49] APROMAR. España, primera potencia mundial en investigación en acuicultura, (2022). https://acuiculturadeespana.es/comite-de-expertos/espana-primera-potencia-mundial-investigacion-acuicultura/ (accessed December 11, 2022).

[50] Instituto Galego de Estadística. Produción de acuicultura mariña en Galicia. https://www.ige.gal/igebdt/selector.jsp?COD=2705&paxina=001&c=0301004 (accessed December 17, 2022).

[51] C.E. Boyd, L.R. D'Abramo, B.D. Glencross, D.C. Huyben, L.M. Juarez, G.S. Lockwood, A.A. McNevin, A.G.J. Tacon, F. Teletchea, J.R. Tomasso, C.S. Tucker, W.C. Valenti, Achieving sustainable aquaculture: Historical and current perspectives and future needs and challenges, J. World Aquac. Soc. 51 (2020) 578–633. https://doi.org/10.1111/jwas.12714.

[52] F.C. Cabello, H.P. Godfrey, A. Tomova, L. Ivanova, H. Dölz, A. Millanao, A.H. Buschmann, Antimicrobial use in aquaculture re-examined: its relevance to antimicrobial resistance and to animal and human health, Environ. Microbiol. 15 (2013) 1917–1942. https://doi.org/10.1111/1462-2920.12134.

[53] FAO. Impacts of climate change on fisheries and aquaculture: synthesis of current knowledge, adaptation and mitigation options. Rome, (2018). https://www.fao.org/3/ca0356en/ca0356en.pdf (accessed December 18, 2022).

[54] M.L. Wells, V.L. Trainer, T.J. Smayda, B.S. O Karlson, R.M. Kudela, A. Ishikawa, S. Bernard, A. Wulff, Harmful algal blooms and climate change: learning from the past and present to forecast the future, 49 (2015) 68–93. https://doi.org/10.1016/j.hal.2015.07.009.

[55] M. Reverter, S. Sarter, D. Caruso, J.-C. Avarre, M. Combe, E. Pepey, L. Pouyaud, S. Vega-Heredía, H. De Verdal, R.E. Gozlan, Aquaculture at the crossroads of global warming and antimicrobial resistance, Nat Commun. 11 (2020). https://doi.org/10.1038/s41467-

020-15735-6.

[56] Y.I. Chu, C.M. Wang, J.C. Park, P.F. Lader, Review of cage and containment tank designs for offshore fish farming, Aquaculture. 519 (2020) 734928. https://doi.org/10.1016/j.aquaculture.2020.734928.

[57] M. Badiola, O.C. Basurko, R. Piedrahita, P. Hundley, D. Mendiola, Energy use in Recirculating Aquaculture Systems (RAS): A review, Aquac. Eng. 81 (2018) 57–70. https://doi.org/10.1016/j.aquaeng.2018.03.003.

[58] S. Huang, Book review: Aquaculture in China: success stories and modern trends, Aquac. Fish. 3 (2018) 174–175. https://doi.org/10.1016/j.aaf.2018.07.001.

[59] L.R. Thomas, T. Clavelle, D.H. Klinger, S.E. Lester, The ecological and economic potential for offshore mariculture in the Caribbean, Nat. Sustain. 2 (2019) 62–70. https://doi.org/10.1038/s41893-018-0205-y.

[60] T. Garlock, F. Asche, J. Anderson, T. Bjørndal, G. Kumar, K. Lorenzen, A. Ropicki, M.D. Smith, R. Tveterås, A Global blue revolution: aquaculture growth across regions, species, and countries, Rev. Fish. Sci. Aquac. 28 (2019) 107–116. https://doi.org/10.1080/23308249.2019.1678111.

[61] J. Zhang, W. Guo, Q. Li, Z. Wang, S. Liu, The effects and the potential mechanism of environmental transformation of metal nanoparticles on their toxicity in organisms, Environ. Sci. Nano. 5 (2018) 2482–2499. https://doi.org/10.1039/c8en00688a.

[62] N.B. Turan, H.S. Erkan, G.O. Engin, M.S. Bilgili, Nanoparticles in the aquatic environment: usage, properties, transformation and toxicity—A review, Process Saf. Environ. Prot. 130 (2019) 238–249. https://doi.org/10.1016/j.psep.2019.08.014.

[63] C. Bai, M. Tang, Toxicological study of metal and metal oxide nanoparticles in zebrafish, J. Appl. Toxicol. 40 (2020) 37–63. https://doi.org/10.1002/jat.3910.

[64] M. Filella, Colloidal properties of submicron particles in natural waters, Environ. Colloids Part. Behav. Sep. Characterisation. (2007) 17–93. https://doi.org/10.1002/9780470024539.ch2.

[65] A.B. Sengul, E. Asmatulu, Toxicity of metal and metal oxide nanoparticles: a review, Environ. Chem. Lett. 18 (2020) 1659–1683. https://doi.org/10.1007/s10311-020-01033-6.

[66] N. Liu, M. Tang, Toxic effects and involved molecular pathways of nanoparticles on cells and subcellular organelles, J. Appl. Toxicol. 40 (2020) 16–36. https://doi.org/10.1002/jat.3817.

[67] J. Bogdan, J. Zarzyńska, J. Pławińska-Czarnak, Comparison of infectious agents susceptibility to photocatalytic effects of nanosized titanium and zinc oxides: a practical approach, Nanoscale Res. Lett. 10 (2015). https://doi.org/10.1186/S11671-015-1023-Z.

[68] V. De Matteis, Exposure to inorganic nanoparticles: routes of entry, immune response, biodistribution and in vitro/in vivo toxicity evaluation, Toxics. 5 (2017). https://doi.org/10.3390/toxics5040029.

[69] E. Fröhlich, E. Roblegg, Oral uptake of nanoparticles: human relevance and the role of in vitro systems, Arch. Toxicol. 90 (2016) 2297–2314. https://doi.org/10.1007/s00204-016-1765-0.

[70] C. McCracken, P.K. Dutta, W.J. Waldman, Critical assessment of toxicological effects of ingested nanoparticles, Environ. Sci. Nano. 3 (2016) 256–282. https://doi.org/10.1039/c5en00242g.

[71] D.J. McClements, G. DeLoid, G. Pyrgiotakis, J.A. Shatkin, H. Xiao, P. Demokritou, The role of the food matrix and gastrointestinal tract in the assessment of biological properties of ingested engineered nanomaterials (iENMs): State of the science and knowledge gaps, NanoImpact. 3–4 (2016) 47. https://doi.org/10.1016/j.impact.2016.10.002.

[72] T.J. Baker, C.R. Tyler, T.S. Galloway, Impacts of metal and metal oxide nanoparticles on marine organisms, Environ. Pollut. 186 (2014) 257–271. https://doi.org/10.1016/j.envpol.2013.11.014.

[73] G. Vale, K. Mehennaoui, S. Cambier, G. Libralato, S. Jomini,

R.F. Domingos, Manufactured nanoparticles in the aquatic environment-biochemical responses on freshwater organisms: A critical overview, Aquat. Toxicol. 170 (2016) 162–174. https://doi.org/10.1016/j.aquatox.2015.11.019.

[74] C.S. Ramsden, T.J. Smith, B.J. Shaw, R.D. Handy, Dietary exposure to titanium dioxide nanoparticles in rainbow trout, (Oncorhynchus mykiss): No effect on growth, but subtle biochemical disturbances in the brain, Ecotoxicology. 18 (2009) 939–951. https://doi.org/10.1007/s10646-009-0357-7.

[75] M. Ates, V. Demir, R. Adiguzel, Z. Arslan, Bioaccumulation, subacute toxicity, and tissue distribution of engineered titanium dioxide nanoparticles in goldfish (carassius auratus), j. nanomater. 2013 (2013). https://doi.org/10.1155/2013/460518.

[76] F. Ribeiro, C. Pinheiro, M. Monteiro, C.A.M. Van Gestel, A.M.V.M. Soares, S. Loureiro, Toxicokinetics of silver in the goldfish Carassius auratus under simultaneous waterborne and diet-borne exposures to silver nanoparticles, Environ. Sci. Pollut. Res. 29 (2022) 56079–56089. https://doi.org/10.1007/s11356-022-19717-7.

[77] M. Asztemborska, M. Jakubiak, R. Stęborowski, E. Chajduk, G. Bystrzejewska-Piotrowska, Titanium dioxide nanoparticle circulation in an aquatic ecosystem, Water. Air. Soil Pollut. 229 (2018). https://doi.org/10.1007/s11270-018-3852-8.

[78] B.J. Shaw, R.D. Handy, Physiological effects of nanoparticles on fish: A comparison of nanometals versus metal ions, Environ. Int. 37 (2011) 1083–1097. https://doi.org/10.1016/j.envint.2011.03.009.

[79] A. Jain, S. Ranjan, N. Dasgupta, C. Ramalingam, Nanomaterials in food and agriculture: An overview on their safety concerns and regulatory issues, Crit. Rev. Food Sci. Nutr. ISSN. 58 (2017) 297–317. https://doi.org/10.1080/10408398.2016.1160363.

[80] H. Rauscher, K. Rasmussen, B. Sokull-Klüttgen, Regulatory aspects of nanomaterials in the EU, Chemie Ing. Tech. 89 (2017) 224–231. https://doi.org/10.1002/cite.201600076.

[81] S. More, V. Bampidis, D. Benford, C. Bragard, T. Halldorsson, A. Hernández-Jerez, S. Hougaard Bennekou, K. Koutsoumanis, C. Lambré, K. Machera, H. Naegeli, S. Nielsen, J. Schlatter, D. Schrenk, V. Silano, D. Turck, M. Younes, J. Castenmiller, Q. Chaudhry, F. Cubadda, R. Franz, D. Gott, J. Mast, A. Mortensen, A.G. Oomen, S. Weigel, E. Barthelemy, A. Rincon, J. Tarazona, R. Schoonjans, Guidance on risk assessment of nanomaterials to be applied in the food and feed chain: human and animal health, EFSA J. 19 (2021). https://doi.org/10.2903/j.efsa.2021.6768.

[82] N. Jakubowski, T. Prohaska, L. Rottmann, F. Vanhaecke, Inductively coupled plasma- and glow discharge plasma-sector field mass spectrometry: Part I. Tutorial: fundamentals and instrumentation, J. Anal. At. Spectrom. 26 (2011) 693–726. https://doi.org/10.1039/c0ja00161a.

[83] I. Rodushkin, E. Engström, A. Stenberg, D.C. Baxter, Determination of low-abundance elements at ultra-trace levels in urine and serum by inductively coupled plasma-sector field mass spectrometry., Anal. Bioanal. Chem. 380 (2004) 247–257. https://doi.org/10.1007/s00216-004-2742-7.

[84] J.M. Harrington, D.J. Young, A.S. Essader, S.J. Sumner, K.E. Levine, Analysis of human serum and whole blood for mineral content by ICP-MS and ICP-OES: Development of a mineralomics method, Biol. Trace Elem. Res. 160 (2014) 132–142. https://doi.org/10.1007/s12011-014-0033-5.

[85] K. Sakata, K. Kawabata, Reduction of fundamental polyatomic ions in inductively coupled plasma mass spectrometry, Spectrochim. Acta Part B At. Spectrosc. 49 (1994) 1027–1038. https://doi.org/10.1016/0584-8547(94)80088-X.

[86] S.D. Tanner, V.I. Baranov, D.R. Bandura, Reaction cells and collision cells for ICP-MS: a tutorial review, Spectrochim. Acta - Part B At. Spectrosc. 57 (2002) 1361–1452. https://doi.org/10.1016/S0584-8547(02)00069-1.

[87] E. Bolea-Fernandez, D. Leite, A. Rua-Ibarz, T. Liu, G. Woods,

M. Aramendia, M. Resano, F. Vanhaecke, On the effect of using collision/reaction cell (CRC) technology in single-particle ICP-mass spectrometry (SP-ICP-MS), Anal. Chim. Acta. 1077 (2019) 95–106. https://doi.org/10.1016/j.aca.2019.05.077.

[88] E. Bolea-Fernandez, D. Leite, A. Rua-Ibarz, L. Balcaen, M. Aramendía, M. Resano, F. Vanhaecke, Characterization of SiO2 nanoparticles by single particle-inductively coupled plasma-tandem mass spectrometry (SP-ICP-MS/MS), J. Anal. At. Spectrom. 32 (2017) 2140–2152. https://doi.org/10.1039/c7ja00138j.

[89] N. Yamada, Kinetic energy discrimination in collision/reaction cell ICP-MS: Theoretical review of principles and limitations, Spectrochim. Acta - Part B At. Spectrosc. 110 (2015) 31–44. https://doi.org/10.1016/j.sab.2015.05.008.

[90] S. Li, Z. Yang, J. Cao, B. Qiu, H. Li, Determination of metallothionein isoforms in fish by cadmium saturation combined with anion exchange HPLC-ICP-MS, Chromatographia. 81 (2018) 881–889. https://doi.org/10.1007/s10337-018-3523-3.

[91] Z.S. Gong, R. Yang, C.Q. Sun, W.N. Han, X.H. Jiang, S.X. Xu, Y. Wang, Simultaneous determination of P and S in human serum, blood plasma and whole blood by ICP-MS with collision/reaction cell technology, Int. J. Mass Spectrom. 445 (2019) 116193. https://doi.org/10.1016/j.ijms.2019.116193.

[92] A.S. Henn, F.S. Rondan, M.F. Mesko, P.A. Mello, M. Perez, J. Armstrong, L.A. Bullock, J. Parnell, J. Feldmann, E.M.M. Flores, Determination of Se at low concentration in coal by collision/reaction cell technology inductively coupled plasma mass spectrometry, Spectrochim. Acta - Part B At. Spectrosc. 143 (2018) 48–54. https://doi.org/10.1016/j.sab.2018.02.014.

[93] S. Candás-Zapico, D.J. Kutscher, M. Montes-Bayón, J. Bettmer, Single particle analysis of TiO2 in candy products using triple quadrupole ICP-MS, Talanta. 180 (2018) 309–315. https://doi.org/10.1016/j.talanta.2017.12.041.

[94] M. Tharaud, A.P. Gondikas, M.F. Benedetti, F. Von Der Kammer, T. Hofmann, G. Cornelis, TiO2 nanomaterial detection in calcium rich matrices by spICPMS. A matter of resolution and treatment, J. Anal. At. Spectrom. 32 (2017) 1400–1411. https://doi.org/10.1039/c7ja00060j.

[95] M.D. Montaño, J.W. Olesik, A.G. Barber, K. Challis, J.F. Ranville, Single Particle ICP-MS: Advances toward routine analysis of nanomaterials, Anal. Bioanal. Chem. 408 (2016) 5053–5074. https://doi.org/10.1007/s00216-016-9676-8.

[96] C. Degueldre, P.Y. Favarger, Colloid analysis by single particle inductively coupled plasma-mass spectroscopy: A feasibility study, Colloids Surfaces A Physicochem. Eng. Asp. 217 (2003) 137–142. https://doi.org/10.1016/S0927-7757(02)00568-X.

[97] I. Abad-Álvaro, E. Peña-Vázquez, E. Bolea, P. Bermejo-Barrera, J.R. Castillo, F. Laborda, Evaluation of number concentration quantification by single-particle inductively coupled plasma mass spectrometry: microsecond vs. millisecond dwell times, Anal. Bioanal. Chem. 408 (2016) 5089–5097. https://doi.org/10.1007/s00216-016-9515-y.

[98] F. Laborda, E. Bolea, J. Jiménez-Lamana, Single particle inductively coupled plasma mass spectrometry for the analysis of inorganic engineered nanoparticles in environmental samples, Trends Environ. Anal. Chem. 9 (2016) 15–23. https://doi.org/10.1016/j.teac.2016.02.001.

[99] C. Degueldre, P.Y. Favarger, S. Wold, Gold colloid analysis by inductively coupled plasma-mass spectrometry in a single particle mode, Anal. Chim. Acta. 555 (2006) 263–268. https://doi.org/10.1016/j.aca.2005.09.021.

[100] C. Degueldre, P.Y. Favarger, Thorium colloid analysis by single particle inductively coupled plasma-mass spectrometry, Talanta. 62 (2004) 1051–1054. https://doi.org/10.1016/j.talanta.2003.10.016.

[101] F. Laborda, J. Jiménez-Lamana, E. Bolea, J.R. Castillo, Critical considerations for the determination of nanoparticle number concentrations, size and number size distributions by single particle ICP-MS, J. Anal. At. Spectrom. 28 (2013) 1220–1232. https://doi.org/10.1039/c3ja50100k.

[102] F. Laborda, E. Bolea, J. Jiménez-Lamana, Single particle inductively coupled plasma mass spectrometry: A powerful tool for nanoanalysis, Anal. Chem. 86 (2014) 2270–2278. https://doi.org/10.1021/ac402980q.

[103] M. Corte-Rodríguez, R. Álvarez-Fernández, P. García-Cancela, M. Montes-Bayón, J. Bettmer, Single cell ICP-MS using on line sample introduction systems: Current developments and remaining challenges, TrAC - Trends Anal. Chem. 132 (2020). https://doi.org/10.1016/j.trac.2020.116042.

[104] Y. Cao, J. Feng, L. Tang, C. Yu, G. Mo, B. Deng, A highly efficient introduction system for single cell- ICP-MS and its application to detection of copper in single human red blood cells, Talanta. 206 (2020) 120174. https://doi.org/10.1016/j.talanta.2019.120174.

[105] L. Amable, C. Stephan, S. Smith, R. Merrifield, An Introduction to single cell ICP-MS analysis, White Pap. (2017) 1–5. https://www.perkinelmer.com/lab-solutions/resources/docs/WHT-Introduction-to-Single-Cell-ICP-MS-012774A_01.pdf.

[106] Perkin Elmer, Single cell ICP-MS analysis: quantification of metal content at the cellular level, White Pap. (2017) 4. http://www.perkinelmer.com/lab-solutions/resources/docs/WHP_Single_Cell_ICP-MS_Analysis-Quantification-of-Metal_Content_at_the_Cellular-Level_013586_01.pdf.

[107] S. Meyer, A. López-Serrano, H. Mitze, N. Jakubowski, T. Schwerdtle, Single-cell analysis by ICP-MS/MS as a fast tool for cellular bioavailability studies of arsenite, Metallomics. 10 (2018) 73. https://doi.org/10.1039/c7mt00285h.

[108] M. Corte Rodríguez, R. Álvarez-Fernández García, E. Blanco, J. Bettmer, M. Montes-Bayón, Quantitative evaluation of cisplatin uptake in sensitive and resistant individual cells by single-sell ICP-MS (scICP-MS), Anal. Chem. 89 (2017) 11491–11497. https://doi.org/10.1021/acs.analchem.7b02746.

[109] J.T.S. Lum, K.S.Y. Leung, Quantifying silver nanoparticle association and elemental content in single cells using dual mass mode in quadrupole-based inductively coupled plasma-mass spectrometry, Anal. Chim. Acta. 1061 (2019) 50–59. https://doi.org/10.1016/j.aca.2019.02.042.

[110] M. Ikehata, J. Woolcock, M.E.P. Murphy, R. Merrifield, C. Stephan, Introduction iron content measurement in individual bacterial cells using scICP-MS, (2018). http://www.perkinelmer.com/lab-solutions/resources/docs/APP_013978_01_NexION_scICP-MS_Iron_in_Bacterial_Cells.pdf.

[111] R.C. Merrifield, C. Stephan, J.R. Lead, Quantification of Au nanoparticle biouptake and distribution to freshwater algae using single cell - ICP-MS, Environ. Sci. Technol. 52 (2018) 2271–2277. https://doi.org/10.1021/acs.est.7b04968.

[112] C.J. Greenhalgh, E. Karekla, G.J. Miles, I.R. Powley, C. Costa, J. De Jesus, M.J. Bailey, C. Pritchard, M. MacFarlane, J.H. Pringle, A.J. Managh, Exploration of matrix effects in laser ablation inductively coupled plasma mass spectrometry imaging of cisplatin-treated tumors, Anal. Chem. 92 (2020) 9847–9855. https://doi.org/10.1021/acs.analchem.0c01347.

[113] F. Blaske, O. Reifschneider, G. Gosheger, C.A. Wehe, M. Sperling, U. Karst, G. Hauschild, S. Höll, Elemental bioimaging of nanosilver-coated prostheses using X-ray fluorescence spectroscopy and laser ablation-inductively coupled plasma-mass spectrometry, Anal. Chem. 86 (2014) 615–620. https://doi.org/10.1021/ac4028577.

[114] P.M. Angel, H.S. Baldwin, D. Gottlieb Sen, Y.R. Su, J.E. Mayer, D. Bichell, R.R. Drake, Advances in MALDI imaging mass spectrometry of proteins in cardiac tissue, including the heart valve,

Biochim. Biophys. Acta. Proteins Proteomics. 1865 (2017) 927–935. https://doi.org/10.1016/j.bbapap.2017.03.009.

[115] H. Tian, L.J. Sparvero, P. Blenkinsopp, A.A. Amoscato, S.C. Watkins, H. Bayır, V.E. Kagan, N. Winograd, Secondary-ion mass spectrometry images cardiolipins and phosphatidylethanolamines at the subcellular level, Angew. Chemie Int. Ed. 58 (2019) 3156–3161. https://doi.org/10.1002/anie.201814256.

[116] A. Limbeck, P. Galler, M. Bonta, G. Bauer, W. Nischkauer, F. Vanhaecke, Recent advances in quantitative LA-ICP-MS analysis: challenges and solutions in the life sciences and environmental chemistry, Anal. Bioanal. Chem. 407 (2015) 6593–6617. https://doi.org/10.1007/S00216-015-8858-0.

[117] Z. Yang, S.E. Jackson, L.J. Cabri, P. Wee, H.P. Longerich, M. Pawlak, Quantitative determination of trace level (ng g-1) contents of rhodium and palladium in copper-rich minerals using LA-ICP-MS, J. Anal. At. Spectrom. 35 (2020) 534–547. https://doi.org/10.1039/c9ja00285e.

[118] C. Arnaudguilhem, M. Larroque, O. Sgarbura, D. Michau, F. Quenet, S. Carrère, B. Bouyssière, S. Mounicou, Toward a comprehensive study for multielemental quantitative LA-ICP MS bioimaging in soft tissues, Talanta. 222 (2021). https://doi.org/10.1016/j.talanta.2020.121537.

[119] C.C. Garcia, H. Lindner, K. Niemax, Laser ablation inductively coupled plasma mass spectrometry—current shortcomings, practical suggestions for improving performance, and experiments to guide future development, J. Anal. At. Spectrom. 24 (2008) 14–26. https://doi.org/10.1039/b813124b.

[120] I. Kroslakova, D. Günther, Elemental fractionation in laser ablation-inductively coupled plasma-mass spectrometry: evidence for mass load induced matrix effects in the ICP during ablation of a silicate glass, J. Anal. At. Spectrom. 22 (2006) 51–62. https://doi.org/10.1039/b606522h.

[121] D.J. Hare, E.J. New, M.D. De Jonge, G. McColl, Imaging metals in biology: balancing sensitivity, selectivity and spatial resolution, Chem. Soc. Rev. 44 (2015) 5941–5958. https://doi.org/10.1039/c5cs00055f.

[122] I.L. Hsiao, F.S. Bierkandt, P. Reichardt, A. Luch, Y.J. Huang, N. Jakubowski, J. Tentschert, A. Haase, Quantification and visualization of cellular uptake of TiO2 and Ag nanoparticles: Comparison of different ICP-MS techniques, J. Nanobiotechnology. 14 (2016) 1–13. https://doi.org/10.1186/s12951-016-0203-z.

[123] R. Torimoto, C. Ishii, H. Sato, K. Saito, Y. Watanabe, K. Ogasawara, A. Kubota, T. Matsukawa, K. Yokoyama, A. Kobayashi, T. Kimura, S.M.M. Nakayama, Y. Ikenaka, M. Ishizuka, Analysis of lead distribution in avian organs by LA-ICP-MS: study of experimentally lead-exposed ducks and kites, Environ. Pollut. 283 (2021). https://doi.org/10.1016/j.envpol.2021.117086.

[124] C. Austin, T.M. Smith, A. Bradman, K. Hinde, R. Joannes-Boyau, D. Bishop, D.J. Hare, P. Doble, B. Eskenazi, M. Arora, Barium distributions in teeth reveal early-life dietary transitions in primates, Nature. 498 (2013) 216–219. https://doi.org/10.1038/nature12169.

[125] L.N. Zheng, L.X. Feng, J.W. Shi, H.Q. Chen, B. Wang, M. Wang, H.F. Wang, W.Y. Feng, Single-cell isotope dilution analysis with LA-ICP-MS: a new approach for quantification of nanoparticles in single cells, Anal. Chem. 92 (2020) 14339–14345. https://doi.org/10.1021/acs.analchem.0c01775.

[126] J.S. Becker, R.C. Dietrich, A. Matusch, D. Pozebon, V.L. Dressler, Quantitative images of metals in plant tissues measured by laser ablation inductively coupled plasma mass spectrometry, Spectrochim. Acta Part B At. Spectrosc. 63 (2008) 1248–1252. https://doi.org/10.1016/j.sab.2008.08.001.

[127] M. Šala, V.S. Šelih, J.T. Van Elteren, Gelatin gels as multi-element calibration standards in LA-ICP-MS bioimaging: fabrication of homogeneous standards and microhomogeneity testing, Analyst.

142 (2017) 3356–3359. https://doi.org/10.1039/c7an01361b.

[128] P.A. Doble, R.G. de Vega, D.P. Bishop, D.J. Hare, D. Clases, Laser ablation-inductively coupled plasma-mass spectrometry imaging in biology, Chem. Rev. 121 (2021) 11769–11822. https://doi.org/10.1021/acs.chemrev.0c01219.

[129] A. Schoeberl, M. Gutmann, S. Theiner, M. Schaier, A. Schweikert, W. Berger, G. Koellensperger, Cisplatin uptake in macrophage subtypes at the single-cell level by LA-ICP-TOFMS imaging, Anal. Chem. 93 (2021) 16456-16465(1) Schoeberl, A.; Gutmann, M.; Theiner. https://doi.org/10.1021/acs.analchem.1c03442.

[130] N.M. Ralbovsky, L. Zou, B. Chen, N.R. Zhang, C.D.G. Hines, M. Vavrek, W. Zhong, J.P. Smith, X. Bu, Simultaneous multielement imaging of liver tissue using laser ablation inductively coupled plasma mass spectrometry, Talanta. 235 (2021) 122725. https://doi.org/10.1016/j.talanta.2021.122725.

[131] M. Togao, S.M.M. Nakayama, Y. Ikenaka, H. Mizukawa, Y. Makino, A. Kubota, T. Matsukawa, K. Yokoyama, T. Hirata, M. Ishizuka, Bioimaging of Pb and STIM1 in mice liver, kidney and brain using Laser Ablation Inductively Coupled Plasma Mass Spectrometry (LA-ICP-MS) and immunohistochemistry, Chemosphere. 238 (2020) 124581. https://doi.org/10.1016/j.chemosphere.2019.124581.

[132] D. Metarapi, M. Šala, K. Vogel-Mikuš, V.S. Šelih, J.T. Van Elteren, Nanoparticle analysis in biomaterials using laser ablation - single particle-inductively coupled plasma mass spectrometry, Anal. Chem. 91 (2019) 6200–6205. https://doi.org/10.1021/acs.analchem.9b00853.

[133] J. Wang, Y. Nie, H. Dai, M. Wang, L. Cheng, Z. Yang, S. Chen, G. Zhao, L. Wu, S. Guang, A. Xu, Parental exposure to TiO2 NPs promotes the multigenerational reproductive toxicity of Cd in Caenorhabditis elegans via bioaccumulation of Cd in germ cells, Environ. Sci. Nano. 6 (2019) 1332–1342. https://doi.org/10.1039/c8en01042k.

[134] O. Reifschneider, A. Vennemann, G. Buzanich, M. Radtke, U. Reinholz, H. Riesemeier, J. Hogeback, C. Köppen, M. Großgarten, M. Sperling, M. Wiemann, U. Karst, Revealing silver nanoparticle uptake by macrophages using SR-μXRF and LA-ICP-MS, Chem. Res. Toxicol. 33 (2020) 1250–1255. https://doi.org/10.1021/acs.chemrestox.9b00507.

[135] S. Mourdikoudis, R.M. Pallares, N.T.K. Thanh, Characterization techniques for nanoparticles: comparison and complementarity upon studying nanoparticle properties, Nanoscale. 10 (2018) 12871–12934. https://doi.org/10.1039/c8nr02278j.

[136] F. Laborda, E. Bolea, G. Cepriá, M.T. Gómez, M.S. Jiménez, J. Pérez-Arantegui, J.R. Castillo, Detection, characterization and quantification of inorganic engineered nanomaterials: A review of techniques and methodological approaches for the analysis of complex samples, Anal. Chim. Acta. 904 (2016) 10–32. https://doi.org/10.1016/j.aca.2015.11.008.

[137] C. Giannini, M. Ladisa, D. Altamura, D. Siliqi, T. Sibillano, L. De Caro, X-ray diffraction: a powerful technique for the multiple-length-scale structural analysis of nanomaterials, Crystals. 6 (2016). https://doi.org/10.3390/cryst6080087.

[138] G. Moreno-Martin, J. Sanz-Landaluze, Y. Madrid, Nanospeciation analysis using field flow fractionation, Encycl. Anal. Chem. (2017) 1–24. https://doi.org/10.1002/9780470027318.A9395.

II. OBJECTIVES

Concerning the unstoppable use of NMs in our society and the rising importance of the aquaculture industry, this doctoral thesis focuses on the impact of NPs in aquaculture. Therefore, the general objective is the development of novel and advanced analytical nanometrological tools for NPs determination/characterization in cultured products as well as the risk assessment for the marine environment and human health. Based on this general goal, the current research aims to accomplish the following specific objectives:

1. The development of novel nanometrological platforms exploiting ammonia as a reaction gas and the application for the determination and characterization of Ag NPs, Cu NPs, CuO NPs, TiO_2 NPs, and ZnO NPs.

2. Optimisation of ultra-sensitive methodologies for the detection of single cells and the application to elucidates Ag NPs and TiO_2 NPs interactions with cell lines from aquaculture fish and molluscs.

3. Bioaccumulation and distribution studies of Ag and TiO_2 NPs in cultured fish and shellfish, revealing the target organs, identifying patterns associated to the NPs exposure, and providing valuable information regarding food safety.

4. Assessment of the bio-accessibility and bioavailability of Ag NPs and TiO_2 NPs in aquaculture products by determining the fraction of NPs capable of being assimilated by the human body and how different culinary processes affect this assimilation, thereby providing useful data on food safety and degradation rate of NPs in the gastro-instestinal tract.

5. Quantitative bioimaging studies by LA-ICP-MS for the visualisation and spatial biodistribution of TiO_2 NPs in different soft tissues from aquaculture products, after the design and optimization of a reliable quantification methodology by using lab-produced standards.

III. METHODOLOGY

The Doctoral Thesis was carried out as follows:

Stage 1. spICP-MS enhancements for the detection and characterization of Ag NPs, Cu NPs, CuO NPs, TiO_2 NPs, and ZnO NPs.
The use of new generation of ICP-MS instrumentation (dwell time within the µs range) and the impact of reaction gases such as ammonia (NH_3) on isobaric interferences removal and on analytical performances, have been explored. Isobaric interferences are especially important for TiO_2 NPs since Ti has mass-to-charge ratios that are similar to adducts from Ca or P (major elements in biological samples). The improvement in the single detection of Ag NPs, Cu NPs, CuO NPs, TiO_2 NPs, and ZnO NPs with reaction gases was explored and the developed conditions were also applied to extracts of mollusc and fish samples, in the following chapters of this doctoral thesis.

Stage 2. Developments in scICP-MS for the detection of Ag NPs and TiO_2 NPs interaction with cells.
After controlled exposure experiments with Ag NPs and TiO_2 NPs, the presence of associated or internalised NPs in different cell lines from sea bass, sea bream, and clams were determined through the acquisition of a specific sampler and Asperon™ spray chamber that guarantees the integrity of cells during their transport to the atomizer. Therefore, the measurement conditions by scICP-MS as well as the parameters inherent to the nebulisation and transport of the cells were optimised. The results after sc-ICP-MS were compared to those offered by conventional methods for cell content analysis (microwave assisted acid digestion followed by ICP-MS analysis), and also TEM analysis was also performed for elucidating the NPs-cell interaction nature (internalization and/or association with cells' membranes).

Stage 3. Bioaccumulation and distribution of Ag NPs and TiO_2 NPs in several tissues from aquaculture products.
Controlled exposure trials of Ag NPs and TiO_2 NPs were conducted in aquaculture facilities (CETGA, within the ACUINANO project),

examining the distribution in the different parts of the organisms (mantle and hepatopancreas, in the case of clams; and muscle-skin, liver, and kidney, in the case of sea bass and sea bream) after several exposure times with Ag NPs and TiO_2 NPs of several sizes and concentrations. Techniques such as TEM, SEM, spICP-MS, and LA-ICP-MS were used to assess the distributions and concentrations of NPs in tissues.

Stage 4. *In-vitro* human bioavailability studies of Ag NPs and TiO_2 NPs.
Human bioavailability of Ag NPs and TiO_2 NPs from cultured products was evaluated by simulating the human gastro-instestinal digestion (*in vitro* bio-accessibility assay) and human intestinal absorption by using an *in vitro* Caco-2 cells model for cellular transport assessment. The contents of Ag NPs and TiO_2 NPs in the bio-accessible fractions from unexposed and exposed clams, sea bass, and sea bream, as well as the basal fractions after cellular transport were assessed by spICP-MS, and the bio-accessible and cellular transport (bioavailability) ratios valued. In addition, NPs sizes changes along the *in vitro* process were also evaluated. Moreover, the influence of culinary processing (boiling and grilling) on the Ag NPs and TiO_2 NPs contents as well as on the bio-accessibility and bioavailability ratios of the cooked samples.

Stage 5. Developments in LA-ICP-MS for the localisation and spatial distribution of TiO_2 NPs in tissues from cultured fish.
A pre-treatment of fish's tissues for applying LA-ICP-MS (tissue fixation and inclusion in polymer blocks) was performed as well as the optimisation of a LA-ICP-MS methodology to visualise and obtain biodistribution maps (images) of bioaccumulated TiO_2 NPs in fish's tissues. In addition to qualitative images, novel calibration strategies were proposed for obtaining quantitative images.

IV. RESULTS AND DISCUSSION

CHAPTER 1

EXPLOITING DYNAMIC REACTION CELL TECHNOLOGY FOR REMOVAL OF SPECTRAL INTERFERENCES IN THE ASSESSMENT OF AG, CU, TI, AND ZN BY INDUCTIVELY COUPLED PLASMA MASS SPECTROMETRY

CHAPTER 1. EXPLOITING DYNAMIC REACTION CELL TECHNOLOGY FOR REMOVAL OF SPECTRAL INTERFERENCES IN THE ASSESSMENT OF AG, CU, TI, AND ZN BY INDUCTIVELY COUPLED PLASMA MASS SPECTROMETRY

*The results from this chapter have already been published as Cristian Suárez-Oubiña, Paloma Herbello-Hermelo, Pilar Bermejo-Barrera, and Antonio Moreda-Piñeiro, exploiting dynamic reaction cell technology for removal of spectral interferences in the assessment of ag, cu, ti, and zn by inductively coupled plasma mass spectrometry, Spectrochim. Acta B: At. Spectrosc. 187 (2022) 944, DOI:10.1016/j.sab.2021.106330.

Group of Trace Element, Spectroscopy, and Speciation (GETEE), Institute of Materials iMATUS. Department of Analytical Chemistry, Nutrition, and Bromatology. Faculty of Chemistry. Universidade de Santiago de Compostela. Avenida das Ciencias, s/n 15782, Santiago de Compostela. Spain.

1.1 ABSTRACT

Analytical methods based on dynamic-reaction cell (DRC) technology using ammonia as a reaction gas have been developed for the determination of ultra-trace Ti, Zn, Cu and Ag by inductively coupled plasma mass spectrometry (ICP-MS). Challenging spectral interferences from complex matrices were demonstrated to be overcome by DRC, and several DRC approaches (on-mass and mass-shift) using ammonium (NH_3) as a reaction gas were assessed and compared to the standard or "vented" mode analysis. Ammonium cluster ions were generated for Ti, Cu, Zn, and Ag (mass shift approach). The on-mass approach was also explored to take advantage of collisional focusing phenomena. In addition, DRC operating conditions were optimized by modifying NH_3 gas flow rate and

rejection parameter q (RPq). The optimised conditions were applied to show the usefulness of either on-mass or mass-shift approaches when removing Ca and P interferences. Finally, the sensitivity of all measurement modes was studied and excellent limits of detection (at few ng L^{-1} levels) were assessed

1.2 INTRODUCTION

Inductively coupled plasma mass spectrometry (ICP-MS) has been demonstrated to be one of the leading techniques for elemental analysis, allowing for the determination of ultra-trace levels of metals and metalloids in a large variety of samples. ICP-MS offers many advantages over other spectrometric techniques, such as high sensitivity, wide linear dynamic range (nine orders of magnitude), and multi-element and isotopic-ratio measurement capabilities. Plasma source high temperature operation of about 7000K allows all chemical bonds present in organic and inorganic compounds (even large biomolecules) to be readily broken, thus providing a more efficient atomization over other atomic based techniques.

Despite these advantages, ICP-MS also possesses some drawbacks. The occurrence of spectral (polyatomic and isobaric interferences) and non-spectral interferences are the most important shortcomings [1,2]. Polyatomic interferences are derived from plasma gas (typically Ar), sample matrix, atmospheric gas or solvent solution (water or organic solvents), and imply the generation of polyatomic species that coincidence at mass-charge ratio with the analyte. Several strategies have been developed to overcome ICP-MS interferences, including cold plasma conditions, mathematical correction equations, and improved mass analysers, such as sector field ICP-MS (SF-ICP-MS) [3,4,5,6,7], and the use of collision-reaction cell (DRC) technology [8]. Although SF-ICP-MS has greatly improved the technical capabilities of ICP- MS and has allowed higher mass resolution than other mass analysers, it is not able to solve all interferences [4].

Cells in DRC are pressurized with a gas, and spectral interferences are removed by either selective reaction of the analyte and/or interfering ion with a reactive gas (typically H_2 [9], CH_4 [10], O_2 [11,12,13], CH_3F [14] and NH_3 [15,16]), or collisions of the ions

with a non-reactive gas (typically He) in combination with kinetic energy discrimination (KED). The literature indicates that O_2 reaction gas has a high and predictable reactivity behaviour which implies high sensitivity [12,13]; whereas, CH_4 gas is inert to fight against possible matrix interferences (limited applications), and H_2 is especially useful for overcoming Ar interferences [9]. On the other hand, NH_3 and CH_3F reaction gases show a high and unpredictable reactivity and offer a wide range of possibilities (the formation of several adducts or ion-products) in contrast to only one adduct generated from O_2 gas. These features provide high selectivity for ICP-MS analysis with DRC technology using NH_3 and CH_3F as reaction gases.

NH_3 ionization energy is lower than that exhibited by most elements due to electrons free-pair, which make easier charge-transfer reactions [17,18], and shows lower reaction efficiency than other reaction gases. However, this lower reactivity is compensated by higher selectivity because several adducts containing more than one ammonium molecule can be formed, and thus mass-charge ratios of interest are shifted to a free-interference spectral region. In addition, the assessment of reaction gas flow rate and dynamic band pass ion guide, which involves Mathieu Parameters (RPq and RPa values), are also required. Formation of new species (potentially new interferences) in the cell could be controlled when a reactive gas is used, and dynamic band pass optimization must be assessed through rejection parameters [8].

In this work we aim to develop several NH_3-based DRC methods for ultra-trace determination of Ti, Zn, Cu and Ag. These elements, except Ag, have been reported to be subjected to interference by large concentrations of Na, P, S, Ca and Mg (elements typically found in biological samples, seafood included [13,19,20,21]). The comprehensive evaluation takes into account the NH_3 flow rate and DRC parameters influence on analytes to find the best conditions both for on-mass (monitoring of the original elemental mass) and mass-shift (monitoring NH_3-based adducts) approaches. Furthermore, the most common interferences in seafood matrices, such as Ca and P, were also evaluated.

1.3 EXPERIMENTAL

1.3.1 Instrumentation

Analysis were performed using a NexION 2000 DRC-ICP-MS (Perkin Elmer, Waltham, MA, USA) equipped with a Single Cell Micro DX autosampler (Perkin Elmer), and the Syngistix™ ICP-MS 2.5 version software (Perkin Elmer). In addition, the instrument was operated with a PFA MicroFlow nebulizer and a cyclonic spray chamber (Glass Expansion, Inc., Melbourne, Australia), a quartz torch with a quartz injector tube (2.5 mm i.d.), and triple cone equipment with nickel sampler cone, skimmer cone and hyperskimmer cone.

1.3.2 Reagents and standards

Ultrapure water (18.2 MΩ cm of resistivity) was obtained from a Milli-Q® IQ 7003 purification device system from Millipore (Bedford, MA, USA). Mono-elemental 1000 mg L^{-1} standards of titanium [$(NH_4)_2TiF_6$], copper [$Cu(NO_3)_2$], and silver($AgNO_3$) were purchased from Perkin Elmer. Mono-elemental standards of zinc [$Zn(NO_3)_2$] and calcium [$Ca(NO_3)_2$] were from Merck (Darmstadt, Germany), and phosphorus ($NH_4H_2PO_4$) was from Scharlau (Barcelona, Spain). NexIONSetup Solution, 10 µg L^{-1}Be, In, U, and Ce, was from Perkin Elmer. Hyperpure nitric acid 69% (w/v) was from Panreac (Barcelona, Spain). Argon (99.998%) and ammonium (99,999%) were from Nippon Gases (Madrid, Spain).

Glassware and plastic ware was decontaminated by soaking in 10% (v/v) nitric acid for at least 48 h. Material was then rinsed with ultra–pure water several times.

1.3.3 ICP-MS measurements

ICP-MS settings and parameters are detailed in **Table 1.1**. Daily performance was assessed by monitoring Be, In, U, and Ce (1.0 µg L^{-1} each one) and verifying intensities higher than 4500 counts s^{-1} (Be), 80000 counts s^{-1} (In), and 60000 counts s^{-1} (U), and a background (mass-to-charge ratio of 202) lower than 3.0, and Ce++/Ce and CeO/Ce ratios lower than 3.0 and 2.5 %, respectively.

Calibration, covering Ti, Ag, Zn, and Cu concentrations within the 0.1–10 µg L−1range (five level concentrations) was prepared in

1.0% (v/v) nitric acid. Reagent blanks (1.0% (v/v) nitric acid) were also analysed throughout the work.

1.3.4 Data treatment

Spectra Analysis was performed using Origin8 Pro Software (Northampton, MA, USA). Data and graph peaks analysis was also performed using Origin8 Pro from Excel exported Data from Syngistix™ ICP-MS 2.5 software (Perkin Elmer).

1.4 RESULTS AND DISCUSSION

As previously mentioned, ammonium shows no predictable reactivity for forming suitable ion products, shifting these ammonium clusters to a free-interference spectral region at higher mass-charge ratios. This fact makes ammonium gas the best option to face interferences in challenging matrices [15]. Several researches have reported two available approaches for DRC technology: on-mass mode working at mass-charge elemental ratio, and shift-mass mode working at mass-charge ratio displaced to another region of the mass spectra (monitoring the formed ion products) [15,22]. In some cases, mass-shift mode could be a more appealing methodology than the on-mass approach in order to avoid interferences. However, sensitivity and measurement stability are also important factors to be taken into account, and they can lead us to consider on-mass approaches as the most suitable strategy in some specific cases.

Ammonium gas generally reacts with elements through charge-transfer reactions to form several adducts by addition of groups such as (-H), (-NH), ($-NH_2$), and mainly ($-NH_3$). The number of groups can be more than one depending on the ammonium flow added and the element's chemical properties. Moreover, especial attention to other possible reactions inside the reaction cell, such as ion products derived from Ar supply and/or from the matrix sample, must be considered. This issue can be solved considering the isotopic pattern or the isotopic ratio of elements because if both isotopes behave equally, we can conclude without doubt that measurements include only the analyte (element) of interest.

Table 1.1. General (common) operating ICP-MS conditions

Spray Chamber Type	Quartz Cyclonic
PC^{3x} Peltier Cooler System	4ºC
Nebulizer Type	PFA MicroFlow
RF power (W)	1600
Plasma Gas Flow (L min^{-1})	15
Auxiliary Gas flow (L min^{-1})	1.2
Nebulizer Gas Flow (L min^{-1})	1.14
Sample uptake rate (µL min^{-1})	≈ 220
Acquisition Mode	Scanning
Dwell time per amu (ms)	50 ms
Quadrupole ion deflector (V)	Set for maximum ion transmission
Mass range (m/z)[a]	Ti: 35-200 Cu: 50-200 Zn: 50-200 Ag: 90-200
Sweeps	20
Readings	1
Replicates	3

[a] Specific conditions (ammonium flow rate, RPq, monitored m/z, ammonium adduct and mode analysis) are given in Table 2

1.4.1 Selection of the best ion-products

The first step to develop a DRC based ICP-MS method is the selection of the ion products (adducts), and the optimization of the formation conditions by selecting the appropriate ammonium flow rate, among others [17,22]. The most suitable ion product for each element has been performed by scanning over a wide mass range between the elemental mass-charge ratio and a mass-charge ratio that allows the inclusion of numerous ammonium molecules [11]. Cu, Zn, Ag, and Ti standards (5 µg L^{-1} in 1.0%(v/v) nitric acid) were used to perform single element mass scanning (ICP-MS operating conditions

in **Table 1.1**) at ammonium flow rates of 0.5, 1.0, 1.5, 2.0, 2.5, and 3.5 mL min^{-1}. **Figure 1.1** shows the mass spectra for each element at the best ammonium flow rate: 1.5 mL min^{-1} for Cu (A), 2.0 mL min^{-1} for Zn (B), 2.5 mL min^{-1} for Ag (C), and 1.0 mL min^{-1} for Ti (D). The highest incidence of spectral interferences for Cu, Zn and Ti were observed at the smaller mass-charge ratio regions; whereas, the several adducts produced at large mass-charge ratios were free of spectral interferences (**Figure 1.1** (A,B,D)). **Figure S1.1** (electronic supplementary information, ESI) shows the complete set of mass spectra for Cu, Zn, Ti, and Ag at the different ammonium flow rates tested. A general trend that can be extracted from these mass spectra is the ability to focus the original mass-charge ratios when using ammonium flow rates lower than 0.5 mL min^{-1}, conditions which lead to obtaining original mass-charge ratios of higher intensity. This effect is referred to as collisional focusing [11,23] and will be studied in greater detail in the following sections. Another general conclusion that can be drawn is the dilution effect at relatively high gas flows, which becomes evident from flow rates of 2.0 mL min^{-1} (spectral interferences are more efficiently eliminated but sensitivity is impaired). Finally, isotopic pattern from ^{49}Ti-based ammonium adducts were not observed (**Figure 1.1D**) since the very low abundance of this isotope (5.41%) versus ^{48}Ti (73.72%).

Therefore, the best ion products (mass-shift approach) were $^{63}Cu(NH_3)_2$ (mass-charge ratio of 97), $^{65}Cu(NH_3)_2$ (mass-charge ratio of 99), $^{64}Zn(NH_3)_3$ (mass-charge ratio of 115), $^{66}Zn(NH_3)_3$ (mass-charge ratio of 117), $^{107}Ag(NH_3)_2$ (mass-charge ratio of 141), $^{109}Ag(NH_3)_2$ (mass-charge ratio of 143), $^{48}Ti(NH)(NH_3)_3$ (mass-charge ratio of 114), and $^{48}Ti(NH)(NH_3)_4$ (mass-charge ratio of 131). Regarding Ti, the selected ammonium adducts are different from those proposed by other authors, for example, $^{48}Ti(NH_3)_6$ (m/z 150) [17-19] and $^{48}TiNH_2(NH_3)_4^+$(m/z 132) [24] for ICP-MS measurements, and $^{48}Ti(NH)$ (m/z 63) for single particle (spICP-MS)[25]. The ammonium flow rate and, probably, the design of the collision/reaction cell, have influence on the formation of ammonium adducts.

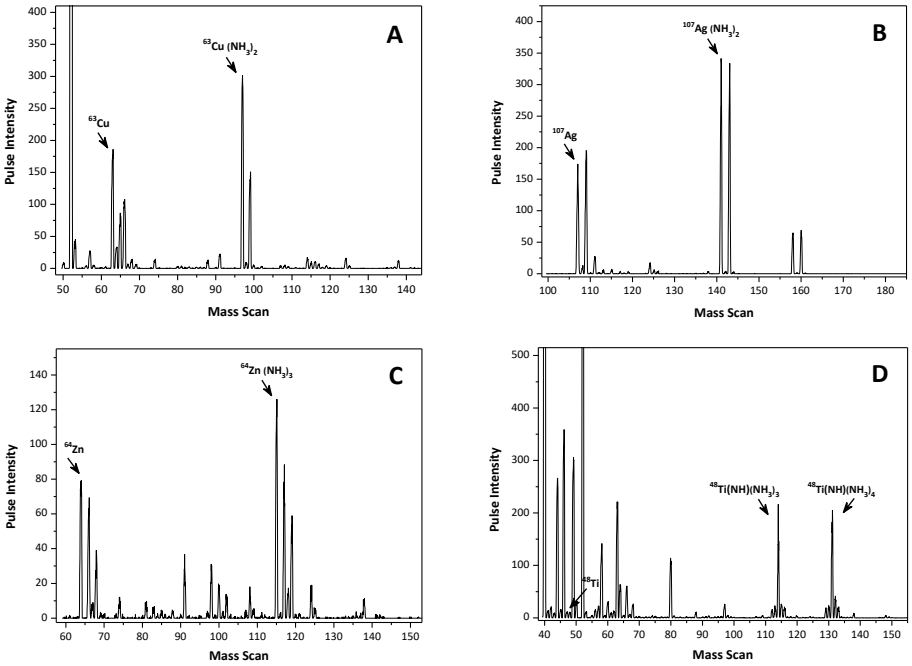

Figure 1.1. Mass spectra illustrating compounds that are formed with ammonium: (A) Cu, 1.5mL min^{-1}, (B) Ag, 2.5mL min^{-1}, (C) Zn, 2.0mL min^{-1}, and (D) Ti, 1.0mL min^{-1}.

1.4.2 Optimization of ammonia flow rate

The effect of the ammonium flow rate was evaluated at the selected adducts (mass-shift approach) and original mass-charge ratios (on mass approach). The RPq Mathieu parameter was fixed at 0.25 throughout the experiment. Results after scanning each mass-charge ratio are plotted in **Figure 1.2**. The isotopic ratio at each elemental mass was used for verifying that the element (element mass) of interest was being measured and for ensuring the minimum influence of the matrix components on the ion products formed from the most abundant isotopes.

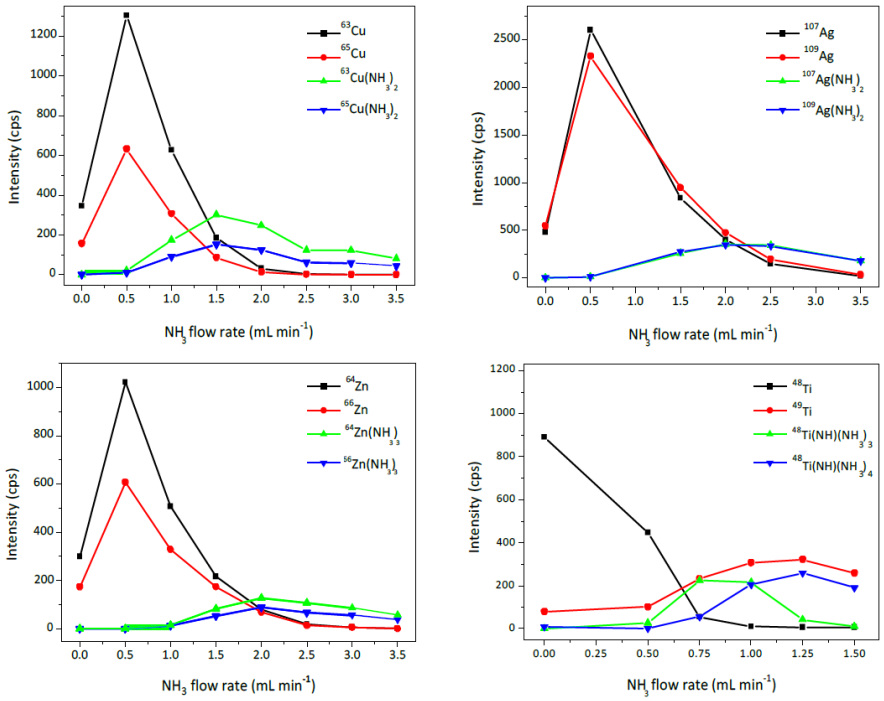

Figure 1.2. Effect of the ammonium flow rate on target's intensities (mass-shift approach).

Mass-charge ratios from Cu, Ag, and Zn show a similar behaviour (**Figure 1.2**). The highest intensities were obtained at the lowest flow rate tested (0.5 mL min^{-1}) for the elemental masses. As previously mentioned, this effect is attributed to the collisional focusing phenomena, which allows sensitive on-mass assessments [11]. The formation of adducts at higher ammonium flow rates were optimum at 1.5mL min^{-1} for Cu, which led to the formation of $^{63}Cu(NH_3)_2$ and $^{65}Cu(NH_3)_2$ adducts (mass-charge ratios of 97 and 99, respectively). Other ion products for Cu were not found even at the high ammonium flow rate, which is in good agreement with the published literature [24]. In the case of Ag, the most prevalent ion products were $^{107}Ag(NH_3)_2$ and $^{109}Ag(NH_3)_2$ (mass-charge ratios of 141 and 143, respectively), with maximum intensities at flow rates within the 2.0-2.5 mL min^{-1} range (a flow rate of 2.0 mL min^{-1} was selected due to

lower ammonium gas consumption). Finally, ion products from Zn ($^{64}Zn(NH_3)_3$ and $^{66}Zn(NH_3)_3$, mass-charge ratios of 115 and 117, respectively) showed lower intensities than those observed for Cu and Ag ion products, which implies that the mass shift approach for Zn determination is less sensitive than the on-mass approach. The highest intensities of $^{64/66}Zn(NH_3)_2$ adducts were observed at an ammonium flow rate of 2.0 mL min^{-1}.

Regarding Ti, the elemental masses (^{48}Ti and ^{49}Ti) intensities are low when using lower ammonium flow rates, mainly for ^{49}Ti. Ammonium clusters from ^{49}Ti were not observed because the very low abundance of this isotope; however, adducts from ^{48}Ti, such as $^{48}Ti(NH)(NH_3)_3$ and $^{48}Ti(NH)(NH_3)_4$ (mass-charge ratio of 114 and 131, respectively), were observed at ammonium flow rates between 0.75 and 1.25 mL min^{-1} (1.0 mL min^{-1}finally selected). Additionally, a Ti(NH) ion product was found to be formed in the cell but was discarded because the short mass-charge ratio is not useful [25].

Table 1.2 summarises the selected ammonium flow rate and ion products for mass-shift approaches, as well the selected flow rate for the on-mass assays (a further re-optimization will be performed by verifying the on-mass results).

1.4.3 Optimization of rejection parameter q value

Mathieu parameters, also called rejection parameters (RPq and RPa) are defined as a stabilized mass band-pass which controls both low-mass cut-off and high-mass cut-off limits, respectively [13]. The influence of these parameters on the reaction cell must be controlled in order to remove the transmitted ions which are outside these stabilization limits [9,13].

The influence of the RPq on mass-shift and on-mass approaches was evaluated after fixing the RPa at 0, the axial field voltage (AFT) at 350V (default values), and the deflector voltage at the specific element mass in the quadrupole ion deflector to achieve maximum ion transmission in the reaction cell. In addition, the ammonium flow rate was fixed at the previous optimised values: 0.5 and 2.0 mL min^{-1} for Ag and Zn when using the on mass and mass shift approaches, respectively; 0.5 and 1.5 mL min^{-1} for Cu when using the on mass and mass shift approaches, respectively; and 1.0 mL min^{-1} for Ti (mass

shift approach). **Figure 1.3** shows that higher intensities are obtained at high RPq values when using the on-mass approach (elemental masses). This is because high RPq values respect shorter masses (elemental ions), allowing for an efficient confinement of the elemental ions in the cell, and hence higher sensitivity. In addition, **Figure 1.3** shows very low signals for ^{48}Ti (values lower than those measured for the less abundant isotope ^{49}Ti). The explanation is because most of ^{48}Ti is efficiently transformed into the $^{48}Ti(NH)(NH_3)_3$ and $^{48}Ti(NH)(NH_3)_4$ ammonium adducts at an ammonium flow rate of 1.0 mL min^{-1}.

Table 1.2. Optimum conditions for standard, mass-shift, and on-mass modes for Ti, Cu, Zn, and Ag determination.

Analyte	Monitored adduct	Monitored m/z	Mode analysis	NH_3 Flow rate (mL min^{-1})	RPq value
Ti	$Ti(NH)(NH_3)_3$	114	Mass-shift	1.0	0.2
	$Ti(NH)(NH_3)_4$	131	Mass-shift	1.0	0.2
	Ti	48	Standard	----	0.25
Cu	Cu	63	On-mass	0.5	0.35
	$Cu(NH_3)_2$	97	Mass-shift	1.5	0.2
	Cu	63	Standard	----	0.25
Zn	Zn	64	On-mass	0.5	0.35
	$Zn(NH_3)_3$	115	Mass-shift	2.0	0.2
	Zn	64	Standard	----	0.25
Ag	Ag	107	On-mass	0.5	0.35
	$Ag(NH_3)_2$	141	Mass-shift	2.0	0.2
	Ag	107	Standard	----	0.25

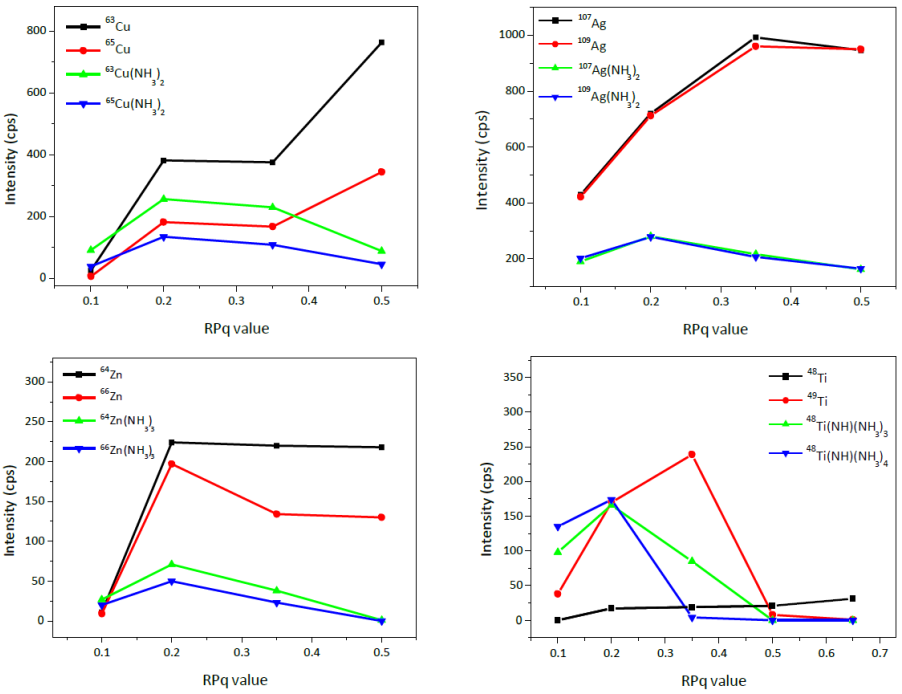

Figure 1.3. Effect of the RPq on the target's intensities (measurements were done for each element at its optimized ammonium flow rate values).

Regarding the mass shift approach, the confinement of ion products is favoured at low RPq values because high RPq values with respect to large masses (ammonium clusters) leads to exclusion of the shorter masses (the elemental masses) minimizing the further formation of the ammonium adducts. Therefore, an RPq value of 0.2 was selected for all analytes when using the mass shift approach (**Table 1.2**). Regarding on-mass approaches, the selection of the RPq will be done after optimising the collisional focussing phenomena.

1.4.4 Collisional focusing phenomena

As previously mentioned, improvements (increases) on the elemental ion intensities are obtained when using small ammonium flow rates (on-mass approach) with respect to the standard working mode (vented mode). This fact is attributed to the collisional focusing effect in instruments with collision/reaction cells as a consequence of

ion confinement (longer traveling path in the ion guide) due to energy losses by several collisions in the cell [11,23]. The phenomena has been reported for gases such as O_2 [17,23], H_2 [11], CH_4 [10] and NH_3 [15,16], and the magnitude is dependent on the monitored ion and the gas (higher loss of ion kinetic energy per collision for heavier gases) [11,23].

Therefore, cell conditions (ammonium flow rate and RPq) were re-evaluated (closer ammonium flow rate and RPq conditions) at the selected elemental ions for on-mass determinations. First, ammonium flow rates of 0.1, 0.3, 0.5 y 0.7 mL min^{-1} were tested at a constant RPq of 0.25 (RPa at 0 and AFT at 350V). **Figure S1.2** (ESI) shows a clear increase on the signal for Cu, Zn and Ag isotopes at low ammonium flow rates, with a maximum value at 0.5 mL min^{-1}. Moreover, intensities when using ammonium were found to be quite higher than those obtained by using the standard mode (absence of ammonium gas). However, the trend is different for Ti (**Figure S1.2**, ESI), and the on-mass approach is not advantageous (higher sensitivity was obtained when using the standard mode).

The effect of the RPq Mathieu parameter was studied for Cu, Zn and Ag (most abundant isotopes for verifying that the isotopic pattern is met) at an ammonium flow rate of 0.5 mL min^{-1}. In addition, the potential ion products formed were also registered. Maximum intensities were observed with RPq of 0.5 for Cu elemental masses, and 0.35 for Zn and Ag; whereas, intensities of the ammonium cluster adducts were negligible (**Figure S1.3**, ESI). However, Cu intensities at 0.35 and 0.5 RPq are similar (**Figure S1.3**, ESI), and an RPq of 0.35 can also be selected for Cu ion monitoring.

Results regarding flow rate and RPq (on-mass mode) have been similar to those previously obtained (section 1.4.3 and 1.4.4), and on-mass conditions for Cu, Zn and Ag were established at 0.5 mL min^{-1} for ammonium flow rate and 0.35 for RPq (**Table 1.2**).

1.4.5 Interferences study: calcium and phosphorus interferences

DRC technology could be an appealing solution [9,14,22,26] when assessing elements exhibiting low mass-charge ratios in biological matrices by ICP-MS because potential spectral

interferences derived from major elements (Mg, K, Na, Ca and P) [12,13,19,20] are efficiently removed/minimised. As shown in **Table 1.3**, Ca and P are potential interferences when assessing Ti and Zn by ICP-MS, and the optimised DRC conditions (on-mass and mass shift approaches) have therefore been tested to know the possibility of a free-interference determination. The on- mass approach (^{63}Cu and ^{64}Zn) and standard mode (^{63}Cu, ^{64}Zn, and ^{48}Ti) measurements were performed with the most abundant isotopes; whereas, the mass shift approach was carried out with $^{63}Cu(NH_3)_2$ (mass-charge ratio of 97), $^{64}Zn(NH_3)_3$ (mass-charge ratio of 115), $^{48}Ti(NH)(NH_3)_3$ (mass-charge ratio of 114), and $^{48}Ti(NH)(NH_3)_4$ (mass-charge ratio of 131). Experiments regarding silver were not performed since this element does not show significant spectral interferences (**Table 3**).

Table 1.3. Isotopes of interest and major polyatomic spectral interferences derived from fish matrix.

Isotope	Major spectral interferences
^{48}Ti	$^{31}P^{17}O$, ^{48}Ca , $^{32}S^{16}O$
^{63}Cu	$^{31}P^{16}O_2$, $^{46}Ca^{16}O^{1}H$, $^{23}Na^{40}Ca$
^{64}Zn	$^{48}Ca^{16}O$, $^{36}Ar^{14}N_2$, $^{32}S^{16}O_2$, $^{31}P^{16}O^{17}O$, $^{31}P^{16}O_2{}^{1}H$
^{107}Ag	Minimum interference

Taking into account the levels of Ca and P in seafood, the study was performed with increasing Ca and P concentrations up to 50 mg L^{-1}. **Figure 1.4** shows that Ca at concentrations higher than 5 mg L^{-1} causes a serious interference when using the standard mode (analytical recoveries close to 500% at the highest Ca concentration level). The mass shift approach using both $^{48}Ti(NH)(NH_3)_3$ and $^{48}Ti(NH)(NH_3)_4$ adducts was found to be successful for Ca interference removal (Ti analytical recoveries within the 80-120% range). The P interference on Ti was less important, and standard and mass shift measurements were found adequate. However, analytical recoveries slightly lower than 80% were obtained when using the $^{48}Ti(NH)(NH_3)_4$ adduct (mass shift approach, **Figure 1.4**).

Similarly to Ti, the interference of Ca on Zn was more notorious than P, and the interference from the latter was successfully compensated when working with the standard mode and also with the on-mass and mass shift ($^{64}Zn(NH_3)_3$ adduct) approach. Regarding Ca interference, the three measurement modes work properly (quantitative analytical recoveries), but both the standard and on-mass mode were found to give Zn analytical recoveries slightly above 120% at the highest Ca level tested.

Finally, Cu experiments (**Figure 1.4**) showed the convenience of the on-mass approach for overcoming the Ca interference; whereas, the mass shift approach ($Cu(NH_3)_3$ adduct) falls at Ca concentrations higher than 10 mg L^{-1}.

1.4.6 Sensitivity study

The limit of detection (LOD) and the limit of quantification (LOQ) have been calculated based on the 3 SD/m and 10 SD/m criterion (*SD*, the standard deviation of eleven measurements of the blank; and *m*, the slope of a calibration graph within the 1.0-10 µg L^{-1} range). Calibration graphs were found to exhibit r^2>0.999, and the RSD% of the blank measurements were always below 4%, except for mass shift ($Zn(NH_3)_3$ adduct) for Zn (RSD within the 9-12% range). The impaired precision for Zn is related to inefficiencies on the ammonium adduct formation (lower intensities and wider peaks than those found for other metal adducts). **Figure 1.5** shows the assessed LOD/LOQ values by using the standard mode and the on-mass and mass shift approaches. In general, higher LOD/LOQ values are obtained for DRC technology (on-mass and mass shift) than for the standard measurement mode since the use of the reaction gas implies a certain dilution. Similar LOD/LOQ were attained for Ti when using the mass shift by monitoring both $^{48}Ti(NH)(NH_3)_3$ and $^{48}Ti(NH)(NH_3)_4$ adducts. The sensitivity (LOD close to 20 ng L^{-1} and LOQ close to 65 ng L^{-1}) were higher than those reported by Fu et al. (lower than 1 and 3 ng L^{-1}, respectively, when using NH_3/He and a NH_3/H_2/He mixtures and tandem mass technology) [18]. Similar LOD values (20 ng L^{-1}) for Ti in blood serum have been reported for DRC

technology using the $^{48}Ti(NH_3)_6$ adduct (mass-charge ratio of 150) [19].

In the case of Cu and Ag, similar sensitivity was achieved when working with the on-mass and mass shift approaches; whereas, the on-mass mode was found to be more sensitive for Zn than the mass shift approach ($Zn(NH_3)_3$ adduct) and even than the standard mode (**Figure 1.5**).

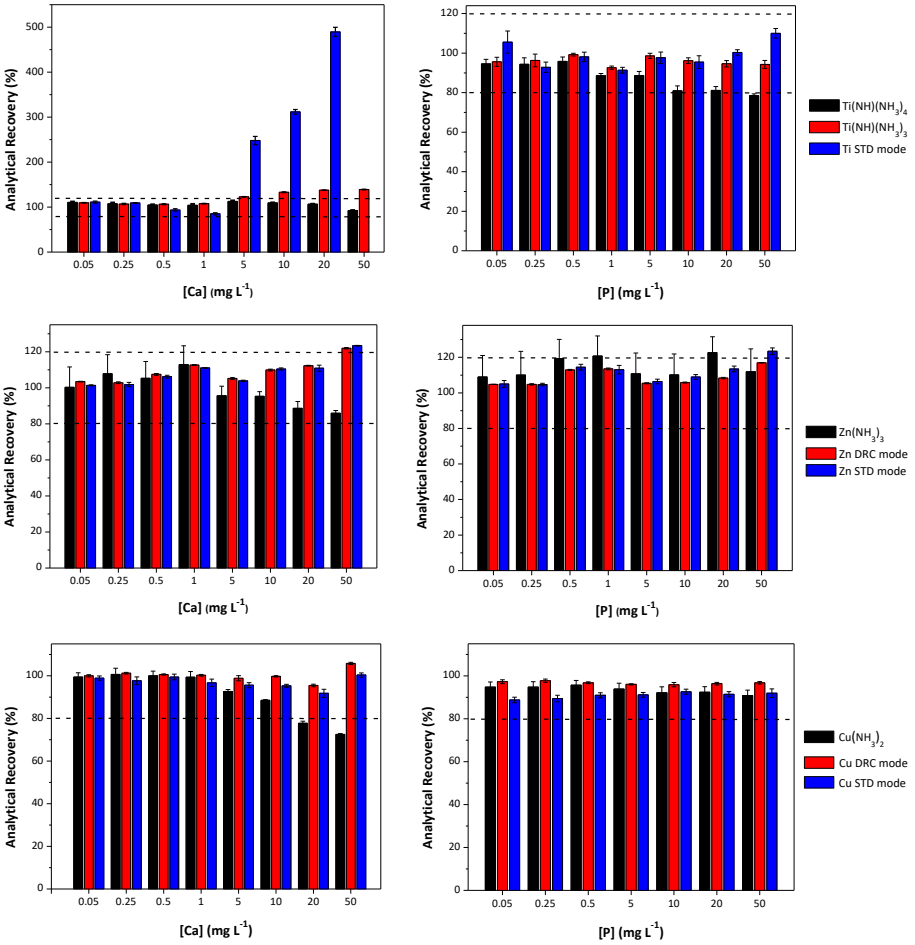

Figure 1.4. Effect of Ca and P concentration on analytical recoveries for Ti, Cu and Zn when using the standard mode, on-mass approach and mass-shift approach. Mass-shift mode with two Ti adducts were used.

Improved sensitivity of the on-mass mode against the mass shift approach can be related to the lack of efficiency in the formation of the $Zn(NH_3)_3$ adduct. Higher sensitivity for on-mass Zn assessment than the standard mode could be attributed to the efficient collisional focusing phenomena. The obtained LOD/LOQ values for Cu, Zn and Ag (standard mode) are lower (LOD/LOQ of 1.7/5.6, 8.5/28.4, and 1.4/4.7 ng L^{-1} for Cu, Zn, and Ag, respectively) than those previously reported for these elements using ICP-MS with collision/reaction cell technology under standard mode (LOD/LOQ of 165/515, 19/63, and 9/32 ng L^{-1} for Cu, Zn, and Ag, respectively) [16]. Moreover, both on-mass and mass shift approches for Cu and Zn have also led to lower LOD/LOQ than the reported values [16]. Finally, sensitivity for Cu (on-mass and mass shift approaches, LOD/LOQ of 1.7/3.2 and 5.6/10.8 ng L^{-1}, respectively) is quite better than previous reported studies based on on-mass measurement mode with ammonium as a reaction gas (280 ng L^{-1}) [27].

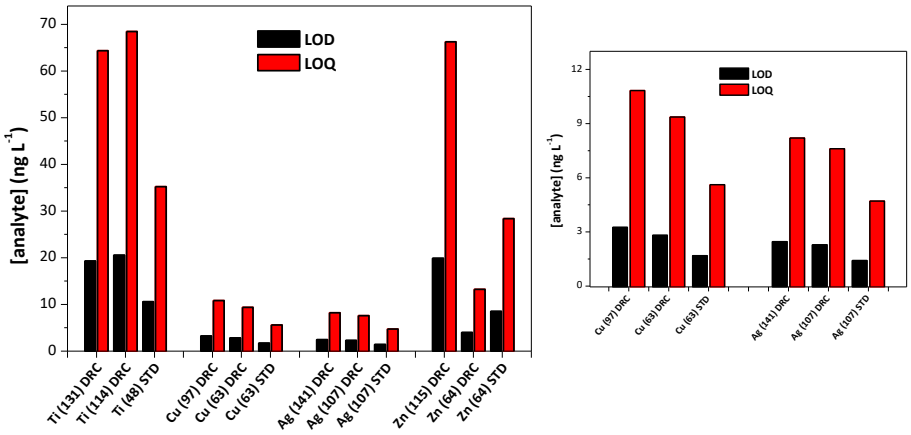

Figure 1.5. LOD and LOQ values obtained for Ag, Ti, Cu and Zn with the standard mode, on-mass and mass shift approaches.

1.5 CONCLUSIONS

DRC technology has been demonstrated to be a useful tool for facing challenging polyatomic and isobaric interferences in ICP-MS determinations. The use of ammonium as a reaction gas has allowed the development of methods based on mass shift and on-mass

approaches. The sensitivity and selectivity have been found to be dependent on the measurement mode as well as the element itself. Ti free-interference determination (high selectivity) can be performed using the mass shift approach with moderate sensitivity; whereas, the on-mass approach has been found more suitable for Zn determination due to lack of efficiency on the formation of ammonium-Zn adducts. However, on-mass and mass shift approaches were found to give similar performances (selectivity and sensitivity) for Cu determination. Finally, a careful optimization of Mathieu parameters is needed for both on-mass and mass shift approaches, but it becomes quite important for on-mass methods due to the great (positive) influence of the collisional focusing phenomena on sensitivity.

SUPPLEMENTARY INFORMATION

Figure S1.1. Set of mass spectra for Cu, Zn and Ti at different tested ammonium flow rates (no ammonia flow, low and high ammonia flow rate): (A) Vented mode, (B) 0.5 mL min^{-1}, (C) 1.5 mL min^{-1} for Ti, 2.5 mL min^{-1} for Cu and 3.0 mL min^{-1} for Zn.

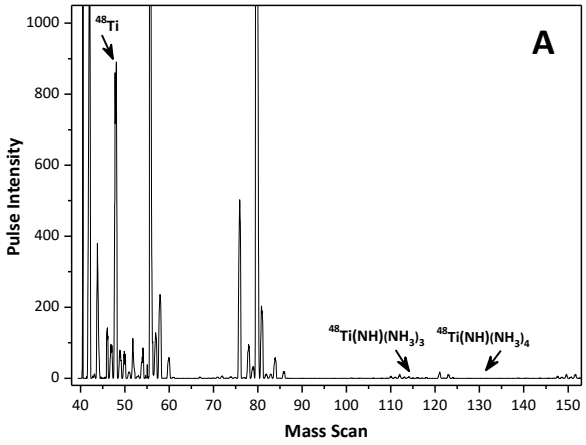

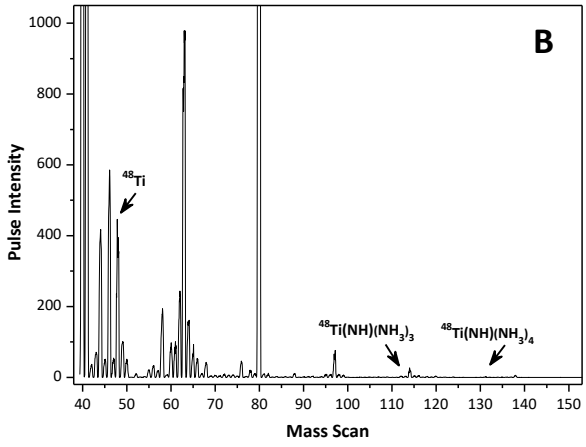

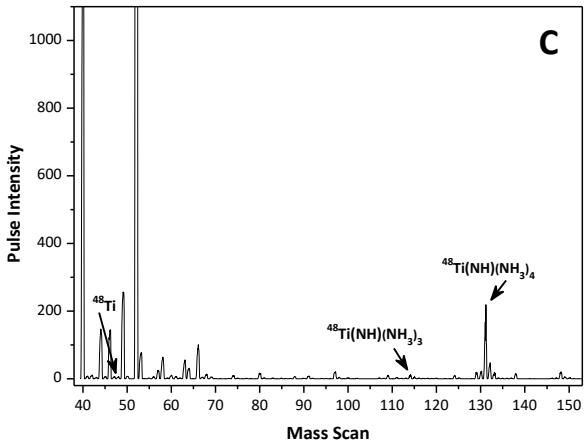

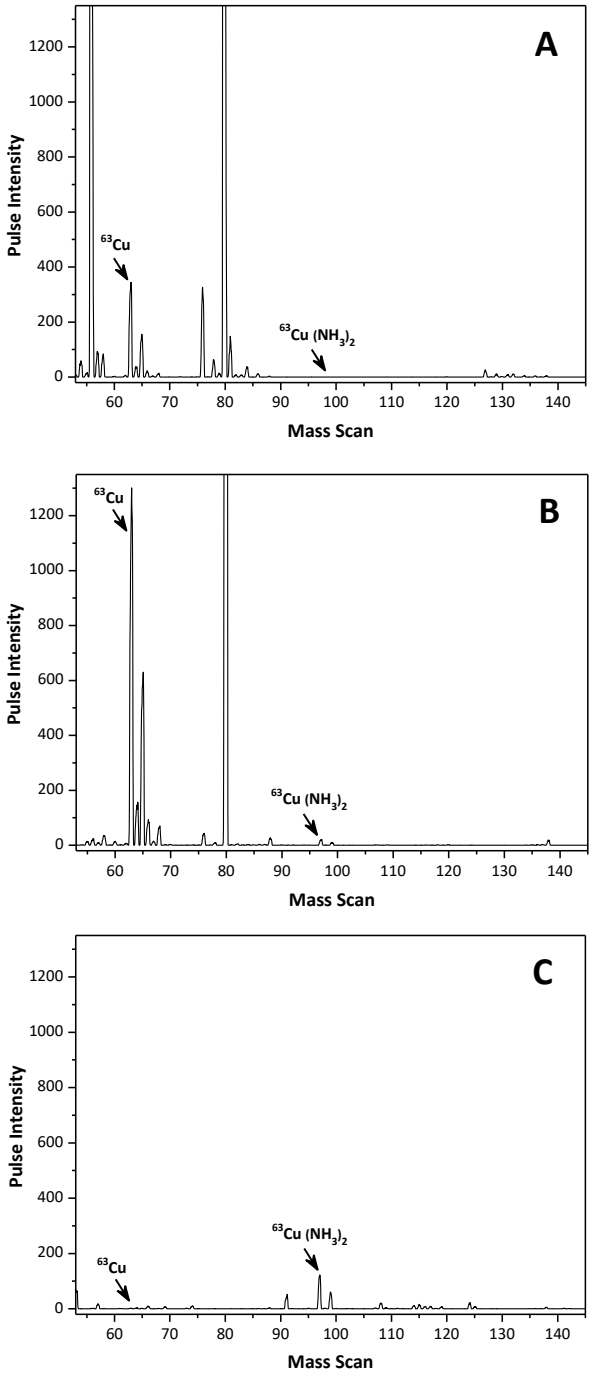

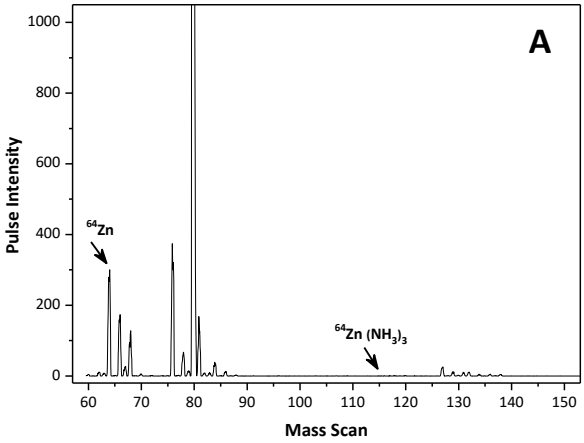

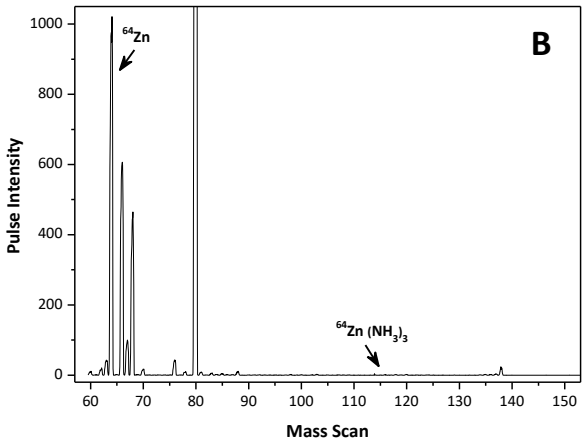

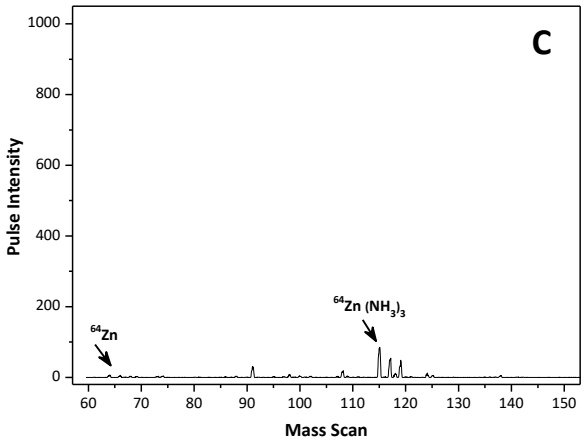

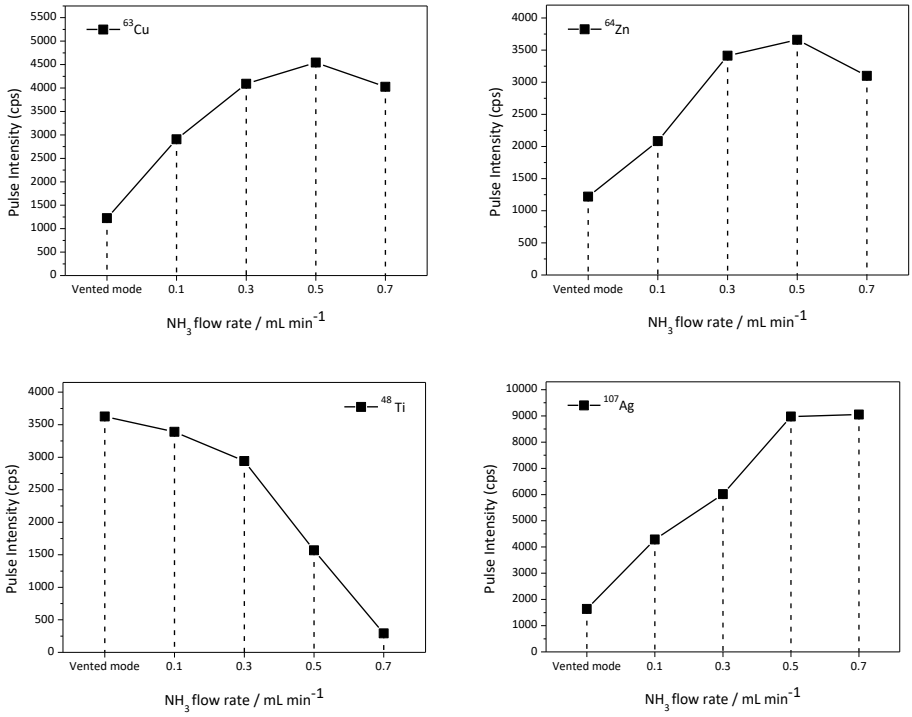

Figure S1.2. Effect of ammonium flow rate on targets intensities. (on-mass approaches)

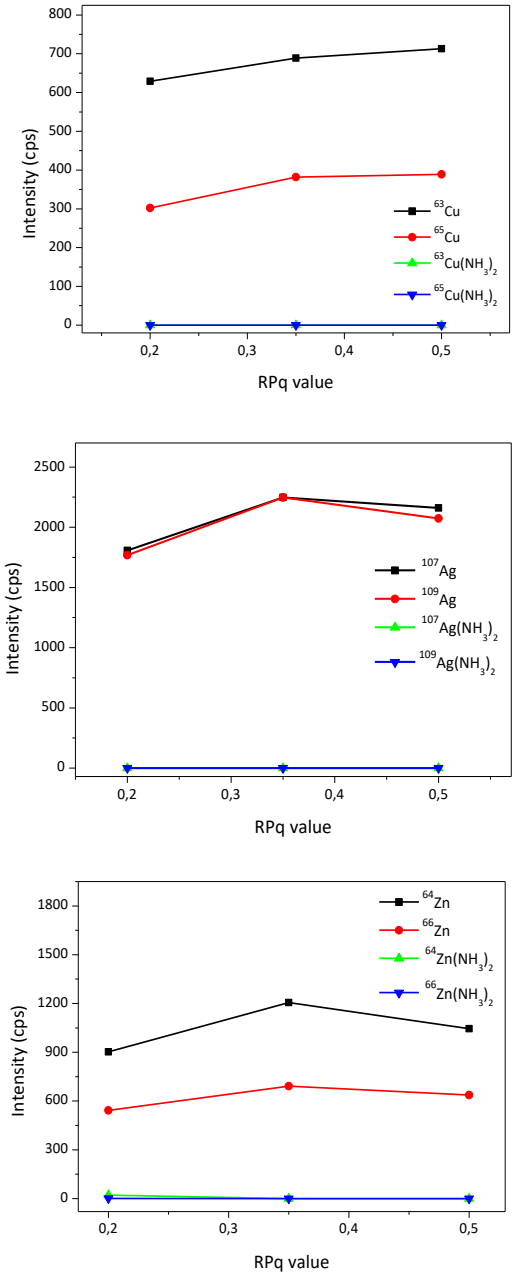

Figure S1.3. Effect of the RPq value on targets intensities. (on-mass approaches)

REFERENCES

[1] R.F.J. Dams, J. Goossens, L. Moens, Spectral and non-spectral interferences in inductively coupled plasma mass-spectrometry, Mikrochim. Acta. 119 (1995) 277–286. https://doi.org/10.1007/BF01244007.

[2] S.H. Tan, G. Horlick, Background spectral features in inductively coupled plasma/mass spectrometry, Appl. Spectrosc. 40 (1986) 445–460. https://doi.org/10.1366/0003702864508944.

[3] N. Jakubowski, L. Moens, F. Vanhaecke, Sector field mass spectrometers in ICP-MS, Spectrochim. Acta Part B At. Spectrosc. 53 (1998) 1739–1763. https://doi.org/10.1016/S0584-8547(98)00222-5

[4] N. Jakubowski, T. Prohaska, L. Rottmann, F. Vanhaecke, Inductively coupled plasma- and glow discharge plasma-sector field mass spectrometry: Part I. Tutorial: Fundamentals and instrumentation, J. Anal. At. Spectrom. 26 (2011) 693–726. https://doi.org/10.1039/c0ja00161a.

[5] I. Rodushkin, E. Engström, A. Stenberg, D.C. Baxter, Determination of low-abundance elements at ultra-trace levels in urine and serum by inductively coupled plasma-sector field mass spectrometry, Anal. Bioanal. Chem. 380 (2004) 247–257. https://doi.org/10.1007/s00216-004-2742-7.

[6] J.M. Harrington, D.J. Young, A.S. Essader, S.J. Sumner, K.E. Levine, Analysis of human serum and whole blood for mineral content by ICP-MS and ICP-OES: Development of a mineralomics method, Biol. Trace Elem. Res. 160 (2014) 132–142. https://doi.org/10.1007/s12011-014-0033-5

[7] K. Sakata, K. Kawabata, Reduction of fundamental polyatomic ions in inductively coupled plasma mass spectrometry, Spectrochim. Acta Part B At. Spectrosc. 49 (1994) 1027–1038. https://doi.org/10.1016/0584-8547(94)80088-X

[8] S.D. Tanner, V.I. Baranov, D.R. Bandura, Reaction cells and collision cells for ICP-MS: A tutorial review, Spectrochim. Acta Part

B At. Spectrosc. 57 (2002) 1361–1452. https://doi.org/10.1016/S0584-8547(02)00069-1.

[9] A.S. Henn, F.S. Rondan, M.F. Mesko, P.A. Mello, M. Perez, J. Armstrong, L.A. Bullock, J. Parnell, J. Feldmann, E.M.M. Flores, Determination of Se at low concentration in coal by collision/reaction cell technology inductively coupled plasma mass spectrometry, Spectrochim. Acta Part B At. Spectrosc. 143 (2018) 48–54. https://doi.org/10.1016/j.sab.2018.02.014).

[10] E. Soriano, V. Yusà, A. Pastor, M. de la Guardia, Dynamic reaction cell inductively couple plasma-mass spectrometry optimization for seawater analysis, Microchem. J. 137 (2018) 363–370. https://doi.org/10.1016/j.microc.2017.11.015.

[11] E. Bolea-Fernandez, D. Leite, A. Rua-Ibarz, L. Balcaen, M. Aramendía, M. Resano, F. Vanhaecke, Characterization of SiO2 nanoparticles by single particle-inductively coupled plasma-tandem mass spectrometry (spICP-MS/MS), J. Anal. At. Spectrom. 32 (2017) 2140–2152. https://doi.org/10.1039/c7ja00138j.

[12] S. Li, Z. Yang, J. Cao, B. Qiu, H. Li, Determination of metallothionein isoforms in fish by cadmium saturation combined with anion exchange HPLC-ICP-MS, Chromatographia 81 (2018) 881–889. https://doi.org/10.1007/s10337-018-3523-3.

[13] Z.S. Gong, R. Yang, C.Q. Sun, W.N. Han, X.H. Jiang, S.X. Xu, Y. Wang, Simultaneous determination of P and S in human serum, blood plasma and whole blood by ICP-MS with collision/reaction cell technology, Int. J. Mass Spectrom. 445 (2019) 116193. https://doi.org/10.1016/j.ijms.2019.116193.

[14] S. Candás-Zapico, D.J. Kutscher, M. Montes-Bayón, J. Bettmer, Single particle analysis of TiO2 in candy products using triple quadrupole ICP-MS, Talanta. 180 (2018) 309–315. https://doi.org/10.1016/j.talanta.2017.12.041.

[15] E. Bolea-Fernandez, D. Leite, A. Rua-Ibarz, T. Liu, G. Woods, M. Aramendia, M. Resano, F. Vanhaecke, On the effect of using

collision/reaction cell (CRC) technology in single-particle ICP-mass spectrometry (spICP-MS), Anal. Chim. Acta. 1077 (2019) 95–106. https://doi.org/10.1016/j.aca.2019.05.077.

[16] Z.S. Gong, X.H. Jiang, C.Q. Sun, Y.P. Tian, G.H. Guo, Y.Z. Zhang, X.H. Zhao, Y. Wang, Determination of 21 elements in human serum using ICP-MS with collision/reaction cell, Int. J. Mass Spectrom. 423 (2017) 20–26. https://doi.org/10.1016/j.ijms.2017.10.001.

[17] L. Balcaen, E. Bolea-Fernandez, M. Resano, F. Vanhaecke, Inductively coupled plasma - Tandem mass spectrometry (ICP-MS/MS): A powerful and universal tool for the interference-free determination of (ultra)trace elements - A tutorial review, Anal. Chim. Acta. 894 (2015) 7–19. https://doi.org/10.1016/j.aca.2015.08.053.

[18]. L. Fu, S.-Y. Shi, J.-C. Ma, Accurate determination of harmful and doping elements in soft magnetic ferrite powders using inductively coupled plasma tandem mass spectrometry, Chinese J. Anal. Chem. 47 (2019) 1382–1389. https://doi.org/10.1016/S1872-2040(19)61189-8.

[19] L. Balcaen, E. Bolea-Fernandez, M. Resano, F., Accurate determination of ultra-trace levels of Ti in blood serum using ICP-MS/MS, Anal. Chim. Acta. 809 (2014) 1–8. https://doi.org/10.1016/j.aca.2013.10.017.

[20] B. Markiewicz, A. Sajnóg, W. Lorenc, A. Hanć, I. Komorowicz, J. Suliburska, R. Kocyłowski, D. Barałkiewicz, Multielemental analysis of 18 essential and toxic elements in amniotic fluid samples by ICP-MS: Full procedure validation and estimation of measurement uncertainty, Talanta. 174 (2017) 122–130. https://doi.org/10.1016/j.talanta.2017.05.078.

[21] I.F. Seregina, K. Osipov, M.A. Bol'shov, D.G. Filatova, S.Y. Lanskaya, Matrix interference in the determination of elements in biological samples by inductively coupled plasma–mass spectrometry and methods for its elimination, J. Anal. Chem. 74 (2019) 182–191. https://doi.org/10.1134/S1061934819020114

[22] T. Van Acker, E. Bolea-Fernandez, E. De Vlieghere, J. Gao, O. De Wever, F. Vanhaecke, Laser ablation-Tandem ICP-mass spectrometry (LA-ICP-MS/MS) imaging of iron oxide nanoparticles in Ca-rich gelatin microspheres, J. Anal. At. Spectrom. 34 (2019) 1846–1855. https://doi.org/10.1039/c9ja00135b.

[23] N. Yamada, Kinetic energy discrimination in collision/reaction cell ICP-MS: Theoretical review of principles and limitations, Spectrochim. Acta Part B At. Spectrosc. 110 (2015) 31–44. https://doi.org/10.1016/j.sab.2015.05.008.

[24] L. Fu, S. Shi, X. Chen, H. Xie, Analysis of impurity elements in high purity cobalt powder by inductively coupled plasma tandem mass spectrometry, Microchem. J. 139 (2018) 236–241. https://doi.org/10.1016/j.microc.2018.03.002.

[25] M. Tharaud, A.P. Gondikas, M.F. Benedetti, F. Von Der Kammer, T. Hofmann, G. Cornelis, TiO2 nanomaterial detection in calcium rich matrices by spICPMS. A matter of resolution and treatment, J. Anal. At. Spectrom. 32 (2017) 1400–1411. https://doi.org/10.1039/c7ja00060j.

[26] P. Petrov, B. Russell, D.N. Douglas, H. Goenaga-Infante, Interference-free determination of sub ng kg−1 levels of long-lived 93Zr in the presence of high concentrations (μg kg−1) of 93Mo and 93Nb using ICP-MS/MS, Anal. Bioanal. Chem. 410 (2018) 1029–1037. https://doi.org/10.1007/s00216-017-0635-9

[27] B.L. Batista, J.L. Rodrigues, J.A. Nunes, V.C. de Oliveira Souza, F. Barbosa, Exploiting dynamic reaction cell inductively coupled plasma mass spectrometry (DRC-ICP-MS) for sequential determination of trace elements in blood using a dilute-and-shoot procedure, Anal. Chim. Acta. 639 (2009) 13–18. https://doi.org/10.1016/j.aca.2009.03.016.

CHAPTER 2

SINGLE-PARTICLE INDUCTIVELY COUPLED PLASMA MASS SPECTROMETRY USING AMMONIA REACTION GAS AS A RELIABLE AND FREE-INTERFERENCE DETERMINATION OF METALLIC NANOPARTICLES

CHAPTER 2. SINGLE-PARTICLE INDUCTIVELY COUPLED PLASMA MASS SPECTROMETRY USING AMMONIA REACTION GAS AS A RELIABLE AND FREE-INTERFERENCE DETERMINATION OF METALLIC NANOPARTICLES

*The results from this chapter have already been published as Cristian Suárez-Oubiña, Paloma Herbello-Hermelo, Pilar Bermejo-Barrera, and Antonio Moreda-Piñeiro, Single-particle inductively coupled plasma mass spectrometry using ammonia reaction gas as a reliable and free-interference determination of metallic nanoparticles, Talanta. 242 (2022) 123286, DOI: 10.1016/j.talanta.2022.123286.

Group of Trace Element, Spectroscopy, and Speciation (GETEE), Institute of Materials iMATUS. Department of Analytical Chemistry, Nutrition, and Bromatology. Faculty of Chemistry. Universidade de Santiago de Compostela. Avenida das Ciencias, s/n 15782, Santiago de Compostela. Spain.

2.1 ABSTRACT

Intensive production of nanomaterials, especially metallic nanoparticles (MNPs), and their release into the environment pose several risks for humans and ecosystem health. Consequently, high-efficiency analytical methodologies are required for control and characterization of these emerging pollutants. Single-particle inductively coupled plasma – mass spectrometry (spICP-MS) is a promising technique which allows the determination and characterization of MNPs. However, several elements or isotopes are hampered by spectral interferences, and dynamic-reaction cell (DRC) technology is becoming a useful tool for free interference determination by ICP-MS. DRC-based spICP-MS methods using ammonia as a reaction gas (either on-mass approach or mass-shift approaches) have been developed for determining titanium dioxide

nanoparticles (TiO_2 NPs), copper oxide nanoparticles (CuO NPs), copper nanoparticles (Cu NPs), and zinc oxide nanoparticles (ZnO NPs). The effects of parameters such as ammonia flow rate and dwell time on the peak width (NP transient signal in spICP-MS) were comprehensively studied. Influence of NP size and nature were also investigated.

2.2 INTRODUCTION

A wide variety of nanomaterials (NMs), metallic nanoparticles (NPs) included, are playing an increasing role in medicine and in many industrial sectors such as construction, cosmetics and food [1-5]. The interest in these nanometer-scale materials is due to their unique properties, which differ from those of the chemically identical bulk materials. Moreover, the outstanding properties of NMs are highly dependent on the NM nature and size distribution [6-7]. The increasing use of NMs, and hence their release into the environment and the potential risk to humans and ecosystem health, concerns the scientific community. Several governmental regulatory agencies have brought about regulations such as those in the cosmetic and food industries [8-10]. Undoubtedly, the development and use of NMs must be sustainable, and analytical methodologies are required for an accurate determination/characterization and monitoring.

The determination and characterization of NPs, mainly in complex matrices, is a difficult task, and most common analytical techniques do not provide enough selectivity and sensitivity. In addition, a complete characterization of NPs requires the assessment of several physical-chemical properties, such as surface porosity and functionality, besides the nature (chemical composition), number of NPs and size distribution. In addition to the well-established transmission and scanning electron microscopy (TEM and SEM) and separation techniques, mainly based on flow field fractionation (FFF), inductively coupled plasma mass spectrometry (ICP-MS) in time resolved analysis mode, referred to as single particle ICP-MS (SP-ICPMS), has gained popularity for metallic NPs detection and characterization [11-15]. SP-ICP-MS is able to provide information about the nanoparticle number concentration, size, and number size distribution by monitoring a mass-to-charge ratio of a certain metal

contained in the nanoparticle**.** Moreover, dissolved and particulate analytes can be properly distinguished by measuring the discrete particles (pulses) over a continuous background (dissolved species). The number of particle events is proportional to the particle number concentration in the suspension; whereas, the intensity of each event is proportional to the mass of element per particle. The great counting and sizing capabilities at very low concentrations makes spICP-MS an appealing technique for the assessment of metallic nanoparticles (MNPs) in biological and environmental samples [12,13]. However, spICP-MS measurements assume that all measured NPs exhibit a spherical shape, which is not always true when coping with MNPs in environmental, food and clinical matrices. In addition, spICP-MS requires improvements for measuring small MNP sizes [12,15].

There are several analytes (elements or isotopes) in which determination by ICP-MS is hampered by spectral interferences caused by isobaric isotopes or polyatomic species. These interferences can be overcome by selecting other free-interference isotopes (if available) or by using mathematical corrections against the interfering species. In addition, interference avoidance can be also achieved by improved mass analysers, such as sector field ICP-MS (SF-ICP-MS), and successful applications have been reported for ICP-MS measurements [16-20]. Spectral interferences in ICP-MS can also be overcome by using a quadrupole (a cell) in which the polyatomic interferences collide with a collision gas (typically He in combination with kinetic energy discrimination, KED) or react with a reaction gas such as H_2, NH_3 and O_2 (dynamic reaction cell, DRC). The use of KED and DRC technologies must be properly optimized for removing spectral interferences in spICP-MS, a task which is not as straightforward as in ICP-MS since potential additional interferences can be derived from pollutants, impurities or colloid stabilizers included in the NPs.

Since spICP-MS is an emerging technique for NPs assessment, there are not many applications of DRC technology for interferences removal. The NPs behaviour in the cell is quite different from those exhibited by dissolved analytes. DRC technology leads to ion burst enhancement in the cell, and the ion burst from MNPs is much larger

than that observed for dissolved analytes. The experimental evidence leads to the need for lower reaction gas (ammonia) flow rates for MNPs than for dissolved metallic ions [21].

In addition to the reaction gas flow rate, ICP-MS instrumentation with quadrupole ion deflector requires the careful optimization of the Mathieu or Rejection Parameters (RPa and RPq) in the reaction cell, parameters which correspond to the high-mass and low-mass cut-off, respectively. Moreover, NPs determination by spICP-MS with DRC requires the evaluation of the effect of the dwell time and the width peak on the number of particle and particle size in order to avoid under- or over-estimations. Research literatures mention the use of O_2 for spICP-MS assessment of SiO_2 NPs [22], TiO_2 NPs [23], and Au, Ag, Pt and Fe_3O_4 NPs [24]. In addition, studies based on the use of H_2, NH_3 and CH_3F as reaction gases for SiO_2 NPs determination [22], H_2 for Au, Ag, Pt and Fe_3O_4 NPs [24], and NH_3 for spICP-MS determination of TiO_2 NPs [25], have also been reported. High reactivity, and hence high sensitivity, and the generation of predictable adducts (mass shift approach), has been reported for O_2; whereas, H_2 has been found useful for overcoming Ar interferences [22,25]. However, an unpredictable reactivity has been reported for NH_3 and CH_3F reaction gases, offering the advantage of generating several adducts or ion-products, and hence higher selectivity in ICP-MS/MS for interferences removal by using either on-mass and mass-shift approaches [26,27].

As previously commented, literature regarding DRC technology for spectral interferences removal is mainly focused on conventional ICP-MS [21], although there are some developments for sedimentation field-flow fractionation (SdFFF) coupled to ICP-MS/MS [28] and more recently for spICP-MS [22-25]. The aim of the current research has been to test the feasibility of DRC-spICP-MS using NH_3 as a reaction gas for a free-interference determination of TiO_2 NPs, Cu NPs, CuO NPs, and ZnO NPs. In addition to the NPs' nature (chemical composition), the effect of the NPs size, as well as the dwell time and NH_3 flow rate, was also investigated in on-mass and mass-shift measurement modes. Findings from this research will

be useful to improve the use of reaction gases in spICP-MS analysis and the application to challenging complex matrix analysis.

2.3 EXPERIMENTAL

2.3.1 Instrumentation

A NexION 2000 inductively coupled plasma mass spectrometer (Perkin Elmer, Waltham, MA, USA) equipped with dynamic reaction cell (DRC) technology and Single Cell Micro DX autosampler (Perkin Elmer) was used for determinations. The instrument is equipped with nickel sampler/skimmer/hyper skimmer cones. The nebulizer was a concentric Meinhard™ type coupled to a cyclonic spray chamber (Glass Expansion, Inc., Melbourne, Australia) and attached to a quartz torch with a quartz injector tube (2.5 mm i.d.). Data acquisition and management was performed with the Syngistix™ Nano Application 2.5 version software (Perkin Elmer), which allows data visualization as it is being acquired in real-time and displays background-corrected intensity histogram which continuously updates during data acquisition [29]. The software uses the same formula regarding the basic principles of spICP-MS [12] for assessing the number of NPs and NPs sizes. An USC-TH ultrasound water bath (45 Hz, 80 W) from VWR International Eurolab S.L (Barcelona, Spain) was used for dispersing NPs before analysis.

2.3.2 Reagents and standards

All solutions were prepared with ultrapure water (18.2 MΩ cm of resistivity) obtained from a Milli-Q® IQ 7003 purification device system (Millipore, Bedford, MA, USA). Mono-elemental 1000 mg L^{-1} standards of titanium [$(NH_4)_2TiF_6$] and copper [$Cu(NO_3)_2$] were purchased from Perkin Elmer; whereas, mono-elemental standard of zinc [$Zn(NO_3)_2$] was from Merck (Darmstadt, Germany). Gold NPs solutions were prepared from a N8151035 (49.6 nm by TEM, 12.4 ng mL^{-1}, 9.89×10^6 NPs mL^{-1}, in aqueous 1mM citrate) certified reference material from nano Composix (San Diego, CA, USA). Titanium dioxide nanoparticles stock suspensions (100 mg L^{-1} as TiO_2 in ultrapure water) were prepared from TiO_2 nanopowder (rutile, 99.9%) of 30, 50 and 100 nm aerodynamic particle size (APS) purchased from

US Research Nanomaterials (Houston, TX, USA), and TiO_2 suspension (mixture of rutile and anatase, 99.5%, size <150 nm, 40wt. % in water) purchased from Sigma-Aldrich. Zinc oxide NPs suspensions (100 mg L^{-1} as ZnO in ultrapure water) were prepared from 35-45 and 80-200 nm ZnO nanopowder from US Research Nanomaterials, and ZnO dispersion (size <100 nm, 20wt. % in water) purchased from Sigma-Aldrich. Copper NPs suspensions were prepared from 40-60 and 60-80 nm Cu nanopowder (99.5%) and Cu O nanopowder (size <50 nm) from Sigma-Aldrich (stock suspensions at 100 mg L^{-1} as Cu and CuO in ultrapure water, respectively). Stock suspensions, as well as further diluted suspension were prepared without adding stabilizing agents and homogenization before sampling was performed by ultrasound stirring (except for Au NPs). NexION Setup Solution, 10 µg L^{-1}Be, In, U, and Ce, was from Perkin Elmer. Hyperpure nitric acid 69% (w/v) was from Panreac (Barcelona, Spain). Argon (99.998%) and ammonia (99,999%) were from Nippon Gases (Madrid, Spain).

Glassware and plastic ware was decontaminated by soaking in 10% (v/v) nitric acid for at least 48 h. The material was then rinsed with ultra–pure water several times.

2.3.3 spICP-MS measurements

SP-ICP-MS settings are listed in **Table 2.1**. Since an exact mass-to-charge ratio is not isolated with the quadrupole ion deflector (axial field voltage, AFT at 350 V), RPa (high-mass cut-off) and RPq (low-mass cut-off) rejection parameters have to be fixed at the optimum values for a better focusing of the mass-to-charge ratio of interest (adduct in mass shift approach, and the analyte in on-mass approach). RPa was found to be less significant for both on-mass and mass shift approaches, and this parameter was fixed at 0 for all NPs and both measurement modes. However, RPq was found to be quite important [21], and the optimized values for on-mass and mass shift measurement modes are displayed in **Table 2.2**.

Daily performance was assessed by monitoring Be, In, U, Ce (Ce++/Ce and CeO/Ce ratios) and background (mass-to-charge ratio of 202), and verifying intensities higher than the values established as optimum by the manufacturer. Transport efficiency (TE%) was

assessed by the particle frequency method, which implies the assessment of the sample flow rate, an aqueous ionic Au calibration, and the measurement of an Au NPs certified reference material. Therefore, sample flow rate was established by aspirating ultrapure water and weighing the solution after and before aspiration at the selected pump conditions (sample flow rates were between 0.19 and 0.21 mL min^{-1}). Ionic Au calibration was performed within the 0-3.5 µg L^{-1} range, and a suspension at 1.0×10^5 particles mL^{-1}, prepared in ultrapure water from a 49.6 nm Au NPs certified reference material, was finally measured. Transport efficiency (TE%) values (close to 8.0%) were automatically calculated by Syngistix™ Nano Application. Matched 1.0% (v/v) nitric acid calibrations covering ionic Ti, Zn, and Cu concentrations within the 0.1–10 µg L^{-1} range (five level concentrations) were prepared for the assessment of NPs size distribution [11]). Reagent blanks (1.0% (v/v) nitric acid) were also analysed throughout the work.

Stock NPs suspensions were properly diluted in ultrapure water and sonicated just before spICP-MS measurements to avoid agglomeration and aggregation phenomena. NPs standards concentrations varied from 0.5 to 5.0 µg L^{-1} depending on the analyte and mainly on the measurement mode. Therefore, the standard mode and the on-mass approach require similar concentrations for achieving an adequate number of peaks in the time window detection of 100 seconds and size distribution close to a Gaussian distribution. However, mass-shift measurements require higher concentrations.

Table 2.1. Operating conditions for spICP-MS measurements.

Parameter (units)	
Instrument	Nex Ion 2000
Spray chamber	QuartzCyclonic
PC^{3x} Peltier Cooler System	4 °C
Nebulizer type	Concentric Meinhard™
RF power (W)	1600
Plasma gas flow rate (L min^{-1})	15
Auxiliary gas flow rate (L min^{-1})	1.2
Nebulizer gas flow rate (L min^{-1})	1.14
Sample flow rate (mL min^{-1})	≈ 0.21
Quadrupole ion deflector (V)	Set for maximum ion transmission
Transport efficiency (%)	≈ 8%
Scan time (s)	100

Table 2.2. Optimized spICP-MS conditions for mass-shift and on-mass approaches.

Analyte	Monitored ion/adduct	Monitored m/z	Mode	NH_3 flow rate (mL min^{-1})	Dwell time (µs)	RPq
Ti	$Ti(NH)(NH_3)_3$	114	Mass-shift	0.5 - 0.75	100	0.2
	$Ti(NH)(NH_3)_4$	131	Mass-shift	0.75 - 1.0	100	0.2
Cu	Cu	63	On-mass	0.5	50	0.5
	$Cu(NH_3)_2$	97	Mass-shift	1.25	100	0.2
Zn	Zn	64	On-mass	0.25	50	0.35
	$Zn(NH_3)_3$	115	Mass-shift	1.75	200	0.2

2.3.4 Data treatment

Spectra Analysis was performed using Origin8 Pro Software Origin8 Pro software (OriginLab Corporation, Northampton, MA, USA) was used for peak integration. Raw data from Syngistix ICP-MS software (1.0 million measurements) were first exported to Excel and treated (filtered) to remove low intense peaks (few cps, as well as 0 cps) and reduced the data set. Filtered data were then exported to Origin8 for peak integration by a semi-automatic procedure. First, the baseline was established by fixing the area without peaks and then the peaks were selected for automatic integration by the software. At least 10 peaks were integrated to assess mean peak widths under each condition, and the selected peaks were those of intermediate height (intensity) for avoiding the selection of peaks located in the wings of the distribution. Integration was carried out and the peak width at the baseline (whole peak) and at different heights (5, 15 and 50% of peak height) was obtained. The data generated was manually checked and listed, and, the mean and the standard deviation of peak widths after integration were calculated for interpretation and/or plotting.

2.4 RESULTS AND DISCUSSION

The effect of the ammonia flow rate, dwell time and work-modes using ammonia as a reaction gas have been evaluated for both on-mass and mass-shift approaches, and compared with vented mode in each specific conditions. In addition, the effect of these experimental parameters on peak shape, peak intensity, and peak stability was also evaluated by measuring the peak width at different heights (baseline, 5%, 15% and 50%). The studies were focused on TiO_2 NPs, Cu NPs, CuO NPs, and ZnO NPs of several size distributions.

2.4.1 Selection of the ammonia-based adducts

After fixing optimum RPq Mathieu parameter and ammonia flow rate [21], mass scanning experiments were performed to obtain the several ammonia ion products for each element using ionic Ti, Cu, and Zn standards at 5 µg L^{-1} (solutions prepared in 1.0 %(v/v) nitric acid) and the ICP-MS operating conditions listed in **Table 2.1**. The most intense signals for Ti were observed at m/z ratios of 63, 114 and 131, which correspond to $^{48}Ti(NH)$, $Ti(NH)(NH_3)_3$ and $Ti(NH)(NH_3)_4$

clusters, respectively (**Figure 2.1A**). Other intense signals have been observed for m/z 49 and 46 (**Figure 2.1**A), but they do not come from Ti (lack of Ti isotopic pattern in the signals). It has been reported in the literature that $^{48}Ti(NH_3)_6$ (m/z 150) is a suitable ammonia ion product for Ti assessment by ICP-MS [26,30,31] and SdFFF-ICP-MS/MS [28]. Other reported ammonia-based adducts for Ti have been $^{48}TiNH_2(NH_3)_4^+$(m/z 132) in ICP-MS measurements [32], and $^{48}Ti(NH)$ (m/z 63) in spICP-MS analysis [25]. The m/z 114 and 131 have been finally selected for further mass shift studies. However, m/z 63 was not further used since the NexIon 2000 is equipped with a quadrupole ion deflector which is not a real quadrupole, and low m/z ratios could be not excluded and be present in the reaction cell (^{63}Cu and ^{63}Zn could be potential interferences).

Figure 2.1B and **Figure 2.1C** show the mass spectra for Cu (ammonium flow rate of 1.5 mL min^{-1}) and Zn (ammonium flow rate of 2.0 mL min^{-1}), respectively (RPq of 0.20). The highest signals were obtained at m/z ratios of 97 and 115 for Cu and Zn, respectively, which correspond to $^{63}Cu(NH_3)_2^+$ and $^{64}Zn(NH_3)_3^+$ ion products (mass shift approach). Findings regarding Cu agree with those obtained by Fu et al. [32] when using an ammonia/helium mixture for DRC-ICP-MS. However, the m/z 115 adduct for Zn is different from that previously proposed (m/z of 100, $^{66}Zn(NH_3)_2^+$) [32]. Other comparisons were not possible because, although ammonia has been used as a reaction gas in DRC-ICP-MS, the measurement methods were based on on-mass approaches [33-37]. It must be noted that the formation of adducts from the m/z of interest is less efficient when using ammonia as a reaction gas than when using other reaction gases such as oxygen and hydrogen [26]. However, ammonia as a reaction gas is appealing in DRC because the high selectivity achieved (adducts of high m/z ratios are formed and mass shift measurements can be carry out at a large and free-interference region of the mass spectra).

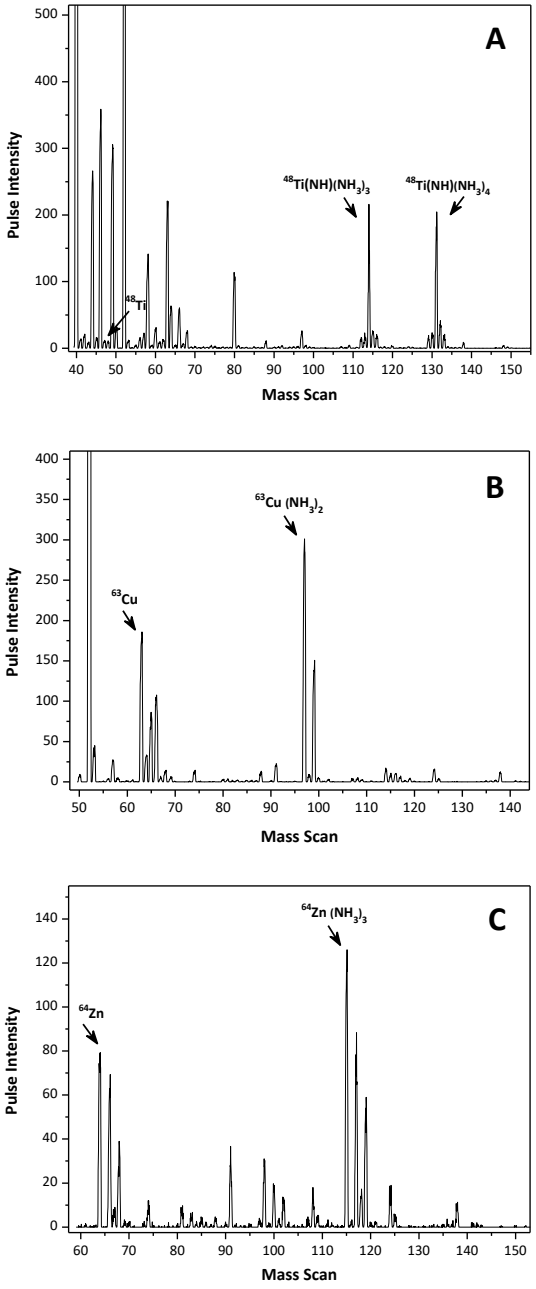

Figure 2.1. Mass spectra illustrating adducts that are formed with ammonia: (A) Ti, 1.0 mL min^{-1}, (B) Cu, 1.5 mL min^{-1} and (C) Zn, 2.0 mL min^{-1}.

2.4.2 Effect of ammonia flow rate

The effect of ammonia flow rate (mass shift and on-mass measurements) has been studied for TiO_2, Cu, CuO, and ZnO NPs of several size distributions. The effect on the formation of metal-ammonia adducts (mass shift approach) was performed for TiO_2, Cu, and CuO NPs; whereas, the on-mass approach was focused on the specific elemental masses ^{63}Cu and ^{64}Zn. On-mass measurements for Ti and mass shift measurements for Zn were not performed due to the low sensitivity and/or inefficient formation of ammonia-based adducts. The axial field voltage (AFT) was set at 350 V (default value) for all measurements. Similarly, the rejection parameter RPa was set at 0 (on mass and mass-shift approaches) for all cases since the influence of this parameter was scarce. Regarding RPq parameter, previous optimised values for each analyte and measurement mode [21] were fixed (**Table 2.2**); whereas, the deflector voltage was daily set at the specific element mass to achieve maximum ion transmission in the reaction cell.

Suspensions of TiO_2 NPs of 30, 50 and 100 nm (1.25 µg L^{-1} of TiO_2), and < 150 nm (2.5 µg L^{-1} of TiO_2) were analysed under ammonia flow rates within the 0.25-1.0 mL min^{-1}(adduct $^{48}Ti(NH)(NH_3)_3$, m/z of 114), and from 0.5 to 1.25 mL min^{-1} when monitoring the $^{48}Ti(NH)(NH_3)_4$ adduct (m/z of 131). RPq value was set at 0.20 (**Table 2.2**) and measurements were performed with a dwell time of 50 µs for monitoring both ammonia-based adducts. As expected [23,24], broad signals (higher peak width at baseline, and also at 5%, 15% and 50% height) were measured when using reaction gas (ammonia) respect to the vented mode (no reaction gas), and the peak width was found to be increased with higher ammonia flow rates (**Figure 2.2**). For Ti, narrower peaks were obtained when monitoring the $^{48}Ti(NH)(NH_3)_3$ adduct (m/z of 114) than those observed for the $^{48}Ti(NH)(NH_3)_4$ adduct (m/z of 131), and therefore$^{48}Ti(NH)(NH_3)_3$ monitoring appears to be more appealing since the narrow peaks obtained (less tailing). However, since the quadrupole ion deflector in the instrument does not select a specific m/z ratio, the adduct of m/z of 114 could be interfered from ^{114}Cd, and from other polyatomic adducts formed from the matrix sample such as $^{98}Mo^{16}O$, $^{98}Ru^{16}O$, and

also from products formed with ammonia ($^{63}Zn(NH_3)_3$). Therefore, although broader peaks (large tailings) are obtained for $^{48}Ti(NH)(NH_3)_4$, the peak weight is lower than 6.0 ms for all ammonia flow rates (**Figure 2.2**), and this adduct is preferable since the measurement is moved to a region of large m/z ratios (m/z of 131) which is potentially free of interferences.

From **Figure 2.2** (peak widths), and also by analysing the number of peaks and peak intensities (**Table S2.1**, electronic supplementary information, ESI), and peak shape from raw spectra (**Figure S2.1** and **S2.2**, ESI), the most suited ammonia flow rates were 0.50 and 0.75 mL min^{-1} when monitoring the $Ti(NH)(NH_3)_3$ adducts, and higher rates, within the 0.75 – 1.0 mL min^{-1} range, for $Ti(NH)(NH_3)_4$ adduct measurement. Low ammonia flow rate have led to low peak intensities and a low number of peaks recorded, but high ammonia flow rate also reduce the peak intensities as well as the number of peaks because a dilution effect. Therefore, intermediate ammonia flow rates, which exhibit low peak widths, high number of peaks and moderate peak intensities, have been selected for Ti-based ammonia adducts. Comparison with ICP-MS based on DRC with ammonia as a reaction gas led to lower ammonia flow rates in spICP-MS than in ICP-MS. This finding is attributed to the hundreds of atoms inside the NPs which increase the ammonia reactivity in the cell due to a vigorous ion-burst compared to single atoms one-by-one [24].

As shown in **Figure 2.2** for TiO_2 NPs, and also for other NPs (Figures in the ESI section), the NP size have a small influence on the peak width, and broader peaks are not related to TiO_2 NPs of higher sizes (**Figure 2.2A**-**2.2C**). In the case of TiO_2 NPs < 150 nm (**Figure 2.2D**), the narrow peaks must be attributed to a high proportion of TiO_2 NPs of small size in the suspension prepared from this standard (the manufacturer states that the material contains TiO_2 NPs < 150 nm). In addition, NPs agglomeration also influences the peak widths since larger ion bursts are produced from the agglomerate than those produced from disperse NPs. Finally, peak widths are strongly dependent on the ion-product selected (Ti-131 against Ti-114) for the same conditions and NPs size (and also for Cu-63 and Cu-97, and for

Zn-64 and Zn-115). Thus, boarder peaks are obtained from to the largest ion-product (Ti-131 against Ti-114).

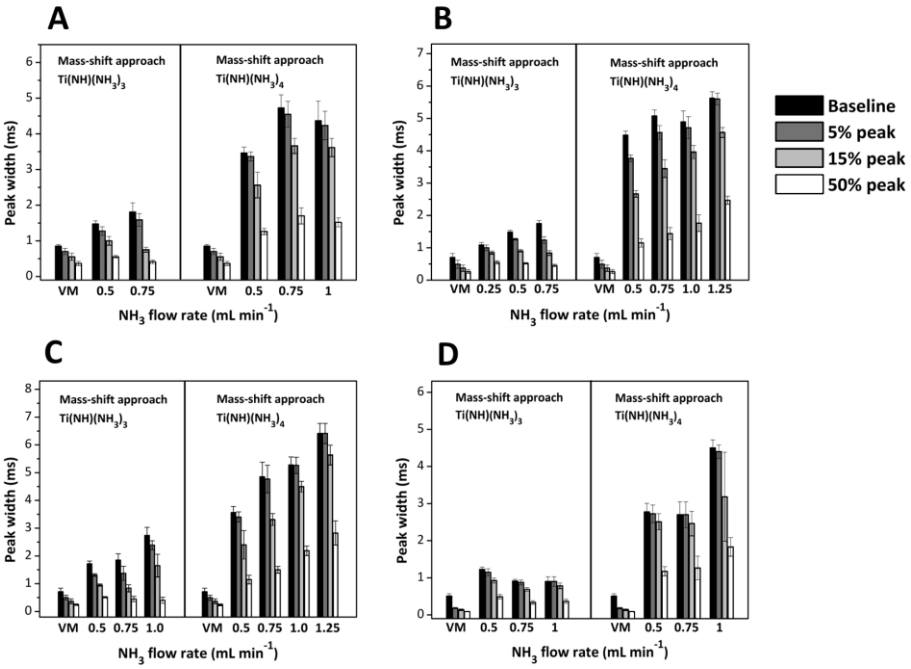

Figure 2.2. Effect of the ammonia flow rate on the peak width recorded by using mass-shift approach from TiO_2 NPs of (A) 30 nm, (B) 50 nm, (C) 100 nm, and (D) <150 nm.

Regarding Cu and CuO NPs, on-mass and mass-shift approaches using several ammonia flow rates were compared using a dwell time of 50 µs, and RPq values of 0.2 for mass-shift approach and 0.5 for on-mass approach. Suspensions of 40-60 nm and 60-80 nm Cu NPs (2.5 µg L^{-1} of Cu), and <50 nm CuO (2.5 µg L^{-1} of CuO) were tested at flow rates from 0.25 to 0.75 mL min^{-1} and from 0.75 to 2.0 mL min^{-1} for the on-mass approach and mass-shift approach, respectively. Similarly to TiO_2 NPs, results showed a clear correlation between the ammonia flow added and the peak width (**Figure S2.3**, ESI); whereas, "noisy" spectra are observed when ammonia flow was added, especially at 1.5 mL min^{-1}ammonia (mass-shift mode), as shown in **Figure S2.4** (ESI). Taking into account parameters such as the number of peaks and peak intensities (**Table S2.1**, ESI) and peak

widths in **Figure S2.3** (ESI), the most suitable flow rates were 0.4-0.5 mL min^{-1} (on-mass approach) and 1.25-1.5 mL min^{-1}(mass shift mode), slightly lower than those required for Cu determination in ICP-MS with ammonia-based DRC (1.5 mL min^{-1} in previous experiments) [21]. As shown in **Figure S2.3** (ESI), CuO and Cu NPs measurements based on the on-mass approach were also possible using low ammonia flow rates.

The effect of the ammonia flow rate on ZnO NPs measurements (dwell time of 50 µs and RPq of 0.2) were performed with suspensions of ZnO NPs of 35-45 nm (1.25 µg L^{-1}), 80-200 nm (2.5 µg L^{-1}), and <150 nm (2.5 µg L^{-1}). As shown in **Figure S2.5B** (ESI) the mass shift approach (RPq of 0.2) was only possible when using the ZnO NPs of largest size (80-200 nm), which shows spectra with enough intense peaks for peak height measurement at high ammonia flow rates (1.5 - 2.25 mL min^{-1}). However, very few and small signals were observed for ZnO NPs standards of lower size distribution (**Table S2.1**, ESI), and improvements were not obtained when using the highest ammonia flow rates (dilution effect). These findings are quite similar to those obtained for other NPs, such as Fe_3O_4 NPs [24,37], and a proper measurement of the adducts was reported to require the use of higher dwell times (the effect of the dwell time will be discussed in the following sections). An ammonia flow rate of 1.75 mL min^{-1} when analysing 80-200 nm ZnO NPs was therefore selected for further studies.

Regarding on-mass mode measurement for ZnO NPs (RPq of 0.35), **Figure S2.5**(A-C) and **Table S2.1** (ESI) shows that low ammonia flow rates (from 0.1 to 0.5 mL min^{-1}) allow the measurement of intense ^{64}Zn signals for all ZnO suspensions (low and high sizes), being the number of peak quite constant within the 0.1 – 0.5 mL min^{-1} ammonia flow rate. On-mass measurement mode seems therefore to be an efficient approach for interferences removal in ZnO NPs assessment. In addition, a dwell time of 50 µs is adequate for ZnO NPs on-mass measurements. An assessment between sta ndard mode and several ammonia flow rates for on-mass approach was performed as well (**Figure S2.6**). Finally, it must be noted that the mass shift approach with high ammonia flow rate, case of the

measurements of $^{48}Ti(NH)(NH_3)_4$ (m/z 131) adduct, may have an effect of the NPs size distribution since the broader peaks obtained.

2.4.3 Influence of dwell time

A suitable dwell time must be selected regarding possible multi-peak coincidence, high backgrounds or under/overestimation in NP concentration or size [12,13,36]. Therefore, dwell times of 20, 50, 100 and 200 µs were studied. As an example, **Figure 2.3** shows TiO_2 NPs peak shapes obtained for low (20 and 50 µs, **Figure 2.3A** and **2.3B**, respectively), intermediate (100 µs, **Figure 2.3**C), and high (200 µs, **Figure 2.3D**) dwell times. The use of low dwell times gives noisy peaks (**Figure 2.3A** and **2.3B**), which are attributed to ion-burst with nanoparticles in reaction cell; whereas, measurements at 200 µs could lead to multi-peak coincidence probability (broad peaks in **Figure 2.3D** and high intensities and low number of peaks as listed in **Table S2.1**, ESI) and hence high background (dissolved analyte) and low particle concentrations (low number of peaks) as listed in **Table S2.1** (ESI). However, a dwell time of 100 µs (**Figure 2.3C**) implies enough time for detection of discrete TiO_2 NPs with several measured points that can define the peaks properly without any fractionation.

The effect of the dwell time on registered peak weight for TiO_2 NPs of several size distributions [suspensions of TiO_2 NPs of 30, 50 and 100 nm (1.25 µg L^{-1} of TiO_2), and < 150 nm (2.5 µg L^{-1} of TiO_2)] is shown in **Figure S2.7** (ESI). This effect was illustrated with TiO_2 NPs of 50 nm registering $^{48}Ti(NH)(NH_3)_4$ ion product as it can be observed in **Figure S2.8**. Ammonia flow rates were fixed at 0.75 mL min^{-1} when recording the $^{48}Ti(NH)(NH_3)_3$ adduct, and 1.0 mL min^{-1} for $^{48}Ti(NH)(NH_3)_4$ measurement. The effect of the dwell time under standard conditions (vented mode) is also shown in **Figure S2.7** (ESI). In general, the peak width follows a clear correlation with the dwell time, and high dwell times lead to the broadest peaks. However, taking into account the peak shape in the spectra (**Figure 2.3**), as well as the peak widths, the number of peaks and the peak intensities (**Table S2.2**, ESI), detected signals with a dwell time of 100 µs seem to be more reliable than peaks recorded with lower dwell times such as 20 and 50 µs. Peak fractionation (mainly when using a dwell time

of 20 µs) can occur (low peak intensities as listed in **Table S2.2**, ESI); whereas, a dwell time of 200 µs led to a lower number of peaks (peak coincidence events) and a higher amount of ionic Ti concentration (**Table S2.2**, ESI), obtaining biased measurements.

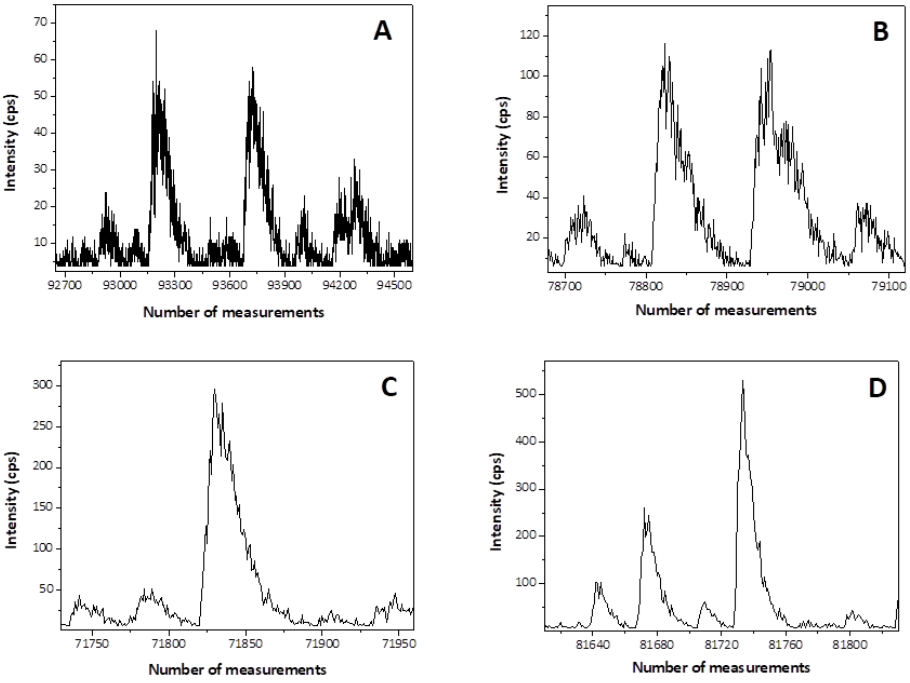

Figure 2.3. Raw data peaks obtained from spICP-MS measurements for TiO_2 NPs of 100 nm. (m/z 131) at 1.0 mL min^{-1} ammonia and dwell times of (A) 20 µs, (B) 50 µs, (C) 100 µs, and (D) 200 µs.

Experiments for Cu and CuO NPs [suspensions of 40-60 nm and 60-80 nm Cu NPs (2.5 µg L^{-1} of Cu), and <50 nm CuO (2.5 µg L^{-1} of CuO)] were performed by setting an ammonia flow rate of 0.5 mL min^{-1} for on-mass measurements (^{63}Cu) and 1.5 mL min^{-1} when using the mass shift approach ($^{63}Cu(NH_3)_2$). The effect of the dwell time on Cu and CuO NPs peak weights (**Figure 2.4**) was similar to those observed for TiO_2 NPs, and moderate peak weights, as well as a large number of intense peaks (**Table S2.2**, ESI)**,** were observed at intermediate dwell times (50 and 100 µs). Large dwell times could lead to multi-peak coincidence (**Figure S2.9** and **S2.10**, ESI) which

agrees with the lower number of peaks detected when using a dwell time of 200 µs (**Table S2.2**, ESI). Recording at low dwell times such as 50 µs gives adequate (clean) peaks and 50 µs is enough to register well-defined peaks and signal stability when using on-mass measurements. Regarding mass shift mode, despite peak tailing is observed at a low dwell time of 50 as well as 100 µs, the ion-burst explosion formed in these conditions due to ammonia clusters suggests no-problematic and accurate acquisition, and following explanations mentioned above similar to the Ti discussion, a dwell time of 100 µs was the best choice (**Figure S2.9** and **S2.10**, ESI).

Regarding ZnO NPs, the effect of the dwell time when using the mass shift approach was performed with ZnO NPs suspensions of 80-200 nm (2.5 µg L^{-1}) and recording the $^{64}Zn(NH_3)_3$ adduct at an ammonia flow rate of 1.75 mL min^{-1}; whereas, on-mass measurement (^{64}Zn) were performed with ZnO NPs suspensions of 35-45 nm(1.25 µg L^{-1}), 80-200 nm (2.5 µg L^{-1}), and <150 nm (2.5 µg L^{-1}) at an ammonia flow rate of 0.5 mL min^{-1}. Similar peak weights were observed $^{64}Zn(NH_3)_3$ adduct (mass shift approach) as shown in **Figure S2.11** (ESI). The study of the peak spectra when using the mass shift approach has shown that short dwell times (50 µs) are not enough for a well-defined peak registration due to poor peak intensity and low number of peaks (**Table S2.2**, ESI). Similarly, better results (peak-shape, peak intensity and number of peaks) were also obtained when using higher dwell times for mass shift monitoring (**Figure S2.12** and **Table S2.2**, ESI). Therefore, the recording of the $^{64}Zn(NH_3)_3$ adduct requires high dwell times, and a value of 200 µs gives the best performance in contrast to the obtained in Ti and Cu experiments. However, since the broader peaks obtained when using the mass-shift mode for Zn (**Figure S2.12**, ESI), on-mass measurements at low ammonia flow rates are preferable for ZnO NPs, and a repeatable acquisition (good peak-shapes and high number of counted peaks) are obtained at low dwell times such as 50 µs (**Figure S2.11**, ESI).

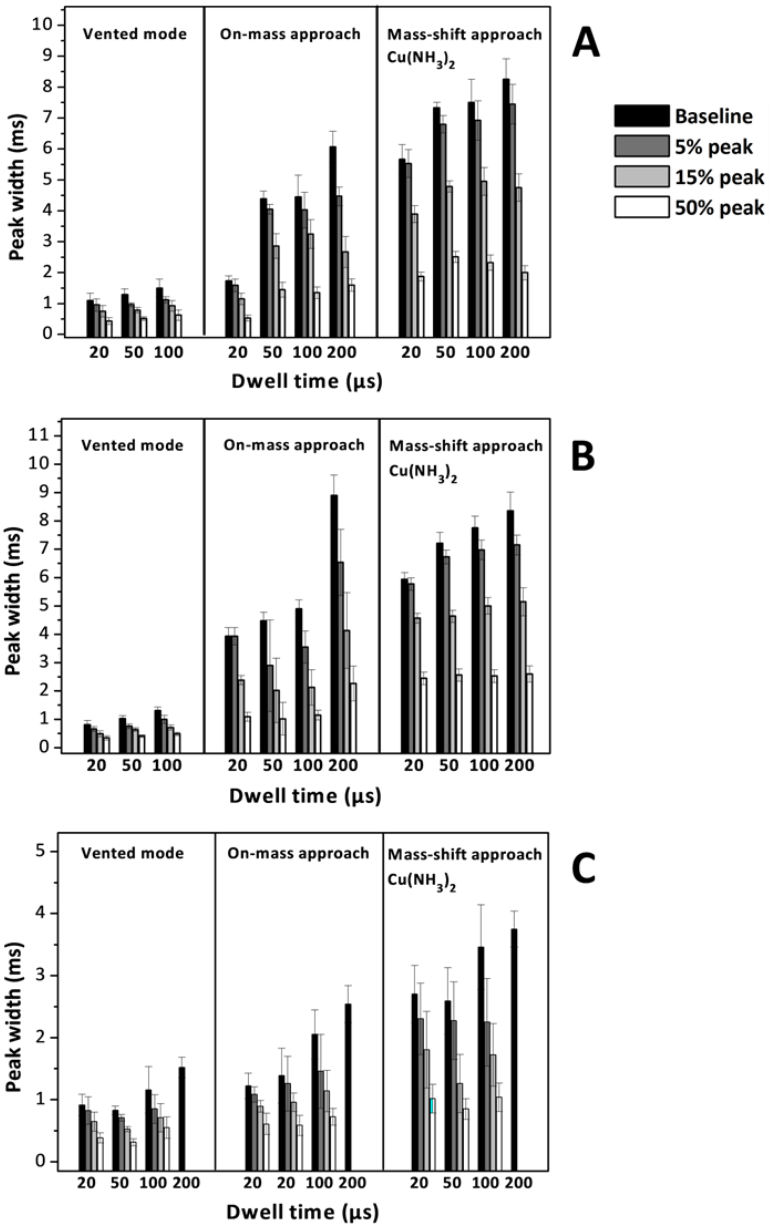

Figure 2.4. Effect of the dwell time influence on peak width recorded by on-mass and mass shift approaches (ammonia flow rate of 0.5 mL min^{-1} for m/z 63 and 1.5 mL min^{-1} for m/z 97) for (A) Cu NPs of 40-60 nm, (B) Cu NPs of 60-80 nm, and (C) CuO NPs of <50 nm.

2.4.4 Influence of NP size and NP type

After fixing the ammonia flow rate and dwell time for each NP type and measurement mode (on-mass and/or mass shift), the influence of the NP size on the peak width and peak shape was investigated. The experiments were performed with suspensions of TiO_2 NPs of 30, 50 and 100 nm (1.25 µg L^{-1} of TiO_2), and < 150 nm (2.5 µg L^{-1} of TiO_2); suspensions of 40-60 nm and 60-80 nm Cu NPs (2.5 µg L^{-1} of Cu), and <50 nm CuO (2.5 µg L^{-1} of CuO); and suspensions of ZnO NPs of 35-45 nm(2.5 µg L^{-1}), 80-200 nm (2.5 µg L^{-1}), and <150 nm (2.5 µg L^{-1}). **Figure 2.5A** shows results regarding the peak width for TiO_2 NPs measurements when recording the $Ti(NH)(NH_3)_3$ (m/z of 114) and the $Ti(NH)(NH_3)_4$(m/z of 131) adducts (mass shift mode). Low influence of the TiO_2 NPs size on the peak width was observed for $Ti(NH)(NH_3)_3$ (m/z of 114) measurements (for instance, the baseline peak width varies between 1.5 and 2.0 ms, whereas $Ti(NH)(NH_3)_4$ (m/z of 131) adduct recording implies a variation between 5.0 and 7.0 ms). Similarly, the size of Cu NPs (either mass shift and on mass approaches) and the size of ZnO NPs (on-mass approach using 0.25 mL min^{-1} of ammonia) do not affect the peak width (**Figure 2.5B-C**). However, an increase on the peak width was observed for ZnO NPs when using an ammonia flow rate of 0.5 mL min^{-1} (gradual increase from 1.9 to 3.0 ms for ZnO NPs sizes of 35-45 nm, <150 nm, and 80-200 nm, **Figure 2.5C**). Results for on-mass measurements for ZnO NPs (ammonia flow rate of 0.5 mL min^{-1}) agree with the literature regarding SiO_2 NPs [22], and Fe_3O_4 NPs, Au NPs, Ag NPs and Pt NPs [24], for which high NPs sizes have been reported to lead broad peaks. However, results for on-mass measurements for Cu/CuO NPs, and for mass shift determinations have shown a different trend.

Finally, from **Figure 2.5B** it can be seen that CuO NPs (size < 50 nm) show narrower peaks than those measured for Cu NPs (sizes 40-60, 60-80 nm), but these findings cannot be exclusively attributed to the NP size since the composition of the NPs is different (Cu mass fraction of 79.89% for CuO NPs, and 100% for Cu NPs). The influence of the NP chemical nature is therefore important and narrower peak widths (on-mass and mass shift approaches) have been

obtained for CuO NPs when comparing with Cu NPs of similar size (**Figure 2.5B**). In addition, on mass measurements for CuO NPs show broader peak widths than ZnO NPs (**Figure 2.5B-C**); whereas, peak widths when using the mass shift approach increase in the order of TiO_2 NPs ($^{48}Ti(NH)(NH_3)_3$) >CuO NPs ($^{63}Cu(NH_3)_2^+$) > TiO_2 NPs ($^{48}Ti(NH)(NH_3)_4$) > Cu NPs ($^{63}Cu(NH_3)_2^+$) >ZnO NPs ($^{64}Zn(NH_3)_3^+$), as shown in **Figure S2.13** (ESI). Ti-ammonia clusters (m/z 114 and 131) exhibit a well-defined peak-shape (**Figure S2.13**, ESI) with high intensities and a high number of detected peaks (**Table S2.1** and **S2.2**, ESI), being narrower than Cu- and Zn-ammonia clusters. As previously mentioned, Cu-ammonia clusters exhibit better performance in their oxide nature (lower peak widths derived from CuO NPs than from Cu NPs), and broad peaks are observed for Zn-ammonia clusters (peak width close to 10 ms).

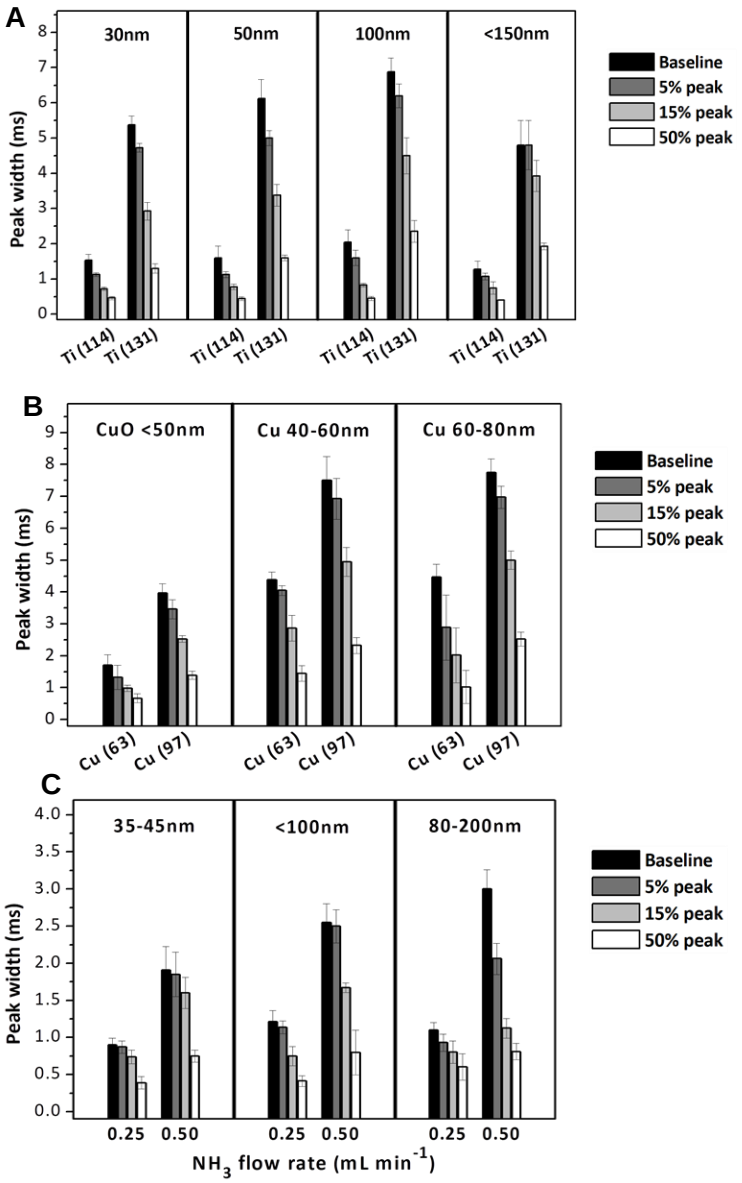

Figure 2.5.Effect of the NPs size on the peak width for (A) TiO_2 NPs, (B) Cu NPs and CuO NPs, and ZnO NPs.

2.4.5 On-mass and mass-shift approaches: selected conditions

On-mass measurements offer narrower peaks than those obtained when using the mass-shift mode, making it an appealing methodology mainly for assessing ZnO NPs. However, on-mass measurements were not found useful for assessing TiO_2 NPs due to the great reactivity of Ti with ammonia (and also the high-stability of Ti-ammonia clusters), which leads to a low ^{48}Ti mass abundance. Peak width related to Ti-ammonia cluster m/z 131 ($^{48}Ti(NH)(NH_3)_4$) is 3-4 times higher than Ti-ammonia cluster m/z 114 ($^{48}Ti(NH)(NH_3)_3$). This behaviour is strongly influenced by ammonia flow rate. High amounts of ammonia in the reaction cell result in a stronger ion-burst in the reaction cell. Moreover, Ti-ammonia cluster m/z 131 contains more molecules, resulting again in a stronger ion explosion and, consequently, a higher peak time measurement. Despite the peak width for Ti-ammonia cluster m/z 131($^{48}Ti(NH)(NH_3)_4$) being large (higher measurement time), the m/z 131 falls in a free-interference region as shown in the mass spectrum given in **Figure S2.14**.

Cu NPs and CuO NPs can be measured by either on-mass and mass shift approaches, but, as previously mentioned, narrower peaks are obtained for on-mass measurements. The selection of one mode or other will be depend on the presence of potential interferences close to m/z ^{63}Cu or m/z $^{63}Cu(NH_3)_2^+$. However, on-mass approach leads to better results when determining ZnO NPs (0.25 mL min^{-1}).

Taking into account the peak width as well as the number of peaks and peak intensities (**Table S2.1** and **S2.2**, ESI), selected conditions for both on-mass and mass shift modes are listed in **Table 2.2**. As previously mentioned, the ammonia flow rate required for NPs assessment is slightly lower than those required/reported for determining dissolved analytes [21], and it can be explained by the successive reaction among hundreds of atoms included in the nanoparticles. Finally, to illustrate a comparison between three different modes, **Figure S2.15** (Cu and CuO NPs) and **Figure S2.16** (ZnO NPs) were shown at their optimized conditions.

2.4.6 Sensitivity

The assessment of the limit of detection (LOD) and the limit of quantification (LOQ) was based on the 3 SD/m and 10 SD/m criterion, where *SD* is the standard deviation of eleven measurements of a blank; and *m* is the slope of a calibration graph. Ionic aqueous calibration for TiO_2 NPs assessment were up 2.0 µg L^{-1} (standard and aqueous calibrations up to 1.0 µg L^{-1} (standard and on-mass mode, m/z 63) and up to 2.0 µg L^{-1} (mass shift mode with $^{63}Cu(NH_3)_2$, m/z 97) were performed for Cu NPs determination; whereas, calibration up to 2.0 µg L^{-1} (standard and on-mass mode, m/z 64) and up to 3.0 µg L^{-1} (mass shift mode with $^{64}Zn(NH_3)_3$, m/z 115) were used for ZnO NPs assessment. For all cases, calibration graphs were found to exhibit r^2>0.999, and the RSD% of the blank measurements were always below 7%.

The limit of detection in size (lowest size measured by spICP-MS) was obtained from the Syngistix™ Nano Application software. These values (LOD in size) and the LOD/LOQ values for number concentrations are listed in **Table 2.3**. The improved sensitivity obtained for the standard mode is expected since the use of reaction/collision gases implies a reduction of sensitivity because the inherent dilution in the reaction/collision cell. Regarding DRC technology for TiO_2 NPs assessment, sensitivity is quite better when using the $^{48}Ti(NH)(NH_3)_4$ (m/z 131) adduct than for $^{48}Ti(NH)(NH_3)_3$ (m/z 114) adduct (**Table 2.3**). Mass shift measurements for Cu NPs ($^{63}Cu(NH_3)_2$, m/z 97) showed similar sensitivity than that obtained when working with the standard mode, but on-mass measurements were more sensitive in number concentration and size. These findings can be attributed to a proper interferences removal and a minimum dilution in the reaction cell since on–mass measurements require a low ammonia flow rate. Similar conclusions can be attained for Zn NPs, and the on-mass approach also showed the highest sensitivity (**Table 2.3**).

Table 2.3. Limit of detection in size and limit of detection and quantification (number concentration) for the standard mode and on-mass and mass shift approaches

	Work-mode (m/z)	LOD_{size} (nm)	$LOD_{number\ concentration}$ (particles L^{-1})	$LOQ_{number\ concentration}$ (particles L^{-1})
TiO_2 NPs	STD (48)	16	2.42×10^5	8.07×10^5
	Mass-shift (114)	41	9.10×10^5	3.03×10^6
	Mass-shift (131)	23	4.51×10^5	1.50×10^6
ZnO NPs	STD (64)	19	1.06×10^6	3.53×10^6
	On-mass (64)	13	8.40×10^4	2.80×10^5
	Mass-shift (115)	31	3.58×10^6	1.19×10^7
Cu NPs	STD (63)	13	3.57×10^5	1.19×10^6
	On-mass (63)	7	3.50×10^4	1.17×10^5
	Mass-shift (97)	16	4.53×10^5	1.51×10^6

2.4.7 Interferences study

Titanium and Zn measurements are interfered in ICP-MS by large amounts of Ca and P, major metals present in many matrices such as biological/food materials. Therefore, the determination of 100 nm TiO_2 NPs (2.5 µg L^{-1}), 60-80 nm Cu NPs (5.0 µg L^{-1}), and 80-200 nm ZnO NPs (5.0 µg L^{-1}) under standard conditions (vented mode, no DRC technology) with the most abundant isotopes (^{63}Cu, ^{64}Zn, and ^{48}Ti), and under the optimised DRC on-mass (^{63}Cu and ^{64}Zn) and mass shift ($^{63}Cu(NH_3)_2$, m/z 97; $^{64}Zn(NH_3)_3$, m/z 115; $^{48}Ti(NH)(NH_3)_3$, m/z 114; and $^{48}Ti(NH)(NH_3)_4$, m/z 131) conditions was performed in the presence of increasing concentrations of Ca and P (up to 50 mg L^{-1} for Ti measurements and up to 10 mg L^{-1} for Cu and Zn measurements). Results in triplicate for ionic background (ionic metal concentration) and NPs concentration are given in **Figure S2.17**. The $^{48}Ti(NH)(NH_3)_4$ (m/z 131) adduct was found to allow a free interference determination of TiO_2 NPs even in the presence of 10 mg L^{-1} plus 10 mg L^{-1} of Ca and P. Determinations based on monitoring the $^{64}Zn(NH_3)_3$ (m/z 115) adduct are not interfered up Ca plus P

concentrations of 5.0 plus 5.0 mg L^{-1}: whereas, interferences were found to be important for Ca plus P concentrations of 1.0 plus 1.0 mg L^{-1} under standard conditions (**Figure S2.17A-B**). Regarding Cu NPs, similar results were observed for on-mass (^{63}Cu) and mass shift ($^{63}Cu(NH_3)_2$, m/z 97) conditions, and interference free determinations were possible even in the presence of 2.0 mg L^{-1} plus 2.0 mg L^{-1} of Ca plus P (**Figure S2.17C-D**). Calcium and P interference on Cu NPs start to be important up to 0.5 mg L^{-1} plus 0.5 mg L^{-1} of Ca plus P under the standard mode measurement (**Figure S2.17C-D**). Finally, **Figure S2.16E-F** shows that Ca plus P are serious interferences on the ZnO NPs assessment at 0.5 mg L^{-1} plus 0.5 mg L^{-1} of Ca plus P under the standard mode measurement and also by using the on-mass and mass shift approaches. However, on-mass measurements appear to control better the Ca plus P interference.

2.5 CONCLUSIONS

Conditions for DRC in ICP-MS working in single-particle mode must be carefully established because conditions, mainly reaction gas (ammonia) flow rate, are different from those required for dissolved analytes in conventional ICP-MS. Optimized conditions can be dependent on the size and the NPs type. On-mass and mass-shift approaches have been found useful for Cu NPs and CuO NPs; whereas on-mass mode was preferred for ZnO NPs assessment. In addition, the mass shift approach is the best option for facing Ti interferences in TiO_2 NPs determinations. Regarding mass-shift mode, the recording metal-ammonia adducts generated from the second most abundant isotopes can also be appealing alternatives for overcoming complex interferences. This is the case of Cu NPs, CuO NPs and ZnO NPs because the abundance of the second most abundant isotopes (^{65}Cu and ^{66}Zn) are 31% and 28%, respectively. Finally, careful optimization has to be performed for NPs in complex samples (extracts) which can increase the background signal and can lead to other conditions for reaction gas (ammonia), flow rate and dwell time.

SUPPLEMENTARY INFORMATION

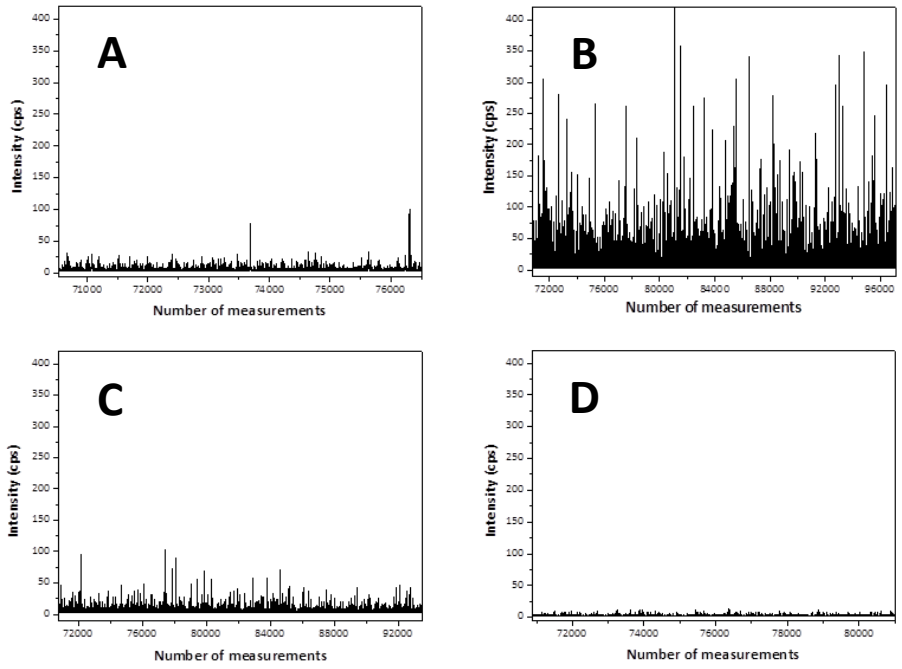

Figure S2.1. Raw data peaks obtained from spICP-MS measurements for TiO_2 NPs of 100 nm (m/z 131, dwell time of 50 µs) at ammonia flow rates of (A) 0.25 mL min^{-1}, (B) 0.75 mL min^{-1}, (C) 1.0 mL min^{-1}, and (D) 1.25 mL min^{-1}.

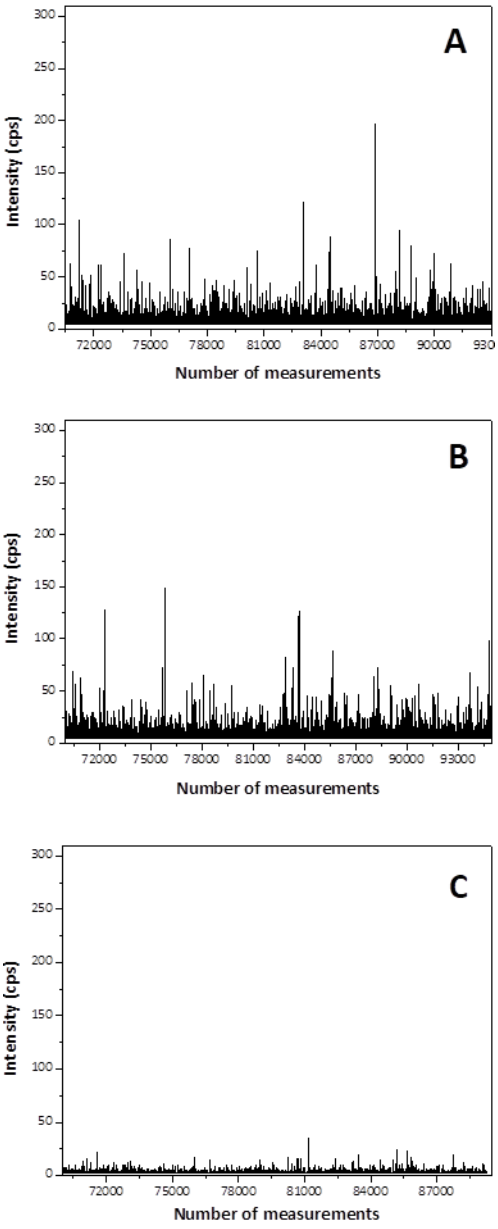

Figure S2.2. Raw data peaks obtained from spICP-MS measurements for TiO_2 NPs of <150nm (m/z 114, dwell time of 50 µs) at ammonia flow rates of (A) 0.5 mL min^{-1}, (B) 0.75 mL min^{-1}, (C) 1.0 mL min^{-1}

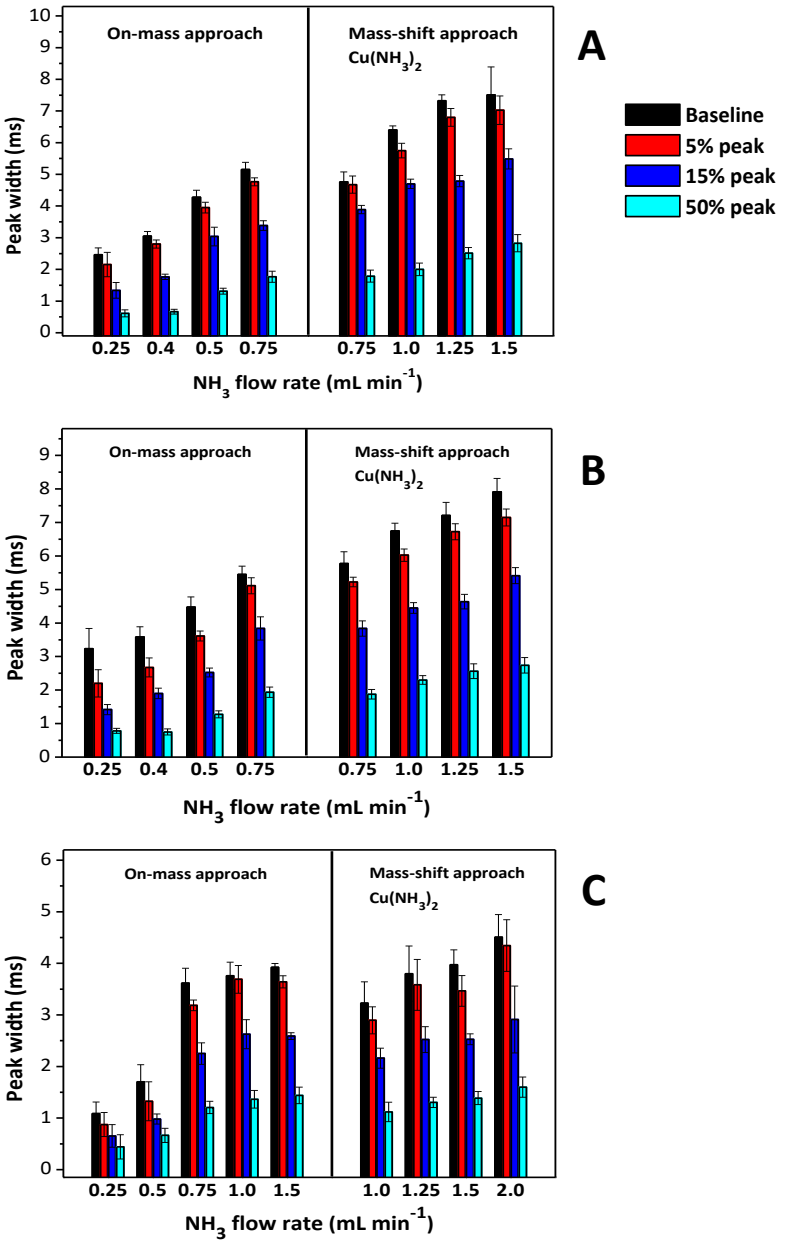

Figure S2.3. Effect of the ammonia flow rate on the peak width recorded by using on-mass and mass-shift approaches from (A) Cu NPs of 40-60 nm, (B) Cu NPs of 60-80 nm, and (C) CuO NPs of <50 nm.

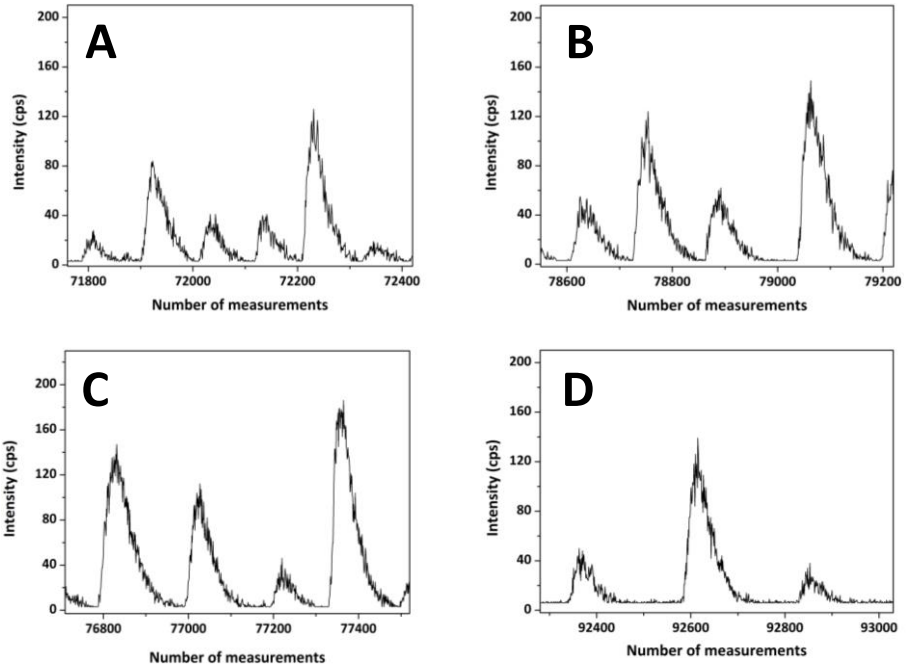

Figure S2.4. Raw data peaks obtained from spICP-MS measurements for Cu NPs 40-60 nm (m/z 97, dwell time of 50 µs) at ammonia flow rates of (A) 0.75 mL min^{-1}, (B) 1.0 mL min^{-1}, (C) 1.25 mL min^{-1}, and (D) 1.5 mL min^{-1}.

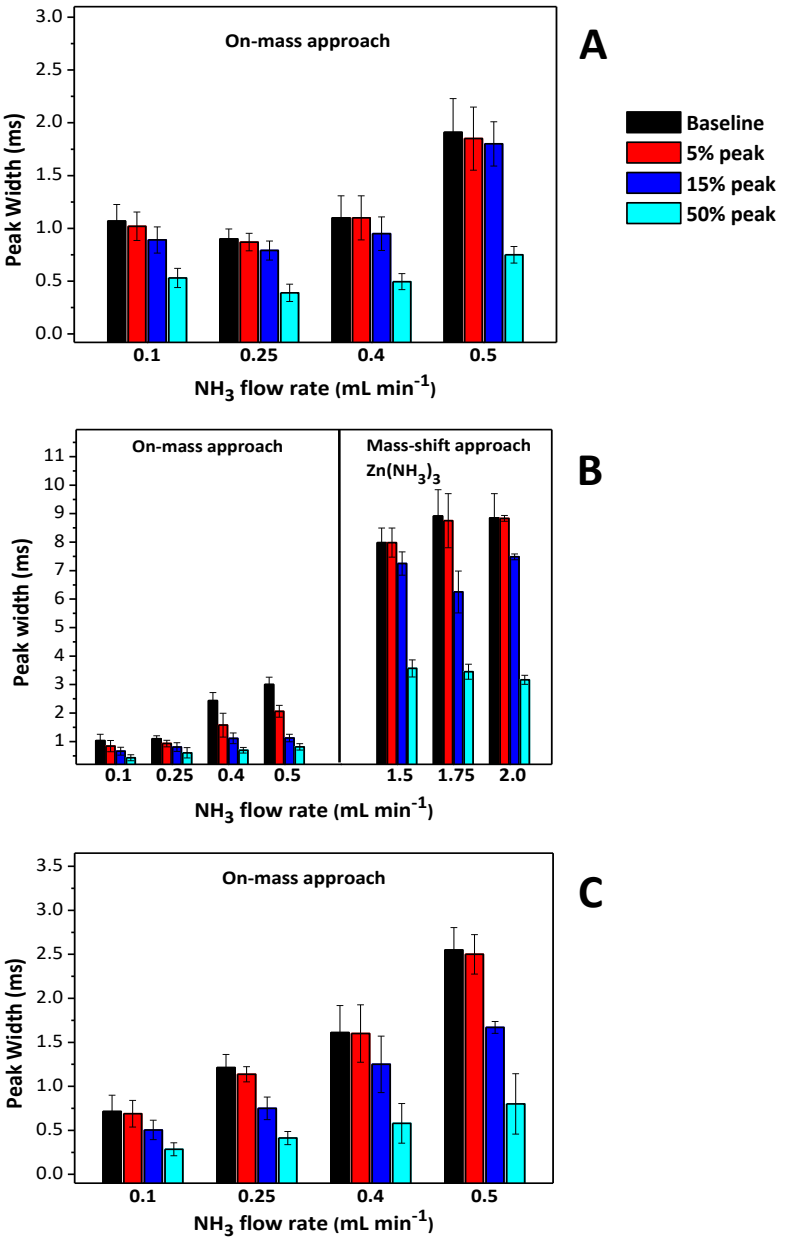

Figure S2.5. Effect of the ammonia flow rate on the peak width recorded by using on-mass and mass-shift approaches from (A) ZnO NPs of 35-45 nm, (B) ZnO NPs of 80-200 nm and (C) ZnO NPs suspension of <100 nm.

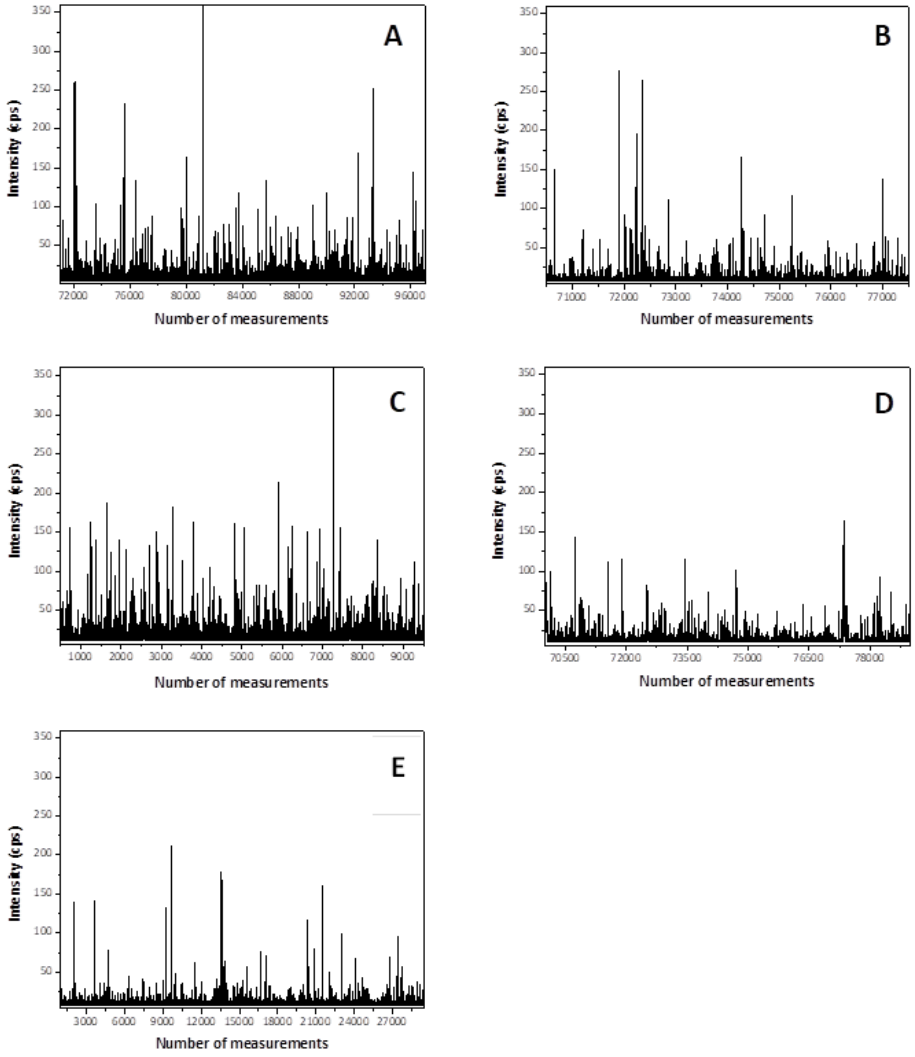

Figure S2.6. Raw data peaks obtained from spICP-MS measurements for ZnO NPs of <100nm under (A) standard mode, then on-mass approach using m/z 64, dwell time of 50 µs and (B) 0.1 mL min^{-1}, (C) 0.25 mL min^{-1}, (D) 0.4 mL min^{-1}, (E) 0.5 mL min^{-1}.

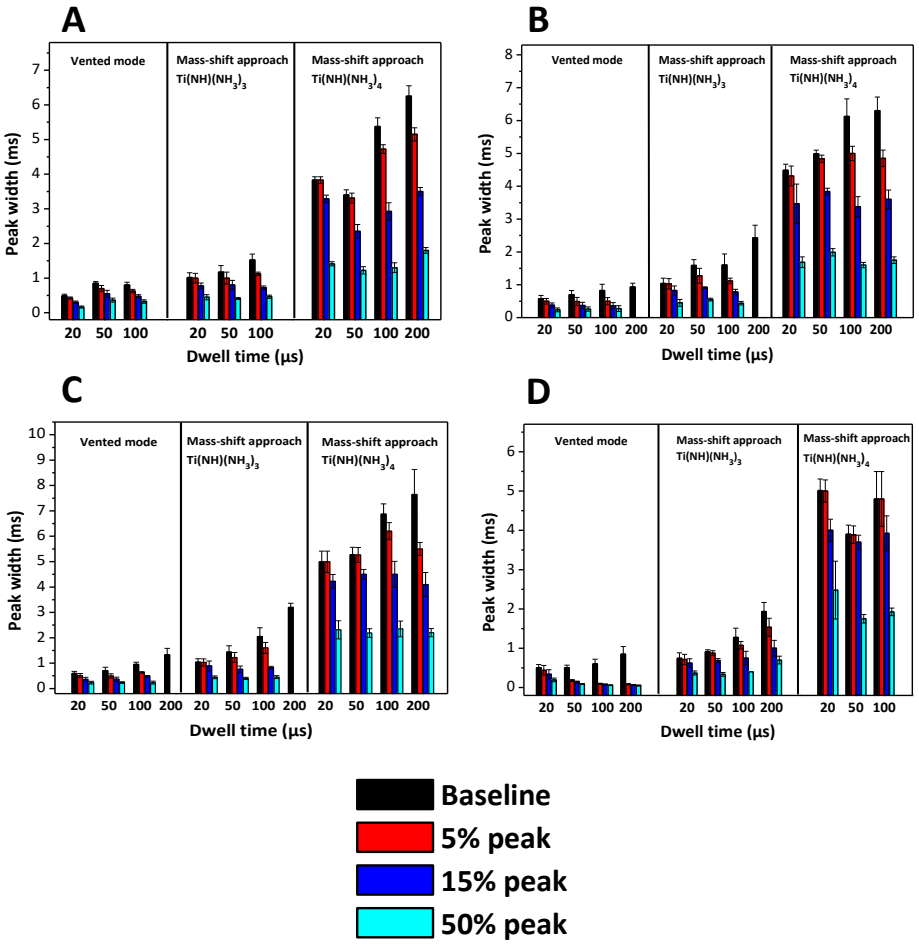

Figure S2.7. Effect of the dwell time on peak width recorded by mass shift approach (ammonia flow rate of 1.0 mL min^{-1} for m/z 131 and 0.75 mL min^{-1} for m/z 114) for TiO2 NPs of (A) 30 nm, (B) 50 nm, (C) 100 nm, and (D) <150 nm suspension.

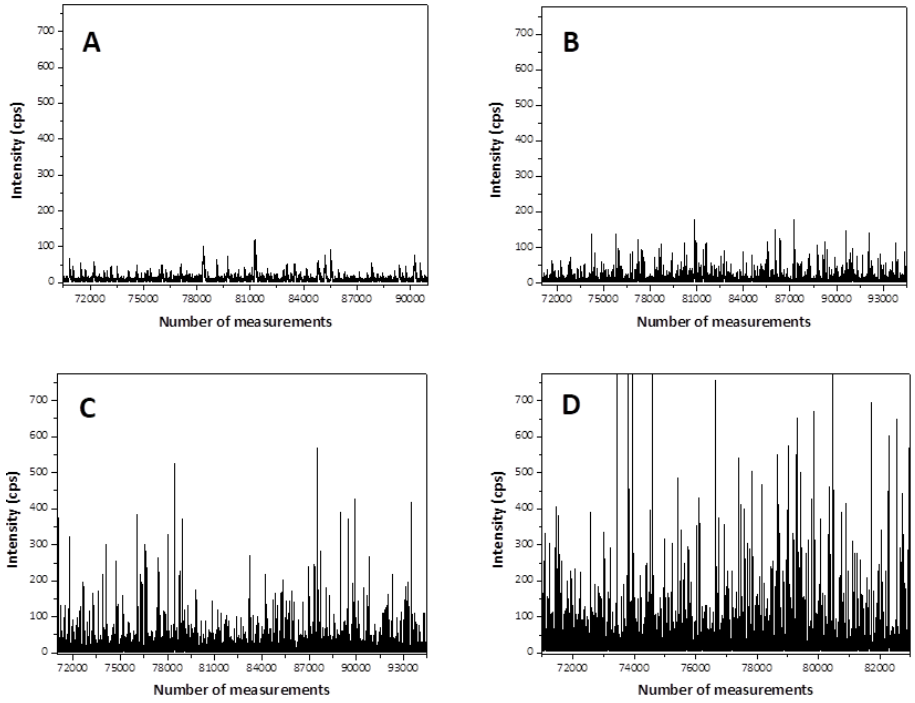

Figure S2.8. Raw data peaks obtained from spICP-MS measurements for TiO_2 NPs of 50 nm (m/z 131) at 0.75 mL min^{-1} ammonia and dwell times of (A) 20 µs, (B) 50 µs, (C) 100 µs, and (D) 200 µs.

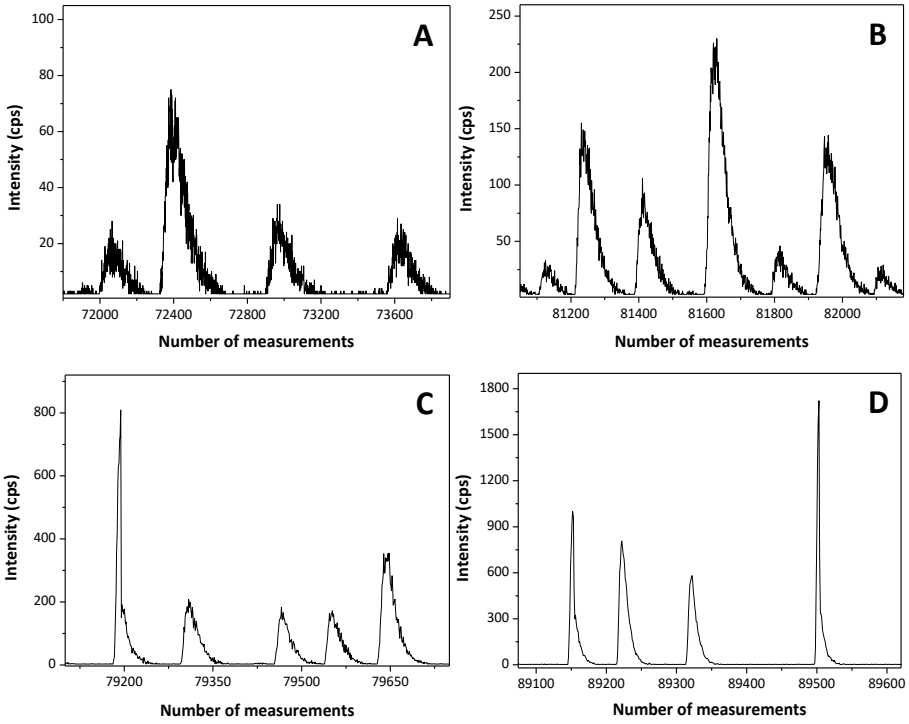

Figure S2.9. Maximized peaks from raw data peaks obtained from spICP-MS measurements for CuO NPs of <50nm (m/z 97) at 1.25 mL min^{-1} ammonia and dwell times of (A) 20 µs, (B) 50 µs, (C) 100 µs, and (D) 200 µs.

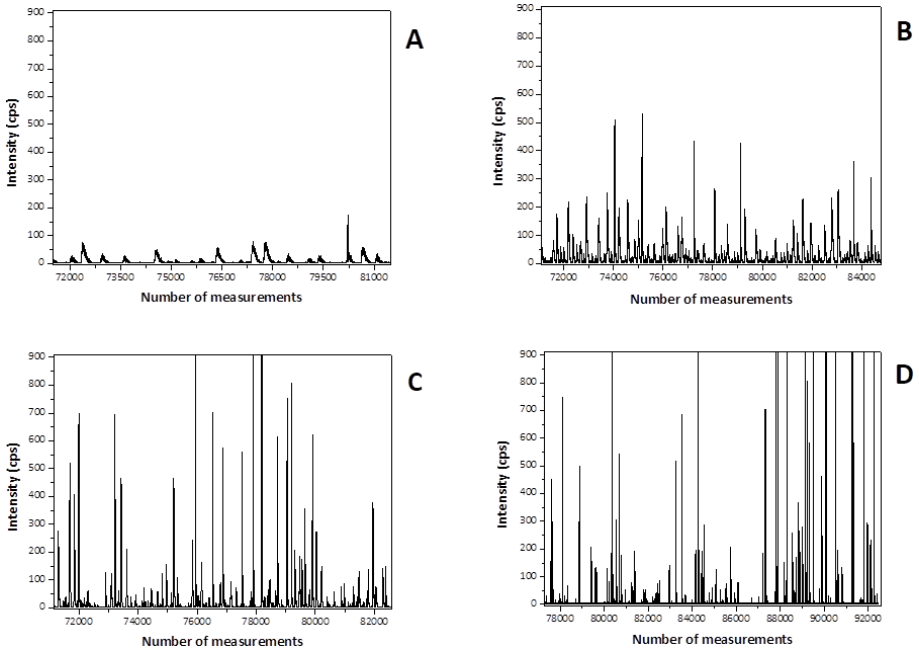

Figure S2.10. Total raw data peaks obtained from spICP-MS measurements for CuO NPs of <50nm (m/z 97) at 1.25 mL min^{-1} ammonia and dwell times of (A) 20 µs, (B) 50 µs, (C) 100 µs, and (D) 200 µs.

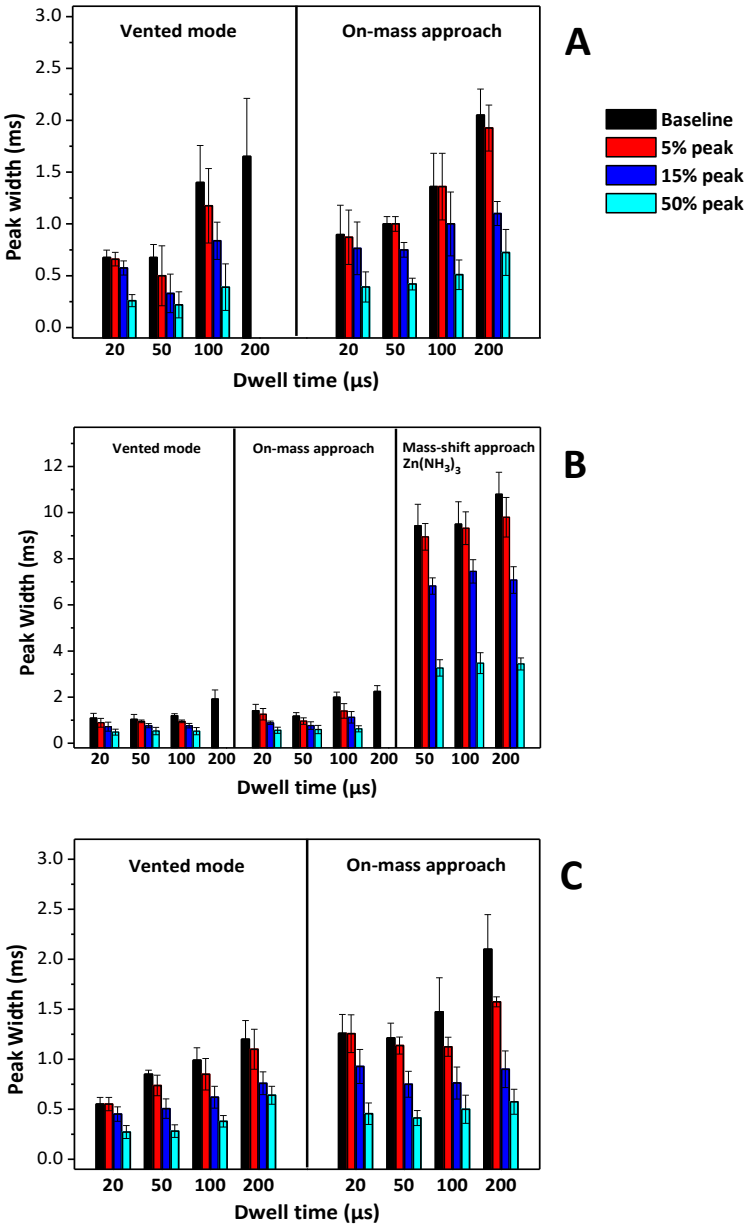

Figure S2.11. Effect of the dwell time on peak width recorded by on-mass and mass shift approaches (ammonia flow rate of 0.25 mL min^{-1} for m/z 64 and 1.75 mL min^{-1} for m/z 115) for ZnO NPs of (A) 35-45 nm, (B) 80-200 nm, and (C) NPs suspension of <100 nm.

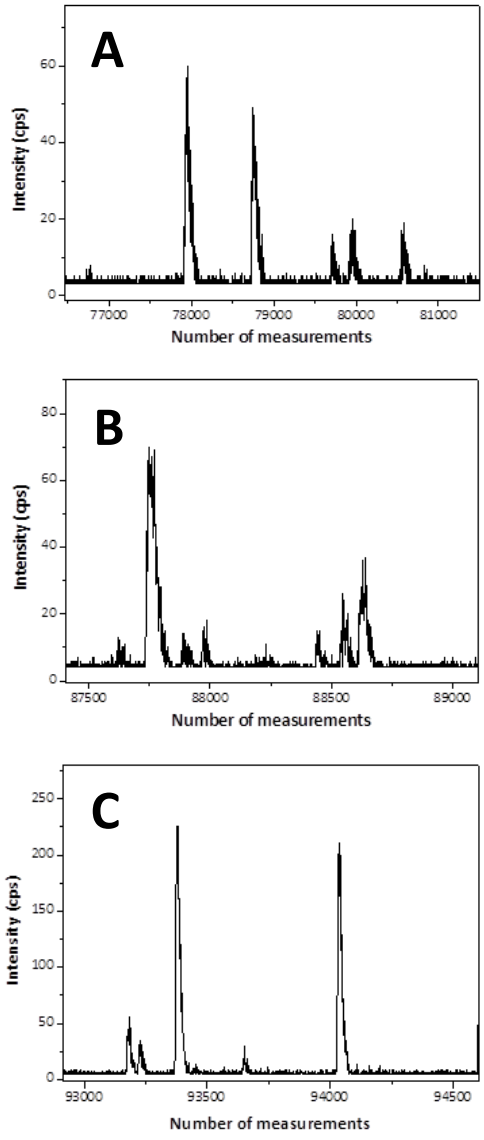

Figure S2.12. Raw data peaks obtained from spICP-MS measurements for ZnO NPs of 80-200 nm (m/z 115, 1.75 mL min^{-1} of ammonia flow rate) at dwell times of (A) 50 µs, (B) 100 µs and (C) 200 µs.

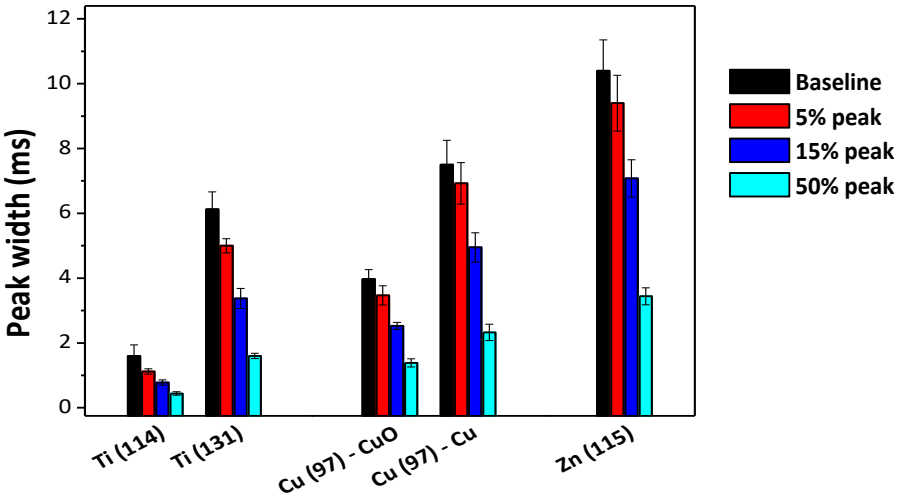

Figure S2.13. Effect of the NP composition on the peak width recorded by mass-shift approach for TiO2 NPs of 100nm, CuO NPs of <50nm, Cu NPs of 60-80nm and, ZnO of 80-200 nm.

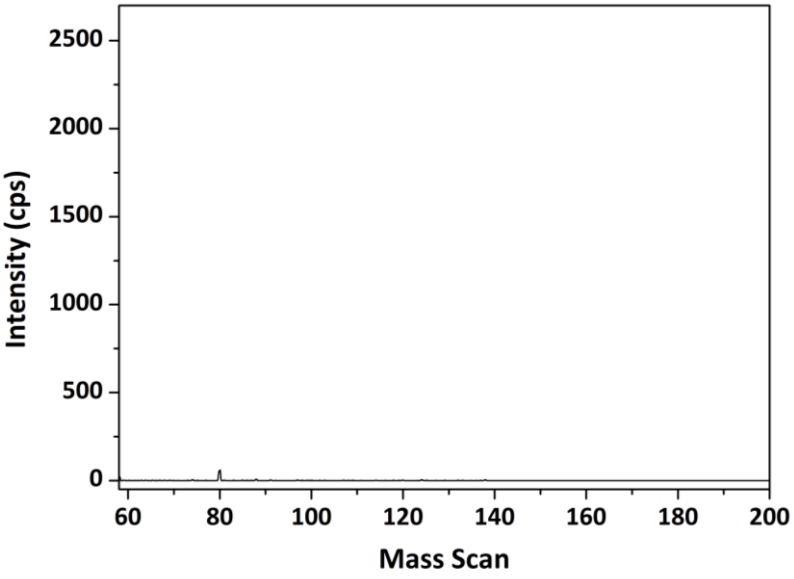

Figure S2.14. Mass spectrum for a blank when using ammonia at a flow rate of 1.0 mL min^{-1}.

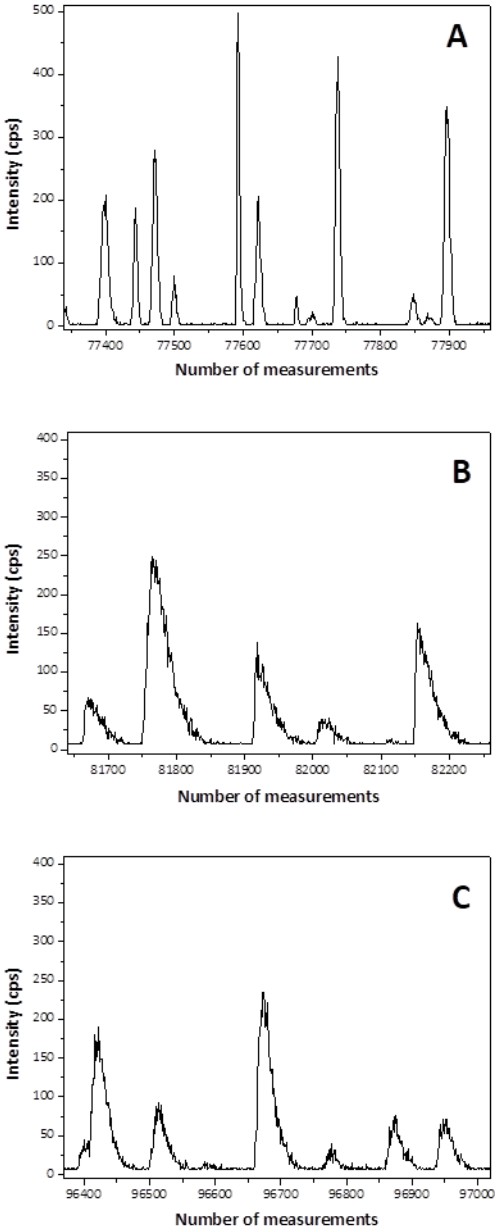

Figure S2.15. Raw data peaks obtained from spICP-MS measurements for Cu NPs of 40-60 nm under (A) standard mode, (B) on-mass approach using m/z 63, dwell time of 50 µs and 0.5 mL min^{-1} , and (C) mass-shift approach using m/z 97, 100 µs and 1.25 mL min^{-1}.

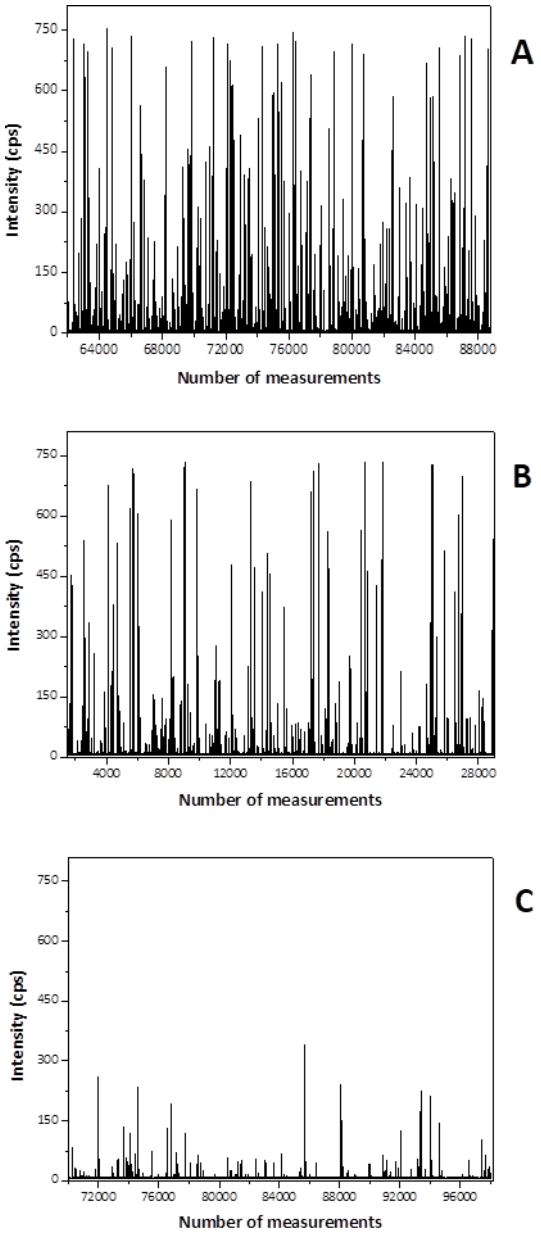

Figure S2.16. Raw data peaks obtained from spICP-MS measurements for ZnO NPs of 80-200 nm under (A) standard mode, (B) on-mass approach using m/z 64, dwell time of 50 µs and 0.4 mL min^{-1}, and (C) mass-shift approach using m/z 115, 100 µs and 1.75 mL min^{-1}.

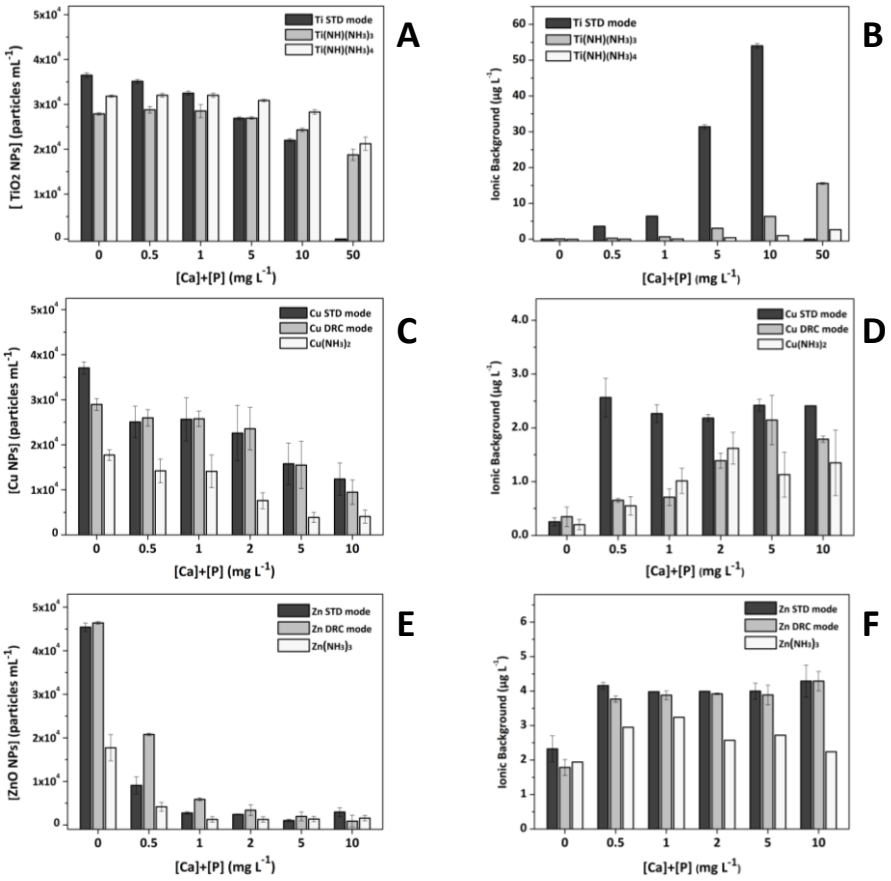

Figure S2.17. Effect of Ca plus P concentration on ionic concentration and NPs concentration for TiO_2 NPs (A-B), Cu NPs (C-D), and ZnO NPs (E-F) when using the standard mode, on-mass approach and mass-shift approach.

Table S2.1. Peak intensity, number of peaks and other statistical data when varying the ammonia flow rate

Work-mode	Parameter (units)	Values studied	Peak intensity (counts)	Particle concentration (p/mL)	Number of peaks	Dissolved Intensity(counts)	Other information
TiO_2 NPs 30 nm							
Ti-114	flow rate (mL min^{-1})	0.5	332.73	73636	1804	0.05	[NPs]=2.5 ppb; 50µs
		0.75	181.35	81024	1985	0.04	
		1	55.38	49390	1210	0.05	
		1.25	8.75	60044	1471	0.04	
Ti-131	flow rate (mL min^{-1})	0.5	307.15	103392	2533	0.05	[NPs]=2.5ppb; 50µs
		0.75	496.12	97800	2396	0.07	
		1	437.27	93229	2284	0.09	
		1.25	276.28	54247	1329	0.17	
TiO_2 NPs 50 nm							
Ti-114	flow rate (mL min^{-1})	0.5	341.86	21434	2191	0.02	[NPs]=2.5ppb; 50µs
		0.75	224.49	20573	2103	0.04	
		1	46.09	15310	1565	0.04	
		1.25	11.15	13588	1389	0.04	
Ti-131	flow rate (mL min^{-1})	0.5	446.17	15874	1597	0.05	[NPs]=2.5ppb; 50µs
		0.75	525.82	17462	1785	0.05	
		1	420.83	16572	1694	0.07	
		1.25	328.6	16034	1639	0.08	
TiO_2 NPs 100nm							
Ti-114	flow rate (mL min^{-1})	0.25	57.9	50615	1240	0.01	[NPs]=2.5ppb; 50µs
		0.5	704.81	62942	1542	0.01	

Work- mode	Parameter (units)	Values studied	Peak intensity (counts)	Particle concentration (p/mL)	Number of peaks	Dissolved Intensity (counts)	Other information
		0.75	494.55	61431	1505	0.02	
		1	64.41	71228	1745	0.03	
		1.25	11.96	115515	2830	0.06	
		100	1104.43	45104	1322	0.02	
		200	1021.21	53962	1105	0.05	
Ti-131	flow rate (mL min^{-1})	0.25	34.87	24436	605	0.01	[NPs]=2.5ppb; 50µs
		0.5	770.8	51744	1220	0.01	
		0.75	1088.3	61758	1513	0.02	
		1	968.74	60942	1493	0.03	
		1.25	719.99	59105	1448	0.04	
TiO_2 NPs <150 nm							
Ti-114	flow rate (mL min^{-1})	0.25	18.5	136155	3727	0.1	[NPs]=2.5ppb; 50µs
		0.5	147.68	259999	7117	0.81	
		0.75	72.4	247323	6770	0.36	
		1	51.7	224365	6134	0.22	
Ti-131	flow rate (mL min^{-1})	0.25	12.74	11179	306	0.06	[NPs]=2.5ppb; 50µs
		0.5	217.96	97687	2674	1.48	
		0.75	297.26	74672	2044	2.09	
		1	200.08	55529	1520	1.77	
CuO NPs <50 nm							
Cu-63	flow rate (mL min^{-1})	0.25	2729.64	69480	822	0.71	[NPs]=2.5ppb; 50µs
		0.5	2741.72	78840	926	0.67	
		0.75	2369.76	66870	793	0.44	

Work- mode	Parameter (units)	Values studied	Peak intensity (counts)	Particle concentration (p/mL)	Number of peaks	Dissolved Intensity (counts)	Other information
		1	1824.12	61200	730	0.25	
		1.5	1057.24	44820	548	0.11	
Cu-97	flow rate (mL min^{-1})	1	951.35	24556	814	0.19	[NPs]=5 ppbs; 50µs
		1.25	1053.51	21720	720	0.33	
		1.5	1168.67	18341	608	0.36	
		2	1011.07	23258	771	0.22	
Cu NPs 60-80 nm							
Cu-63	flow rate (mL min^{-1})	0.25	2792.7	8309	225	3.6	[NPs]=2.5ppb; 50µs
		0.4	3145.07	7127	193	3.55	
		0.5	3344.17	8085	220	2.61	
		0.75	3208.8	6943	188	1.79	
		1	1864.79	5613	152	0.89	
Cu-97	flow rate (mL min^{-1})	1	1643.91	11079	300	1.6	[NPs]=5 ppbs; 50µs
		1.25	2031.22	11485	311	1.98	
		1.5	2174.54	9971	270	1.96	
		1.75	1803.61	9454	256	1.91	
		2	1512.86	8715	236	1.61	
Cu NPs 40-60 nm							
Cu-63	flow rate (mL min^{-1})	0.25	2334.23	9562	357	3.56	[NPs]=2.5ppb; 50µs
		0.4	3405.47	11545	431	3.33	
		0.5	2691.11	7554	282	2.56	
		0.75	1975.24	6696	250	1.78	
		1	1127.93	4955	185	0.75	
Cu-97	flow rate (mL min^{-1})	1	1324.45	6831	255	0.19	[NPs]=5 ppb; 50µs

Work-mode	Parameter (units)	Values studied	Peak intensity (counts)	Particle concentration(p/mL)	Number ofpeaks	Dissolved Intensity(counts)	Other information
		1.25	1291.67	7844	297	0.2	
		1.5	1304.35	8460	327	0.2	
		1.75	1173.22	7233	270	0.19	
		2	807.69	5787	216	0.17	
ZnO NPs 35-45 nm							
Zn-64	flow rate (mL min^{-1})	0.1	469.7	3459	441	9.11	[NPs]=2.5ppb; 50µs
		0.25	528.76	5247	669	12.27	
		0.4	659.95	2046	261	16.13	
		0.5	670.78	1293	165	24.91	
		0.75	413.38	681	87	21.37	
ZnO NPs <100 nm							
Zn-64	flow rate (mL min^{-1})	0.1	238.76	31746	1443	3.94	[NPs]=2.5ppb; 50µs
		0.25	315.25	29931	1360	5.19	
		0.4	350.45	22055	1002	5.41	
		0.5	346.7	16038	729	4.83	
ZnO NPs 80-200 nm							
Zn-64	flow rate (mL min^{-1})	0.1	2067.97	12166	553	1.91	[NPs]=2.5ppb ; 50µs
		0.25	2739.23	12826	583	2.54	
		0.4	2616.52	12364	562	2.61	
		0.5	2600.72	11638	529	2.57	
Zn-115	flow rate (mL min^{-1})	0.75	24.36	7480	250	0.05	[NPs]=2.5ppb ; 50µs
		1	54.04	10672	314	0.14	

Work-mode	Parameter (units)	Values studied	Peak intensity (counts)	Particle concentration(p/mL)	Number of peaks	Dissolved Intensity(counts)	Other information
		1.25	282.24	7331	247	0.35	
		1.5	733.99	5336	207	0.5	
		1.75	688.1	5087	202	0.63	
		2	396.84	5984	220	0.55	

Table S2.2. Peak intensity, number of peaks and other statistical data when varying the dwell time

Work-mode	Parameter	Values studied	Peak intensity (counts)	Particle concentration(p/mL)	Number of peaks	Dissolved Intensity (counts)	Other information
TiO_2 NPs 30nm							
Ti-STD	dwell time (µs)	20	589.82	66697	1634	0.05	[NPs]=1.25ppb
		50	573.9	73473	1800	0.09	
		100	576.08	67391	1651	0.16	
		200	538.29	65472	1604	0.35	
Ti-114	dwell time (µs)	20	128.38	107066	2623	0.02	[NPs]=2.5 ppb; 0.75mL min^{-1}
		50	194.81	77146	1890	0.04	
		100	172.51	83351	2042	0.03	
		200	198.36	75310	1845	0.05	
Ti-131	dwell time (µs)	20	119.02	204499	5010	0.07	[NPs]=2.5ppb; 1.0mL min^{-1}
		50	414.63	89106	2183	0.09	
		100	401.24	92494	2266	0.1	
		200	508.07	87800	2151	0.13	
TiO_2 NPs 50nm							
Ti-STD	dwell time (µs)	20	769	12130	1240	0.02	[NPs]=1.25ppb
		50	701.41	13842	1415	0.07	
		100	668.41	13745	1405	0.09	
		200	704.27	12325	1260	0.16	
Ti-114	dwell time (µs)	20	159.82	24398	2494	0.02	[NPs]=2.5ppb; 0.75mL min^{-1}

Work-mode	Parameter	Values studied	Peak intensity (counts)	Particle concentration (p/mL)	Number of peaks	Dissolved Intensity (counts)	Other information
		50	213.59	20514	2097	0.04	
		100	214.43	20201	2065	0.03	
		200	217.71	18391	1880	0.07	
Ti-131	dwell time (µs)	20	169.86	34660	3543	0.06	[NPs]=2.5ppb; 1.0mL min^{-1}
		50	420.83	16572	1694	0.07	
		100	445.55	15858	1621	0.11	
		200	542.71	14498	1482	0.18	
TiO_2 NPs 100 nm							
Ti-STD	dwell time (µs)	20	1363.33	78412	1921	0.03	[NPs]=1.25ppb
		50	1331.22	78820	2074	0.07	
		100	1305.03	71718	1757	0.11	
		200	1398.17	70452	1726	0.16	
Ti-114	dwell time (µs)	20	296.11	66942	1640	0.02	[NPs]=2.5ppb; 0,75mL min^{-1}
		50	395.35	53349	1307	0.02	
		100	394.34	56125	1375	0.04	
		200	486.66	43704	1054	0.09	
Ti-131	dwell time (µs)	20	492.35	106086	2599	0.01	[NPs]=2.5ppb; 1.0mL min^{-1}
		50	968.11	58819	1441	0.01	
		100	1104.43	45104	1322	0.02	
		200	1021.21	53962	1105	0.05	

Work-mode	Parameter	Values studied	Peak intensity (counts)	Particle concentration(p/mL)	Number of peaks	Dissolved Intensity (counts)	Other information
TiO_2 NPs <150nm							
Ti-STD	dwell time (µs)	20	386.1	91741	9378	0.07	[NPs]=1.25ppb
		50	363.66	109917	11236	0.12	
		100	374.58	108000	11040	0.17	
		200	410.7	101182	10343	0.37	
Ti-114	dwell time (µs)	20	102.14	288860	7907	0.33	[NPs]=2.5ppb; 0.5mL min^{-1}
		50	147.68	259999	7117	0.81	
		100	168.26	248126	6792	1.54	
		200	181.75	216782	5934	2.84	
Ti-131	dwell time (µs)	20	85.27	170386	4664	0.58	[NPs]=2.5ppb; 0.5mL min^{-1}
		50	217.96	97687	2674	1.48	
		100	299.66	90198	2469	2.88	
		200	352.7	76389	2091	5.35	
CuO NPs <50 nm							
Cu-STD	dwell time (µs)	20	1300.6	68372	1047	0.56	[NPs]=5 ppb
		50	1442.42	69156	1059	0.17	
		100	1635.25	59426	910	0.6	
Cu-63	dwell time (µs)	20	2560.01	54332	832	0.58	[NPs]=5 ppb; 0.5mL min^{-1}
		50	2209.61	73401	1124	0.05	
		100	2450.45	73009	1118	0.05	
		200	2930.8	63111	965	0.21	
Cu-97	dwell time (µs)	20	1117	22957	761	0.14	[NPs]=5ppbs; 1.5 mL min^{-1}
		50	1168.67	18341	608	0.36	

Work-mode	Parameter	Values studied	Peak intensity (counts)	Particle concentration (p/mL)	Number of peaks	Dissolved Intensity(counts)	Other information
		100	1031.54	20574	682	0.7	
		200	1312.56	17251	575	1.62	
Cu NPs 60-80 nm							
Cu-STD	dwell time (µs)	20	1125.47	8789	238	0.18	[NPs]=2.5 ppb; 0.5 mL min^{-1}
		50	1537.79	9860	267	0.22	
		100	1229.92	9269	251	1.12	
		200	1265.41	6056	164	2.41	
Cu-63	dwell time (µs)	20	3381.41	7238	196	1.17	[NPs]=2.5 ppb
		50	3691.55	9085	246	2.47	
		100	3447	6241	169	6.07	
		200	3230.54	7312	198	12.43	
Cu-97	dwell time (µs)	20	1653.37	10414	282	0.77	[NPs]=5ppbs; 1.5 mL min^{-1}
		50	2174.54	9971	270	1.96	
		100	2454.54	10894	295	4.01	
		200	2245.98	9306	252	7.92	
		1	1643.91	11079	300	1.6	[NPs]=5 ppbs; 50µs
Cu NPs 40-60nm							
Cu-STD	dwell time (µs)	20	1734.49	4982	186	0.13	[NPs]=2.5 ppb
		50	1367.47	5973	223	0.35	
		100	1477.44	5464	204	0.92	
		200	1324.59	6000	224	2.79	
Cu-63	dwell time (µs)	20	2518.36	6750	252	2.61	[NPs]=2.5 ppb; 0.5mL min^{-1}

Work-mode	Parameter	Values studied	Peak intensity (counts)	Particle concentration (p/mL)	Number of peaks	Dissolved Intensity (counts)	Other information
		50	2691.11	7554	282	2.56	
		100	2515.65	7098	265	5.34	
		200	2346.91	7259	271	10.78	
Cu-97	dwell time (µs)	20	226.87	17545	655	0.69	[NPs]=5ppb; 1.5 mL min^{-1}
		50	853.81	8196	306	1.72	
		100	875.89	8438	315	3.53	
		200	1070.18	5786	216	4.39	
		1	1324.45	6831	255	0.19	[NPs]=5 ppb; 50µs
ZnO NPs 35-45nm							
Zn-STD	dwell time (µs)	20	268.32	9306	423	1.41	[NPs]=2.5 ppb
		50	265.73	9526	433	4.47	
		100	237.52	9658	439	7.49	
		200	215.51	7260	330	19.08	
Zn-64	dwell time (µs)	20	514.57	4290	195	5.13	[NPs]=2.5 ppb; 0.5mL min^{-1}
		50	577.41	3718	169	12.86	
		100	509.67	7964	362	20.4	
		200	559.5	5830	265	41.27	
ZnO NPs <100nm							
Zn-STD	dwell time (µs)	20	102.17	29887	1358	0.53	[NPs]=2.5 ppb
		50	136.06	25707	1168	1.49	
		100	126.45	28006	1273	3.16	
		200	139.38	28897	1313	6.56	
Zn-64	dwell time (µs)	20	331.03	29909	1359	5.02	[NPs]=2.5 ppb; 0.5mL min^{-1}

REFERENCES

[1] V. Sogne, F. Meier, T. Klein, C. Contado, Investigation of zinc oxide particles in cosmetic products by means of centrifugal and asymmetrical flow field-flow fractionation, J. Chromatogr. A. 1515 (2017) 196–208. https://doi.org/10.1016/j.chroma.2017.07.098.

[2] J. Athinarayanan, V.S. Periasamy, M.A. Alsaif, A.A. Al-Warthan, A.A. Alshatwi, Presence of nanosilica (E551) in commercial food products: TNF-mediated oxidative stress and altered cell cycle progression in human lung fibroblast cells, Cell Biol. Toxicol. 30 (2014) 89–100. https://doi.org/10.1007/s10565-014-9271-8.

[3] A. Weir, P. Westerhoff, L. Fabricius, K. Hristovski, N. Von Goetz, Titanium dioxide nanoparticles in food and personal care products, Environ. Sci. Technol. 46 (2012) 2242–2250. https://doi.org/10.1021/es204168d

[4] P. Van Broekhuizen, F. Van Broekhuizen, R. Cornelissen, L. Reijnders, Use of nanomaterials in the European construction industry and some occupational health aspects thereof, J. Nanoparticle Res. 13 (2011) 447–462. https://doi.org/10.1007/s11051-010-0195-9

[5] A.M. Alkilany, L.B. Thompson, S.P. Boulos, P.N. Sisco, C.J. Murphy, Gold nanorods: Their potential for photothermal therapeutics and drug delivery, tempered by the complexity of their biological interactions, Adv. Drug Deliv. Rev. 64 (2012) 190–199. https://doi.org/10.1016/j.addr.2011.03.005

[6] B. Jovanović, G. Bezirci, A.S. Çağan, J. Coppens, E.E. Levi, Z. Oluz, E. Tuncel, H. Duran, M. Beklioğlu, Food web effects of titanium dioxide nanoparticles in an outdoor freshwater mesocosm experiment, Nanotoxicology. 10 (2016) 902–912. https://doi.org/10.3109/17435390.2016.1140242

[7] J.J. Faust, K. Doudrick, Y. Yang, P. Westerhoff, D.G. Capco, Food grade titanium dioxide disrupts intestinal brush border microvilli

in vitro independent of sedimentation, Cell Biol. Toxicol. 30 (2014) 169–188. https://doi.org/10.1007/s10565-014-9278-1.

[8] European Commission, Regulation (EC) No 1223/2009 of the European Parliament and of the Council of 30 November 2009 on cosmetic products, Off. J. Eur. Union 22.12 (2009) L342/59–L342/209.

[9] European commission, Regulation (EC) No 450/2009 of 29 May2009 on active and intelligent materials and articles intended to come into contact with food, Off. J. Eur. Union 30.5 (2009) L135/3–L135/11.

[10] European Commission, Regulation (EU) No 10/2011 of 14 January 2011 on plastic materials and articles intended to come into contact with food, Off. J. Eur. Union 15.1 (2011) L12/1–L12/89.

[11] H. E. Pace, N. J. Rogers, C. Jarolimek, V. A. Coleman, C. P. Higgins, J. F. Ranville, Determining transport efficiency for the purpose of counting and sizing nanoparticles via single particle inductively coupled plasma mass spectrometry, Anal. Chem. 83 (2011) 9361–9369.

[12] F. Laborda, E. Bolea, J. Jiménez-Lamana, Single particle inductively coupled plasma mass spectrometry: A powerful tool for nanoanalysis, Anal. Chem. 86 (2014) 2270–2278. https://doi.org/10.1021/ac402980q

[13] F. Laborda, E. Bolea, J. Jiménez-Lamana, Single particle inductively coupled plasma mass spectrometry for the analysis of inorganic engineered nanoparticles in environmental samples, Trends Environ. Anal. Chem. 9 (2016) 15–23. https://doi.org/10.1016/j.teac.2016.02.001.

[14] M.D. Montaño, J.W. Olesik, A.G. Barber, K. Challis, J.F. Ranville, Single Particle ICP-MS: Advances toward routine analysis

of nanomaterials, Anal. Bioanal. Chem. 408 (2016) 5053–5074. https://doi.org/10.1007/s00216-016-9676-8

[15] D. Mozhayeva, C. Engelhard, A critical review of single particle inductively coupled plasma mass spectrometry-A step towards an ideal method for nanomaterial characterization, J. Anal. At. Spectrom. 35 (2020) 1740–1783. https://doi.org/10.1039/c9ja00206e.

[16] N. Jakubowski, L. Moens, F. Vanhaecke, Sector field mass spectrometers in ICP-MS, Spectrochim. Acta Part B At. Spectrosc. 53 (1998) 1739–1763. https://doi.org/10.1016/S0584-8547(98)00222-5

[17] N. Jakubowski, T. Prohaska, L. Rottmann, F. Vanhaecke, Inductively coupled plasma- and glow discharge plasma-sector field mass spectrometry: Part I. Tutorial: Fundamentals and instrumentation, J. Anal. At. Spectrom. 26 (2011) 693–726. https://doi.org/10.1039/c0ja00161a.

[18] I. Rodushkin, E. Engström, A. Stenberg, D.C. Baxter, Determination of low-abundance elements at ultra-trace levels in urine and serum by inductively coupled plasma-sector field mass spectrometry, Anal. Bioanal. Chem. 380 (2004) 247–257. https://doi.org/10.1007/s00216-004-2742-7.

[19] J.M. Harrington, D.J. Young, A.S. Essader, S.J. Sumner, K.E. Levine, Analysis of human serum and whole blood for mineral content by ICP-MS and ICP-OES: Development of a mineralomics method, Biol. Trace Elem. Res. 160 (2014) 132–142. https://doi.org/10.1007/s12011-014-0033-5

[20] K. Sakata, K. Kawabata, Reduction of fundamental polyatomic ions in inductively coupled plasma mass spectrometry, Spectrochim. Acta Part B At. Spectrosc. 49 (1994) 1027–1038. https://doi.org/10.1016/0584-8547(94)80088-X

[21] C. Suárez-Oubiña, P. Herbello-Hermelo, P. Bermejo-Barrera, A. Moreda-Piñeiro, Exploiting dynamic reaction cell technology for

removal of spectral interferences in the assessment of Ag, Cu, Ti, and Zn by inductively coupled plasma mass spectrometry, Spectrochim. Acta B. 187 (2022) 106330. https://doi.org/10.1016/j.sab.2021.106330

[22] E. Bolea-Fernandez, D. Leite, A. Rua-Ibarz, L. Balcaen, M. Aramendía, M. Resano, F. Vanhaecke, Characterization of SiO_2 nanoparticles by single particle-inductively coupled plasma-tandem mass spectrometry (spICP-MS/MS), J. Anal. At. Spectrom. 32 (2017) 2140–2152. https://doi.org/10.1039/c7ja00138j.

[23] S. Candás-Zapico, D.J. Kutscher, M. Montes-Bayón, J. Bettmer, Single particle analysis of TiO_2 in candy products using triple quadrupole ICP-MS, Talanta. 180 (2018) 309–315. https://doi.org/10.1016/j.talanta.2017.12.041.

[24] E. Bolea-Fernandez, D. Leite, A. Rua-Ibarz, T. Liu, G. Woods, M. Aramendia, M. Resano, F. Vanhaecke, On the effect of using collision/reaction cell (CRC) technology in single-particle ICP-mass spectrometry (spICP-MS), Anal. Chim. Acta. 1077 (2019) 95–106. https://doi.org/10.1016/j.aca.2019.05.077

[25] M. Tharaud, A.P. Gondikas, M.F. Benedetti, F. Von Der Kammer, T. Hofmann, G. Cornelis, TiO_2 nanomaterial detection in calcium rich matrices by spICPMS. A matter of resolution and treatment, J. Anal. At. Spectrom. 32 (2017) 1400–1411. https://doi.org/10.1039/c7ja00060j.

[26] L. Balcaen, E. Bolea-Fernandez, M. Resano, F. Vanhaecke, Inductively coupled plasma - Tandem mass spectrometry (ICP-MS/MS): A powerful and universal tool for the interference-free determination of (ultra)trace elements - A tutorial review, Anal. Chim. Acta. 894 (2015) 7–19. https://doi.org/10.1016/j.aca.2015.08.053

[27] E. Bolea-Fernandez, L. Balcaen, M. Resano, F. Vanhaecke, Tandem ICP-mass spectrometry for Sr isotopic analysis without prior Rb/Sr separation, J. Anal. At. Spectrom. 31 (2016) 303–310. https://doi.org/10.1039/c5ja00157a

[28] J. Soto-Alvaredo, F. Dutschke, J. Bettmer, M. Montes-Bayón, D. Pröfrock, A. Prange, Initial results on the coupling of sedimentation field-flow fractionation (SdFFF) to inductively coupled plasma-tandem mass spectrometry (ICP-MS/MS) for the detection and characterization of TiO2 nanoparticles, J. Anal. At. Spectrom. 31 (2016) 1549–1555. https://doi.org/10.1039/c6ja00079g.

[29] Syngistix Nano Application Software Module for Single Particle ICP-MS. https://resources.perkinelmer.com/lab-solutions/resources/docs/PRD_Syngistix-Nano-Software-Module_011657_01.pdf (accessed January 18th 2022).

[30] L. Balcaen, E. Bolea-Fernandez, M. Resano, F. Vanhaecke, Accurate determination of ultra-trace levels of Ti in blood serum using ICP-MS/MS, Anal. Chim. Acta. 809 (2014) 1–8. https://doi.org/10.1016/j.aca.2013.10.017

[31] L. Fu, S.Y. Shi, J.C. Ma, Accurate Determination of harmful and doping elements in soft magnetic ferrite powders using inductively coupled plasma tandem mass spectrometry, Chinese J. Anal. Chem. 47 (2019) 1382–1389.https://doi.org/10.1016/S1872-2040(19)61189-8

[32] L. Fu, S. Shi, X. Chen, H. Xie, Analysis of impurity elements in high purity cobalt powder by inductively coupled plasma tandem mass spectrometry, Microchem. J. 139 (2018) 236–241. https://doi.org/10.1016/j.microc.2018.03.002.

[33] E. Soriano, V. Yusà, A. Pastor, M. de la Guardia, Dynamic reaction cell inductively couple plasma-mass spectrometry optimization for seawater analysis, Microchem. J. 137 (2018) 363–370. https://doi.org/10.1016/j.microc.2017.11.015

[34] Y. Cao, J. Feng, L. Tang, C. Yu, G. Mo, B. Deng, A highly efficient introduction system for single cell- ICP-MS and its application to detection of copper in single human red blood cells, Talanta. 206 (2020) 120174. https://doi.org/10.1016/j.talanta.2019.120174

[35] B.L. Batista, J.L. Rodrigues, J.A. Nunes, V.C. de Oliveira Souza, F. Barbosa, Exploiting dynamic reaction cell inductively coupled plasma mass spectrometry (DRC-ICP-MS) for sequential determination of trace elements in blood using a dilute-and-shoot procedure, Anal. Chim. Acta. 639 (2009) 13–18. https://doi.org/10.1016/j.aca.2009.03.016

[36] B. Meermann, V. Nischwitz, ICP-MS for the analysis at the nanoscale-a tutorial review, J. Anal. At. Spectrom. 33 (2018) 1432–1468. https://doi.org/10.1039/c8ja00037a.

[37] A. Rua-Ibarz, E. Bolea-Fernandez, G. Pozo, X. Dominguez-Benetton, F. Vanhaecke, K. Tirez, Characterization of iron oxide nanoparticles by means of single-particle ICP-mass spectrometry (spICP-MS)-chemical: Versus physical resolution to overcome spectral overlap, J. Anal. At. Spectrom. 35 (2020) 2023–2032. https://doi.org/10.1039/d0ja00183j.

CHAPTER 3

SINGLE-CELL-ICP-MS FOR STUDYING THE ASSOCIATION OF INORGANIC NANOPARTICLES WITH CELL LINES DERIVED FROM AQUACULTURE SPECIES

CHAPTER 3. SINGLE-CELL-ICP-MS FOR STUDYING THE ASSOCIATION OF INORGANIC NANOPARTICLES WITH CELL LINES DERIVED FROM AQUACULTURE SPECIES

3.1 ABSTRACT

The current research deals with the use of single cell inductively coupled plasma – mass spectrometry (scICP-MS) for the assessment of titanium dioxide nanoparticles (TiO_2 NPs) and silver nanoparticles (Ag NPs) association in cell lines derived from aquaculture species (sea bass, sea bream and clams). The optimization studies have considered the avoidance of high dissolved background, multi-cell peak coincidence, and possible spectral interferences. Optimum operating conditions were found when using a dwell time of 50 µs for silver and 100 µs for titanium. The assessment of associated TiO_2 NPs by scICP-MS required the use of ammonia as a reaction gas (flow rate at 0.75 mL min^{-1}) for free-interference titanium determinations (measurements at a m/z ratio of 131 from the $^{48}Ti(NH)(NH_3)_4$ adduct). The influence of other parameters such as the number of washing cycles and the cell concentration on the accurate determinations by scICP-MS was also fully investigated. Cell exposure trials were performed using PVP-Ag NPs (15 and 100 nm, nominal diameter) and citrate-TiO_2 NPs (5, 25, and 45, nominal diameter) at nominal concentrations of 10 and 50 µg mL^{-1} for citrate-TiO_2 NPs and 5.0 and 50 µg mL^{-1} for PVP-Ag NPs. Results have shown that citrate-TiO_2 NPs interact with the outer cell membranes, being quite low the number of citrate-TiO_2 NPs that enters in the cells (the high degree of aggregation is the main factor which leads to the aggregates be in the extracellular medium). In contrast, PVP-Ag NPs have been found to enter in the cells.

3.2 INTRODUCTION

The widespread use of NPs in several industrial sectors, including medicine, food, cosmetics and even construction [1–4], has led to the presence of these new pollutants in the aquatic environment, and there is great concern about the risk for humans [5–7]. Among NPs, titanium dioxide nanoparticles (TiO_2 NPs) and silver nanoparticles (Ag NPs) deserve special mention because of the huge use and applications: strong UV absorbance, photocatalytic capabilities, visible light transparency, iridescent qualities, and anti-bacterial activity for TiO_2 NPs [8]; and catalytic activity, and optical and anti-bacterial properties for Ag NPs [9,10]. The aquaculture sector could be affected by the increasing presence of NPs in the marine environment, and since this sector has experienced a continuous growth over the last decades [11,12], concerns about potential hazards linked to emerging pollutants such as NPs are being considered to guarantee high-quality and safe products to the consumers.

As a preliminary step for elucidating pollutants bioaccumulation in cultured seafood, *in vitro* assays for assessing NPs association, either interaction with the cellular membrane or internalization, in cells are appealing approaches but, currently, there is not a consensual protocol for establishing this NPs–cells interaction [13–15]. Most analytical developments for elucidating metals internalization and NPs interaction in/with cells require the analysis of large number of cells after several pre-treatments such as cellular lysis, extraction and digestion procedures [16–19].

Single cell- inductively coupled plasma – mass spectrometry (scICP-MS) has opened a new area of research which allows the quantification of dissolved metals and inorganic NPs in single cells at ultra-low levels (attograms per cell). The mass of metal per cell, the mass distribution within a cell population, the concentration of metal or nanoparticle-containing cells, and the number of NPs per cell can be determined using this cutting-edge technique. Among other high-quality features, scICP-MS can distinguish single cells, operates at a minimal sample uptake rate of 10 µL min^{-1}, and analysis are performed close to native cell- state.

In scICP-MS a suspension of cells must be nebulized using a nebulization system that allows cells integrity so that the single particle-ICP-MS (spICP-MS) principles can be used. As each cell enters the plasma, it is atomised, and the resulting ion-burst from the corresponding metal is detected by ICP-MS. Cells transfer into the plasma is one of the main challenges which faces scICP-MS. Cells transport system must keep the cell integrity and transfer the highest number of cells into the ICP-MS. Although several pneumatic nebulizers have been proposed for scICP-MS [16], microflow-based nebulizers in combination with special spray chambers, guarantee cells integrity during the transport and hence, high transport efficiencies and low background signals. The special spray chambers have a dual make-up gas entrance specifically positioned to provide a tangential flow to the spray chamber walls, preventing cell collision and deposition onto the walls. Single-cell analysis by scICP-MS has been used for assessing the internalization of arsenite in A549 cells [17], copper in human red blood cells [18], copper-based algaecides in algae [20], and cisplatin in cancer cells [21]. Some scICP-MS applications have been also developed for elucidating NPs association to cells, mainly gold nanoparticles (Au NPs) in microalgae, and in MCF-7, K562 and HeLa cells [22–24], Ag NPs in THP-1 monocytes and HepG2 cells [25,26] , biogenic selenium nanoparticles (Se NPs) in yeast [27], ZnO NPs in HepG2 cells [28], tellurium nanoparticles (Te NPs) in bacterial cells [29], and CdSeS quantum dots in Raw 264.7 cells [30].

In this sense, the aim of this work has been the optimization and application of scICP-MS to assess the association, either membrane adsorption or internalization, of PVP-Ag NPs and citrate-TiO_2 NPs in cells from sea bass (*Dicentrarchus labrax*) kidney, sea bream (*Sparus aurata*) kidney, and clam (*Ruditapes philippinarum*) gills after several exposure trials. Optimization has implied the study of several parameters to avoid high dissolved background, multi-cell peak coincidence, and possible spectral interferences. The latter task is quite important for titanium determination, and the use of ammonia, previously used as a reaction gas in collision/reaction cell technologies for total titanium [31] and TiO_2 NPs [32] assessment by

ICP-MS/MS and spICP-MS/MS, respectively, has been novelty used for scICP-MS analysis when assessing the titanium content at cells (monitoring the $^{48}Ti(NH)(NH_3)_4$ adduct at a m/z ratio of 131) [33,34].

3.3 EXPERIMENTAL

3.3.1 Instrumentation

Analysis have been performed using a NexION 2000 quadrupole-based inductively coupled plasma mass spectrometer (Perkin Elmer, Waltham, MA, USA), equipped with a quartz torch with a quartz injector (2.5 mm i.d.), triple cone equipment, and collision/reaction cell. The instrument is also equipped with the specialized Single Cell Micro DX autosampler and with high-efficiency introduction system consisting of a CytoNeb with PFA gas line nebuliser (Perkin Elmer), fitted onto the Asperon spray chamber (Perkin Elmer). Microjet adapter is positioned to the Asperon spray chamber for dual make-up gas inlet to create a tangential flow. All analyses were carried out using the Syngistix™ Single Cell Application Software Module for data collection and processing. Microwave-assisted acid digestions were performed using Ethos Easy Advanced Microwave Digestion System (Milestone, Sorisole, Italy). A Laborcentrifugen 2K15 (Sigma, Osterode, Germany) was used for centrifugation (washing of cells suspension) and a USC-TH ultrasound water bath (45 Hz, 80 W) from VWR International Eurolab S.L (Barcelona, Spain) was used for dispersing NPs standards before calibrations. Cell counting was performed in a counting Neubauer chamber improved bright-line hemocytometer (Brand, Wertheim, Germany).

Electron microscopy (EM) characterization of exposed cells were performed using JEOL JEM 1010 transmission electron microscope (TEM) operating at voltage of 100 kV for cells from clams and scanning electron microscope (SEM) FEI Quanta 650 FEG, operating at high vacuum, an acceleration voltage of 5 kV and spot size set at position 3 for kidney cells from seabream. The cell samples for SEM analysis were coated with conductive carbon using an EM ACE600 coating system (Leica microsystems). The cell samples for TEM analysis were treated using a Leica EM TP Tissue processor and the

ultrathin sections with a thickness of ≈ 70 nm were prepared using a RMC Boecketer PowerTome PC ultramicrotome system.

3.3.2 Reagents and standards

Ultrapure water (18.2 MΩ cm of resistivity) was obtained from a Milli-Q® IQ 7003 purification device system from Millipore (Bedford, MA, USA). Mono-elemental standards of ionic titanium [$(NH_4)_2TiF_6$] and silver ($AgNO_3$) were purchased from Perkin Elmer. Hyperpure nitric acid 69% (w/v) and 33% (w/v) hydrogen peroxide were from Panreac (Barcelona, Spain). Phosphate-buffered saline (PBS) was from Thermo Fisher (Dublin, Ireland). NexION Setup Solution (Be, Ce, Fe, In, Li, Mg, Pb, U), 10 μg L^{-1} was from Perkin Elmer. Glassware and plastic ware were decontaminated by soaking in 10% (v/v) nitric acid for at least 48 h. Material was then rinsed with ultra–pure water several times. Gold nanospheres dispersions were prepared from a N8151035 standard (nanoComposix, San Diego, CA, USA). The material consists of 49.6 ± 2.1 nm nanospheres (TEM diameter) and particle concentration of 9.89×10^6 NPs mL^{-1} (2% RSD) obtained by spICP-MS. The nanospheres are covered by PEG carboxyl and they are suspended in aqueous 1 mM citrate. Silver NPs dispersions used for calibration were prepared from bare (citrate) Ag NPs standards (aqueous 2 mM sodium citrate) from nanoComposix. The standards were 60 nm Ag NPs (nominal diameter of 59±6 nm obtained by TEM, mass concentration of 0.020 mg mL^{-1} obtained by ICP-MS, particle concentration of 1.8×10^{10} particles mL^{-1}, and a hydrodynamic diameter of 64 nm); 40 nm Ag NPs (nominal diameter of 41±5 nm obtained by TEM, mass concentration of 0.021 mg mL^{-1} obtained by ICP-MS, particle concentration of 5.4×10^{10} particles mL^{-1}, and a hydrodynamic diameter of 44 nm); and 20 nm Ag NPs (nominal diameter of 20.8±3.0 nm obtained by TEM, mass concentration of 0.021 mg mL^{-1} obtained by ICP-MS, particle concentration of 4.2×10^{11} particles mL^{-1}, and a hydrodynamic diameter of 27 nm). Titanium dioxide NPs stock dispersions (also used for calibration) were prepared from TiO2 suspensions (mixture of rutile and anatase, 99.5%) with particle size <150 nm (volume distribution by dynamic light scattering) at 40wt. % in water,

purchased from Sigma-Aldrich (Osterode, Germany). Regarding cell exposure trials, polyvinylpyrrolidone (PVP)-coated Ag NPs with primary nominal diameter of 15 nm and 100 nm and citrate-coated TiO_2 NPs with a primary nominal diameter of 5 nm, 25 and 45 nm were prepared from Ag NPs and TiO_2 NPs from several suppliers. A complete description of the preparation of PVP-Ag NPs and citrate-TiO_2 NPs dispersions can be found in section 2.3.

Ammonia (99,999%) reaction gas used in the reaction cell and 99.998% Argon used for plasma generation, nebulization, and as auxiliary gas, were supplied by Nippon Gases (Madrid, Spain). Leibovitz medium (L15) and fetal bovine serum (FBS) suitable for cell growth, and ACS grade dimethyl sulfoxide (DMSO) were purchased from Thermo Fisher. Sodium cacodylate buffer was prepared by dissolving 98% sodium cacodylate trihydrated (Thermo Fisher) in distilled water and adjusting the pH to 7.2 with diluted hydrochloric acid prepared from technical grade 37% hydrochloric acid (Panreac). Karnovsky fixative was prepared at 2.0 % (v/v) paraformaldehyde (96% extra pure) and 2.5 % (v/v) glutaraldehyde (50% solution, ≥48.0 to ≤52.0%) from Thermo in 0.1 M sodium cacodylate buffer. Propylene oxide (ReagentPlus® ≥ 99%; Sigma-Aldrich, Merck Life Science, Algés, PT), osmium tetroxide solution (2 % and 4 % aqueous solution; Science Services, Munich, Germany), ethanol and EMBed-812 epoxy resin kit (Science Services, Munich, Germany) were used for the fixation, staining, dehydration and resin embedding of the cells for TEM analysis.

3.3.3 Preparation of PVP-Ag NPs and citrate-TiO_2 NPs dispersions used for cell exposure trials

Polyvinylpyrrolidone (PVP)-coated Ag NPs with a diameter of 15 nm (15 nm Ag NPs). Commercial PVP-coated Ag NPs powder was purchased from SSNano (Houston, Tx, USA; product code: 0127SH). The powder composition was 25% wt silver and 75% wt PVP. Ag NPs stock dispersion at 6.2 g L^{-1} was prepared in ultrapure water by dispersing the powder for 15 min using a bath sonicator (37 kHz, 100 %). PVP-coated Ag NPs with a diameter of 100 nm (100 nm Ag NPs). The 100 nm Ag NPs stock dispersion with a concentration of 2.9 g L^{-1}

was prepared from Ag ink containing 30 % AgNPs with a diameter of 100 nm dispersed in ethylene glycol (Sigma-Aldrich). The ethylene glycol was removed by dialysis using a 12 kDa cellulose membrane against water. The purified Ag NPs was mixed with PVP (Mw = 40kDa) solution to reach a Ag:PVP ratio of 1:3 wt:wt.

Citrate-coated TiO_2 NPs with a primary size of 5 nm (5.0 nm TiO_2 NPs). Pristine 5 nm TiO_2 NPs were purchased from Nanostructured & Amorphous Materials, Inc. (Katy, TX, USA; anatase, 5 nm size, 99%). The 5 nm TiO_2 NPs stock dispersion was prepared in ultrapure water by dispersing a mixture of trisodium citrate dehydrate and titanium dioxide powder at weight ratio of 1.5:1 wt:wt for 30 min using an ultrasonic probe (Branson Disintegrator Ultrasonic Model 450; 30 s pulse on / 5 s pulse off, and 50 % amplitude). The final concentration of citrate-coated TiO_2 NPs was 13.3 - 15.5 g L^{-1} depending on the batch.

Citrate-coated TiO_2 NPs with a primary size of 25 nm (25 nm TiO_2 NPs) Pristine 25 nm TiO_2 NPs were supplied by Sigma-Aldrich (99.5% purity, mixture of rutile and anatase). The 25 nm TiO_2 NPs stock dispersion was prepared in ultrapure water by dispersing a mixture of trisodium citrate dehydrate and titanium dioxide powder at weight ratio of 0.8:1 wt:wt for 30 min using an ultrasonic probe (Branson Disintegrator Ultrasonic Mod. 450, 30 s pulse on / 5 s pulse off, and 50 % amplitude). The final concentration of citrate-coated TiO_2 NPs was 13.3 - 15.5 g L^{-1} depending on the batch.

Citrate-coated TiO_2 NPs with a primary size of 45 nm (45 nm TiO_2 NPs). Pristine 45 nm TiO_2 NPs were purchased from Sigma-Aldrich (99.5% purity, mixture of rutile and anatase; nanoparticle size of < 100 nm (BET) and < 50 nm (XRD)) and were used without any further purification. The 45 nm TiO_2 NPs were stabilized with trisodium citrate dehydrate aqueous solution reaching a weight ratio of 1:1.5 TiO_2:citrate. The mixture was dispersed for 30 min using an ultrasonic probe (Branson Disintegrator Ultrasonic Mod. 450; with 30 s pulse on / 5 s pulse off, and 50 % amplitude). The final concentration of citrate-coated TiO_2 NPs was 13.3 - 15.5 g L^{-1} depending on the batch.

TEM from several prepared Ag NPs and TiO_2 NPs are shown in **Figure S3.1** (electronic supplementary information, ESI).

3.3.4 Cytometry measurements

After appropriate dilution, 10 µL of cell suspensions were introduced in the chamber following manufacturer's instructions) and cells included in the 4 ruled areas of the corners were counted and the average number was accounted. Cells were stained with Trypan Blue classical method, to differentiate dead and alive cells. The final number of cells was calculated by multiplying average number by a factor of 10^4 (manufacturer's instructions) as well as by the dilution factor.

3.3.5 Cell culture conditions and pre-treatments for scICP-MS and EM analysis

Assays regarding exposure tests and cell toxicity to PVP-Ag NPs and citrate-TiO_2 NPs for gill's clams, and sea bass and sea bream kidney cells were carried out at the facilities of the Aquaculture Cluster Technology Centre (CETGA). The species [clam (*Ruditapes philippinarum*), sea bass (*Dicentrarchus labrax*), and sea bream (*Sparus aurata*)] followed the standard procedure for growth under controlled conditions until they were harvested. On the one hand, sea bass and sea bream specimens were fasted for one day before sampling, whereas the fasting period for clams was three days. The specimens were sacrificed after anaesthesia overdose, and the surface of the fish and the clam shells were disinfected with 70% ethanol. In the case of sea bass and sea bream, the kidney was removed under sterile conditions. The clams were opened by sectioning the anterior and posterior adductor muscles with a scalpel, and the entire contents of the clam's belly were then removed under sterile conditions.

Both the kidney cells (sea bass and sea bream) and the entire contents of the soft tissues of clam were disaggregated, and the cells of interest were collected using a Percoll gradient, discarding impurities and non-viable cells. A Neubauer chamber was used to count total/viable cells. After counting, the cells were adjusted to the desired concentration, distributed in the wells, and loaded in multiwell

plates for different exposures with NPs (size and concentrations). The cell culture was adjusted to a concentration of 4.0×10^6 cell mL^{-1}. The culture medium used was L-15 without phenol red supplemented with 5-10% FBS (v/v) and 1% penicillin/streptomycin (Thermo Fisher, 10,000 IU/ mL^{-1} penicillin, 10,000 µg/ mL^{-1} streptomycin) at 19ºC. Cell viability was tested by the MTT (tetrazolium salt (2-(4,5-dimethyl- 2-thiazolyl)-3,5-diphe-nyl-2H-tetrazolium bromide) method to ensure that the cell cultures are in good condition for carrying out bioaccumulation assays. Toxicity tests were performed with an initial cell amount of 9.0×10^5 cells (volume of 3.0 mL and 3.0×10^5 cell mL^{-1}). Cell toxicity assays (24 h exposure) was performed under sterile conditions in a type II laminar flow cabinet by adding to each well 1.0 mL of cell culture and 3.0 mL of NPs dispersions (experiment in duplicate) at several concentrations (dilutions with the cell culture medium). First NPs dispersions were redispersed by sonication (10 min, 50% amplitude, pulse 15 on/10 off) for citrate-TiO_2 NPs, and by vortexing for PVP-Ag NPs. After exposure, the cells were transferred to 15 mL tubes for further centrifugation (1500 g, 10 min), and the supernatant was removed. The pellet was mixed with 1.0 mL of freezing medium (Leibovitz Medium (L15) with 20% fetal bovine serum (FBS) and 10% DMSO) to preserve the integrity of the cells during freezing and were frozen at -20ºC until analysis.

The obtained cells were further subjected to two different pre-treatments for leading scICP-MS and TEM analysis. Cells for scICP-MS analysis were suspended with 4.0 mL of L15/20% FBS/10% DMSO freezing mixture, and were then frozen and kept at -20°C. Pre-treatment for TEM analysis consisted of a centrifugation stage of the cell suspension at 320 g, 4°C for 5.0 min and careful supernatant removal, followed by dropwise addition of 500 µL of Karnovsky fixative and keeping the mixture at 4°C 24 h under gentle shaking. After Karnovsky fixative removal, the pellet was washed with sodium cacodylate buffer (0.1 M) for 20 min (two washing steps), and was kept at 4°C.

3.3.6 Cell suspension preparation for scICP-MS

Cell suspensions were thawed and homogenised through pipette mixing, and then an aliquot was sampled and re-suspended in 1.0 %(wt/v) PBS in 1.0 mL Eppendorf tubes. The diluted cell suspensions were subjected to a short and gentle centrifugation washing step (300 g, 4.0°C, 5.0 min). The supernatant was removed, and the pellet was again re-suspended in 1.0 %(wt/v) PBS for scICP-MS analysis after appropriate dilution.

3.3.7 Microwave assisted acid digestion

For comparison purposes, 1.0 mL of cell suspensions in 1.0 %(wt/v) PBS (one replicate for each case) were subjected to microwave assisted acid digestion by using 2.0 mL of ultrapure water, 3.0 mL of 69% nitric acid, and 1.0 mL of 33% hydrogen peroxide. The mixtures were exposed to microwave under a controlled-temperature program consisted of a ramp from room temperature to 130°C in 20 min, and a hold stage at 130°C for 15 min. After cool-down, the acid digests were diluted to 25 mL with ultrapure water and kept at room temperature until ICP-MS analysis (operating conditions given in **Table S3.1**, electronic supplementary information – ESI).

3.3.8 TEM and SEM analysis

The fixated pellets of clam cells were processed following a routine methodology for TEM. Briefly, the cells pellets were post-fixated in a 1 % osmium tetroxide solution. Then, they were dehydrated with increasing ethanol from 50 to 100% and with a final emersion step in propylene oxide. The infiltration was performed using mixtures of propylene oxide: epoxy resin (EMBed-812 kit) at different proportion increasing the amount of resin until having finally pure epoxy resin. Fragments of each pellet embedded were placed in the edge of a silicon template forming blocks. The blocks were cured at 60 °C for three days. Ultrathin sections (≈70 nm thick) were prepared using an ultramicrotome with a diamond knife (Diatome) and placed on formvar/carbon-coated 200 mesh copper grids for cells exposed to citrate-TiO_2 NPs and carbon-coated 400 mesh titanium grids for cells exposed to PVP-Ag NPs to be analysed by TEM.

The fixated pellets of seabream' cells were washed in cacodylate buffer and subsequently filtered through 2 µm polycarbonate membrane. Cells-supported polycarbonate filters were placed on pin stubs (Standard 12.7 mm, 8 mm pin length, Ted Pella) and subsequently, they were coated with conductive carbon for SEM analysis.

3.3.9 Single-cell ICP-MS measurements

Daily performance for ICP-MS was assessed (Be intensity >2500 counts s^{-1}, In intensity >40000 counts s^{-1}, U intensity >30000 counts s^{-1}, and Bkgd ≤ 3 for standards at 1.0 µg L^{-1}, and Ce^{++}/Ce ratio ≤0.05 and the CeO/Ce ratio ≤0.025). Daily performance (torch alignment and voltages) was performed with Ti (10 µg L^{-1}) and Ag (3.0 µg L^{-1}) prior to analysis. Analytical results were calculated using Syngistix™ ICP-MS 2.5 version software. Operating conditions for scICP-MS are listed in **Table 3.1**. The scICP-MS analytical data was processed using an iterative approach previously described [21,35] aiming the cell event threshold. The transport efficiency (TE%) was automatically calculated after measuring the 49.6 nm Au NPs certified reference material at 1.00×10^5 NPs mL^{-1} by the particle frequency method. The TE% value obtained was from 45% to 55%.

Determinations implied external calibrations at five level concentrations for ionic titanium (0.5–10 µg L^{-1}) for titanium assessment, whereas calibrations with Ag NPs (20, 40 and 60 nm, 1.0 µg L^{-1}, each one) were used for silver determinations (Ag NPs dispersions were manually shaken just before measurements). Cell suspensions (after dilution in PBS) were placed in 1.0 mL cuvettes of the autosampler. The autosampler automatically mixes the cell suspensions to favour the representativeness of the sample taken and aspirates 150 µL for filling a 100 µL loop. The loaded sample is then pumped at 10 µL min^{-1} and nebulised with a CytoNeb nebuliser coupled to an Asperon chamber which allows a tangential flow that prevents cell damage, collisions, or cell deposition onto the chamber walls. After each injection, the sample loop is rinsed with a wash solution (1% nitric acid and 2% hydrogen peroxide).

Standard mode and mass-shift approach were used for the measurement of silver and titanium, respectively. Ammonia clusters of mass-charge ratio 131 (1.0 mL min^{-1} of ammonia and RPq 0.2 value [33,34]) were used for titanium determinations. The scICP-MS analytical data were processed using an iterative approach aiming the cell event threshold. Data, graphs, and spectra analysis were performed after data being exported from 2.5 Syngistix ICP-MS software (Single Cell Application). The amount of titanium and silver in cells was determined by applying **Equation 3.1**.

$$m_c = \frac{\varepsilon \cdot Q_{sam} \cdot t_{dwell} \cdot (I_c - I_{bgd})}{m} \quad (\mathbf{Eq.\,3.\,1})$$

where m_c is the mass of element of interest in single cell, ε is the transport efficiency, Q_{sam} is the sample uptake rate, t_{dwell} is the dwell time, m is the calibration slope, and I_c and I_{bgd} the analyte and background intensity, respectively.

Table 3.1. Operating conditions and data acquisition parameters for scICP-MS

Parameter (unit)	
RF power (W)	1600
Plasma Gas Flow rate (L min^{-1})	15
Make up Gas flow (L min^{-1})	0.70
Nebulizer Gas Flow (L min^{-1})	0.35
Sample flow rate (µL min^{-1})	10
Quadrupole Ion Deflector (V)	Set for maximum ion transmission
Triple Cone Equipment	Sampler, skimmer and hyperskimmer cones made of nickel
Transport efficiency (%)	≈ 45-55%
Scan time (s)	100
Sample loop (µL)	100

Analyte (m/z)	Ag (107)
Density (g cm^{-3})	10.49
Mass Fraction	100 %
Mode	Standard
Dwell time (µs)	50

Analyte (m/z)	Ti (131)
Density (g cm^{-3})	4.23
Mass Fraction	59.90 %
Dwell time (µs)	100
Mode	Reaction Cell
Ammonia flow rate (mL min^{-1})	0.75
Ion-product registered	$^{48}Ti(NH)(NH_3)_4$
Rejection parameter q	0.20

3.4 DISCUSSION AND RESULTS

3.4.1 Optimization study

The influence of several parameters affecting scICP-MS, such as dwell time and cell concentration, has been evaluated for assessing the content of TiO_2 NPs and Ag NPs in PVP- 100nm Ag NPs-exposed and citrate-45nm TiO_2 NPs-exposed cells culture from clam' gill, sea bass's kidney and sea bream's kidney. Other parameters such as those involved in reaction cell (use of ammonia as a reaction gas) when measuring titanium have also been carefully optimised. To date, DRC technology has scarcely been used for single-cell analysis (one development based on oxygen as a reaction gas [29]) and special consideration must be taken since the minimal sample flow rates (10 µL min^{-1}) used in scICP-MS. In addition, the obtained signals by scICP-MS could be attributed to cells that contain NPs, cells in which the NPs are attached to membranes, and NPs in the extracellular matrix. Therefore, a washing process is required for removing NPs not tightly attached to cells, and the effect of a washing process (number of washing cycles) has been also evaluated.

Finally, we must consider the existence of NPs disaggregation (citrate-TiO_2 NPs and PVP-Ag NPs conversion into smaller NPs aggregates or single NP) and dissolution (citrate-TiO_2 NPs and PVP-Ag NPs conversion into ionic species) processes, and signals derived from cells could not exclusively been attributed to the citrate-TiO_2 NPs and PVP-Ag NPs used in the exposure experiments.

3.4.1.1 Dwell time

The dissolved metal content (background signal and extracellular content) and the mean intensity related to the mean mass per cell have been recorded at several dwell times (20, 50, 100, and 200 µs for silver, and 50, 100 and 200 µs for titanium) for cell suspensions from sea bass' kidney (1: 3000 dilution from cell suspensions at 9.0×10^5 cells mL^{-1}) previously exposed to PVP-Ag NPs (100 nm, 100 mg L^{-1}) and cell suspensions from gill clams (1:2000 and 1:200 dilution from cell suspensions at 9.0×10^5 cells mL^{-1}) previously exposed to citrate-TiO_2 NPs (45 nm, 100 mg L^{-1}). Regarding PVP-Ag NPs (**Figure S3.1**, ESI) the average intensity due

to the mass of internalised PVP-Ag NPs remains constant at both low and high dwell time values. Small dwell times are preferable to define the peak of cellular events in scICP-MS since low background signal are recorded and the occurrence of double cell peaks (maximising the number of detected events) is minimised [27,36]. Therefore, good results have been obtained for dwell time of 20 and 50 μs (**Figure S3.2**, ESI), and a dwell time of 50 μs has been chosen for further silver determinations.

Regarding titanium assessment (1:1200 and 1:200 dilutions), mean intensity due to the mass of internalised citrate-TiO_2 NPs (**Figure S3.3**, ESI) was found to be similar for dwell times of 50 and 100 μs, but it was slightly higher when recording at 200 μs. These findings can be explained considering the use of reaction cell technology for interferences removal for the determination of titanium. The use of ammonia has been reported to broaden the transient signals in spICP-MS [37] leading to tailoring peaks, and a proper recording of the signals is achieved by using high dwell times (100 μs or even 200 μs). However, large dwell times could lead to double event counting, and a dwell time of 100 μs was finally selected for titanium determinations (value in accordance with spICP-MS developments when using ammonia as a reaction gas in the reaction cell [34]).

3.4.1.2 Number of washing cycles

After cell lines exposure to NPs (section 3.3.5) non-associated NPs and NPs derived from cell lysis can be present in the extracellular medium of the cell suspensions, and the direct analysis could lead to count non-associated NPs together with cells. The characterization of the NPs- cell interaction by TEM and SEM shows that the NPs not only internalized, but also associated strongly to the cellular membrane. The morphology and ultrastructure of the non-exposed cells observed by TEM indicated that haemocytes [38] are the predominant cells (**Figure 3.1**, controls). In addition, TEM images show that citrate-TiO_2 NPs are mostly adsorbed on the cellular membrane, while cellular uptake of PVP-Ag NPs is observed (**Figure 3.1**). Moreover, SEM images of the non-exposed cells sample show

features with similar or smaller size and different shape to the cells, which could be attributed to cell debris or apoptotic vesicles (**Figure 3.2** controls), while SEM images of the exposed cells samples show big NP aggregates, which seem to be closely associated to the cell membranes (**Figure 3.2**). It is worth to mention that great part of the cells observed in the SEM were blood cells such as blood erythrocytes and lymphocytes [39], which are extensively present in the kidney [40].

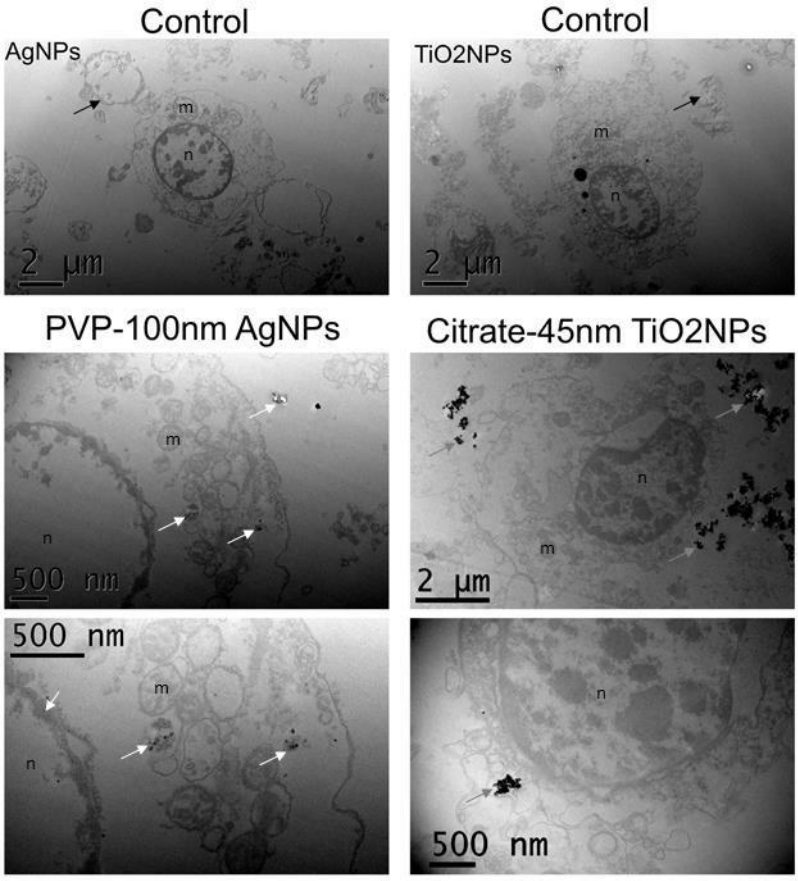

Figure 3.1. Representative TEM images of non-exposed (controls), PVP-100nm Ag NPs- exposed and citrate-45nm TiO_2 NPs-exposed cells culture from clam' gill. The cells culture were exposed to 50 µg mL^{-1} of PVP-100nm Ag NPs and 5.0 µg mL^{-1} of citrate-45nm TiO_2 NPs. Black arrows indicate cell debris; grey arrows indicate TiO_2 NPs agglomerates associated to membranes out of the cells; white arrows indicate possible Ag NPs out and inside the cells (of lowers size than the primary NPs). m= mitochondria, n= nucleus.

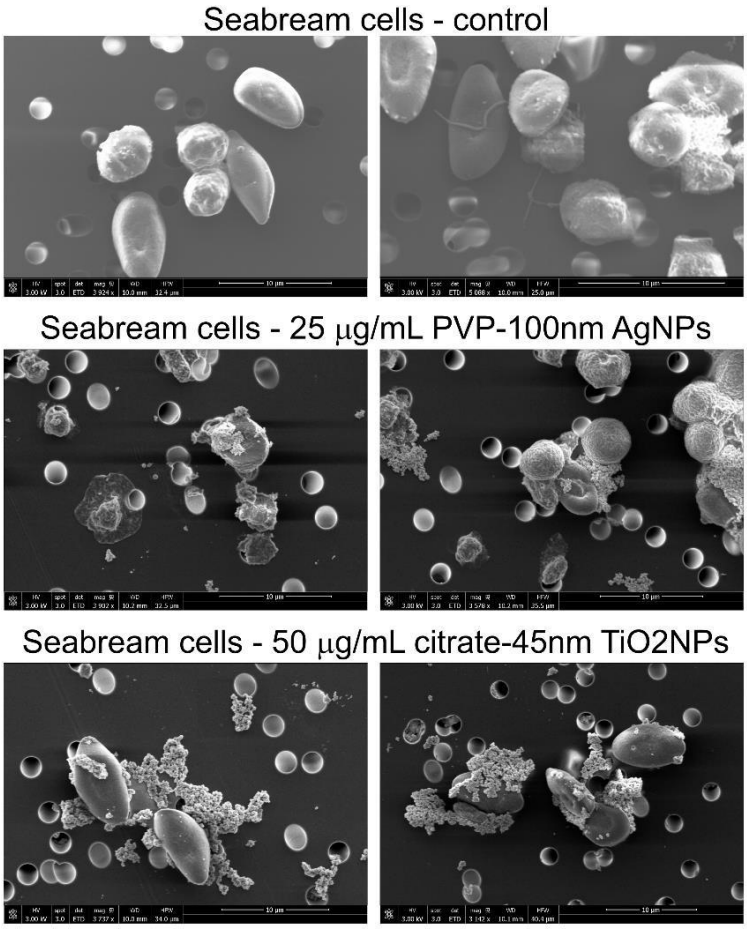

Figure 3.2. Representative SEM images for seabream' cells exposed to no NPs (control), 100 nm Ag NPs, 25.0 μg mL^{-1} and (C) 45 nm TiO_2 NPs, 50.0 μg mL^{-1}

The overestimation due to the presence of non-tightly associated NPs to cells can be overcome, in part, by performing a washing procedure with an appropriate medium under gentle centrifugation (cells pellet separation from the bulk solution). Gentle centrifugation conditions must be applied to avoid cell damage, but the procedure must guarantee a minimum amount of cells remaining in the supernatant. Longer centrifugation times would result in a more compact pellet, but it would lead to a more difficult re-suspension of the cell pellet.

Therefore, short centrifugation times (within the 3.0-15 min range) at relative centrifugal field (RCF) of 150 and 300 have been commonly used [41–43].

The number of washing cycles (one, two and three) using 1.0 mL of 1.0 %(wt/v) PBS pH 7.4 as a washing buffer and centrifugation at 300 RFC and 4°C for 5.0 min was studied for cell suspensions from sea bass' kidney (1:12000 and 1:3000 dilution from cell suspensions at 9.0×10^5 cells mL^{-1}) previously exposed to PVP-Ag NPs (100 nm, 100 mg L^{-1}) and cell suspensions from gill clams (1:1200 and 1:300 dilution from cell suspensions at 9.0×10^5 cells mL^{-1}) previously exposed to citrate-TiO_2 NPs (45 nm, 100 mg L^{-1}). The supernatant obtained, as well as the cells pellet after re-suspension in 1.0 % (wt/v) PBS, were analysed by scICP-MS. Results regarding supernatants (washing fractions) analysis (**Figure 3.3**) show a high number of signals (around 3000 in **Figure 3.3A** and 2500 in **Figure 3.3B** for silver and titanium, respectively) and low ionic silver and titanium concentrations (lower than 1.0 µg L^{-1}, **Figure 3.3(C-D)** after performing the first washing cycle; whereas the number of signals decreases considerably after the second and the third washing cycles and the ionic silver and titanium concentration remains constant. These findings suggest that most of the free NPs are efficiently removed during the first washing stage, and one washing cycle with 1.0 mL of 1.0 % (wt/v) PBS and centrifugation (300 RFC, 4°C) for 5.0 min was chosen.

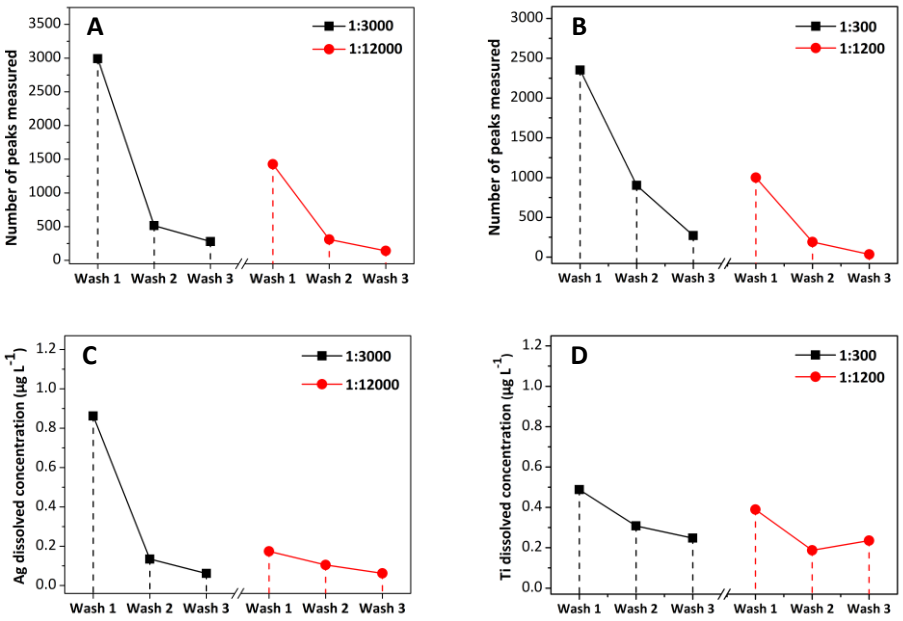

Figure 3.3. Number of measured peaks for silver and dissolved silver concentration (A and C, respectively), and number of measured peaks for titanium and dissolved titanium concentration (B and D, respectively) in the washing buffer (PBS) after several washing cycles. Experiments performed with cell suspensions from sea bass' kidney previously exposed to Ag NPs (100 nm, 100 mg L^{-1}) and cell suspensions from gill clams previously exposed to TiO_2 NPs (45 nm, 100 mg L^{-1}).

Finally, **Figure S3.4** (ESI) shows TEM images of gill's clam cells exposed to PVP-15 nm Ag NPs (5 mg L^{-1}) and to citrate-45 nm TiO_2 NPs (5 mg L^{-1}). PVP-Ag NPs were found to be removed from the extracellular medium (they were found to be attached to the inner membrane surface or just phagocytised, but citrate-TiO_2 NPs were found to remain in part as quite large agglomerates in the extracellular medium and may not have been totally removed during the washing steps of the centrifugation (similar or higher weight than the cells, implying their settlement in the cell pellet).

3.4.1.3 Cellular concentration

Data from the available scICP-MS literature has shown that the cell concentration should not change the average mass per cell

measured, and only the frequency (number) of signals will be dependent on the cell concentration [18,36]. High dilution could therefore be needed for trials carried out at high NPs concentrations and/or long exposure times for avoiding saturation in the detector because of the large number of incorporated nanoparticles (high mass of the element per cell).

Different dilutions of cells suspensions from sea bass' kidney or gill's clam (9.0 10^5 cells mL^{-1}) after exposure previously exposed to 100 nm PVP-Ag NPs (nominal mass concentration at 100 mg L^{-1}) and 45 nm citrate-TiO_2 NPs (nominal mass concentration at 100 mg L^{-1}) have been tested (experiments in triplicate), and **Figure S3.5** (ESI) shows that the mean mass is within the 10 - 12 femtograms per cell range for silver (1:3000 to 1:30000 dilution), and from 40 to 45 femtograms per cell for titanium (1:300 to 1:9000 dilution). The small differences observed can be attributed to the scICP-MS analysis variability itself. Results are quite convenient since the cell concentration will be strongly influenced by the cell and NPs nature, and the exposure conditions (NPs concentration and exposure time) and dilutions can be performed without information losses.

3.4.2 Comparison of scICP-MS with microwave assisted acid digestion and ICP-MS

The amount of cells-associated citrate-TiO_2 NPs and PVP-Ag NPs in selected cells isolated from tissues after NPs exposure was assessed by the proposed scICP-MS method and after applying a conventional microwave acid digestion process and direct ICP-MS analysis. Selected cell samples consisted of cells isolated from clam gill exposed to 5 nm citrate-TiO_2 NPs at 50 µg mL^{-1} and to 25 nm citrate-TiO_2 NPs at 50 and 100 µg mL^{-1}; cells isolated from sea bass and sea bream kidney exposed to 25 nm citrate-TiO_2 NPs at 50 µg mL^{-1}; of cells isolated from clam gill exposed to 15 nm PVP-Ag NPs at 100 µg mL^{-1}; cells isolated from sea bass kidney exposed to 100 nm PVP-Ag NPs at 100 µg mL^{-1}; and cells from sea bream's kidney exposed to 15 nm PVP-Ag NPs at 100 µg mL^{-1}. For comparison (concentrations expressed as femtograms per cell), the total titanium and silver content obtained by ICP-MS after microwave assisted acid

digestion was divided by the number of cells counted by cytometry (9.24 10^4 cells). Results are listed in **Table 3.2** and slightly higher concentrations (about to 1.3 to 3.6 times higher) were obtained when using ICP-MS after microwave assisted acid digestion when analysis clam's cells for citrate-TiO_2 NPs. High differences were also obtained for cells isolated from both fish' kidneys (about to 3.3 to 9.0 times higher) for citrate-TiO_2 NPs assessment. In the case of PVP-Ag NPs, higher differences were observed: 6.4 times higher for clam's cells and 10 to 17 times higher sea bass and sea bream cells. Reports focused on studying the internalization of dissolved metal/metalloid have revealed that concentrations by ICP-MS after acid digestion are slightly higher than those obtained by scICP-MS, about 1.3 times higher for copper in human red blood cells [18], and about 3 times higher for total carbon and platinum in cell samples [41]. Differences, also reported by Meyer et al. [17] for arsenite assessment in A549 cells, have been attributed to a lower number of cells involved in scICP- MS measurements. Regarding experiments for NPs associated with cells, López-Serrano et al.[26] have reported that the lower element concentration when using scICP-MS could be also attributed to saturation of the detector when the cells contain a high number of NPs (around 100 per cell in the case of Ag NPs in THP-1 monocytes). The saturation of the detector may be the most possible explanation for the differences found in our experiments because cells exposure tests have been conducted at high NPs concentrations.

Table 3.2. Titanium and silver concentration in some cell lines exposed to Ag NPs and TiO_2 NPs after microwave assisted acid digestion and ICP-MS measurement and after scICP-MS.

Sample ID	[Ti] (fg cell^{-1})[a]	RSD	[Ti] (fg cell^{-1})[b]	RSD	Ratio[c]
Clam (5.0 nm TiO_2 NPs, 50 μg mL^{-1})	146	2	41	5	3.6
Clam (25 nm TiO_2 NPs, 50 μg mL^{-1})	167	8	47	1	3.5
Sea bass (5.0 nm TiO_2 NPs, 50 μg mL^{-1})	873	8	35	-	25
Sea bass (25 nm TiO_2 NPs, 50 μg mL^{-1})	152	13	46	4	3.3
Sea bream (5.0 nm TiO_2 NPs, 50 μg mL^{-1})	562	2	57	1	9.9

Sample ID	[Ag] (ag cell^{-1})[a]	RSD	[Ag] (ag cell^{-1})[b]	RSD	Ratio[c]
Clam (15 nm Ag NPs, 5.0 μg mL^{-1})	69	4	19	5	37
Clam (100 nm Ag NPs, 5.0 μg mL^{-1})	24	9	38	-	6.4
Sea bass (100 nm Ag NPs, 100 μg mL^{-1})	367	16	21	7	17
Sea bream (100 nm Ag NPs, 5.0 μg mL^{-1})	147	10	16	6	9.7

(a) Microwave assisted acid digestion and ICP-MS measurement; (b) scICP-MS measurement; (c) ratio between the concentrations after microwave assisted acid digestion and ICP-MS measurement and scICP-MS measurement

3.4.3 Limit of detection of the method

The limits of detection (LODs), referred to the mass of element (titanium and silver) associated with cells, have been automatically obtained with the NanoSyngistix™ ICP-MS software after stablishing the transport efficiency and dissolved titanium calibrations within 0.5–10 µg L−1, or calibrations based on Ag NPs (nominal diameters of 20, 40 and 60 nm, 1.0 µg L-1, each one). Calculated values were 0.095±0.011 femtograms per cell for titanium, and 0.005±0.001 femtograms per cell for silver.

3.4.4 Applications

Exposure assays for cells isolated from gill clam were performed with 15 and 100 nm PVP-Ag NPs at two concentration levels (5.0 and 50 µg mL^{-1}) and with 5.0 and 25 nm citrate-TiO_2 NPs at 50 µg mL^{-1}. Regarding cells from sea bass kidney, exposure assays were carried out with 15 and 100 nm PVP-Ag NPs at 50 and 100 µg mL^{-1}; whereas 5.0 and 25 nm citrate-TiO_2 NPs were used at 50 µg mL^{-1}. Finally, 15 and 100 nm PVP-Ag NPs (10, 50 and 100 µg mL^{-1}) and 5.0 and 25nm citrate-TiO_2 NPs (10 and 50 µg mL^{-1} were tested for sea bream cells. After scICP-MS analysis (dilution between 100 and 600 for titanium, and within the 600-3000 range for silver), the average mass of the element (silver and titanium) per cell, as well as the element concentration in the supernatant from cell washing steps, and the theoretical NPs internalization and/or NPs adsorption onto the cellular membranes (range-mass levels) are obtained for each case.

Results on mean mass per cell and dissolved metal concentration are plotted in **Figure 3.4** and **Figure 3.5** for silver and titanium assessment, respectively. The levels of dissolved silver and titanium in the extracellular medium for the three types of cells were found to be very small (lower than 0.5 µg L^{-1}), even for exposure experiments at high PVP-Ag NPs and citrate-TiO_2 NPs concentrations.

The mean silver mass per cell in cells from gill clam (**Figure 3.4A**) was found to be dependent on the PVP-Ag NPs concentration used for the exposure assays, being lower for cells exposed to the lowest PVP-Ag NPs concentration independently of the PVP-Ag NPs nominal size (15 and 100 nm). Concerning PVP-Ag NPs' size, there is

a big difference between the mean silver mass per cell for experiments using the lowest PVP-Ag NPs concentration (5.0 µg mL^{-1}, 15 and 100 nm), but the mean silver content per cell is quite similar when the highest concentration (100 µg mL^{-1}) was used, and values of 6.3±0.094 and 6.7±0.83 femtograms per cell were assessed for experiments with 15 and 100 nm, respectively.

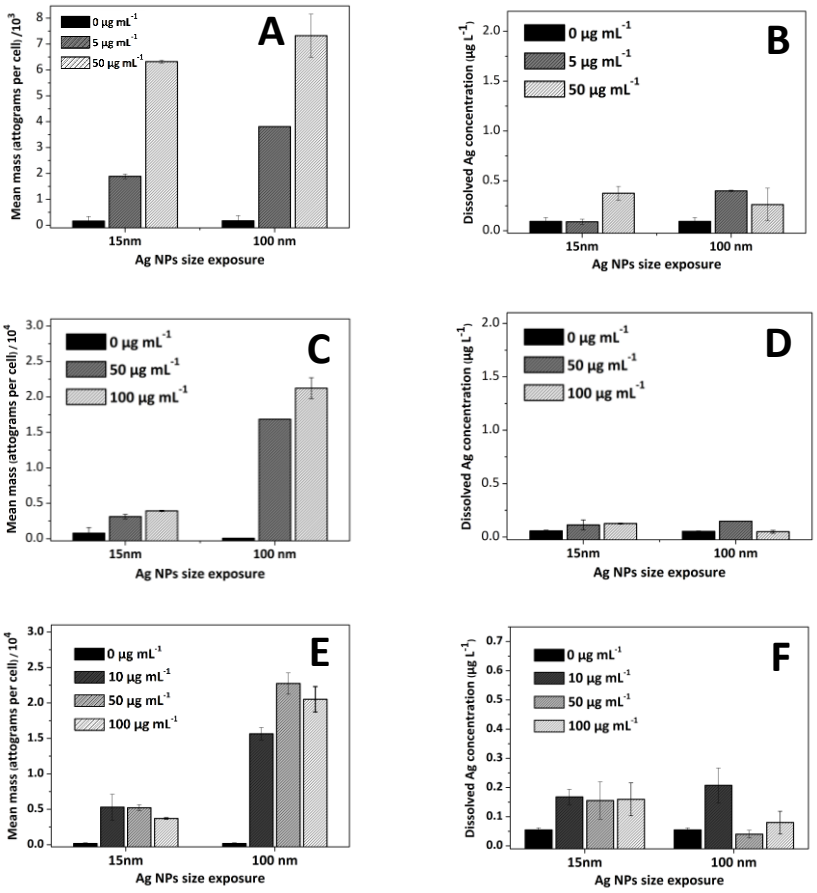

Figure 3.4. Cellular silver (attograms per cell, A, C, and E) and extracellular (dissolved, B, D, and F) silver concentration in gill clam cells (A and B), sea bass kidney cells (C and D), and sea bream kidney cells (E and F).

Regarding silver interaction with cells isolated from sea bass and sea bream' kidney, a quite different trend has been obtained (**Figure 3.4C**), and there is a big difference for silver in the cellular fraction when exposing with 15 and 100 nm PVP-Ag NPs. However, comparison within the same size, quite similar silver concentrations were obtained, mainly for 15 nm PVP- Ag NPs (3.1±0.32 and 3.9±0.098 femtograms per cell in sea bass kidney cells for 50 and 100 µg mL^{-1}, respectively). In the case of sea bream kidney cells (**Figure 3.4E**), quite similar silver concentrations were obtained for 15 nm PVP-Ag NPs (5.3±1.8 and 5.2±0.43 femtograms per cell for 10 and 50 µg mL^{-1}, respectively), but a lower value was assessed when using the highest PVP-Ag NPs concentration (3.7±0.092 femtograms per cell at 100 µg mL^{-1}).

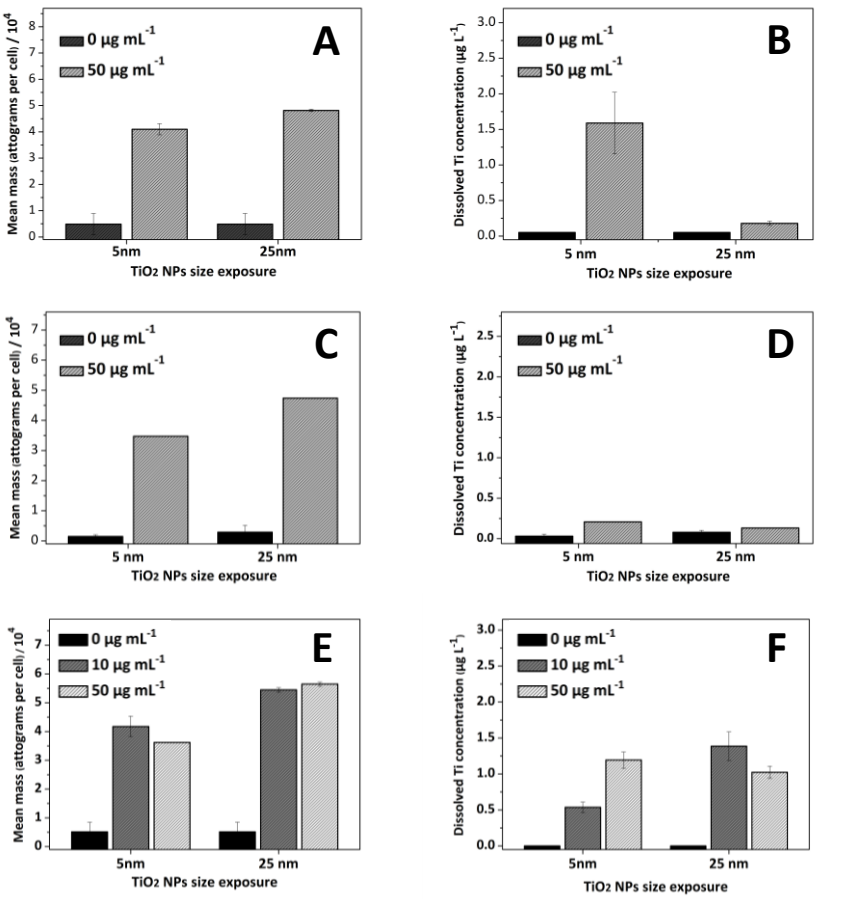

Figure 3.5. Cellular titanium (attograms per cell, A, C, and E) and extracellular (dissolved, B, D, and F) titanium concentration in gill clam cells (A and B), sea bass kidney cells (C and D), and sea bream kidney cells (E and F).

Citrate-TiO_2 NPs interaction with cells is also quite different than that observed for PVP-Ag NPs, and quite similar mean titanium mass per cell was obtained independently of the citrate- TiO_2 NPs concentration and size used, and the cell nature (**Figure 3.5A**, **3.5C**, and **3.5E** for gill clam, sea bream kidney, and sea bass kidney, respectively).

The theoretical number of cellular PVP-Ag NPs is given in **Table S3.2** to **S3.4** for gill clam cells, sea bass kidney cells and sea bream

kidney cell, respectively. The theoretical approximation considers the measured femtograms for each element (titanium and silver) and values such as density, mass fraction and radius of the citrate-TiO_2 NPs and PVP-Ag NPs used for the interaction assays. Therefore, a 100 nm PVP-Ag NPs equals to 5.5 femtograms under this criterion, whereas, for 15 nm PVP-Ag NPs the calculated femtograms are close to the LOD of the technique for silver (0.005±0.001 femtograms per cell).

Data, after applying this theoretical calculation and distributing the data obtained in intervals of 5.0 femtograms up to the upper limit of the technique (5.0 femtograms), are listed in **Tables S3.2** to **S3.4** (ESI) for cells from gill clam and sea bass and sea bream kidney exposed to 100 nm PVP-Ag NPs. The number of peaks (number of cells containing silver) appears to be independent on the Ag NPs concentration for cells derived from gill clams (1207 and 1187 peaks for 5.0 and 50 μg mL^{-1}, respectively) and sea bream kidney (902, 1108, and 959 peaks for 10, 50, and 100 μg mL^{-1}, respectively). However, PVP-Ag NPs concentration influences the amount of silver in cells from sea bass kidney (1918 and 1256 peaks for 50 and 100 μg mL^{-1}, respectively). **Table S3.2** shows that the percentage of PVP-Ag NPs lower than 100 nm is higher in gill clam cells (82 and 47% for 5.0 and 50 μg mL^{-1}, respectively) than in sea bream (30, 16, and 19% for 10, 50, and 100 μg mL^{-1}, respectively) and sea bass (12 and 7% for 50 and 100 μg mL^{-1}, respectively) kidney cell, which could imply a higher dissolution (ionization) of PVP-Ag NPs by gill clam cells. **Table 3.3** also shows that the number of (theoretically) internalized 100 nm PVP-Ag NPs is gradually reduced and no more than nine 100 nm Ag NPs per cell can be identified. These results lead to narrow frequency histograms (**Figure 3.6A**) where most of the silver refers to few femtograms (dissolved silver, PVP-Ag NPs lower than 100 nm and a very small amount of 100 nm PVP-Ag NPs).

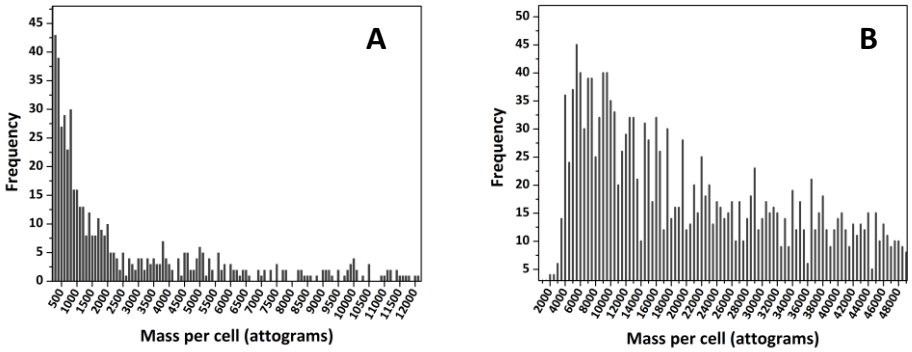

Figure 3.6. Frequency histograms from sea bream kidney cells after exposure to (A) 100 nm Ag NPs (5.0 µg mL^{-1}) and (B) to 5.0 nm TiO_2 NPs (50 µg mL^{-1}).

Regarding titanium, 5.0 nm citrate-TiO_2 NPs and 25 nm citrate-TiO_2 NPs lead to theoretical femtograms per cell close/lower than the LOD (0.095±0.011 femtograms per cell). However, titanium in the cellular fraction has been assessed because of the high degree of agglomeration of citrate-TiO_2 NPs. Therefore, **Tables S3.5 to S3.7** (gill clam cells, sea bass kidney cells and seabream kidney cells, respectively) show the range (5.0 intervals) of femtograms per cell (associated titanium) instead of the theoretical number of associated citrate-TiO_2 NPs. Results show that interaction with gill clam cells appears to be independent on the size of citrate-TiO_2 NPs (5.0 and 25 nm). Therefore, the highest percentages of cellular titanium in gill clam cells (percentages higher than 10%) have been found for femtograms per cell within the < 5.0 to 15- 20 range for both citrate-TiO_2 NPs sizes (**Table S3.5**). Regarding sea bass and sea bream cells (**Table S3.6** and **S3.7**, respectively), differences since the citrate-TiO_2 NPs size were attempted, and higher percentages of associated NPs to the cell were obtained for experiments with 5.0 nm citrate-TiO_2 NPs (31.7% of < 5.0 femtograms per cell for sea bass kidney, and percentages of 37.2 and 29.7% of < 5.0 femtograms per cell for sea bream kidney exposed to 50 and 10 µg mL^{-1}, respectively). **Table S3.6** and **S3.7** show, therefore, that the degree of citrate-TiO_2 NPs interaction with cells from sea bass and sea bream kidney is dependent on the citrate-TiO_2 NPs size. In addition, the histograms obtained

(such as the one shown in **Figure 3.6B**) present large frequencies for all the ranges of masses per cell recorded.

3.5 CONCLUSIONS

Parameters such as dwell time, cells concentration, and mainly, the presence of NPs in the extracellular medium have been found to condition the reliable assessment of PVP-Ag NPs and citrate-TiO_2 NPs direct interaction with clam and fish kidney cells by scICP-MS. In addition, free-interference titanium determinations have been possible by using ammonia as a reaction gas in the scICP-MS measurement mode. The developed procedure offers great potential for studying NPs interactions with cells, including internalization, and results show that the interaction is mainly dependent on the cell nature and the NPs type, and the effects of the NP concentration and size is less important. The degree of internalization of citrate-TiO_2 NPs was found to be lower than that observed for PVP-Ag NPs due to the high degree of agglomeration of citrate-TiO_2 NPs (TEM analysis has revealed citrate-TiO_2 NPs interactions with the external part of cell membranes as well as citrate-TiO_2 NPs agglomerates in the extracellular fluid). On the other hand, the scICP-MS results for both the silver and titanium contents show significant differences with those found after acid digestion of the cells and direct ICP-MS measurement, results that agree with those reported in the literature and that in our case may be due to the high nanoparticles concentrations used in the cell exposure trials.

SUPPLEMENTARY INFORMATION

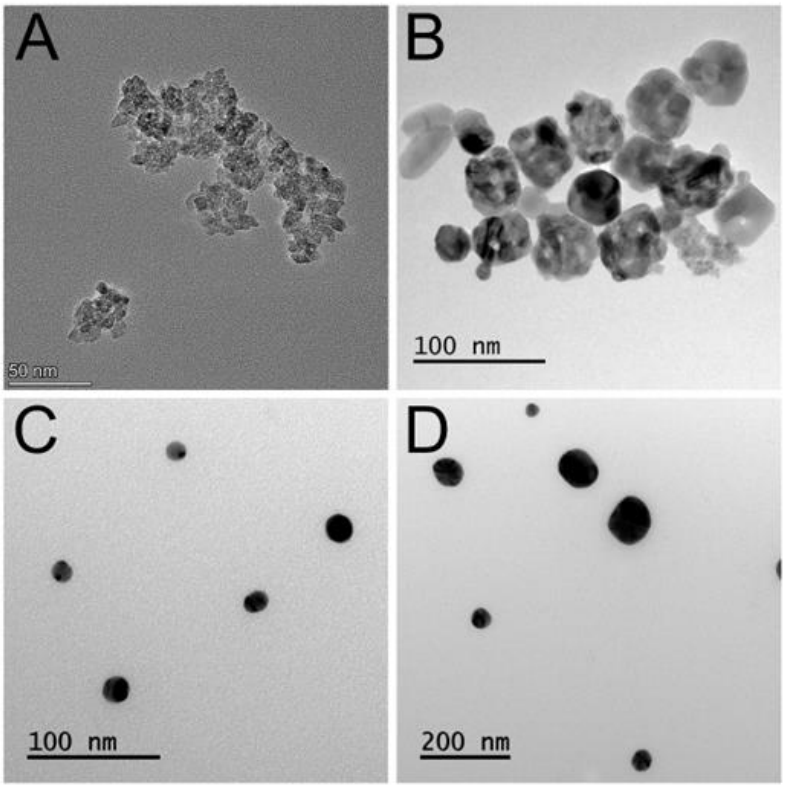

Figure S3.1. Representative TEM images of (A) Citrate-5nm TiO_2 NPs, (B) Citrate-45nm TiO_2 NPs, (C) PVP-15nm Ag NPs, and (D) PVP-100nm Ag NPs. High-resolution TEM analysis of citrate-5nm TiO_2 NPs was performed using FEI Titan (G3) Cubed Themis 60-300 kV electron microscope, operating at 200 kV. TEM images of the rest of NPs were acquired using JEOL JEM 1010 transmission electron microscope operating at 100 kV.

Table S3.1.Operating ICP-MS conditions

Spray Chamber Type	Quartz Cyclonic
PC^{3x} Peltier Cooler System	4ºC
Nebulizer Type	PFA MicroFlow
RF power (W)	1600
Plasma Gas Flow (L min^{-1})	15
Auxiliary Gas flow (L min^{-1})	1.2
Nebulizer Gas Flow (L min^{-1})	1.14
Sample uptake rate (µL min^{-1})	≈ 220
Acquisition Mode	Scanning
Dwell time per amu (ms)	50 ms
Quadrupole ion deflector (V)	Set for maximum ion transmission
Sweeps	20
Readings	1
Replicates	3
Analyte (m/z)	Ag (107) Standard mode
Analyte (m/z)	Ti (131) DRC mode (0.75 mL min^{-1} ammonia flow rate) Ion-product registered: $^{48}Ti(NH)(NH_3)_4$ Rejection parameter (q): 0.20

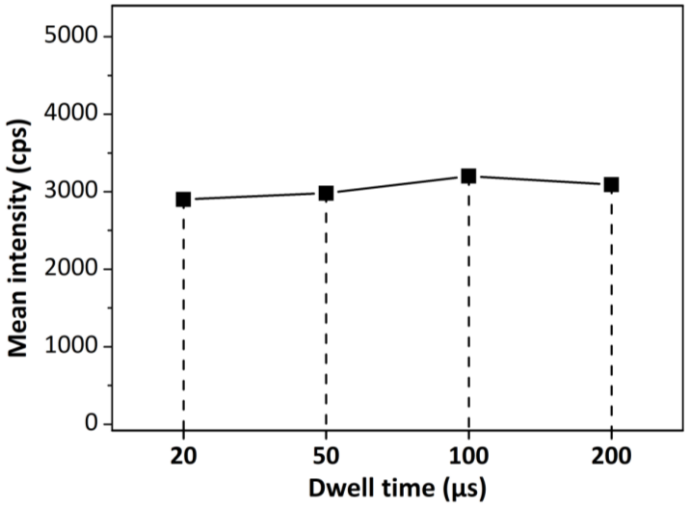

Figure S3.2. Effect of the dwell time on the silver mean intensities (n=5). RSD values were lower than 1%.

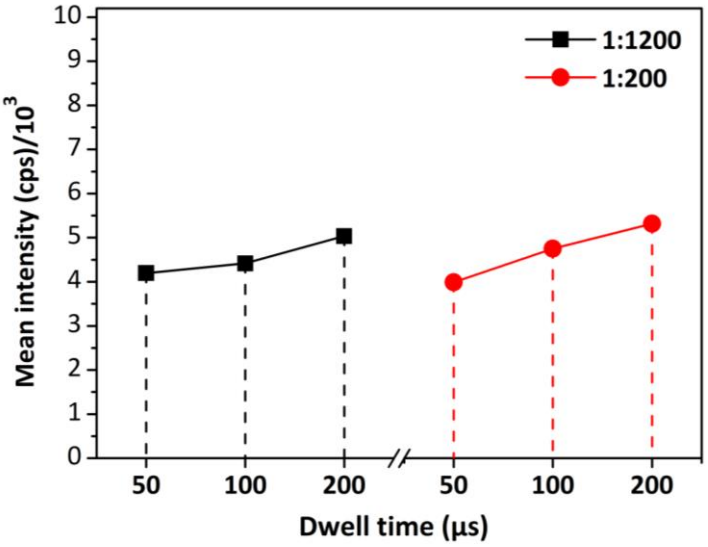

Figure S3.3. Effect of the dwell time on the titanium mean intensities (n=5). RSD values were lower than 1%.

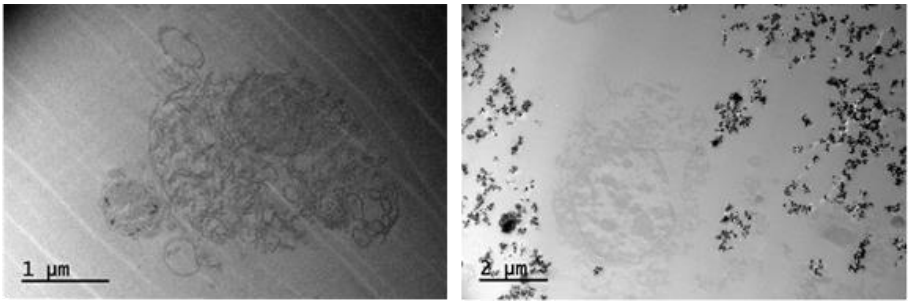

Figure S3.4. Complementary studies using Transmission Electron Microscopy: (left) cell clams, PVP-15 nm Ag NPs, 5 mg L^{-1} and (right) cell clams, CT-45 nm TiO_2 NPs, 5 mg L^{-1}.

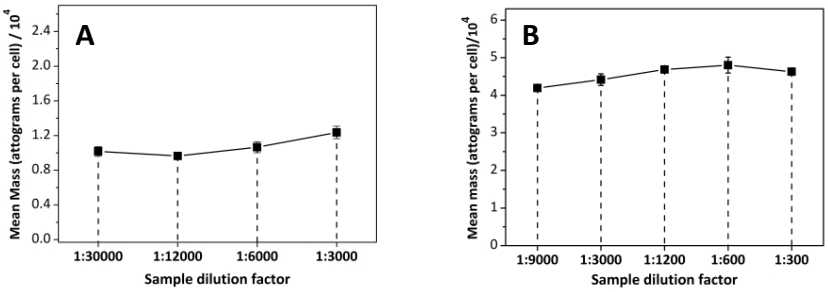

Figure S3.5. Effect of the cells concentration (n=3) on internalised silver (A) and titanium (B) contents. RSD values were lower than 3%.

Table S3.2. Theoretical Ag NPs internalization in mantle clam (*Ruditapes philippinarum*) cells.

	100nm, 5.0 μg mL^{-1}		100nm, 50 μg mL^{-1}	
Ag NPs per cell	Found peaks[a]	Percent. (%)	Found peaks[b]	Percent. (%)
< 100 nm	972	81.9	555	46.8
1	64	5.4	116	9.8
2	25	2.1	65	5.5
3	18	1.5	57	4.8
4	20	1.7	66	5.6
5	17	1.4	71	6.0
6	29	2.4	60	5.0
7	20	1.7	57	4.8
8	30	2.5	81	6.8
9	12	1.0	59	5.0

(a) Total number of peaks = 1207; (b) Total number of peaks = 1187

Table S3.3. Theoretical Ag NPs internalization in sea bass (*Dicentrarchus labrax*) kidney cells.

	100nm, 50 μg mL^{-1}		100nm, 100 μg mL^{-1}	
NPs per cell	Found peaks[a]	Percent. (%)	Found peaks[b]	Percent. (%)
<100nm	223	11.6	85	6.8
1	176	9.2	130	10.4
2	238	12.4	184	14.7
3	220	11.5	156	12.4
4	208	10.8	153	12.2
5	194	10.1	150	11.9
6	184	9.6	131	10.4
7	205	10.7	109	8.7
8	186	9.7	108	8.6
9	84	4.4	50	4.0

(a) Total number of peaks = 1918; (b) Total number of peaks = 1256

Table S3.4. Theoretical Ag NPs internalization in sea bream bream (*Sparus aurata*) kidney cells.

	100nm, 100 μg mL^{-1}		100nm, 50 μg mL^{-1}		100nm, 10 μg mL^{-1}	
NPs per cell	Found peaks[a]	Percent. (%)	Found peaks[b]	Percent. (%)	Found peaks[c]	Percent. (%)
<100nm	178	18.6	159	15.8	271	30.0
1	111	11.6	110	10.9	102	11.3
2	84	8.8	99	9.8	83	9.2
3	98	10.2	83	8.2	86	9.5
4	71	7.4	77	7.6	86	9.5
5	84	8.8	117	11.6	65	7.2
6	67	7.0	86	8.5	49	5.4
7	84	8.8	85	8.4	52	5.8
8	95	9.9	101	10.0	64	7.1
9	87	9.1	91	9.0	44	4.9

(a) Total number of peaks = 959; (b) Total number of peaks = 1108; (c) Total number of peaks = 902

Table S3.5. Theoretical TiO_2 NPs internalization in mantle clam (*Ruditapes philippinarum*) cells.

	25nm, 50 µg L^{-1}		5nm, 50 µg L^{-1}	
Femtograms per cell	Found peaks[a]	Percent. (%)	Found Peaks[b]	Percent. (%)
1.0 – 5.0	102	14.6	551	18.0
5.0 - 10	82	11.7	585	19.0
10 - 15	87	12.4	399	13.0
15 - 20	77	11.0	347	11.3
20 - 25	67	9.6	280	9.1
25 - 30	71	10.1	227	7.4
30 - 35	57	8.1	193	6.3
35 - 40	62	8.9	185	6.0
40 - 45	58	8.3	164	5.3
45 - 50	37	5.3	138	4.5

(a) Total number of peaks = 934; (b) Total number of peaks = 3132

Table S3.6. Theoretical TiO_2 NPs internalization in sea bass (*Dicentrarchus labrax*) kidney cells.

	25nm, 50 μg L^{-1}		5nm, 50 μg L^{-1}	
Femtograms per cell	Found peaks[a]	Percent. (%)	Found Peaks[b]	Percent. (%)
1.0 – 5.0	136	14.6	1056	31.7
50 - 10	111	11.9	533	16.0
10 - 15	111	11.9	381	11.4
15 - 20	91	9.7	333	10.0
20 - 25	85	9.1	259	7.8
25 - 30	93	10.0	201	6.0
30 - 35	82	8.8	191	5.7
35 - 40	89	9.5	157	4.7
40 - 45	77	8.2	118	3.5
45 - 50	59	6.3	102	3.1

(a) Total number of peaks = 934; (b) Total number of peaks = 3332

Table S3.7. Theoretical TiO_2 NPs internalization in sea bream (*Sparus aurata*) kidney cells.

	25nm, 10 μg L^{-1}		25nm, 50 μg L^{-1}		5nm, 10 μg L^{-1}		5nm, 50 μg L^{-1}	
Fg per cell	Found peaks[a]	Percent (%)	Found peaks[b]	Percent (%)	Found peaks[c]	Percent (%)	Found peaks[d]	Percent (%)
1.0-5.0	41.00	13.4	50	6.3	903	29.7	817	37.2
5.0-10	28.00	9.1	67	8.4	561	18.4	345	15.7
10-15	30.00	9.8	70	8.8	391	12.9	234	10.7
15-20	30.00	9.8	71	8.9	277	9.1	151	6.9
20-25	31.00	10.1	94	11.8	242	8.0	149	6.8
25-30	32.00	10.4	84	10.5	175	5.8	129	5.9
30-35	31.00	10.1	92	11.5	169	5.6	106	4.8
35-40	33.00	10.8	99	12.4	133	4.4	110	5.0
40-45	24.00	7.8	88	11.0	125	4.1	80	3.6
45-50	27	8.8	82	10.3	67	2.2	75	3.4

(a) Total number of peaks = 307; (b) Total number of peaks = 797;
(c) Total number of peaks = 3043; (d) Total number of peaks = 2196

REFERENCES

[1] A. Weir, P. Westerhoff, L. Fabricius, K. Hristovski, N. Von Goetz, Titanium dioxide nanoparticles in food and personal care products, Environ. Sci. Technol. 46 (2012) 2242–2250. https://doi.org/10.1021/es204168d.

[2] V. Sogne, F. Meier, T. Klein, C. Contado, Investigation of zinc oxide particles in cosmetic products by means of centrifugal and asymmetrical flow field-flow fractionation, J. Chromatogr. A. 1515 (2017) 196–208. https://doi.org/10.1016/j.chroma.2017.07.098.

[3] A.M. Alkilany, L.B. Thompson, S.P. Boulos, P.N. Sisco, C.J. Murphy, Gold nanorods: Their potential for photothermal therapeutics and drug delivery, tempered by the complexity of their biological interactions, Adv. Drug Deliv. Rev. 64 (2012) 190–199. https://doi.org/10.1016/j.addr.2011.03.005.

[4] P. Van Broekhuizen, F. Van Broekhuizen, R. Cornelissen, L. Reijnders, Use of nanomaterials in the European construction industry and some occupational health aspects thereof, J. Nanoparticle Res. 13 (2011) 447–462. https://doi.org/10.1007/s11051-010-0195-9.

[5] M.E. Vance, T. Kuiken, E.P. Vejerano, S.P. McGinnis, M.F. Hochella, D.R. Hull, Nanotechnology in the real world: redeveloping the nanomaterial consumer products inventory, Beilstein J. Nanotechnol. 6 (2015) 1769–1780. https://doi.org/10.3762/bjnano.6.181.

[6] S.J. Klaine, P.J.J. Alvarez, G.E. Batley, T.F. Fernandes, R.D. Handy, D.Y. Lyon, S. Mahendra, M.J. McLaughlin, J.R. Lead, Nanomaterials in the environment: behavior, fate, bioavailability, and effects, Environ. Toxicol. Chem. 27 (2008) 1825–1851. https://doi.org/10.1897/08-090.1.

[7] S.H. Joo, D. Zhao, Environmental dynamics of metal oxide nanoparticles in heterogeneous systems: a review, J. Hazard. Mater. 322 (2017) 29–47. https://doi.org/10.1016/j.jhazmat.2016.02.068.

[8] A. Wiesenthal, L. Hunter, S. Wang, J. Wickliffe, M. Wilkerson, Nanoparticles: small and mighty, Int. J. Dermatol. 50 (2011) 247–254. https://doi.org/10.1111/j.1365- 4632.2010.04815.x.

[9] A. Syafiuddin, Salmiati, M.R. Salim, A. Beng Hong Kueh, T. Hadibarata, H. Nur, A review of silver nanoparticles: research trends, global consumption, synthesis, properties, and future challenges, J. Chinese Chem. Soc. 64 (2017) 732–756. https://doi.org/10.1002/jccs.201700067.

[10] X.F. Zhang, Z.G. Liu, W. Shen, S. Gurunathan, Silver nanoparticles: synthesis, characterization, properties, applications, and therapeutic approaches, Int. J. Mol. Sci. 17 (2016) 1534. https://doi.org/10.3390/ijms17091534.

[11] R.L. Naylor, R.W. Hardy, A.H. Buschmann, S.R. Bush, L. Cao, D.H. Klinger, D.C. Little, J. Lubchenco, S.E. Shumway, M. Troell, A 20-year retrospective review of global aquaculture, Nature. 591 (2021) 551–563. https://doi.org/10.1038/s41586-021-03308-6.

[12] C.E. Boyd, L.R. D'Abramo, B.D. Glencross, D.C. Huyben, L.M. Juarez, G.S. Lockwood, A.A. McNevin, A.G.J. Tacon, F. Teletchea, J.R. Tomasso, C.S. Tucker, W.C. Valenti, Achieving sustainable aquaculture: historical and current perspectives and future needs and challenges, J. World Aquac. Soc. 51 (2020) 578–633. https://doi.org/10.1111/jwas.12714.

[13] M. Auffan, J. Rose, M.R. Wiesner, J.Y. Bottero, Chemical stability of metallic nanoparticles: a parameter controlling their potential cellular toxicity in vitro, Environ. Pollut. 157 (2009) 1127–1133. https://doi.org/10.1016/j.envpol.2008.10.002.

[14] K. Aschberger, C. Micheletti, B. Sokull-Klüttgen, F.M. Christensen, Analysis of currently available data for characterising the risk of engineered nanomaterials to the environment and human health - Lessons learned from four case studies, Environ. Int. 37 (2011) 1143–1156. https://doi.org/10.1016/j.envint.2011.02.005.

[15] F. Perreault, A. Oukarroum, S.P. Melegari, W.G. Matias, R. Popovic, Polymer coating of copper oxide nanoparticles increases nanoparticles uptake and toxicity in the green alga Chlamydomonas reinhardtii, Chemosphere. 87 (2012) 1388–1394. https://doi.org/10.1016/j.chemosphere.2012.02.046.

[16] M. Corte-Rodríguez, R. Álvarez-Fernández, P. García-Cancela, M. Montes-Bayón, J. Bettmer, Single cell ICP-MS using on line sample introduction systems: current developments and remaining challenges, TrAC - Trends Anal. Chem. 132 (2020) 116042. https://doi.org/10.1016/j.trac.2020.116042.

[17] S. Meyer, A. López-Serrano, H. Mitze, N. Jakubowski, T. Schwerdtle, Single-cell analysis by ICP-MS/MS as a fast tool for cellular bioavailability studies of arsenite, Metallomics. 10 (2018) 73–76. https://doi.org/10.1039/c7mt00285h.

[18] Y. Cao, J. Feng, L. Tang, C. Yu, G. Mo, B. Deng, A highly efficient introduction system for single cell - ICP-MS and its application to detection of copper in single human red blood cells, Talanta. 206 (2020) 120174. https://doi.org/10.1016/j.talanta.2019.120174

[19] T.A. Marschall, J. Bornhorst, D. Kuehnelt, T. Schwerdtle, Differing cytotoxicity and bioavailability of selenite, methylselenocysteine, selenomethionine, selenosugar 1 and trimethylselenonium ion and their underlying metabolic transformations in human cells, Mol. Nutr. Food Res. 60 (2016) 2622–2632. https://doi.org/10.1002/mnfr.201600422.

[20] X. Shen, H. Zhang, X. He, H. Shi, C. Stephan, H. Jiang, C. Wan, T. Eichholz, Evaluating the treatment effectiveness of copper-based algaecides on toxic algae Microcystis aeruginosa using single cell-inductively coupled plasma-mass spectrometry, Anal. Bioanal. Chem. 411 (2019) 5531–5543. https://doi.org/10.1007/s00216-019- 01933-9.

[21] M. Corte Rodríguez, R. Álvarez-Fernández García, E. Blanco, J. Bettmer, M. Montes- Bayón, Quantitative evaluation of cisplatin uptake in sensitive and resistant individual cells by single-cell ICP-MS (SC-ICP-MS), Anal. Chem. 89 (2017) 11491–11497. https://doi.org/10.1021/acs.analchem.7b02746.

[22] X. Wei, D.H. Zheng, Y. Cai, R. Jiang, M.L. Chen, T. Yang, Z.R. Xu, Y.L. Yu, J.H. Wang, High-throughput/high-precision sampling of single cells into ICP-MS for elucidating cellular nanoparticles, Anal. Chem. 90 (2018) 14543–14550. https://doi.org/10.1021/acs.analchem.8b04471.

[23] X. Wei, X. Zhang, R. Guo, M.L. Chen, T. Yang, Z.R. Xu, J.H. Wang, A spiral-helix (3D) tubing array that ensures ultrahigh-throughput single-cell sampling, Anal. Chem. 91 (2019) 15826–15832. https://doi.org/10.1021/acs.analchem.9b04122

[24] H. Wang, B. Chen, M. He, X. Li, P. Chen, B. Hu, Study on uptake of gold nanoparticles by single cells using droplet microfluidic chip-inductively coupled plasma mass spectrometry, Talanta. 200 (2019) 398–407. https://doi.org/10.1016/j.talanta.2019.03.075.

[25] X. Yu, B. Chen, M. He, H. Wang, B. Hu, 3D droplet-based microfluidic device easily assembled from commercially available modules online coupled with ICPMS for determination of silver in single cell, Anal. Chem. (2019). https://doi.org/10.1021/acs.analchem.8b04844

[26] A. López-Serrano Oliver, S. Baumgart, W. Bremser, S. Flemig, D. Wittke, A. Grützkau, A. Luch, A. Haase, N. Jakubowski, Quantification of silver nanoparticles taken up by single cells using

inductively coupled plasma mass spectrometry in the single cell measurement mode, J. Anal. At. Spectrom. 33 (2018) 1256–1263. https://doi.org/10.1039/c7ja00395a.

[27] R. Álvarez-Fernández García, M. Corte-Rodríguez, M. Macke, K.L. Leblanc, Z. Mester, M. Montes-Bayón, J. Bettmer, Addressing the presence of biogenic selenium nanoparticles in yeast cells: analytical strategies based on ICP-TQ-MS, Analyst. 145 (2020) 1457–1465. https://doi.org/10.1039/c9an01565e.

[28] H. Wang, B. Chen, M. He, B. Hu, A facile droplet-chip-time-resolved inductively coupled plasma mass spectrometry online system for determination of zinc in single cell, Anal. Chem. 89 (2017) 4931–4938. https://doi.org/10.1021/acs.analchem.7b00134.

[29] B. Gomez-Gomez, M. Corte-Rodríguez, M.T. Perez-Corona, J. Bettmer, M. Montes- Bayón, Y. Madrid, Combined single cell and single particle ICP-TQ-MS analysis to quantitatively evaluate the uptake and biotransformation of tellurium nanoparticles in bacteria, Anal. Chim. Acta. 1128 (2020) 116–128. https://doi.org/10.1016/j.aca.2020.06.058.

[30] L.N. Zheng, M. Wang, B. Wang, H.Q. Chen, O. Hong, Y.L. Zhao, Z.F. Chai, W.Y. Feng, Determination of quantum dots in single cells by inductively coupled plasma mass spectrometry, Talanta. 116 (2013) 782–787. https://doi.org/10.1016/j.talanta.2013.07.075.

[31] E. Bolea-Fernandez, D. Leite, A. Rua-Ibarz, L. Balcaen, M. Aramendía, M. Resano, F. Vanhaecke, Characterization of SiO2 nanoparticles by single particle-inductively coupled plasma-tandem mass spectrometry (SP-ICP-MS/MS), J. Anal. At. Spectrom. 32 (2017) 2140–2152. https://doi.org/10.1039/c7ja00138j.

[32] S. Candás-Zapico, D.J. Kutscher, M. Montes-Bayón, J. Bettmer, Single particle analysis of TiO2 in candy products using triple quadrupole ICP-MS, Talanta 180 (2018) 309-315. https://doi.org/10.1016/j.talanta.2017.12.041.

[33] C. Suárez-Oubiña, P. Herbello-Hermelo, P. Bermejo-Barrera, A. Moreda-Piñeiro, Exploiting dynamic reaction cell technology for removal of spectral interferences in the assessment of Ag, Cu, Ti, and Zn by inductively coupled plasma mass spectrometry, Spectrochim. Acta - Part B At. Spectrosc. 187 (2022) 106330. https://doi.org/10.1016/j.sab.2021.106330.

[34] C. Suárez-Oubiña, P. Herbello-Hermelo, P. Bermejo-Barrera, A. Moreda-Piñeiro, Single-particle inductively coupled plasma mass spectrometry using ammonia reaction gas as a reliable and free-interference determination of metallic nanoparticles, Talanta. 242 (2022) 123286. https://doi.org/10.1016/j.talanta.2022.123286.

[35] H.E. Pace, N.J. Rogers, C. Jarolimek, V.A. Coleman, C.P. Higgins, J.F. Ranville, Erratum: Determining transport efficiency for the purpose of counting and sizing nanoparticles via single particle inductively coupled plasma mass spectrometry, Anal. Chem. 84 (2012) 4633. https://doi.org/10.1021/ac300942m.

[36] Z. Liu, A. Xue, H. Chen, S. Li, Quantitative determination of trace metals in single yeast cells by time-resolved ICP-MS using dissolved standards for calibration, Appl. Microbiol. Biotechnol. 103 (2019) 1475–1483. https://doi.org/10.1007/s00253-018-09587-w.

[37] E. Bolea-Fernandez, D. Leite, A. Rua-Ibarz, T. Liu, G. Woods, M. Aramendia, M. Resano, F. Vanhaecke, On the effect of using collision/reaction cell (CRC) technology in single-particle ICP-mass spectrometry (SP-ICP-MS), Anal. Chim. Acta. 1077 (2019) 95–106. https://doi.org/10.1016/j.aca.2019.05.077.

[38] F. Wu, Z. Xie, M. Yan, Q. Li, J. Song, M. Hu, Y. Wang, Classification and characterization of hemocytes from two Asian horseshoe crab species Tachypleus tridentatus and Carcinoscorpius rotundicauda, Sci. Rep. 9 (2019) 1–10. https://doi.org/10.1038/s41598-019-43630-8.

[39] E. Falcieri, A. Bassini, S. Pierpaoli, F. Luchetti, L. Zamai, M. Vitale, L. Guidotti, G. Zauli, Ultrastructural characterization of maturation, platelet release, and senescence of human cultured megakaryocytes, Anat. Rec. 258 (2000) 90–99. https://doi.org/10.1002/(sici)1097-0185(20000101)258:1<90::aid-ar10>3.0.co;2-g.

[40] K. Sasaki, G. Matsumura, Mononuclear cells in the extraembryonic and intraembryonic coelom of the mouse embryo: a semithin light microscopic cytometry, Arch. Histol. Cytol. 52 (1989) 421–426. https://doi.org/10.1679/aohc.52.421.

[41] M. Riisom, B. Gammelgaard, I.H. Lambert, S. Stürup, Development and validation of an ICP-MS method for quantification of total carbon and platinum in cell samples and comparison of open-vessel and microwave-assisted acid digestion methods, J. Pharm. Biomed. Anal. 158 (2018) 144–150. https://doi.org/10.1016/j.jpba.2018.05.038.

[42] A.C. Quevedo, I. Lynch, E. Valsami-Jones, Mechanisms of silver nanoparticle uptake by embryonic zebrafish cells, Nanomaterials. 11 (2021) 2699. https://doi.org/10.3390/nano11102699.

[43] Y. Yue, X. Li, L. Sigg, M.J.F. Suter, S. Pillai, R. Behra, K. Schirmer, Interaction of silver nanoparticles with algae and fish cells: A side by side comparison, J. Nanobiotechnology. 15 (2017) 1–11. https://doi.org/10.1186/s12951-017-0254-9.

CHAPTER 4

BIOACCUMULATION AND HUMAN RISK ASSESSMENT OF INORGANIC NANOPARTICLES IN AQUACULTURE SPECIES

CHAPTER 4. BIOACCUMULATION AND HUMAN RISK ASSESSMENT OF INORGANIC NANOPARTICLES IN AQUACULTURE SPECIES

4.1 ABSTRACT

The widespread use of nanomaterials, especially inorganic nanoparticles (NPs), has raised concerns about their potential toxicity due to their release into the environment and, consequently, the risk to humans and the marine ecosystem. The assessment of the degree of NPs uptake by marine and freshwater biota is challenging because NPs are emerging pollutants and few studies regarding NPs biomagnification in the food chain have been reported. Knowledge of potential NPs bioaccumulation in marine biota, mainly in aquaculture species, is important since human consumption of aquaculture species constitutes an important part of the human diet. Exposure experiments were performed in aquaculture species (sea bream, sea bass, and Japanese carpet shell) using dietary exposure of titanium dioxide nanoparticles (TiO_2 NPs) and silver nanoparticles (Ag NPs) by setting different exposure times and NPs concentrations. Target organs such as liver, kidney, and muscle (flesh) from sea bass and sea bream were analysed in order to provide comprehensive data regarding NPs bioaccumulation. Additionally, information on food safety and human bioavailability (*in vitro* Caco-2 model for simulating human gastro-intestinal digestion) when consuming aquaculture products was accomplished.

4.2 INTRODUCTION

Nanotechnology is now an emerging area of study with many applications in science and technology. According to the European Commission (EC) the term ―nanomaterial‖ embraces all materials specified by EC Recommendation 2022/C229/01 of 10 June 2022 as ―a natural, incidental or manufactured material consisting of solid

particles that are present, either on their own or as identifiable constituent particles in aggregates or agglomerates, and where 50% or more of these particles in the number‖ (European Comission (C229/01), 2022). The group of most extended NPs includes silver nanoparticles (Ag NPs) and titanium dioxide nanoparticles (TiO_2 NPs) [2–5], the first due to their antimicrobial properties are often used in a variety of fields as medicine or textile industries [6–8]; and the latter because of UV absorption and scattering characteristics [9–11].

Due to the large-scale production and use of NPs their release and presence in the environment is expected. However, studies are required to evaluate the environmental risk associated by these novel pollutants in terms of uptake and biological impact. In addition, the true impacts of the presence of NPs in the aquatic environment are yet unknown and difficult to assess because the released NPs vary their characteristics when being in the aquatic environment [12]. Chemical composition, size, shape, surface coating or modification, solubility properties, and other physical and chemical properties are important factors that may influence how dangerous NPs are [13,14]. To increase the available data about the possible toxicity of NPs, three key terms— bioaccumulation, bio-accessibility, and bioavailability— have gained significant importance in recent years. Bioaccumulation can be defined as the build-up of chemicals, usually harmful, in the body of an organism from different exposure sources (mainly water, air, and diet) that are not metabolized or excreted, and consequently accumulate in the organisms over time. Regarding human consumption, the term bioavailability names the fraction of a compound that can be taken up by the body, entering the circulation and being able to have an active effect, whereas bio- accessibility refers to the fraction of a compound that is released from the food matrix in the gastrointestinal tract and consequently, is available for absorption. The knowledge of these three parameters enable to assess the risk related to pollutants in the environment and humans. Caco-2 cells are typically used as a model to perform bioavailability studies since they are derived from human colorectal adenocarcinoma and exhibit remarkable morphological and physiological similarities to the human intestine [15]. Previous studies with Caco-2 cultures and Caco-

2/HT29 cultures for transcellular transport and uptake of NPs can be found elsewhere [16–19].

Regarding marine organisms, the small size and rapid development of zebrafish embryos make these species the preferred candidates for bioaccumulation studies [20]. In addition, some investigations have been conducted in fish organs, such as rainbow trout [21], goldfish [22,23], and zebrafish [24], which have shown potential toxicity and effective bioaccumulation after NPs exposure. Other studies have stated that gills, intestine, liver, and brain are the most affected organs in fish species. Oxidative stress is a potential mechanism of NPs toxicity in fish, as well as the induction of new enzymes involved in antioxidant defences [25]. However, the concentration of metals and NPs in the natural environment (especially in the aquatic environment) is quite low, far from the high dose conditions required for acute toxicity testing.

Aquaculture has emerged as a possible response to the requirement of an effective production of protein to meet the demands of an anticipated global population, as well as declining fish stocks worldwide [26,27]. Despite the variety of cultured species that are produced in aquaculture facilities, global aquaculture production today continues to be heavily weighted by the production of only a few species [28,29]. The top three fish species in marine aquaculture [gilthead seabream (*Sparus aurata*), European sea bass (*Dicentrarchus labrax*), and Japanese amberjack (*Seriola quinqueradiata*)] have accounted for about 40% of the world's production in 2013 [30].

The aim of this research has been the evaluation of Ag NPs and TiO_2 NPs bioaccumulation in cultured fish sea bass (*Dicentrarchus labrax*) and sea bream (*Sparus aurata*), and in Japanese carpet shell (*Ruditapes philippinarum*) through controlled-NPs exposure experiments. The total amount of Ag and Ti was determined by inductively coupled plasma – mass spectrometry (ICP-MS) after microwave-assisted acid digestion as a sample pre-treatment, whereas Ag NPs and TiO_2 NPs were determined/characterised by single particle ICP-MS (spICP-MS) after enzymatic hydrolysis for NPs isolation. In addition, *in-vitro* bio-accessibility and bioavailability

(Caco-2 cells model for transcellular transport assessment) assays were used to obtain information regarding the human risk assessment. Both ICP-MS and spICP-MS have been used for determining total Ag and Ti, and for assessing/characterising Ag NPs and TiO_2 NP, respectively, in the bio-accessible fractions and in the basolateral and apical solutions from the *in vitro* Caco-2 assays. Novel approaches based on using ammonia as a reaction gas (Ti based ammonia-cluster at mass-charge ratio of 131) were used to remove Ti isobaric interferences in ICP-MS and sp-ICP-MS determinations [31,32].

4.3 EXPERIMENTAL

4.3.1 Instrumentation

Measurements were performed with a NexION 2000 inductively coupled plasma mass spectrometer (PerkinElmer, Waltham, MA, USA) with dynamic reaction cell (DRC) technology. The instrument is equipped with triple nickel cone interface, a concentric Meinhard™ type nebulizer coupled to a cyclonic spray chamber (Glass Expansion, Inc., Melbourne, Australia) and attached to a quartz torch with a 2.5 mm i.d. quartz injector tube. Data acquisition and management was performed with Syngistix™ Nano Application 2.5 version software (PerkinElmer), which allows data visualization and acquisition in real-time and displays background-corrected intensity histograms which continuously updates during data acquisition. An USC-TH ultrasound water bath (45 Hz, 80 W) from VWR International Eurolab S.L (Barcelona, Spain) was used for dispersing NPs before analysis. An Ethos Easy Advanced Microwave Digestion System (Milestone, Sorisole, Italy) with 100 mL closed Teflon vessels and Teflon covers were used for assisting the acid digestion procedure. *In vitro* digestion (bio-accessibility) was performed in a Boxcult temperature-controlled chamber (Stuart Scientific, Surrey, UK) with a Rotabit orbital-rocking platform shaker (J.P. Selecta, Barcelona, Spain). Freezing point Osmometer model K-7400S (Knauer, Berlin, Germany) was used for adjusting the osmolarity of the bio-accessible fraction. Millicell ERS-2 (Millipore Co., Bedford, MA, USA) and FLUOstar OPTIMA fluorimeter Microplate reader (BMG Labtech, Leicester, UK) were used for verifying Caco-2 cell integrity. All operations were

performed inside a SMH-100 laminar flow cupboard from Telstar (Tarrasa, Spain). Other equipment used were an icoMed incubator with controlled atmosphere for cell culturing (Memmert, Schwabach, Germany), a pH- meter model Instruments XS (Carpi Mo, Italy), a Raypa UCI-150 ultrasonic cleaner water-bath (ultrasound frequencies of 17 and 35 kHz, 325 W) from R. Espinar S.L. (Barcelona, Spain), a Laborcentrifugen 2K15 centrifuge (Sigma, Osterode, Germany), a heating bath and a 2000209 oven from J.P. Selecta.

4.3.2 Material and reagents

All solutions were prepared with ultrapure water (18.2 MΩ cm of resistivity) obtained from a Milli- Q® IQ 7003 purification device system (Millipore). Mono-elemental 1000 mg L^{-1} standards of titanium [$(NH_4)_2TiF_6$] and silver ($AgNO_3$) were from Merck (Darmstadt, Germany). Gold NPs solutions were prepared from a N8151035 (49.6 nm by TEM, 12.4 ng mL^{-1}, 9.89×10^6 NPs mL^{-1}, in 1.0 mM aqueous citrate) certified reference material from nanoComposix (San Diego, CA, USA). Argon (99.999%) and ammonia (99.999%) were from Nippon Gases (Madrid, Spain). NexION Setup Solution (10 µg L^{-1} Be, Ce, Fe, In, Li, Mg, Pb, U in HNO_3 1%) was from Perkin Elmer. Pepsin from porcine gastric mucosa, pancreatin from porcine pancreas, lipase from *Candida rugose* and bile salts were from Sigma Aldrich (Osterode, Germany). Hydrochloric acid (37%) was from Merck, and sodium hydrogen carbonate from Panreac (Barcelona, Spain). Minisart™ NML syringe filters (5µm pore size) were from Sartorius (Goettingen, Germany). Commercial fish feed pellets were from Biomar Iberia, S.A. (Palencia, Spain). Micronized calcium carbonated was from C.T.S. España S.L. (Madrid, Spain). Caco-2 cells, Lucifer Yellow, and Hanks' Balanced Salt Solution (HBSS) were from Sigma Aldrich. Phosphate-Buffered Saline (PBS (1x)) was from Thermo Fisher (Dublin, Ireland). Dulbecco's Modified Eagle Medium (DMEM), trypsin (3x) and six-well Transwell® (24 mm diameter, 0.4 µm pore size polyester membrane) were from Corning (New York, USA). Sterilin black 96-well microtiter plates (400 µL) were from Thermo Fisher. Other

reagents were 99.5% glycerol, sodium chloride, and D-(+)-glucose from Sigma Aldrich, and 33% (w/v) hydrogen peroxide and 69% (w/v) hyperpure nitric acid from Panreac. To avoid metal contamination, all glassware and plastic ware were washed with ultrapure water and kept in 10% (v/v) HNO_3 for 48 h, and then rinsed several times with ultrapure water before use.

4.3.3 Sea bream, sea bass and Japanese carpet shell exposure trials and sample preparation

Exposure trials for sea bass (*Dicentrarchus labrax*), sea bream (*Sparus aurata*), and Japanese carpet shell (*Ruditapes philippinarum*) with NPs were carried out by personnel qualified in animal experimentation, in authorized facilities of Centro Tecnológico de Acuicultura, CETGA (Ribeira, A Coruña, Spain). All experimental procedures were carried out in accordance with European Union and Spanish Regulations (Council Directive 2010/63/EU (European Union, 2010) and R.D. 53/2013 (BOE, 2013), respectively), for the protection of animals used for experimental purposes. Commercial fish feed pellets were used for feeding seabreams and seabass along the bioaccumulation assay (Biomar Iberia, S.A.). Titanium dioxide NPs and Ag NPs were incorporated to food following the method described in previous investigations [33]: first, a premixture was prepared by combining micronized calcium carbonated and TiO_2 NPs or Ag NPs NPs at an equivalent of 5% of the weight of pellets. The premixture was then added to commercial fish feed pellets for pellet coating until achieving 0.25, 0.75, and 1.5 mg kg^{-1} of fish per day. Feed used in the control group (unexposed specimens) was also coated with micronized $CaCO_3$ but without NPs.

Sea bass specimens (fifty individuals in each tank, average initial weight of 121.6 g) were kept in open circuit 400 L open circuit tanks and exposed to 100 nm Ag NPs (PVP coating) for 90 days. Similarly, sea bream (one hundred and twenty individuals in each tank, average initial weight of 7.7 g) were kept in 300 L f and were exposed to 45 nm TiO_2 NPs (citrate coating) for 90 days. Sampling was performed each 15 days obtaining exposure times of 0 (experiment beginning), 15, 30, 45, 60, 75, and 90 days. Different exposure NPs concentrations

were tested for both cultured species: 0 (control tanks), and 0.25, 0.75 and 1.5 mg kg^{-1} (concentration referred as the mg of Ag NPs or TiO_2 NPs per kg of fish). Fish were fed at a daily feeding rate of 0.7-1% for sea bass and of 2.5-3% for sea bream. Each NPs concentration condition was replicated three times (three different tanks for control and each tested concentration). At the end of the experiment (after 90 days), the specimens were fasted for one day before being killed with an overdose of anaesthetic and exsanguination. Finally, the specimens were dissected and divided in muscle-skin, liver, and kidney, obtaining three replicates (three tanks) for each NPs concentration exposure and time. The samples were frozen and preserved at -20ºC until their analysis. Data regarding weight and growth parameters for sea bass and sea bream are given in Electronic Supplementary Information (ESI).

Japanese carpet shell specimens (forty individuals in each tank) were kept in 50 L close circuit tanks (50% water renewal on Monday and Friday, and 100% on Wednesday) and exposed to 100 nm Ag NPs (PVP coating) or 45 nm TiO_2 NPs (citrate coating) for 28 days. Parameters such as pH, temperature, salinity and O_2 content were daily monitored. Carpet shells were fed with microalgae mixture (*Isochrysis galbana* (T-ISO) and *Phaeodactylum tricornutum* (50:50, v/v)) on Monday, Wednesday and Friday and NPs were added together with the feed on Wednesday. Different exposure NPs concentrations were tested: 0 (control tanks), and 0.10 and 1.0 mg L^{-1} (each NPs concentration condition was replicated three times (three different tanks for control and each tested concentration). Sampling was performed each 7 days (on Wednesday) obtaining exposure times of 0 (experiment beginning), 7, 14, 21, and 28 days. Data regarding weight, as well as shell length for Japanese carpet shells throughout the exposure trial are included in ESI.

4.3.4 Microwave assisted acid digestion

Muscle-skin samples, approximately 1.000 g of homogenised tissue (manually homogenized before storing) were subjected to microwave assisted acid digestion in triplicate, whereas only one replicate of liver and kidney tissues (0.1500 g) per specimen was used

for digestion (small sample size). Regarding clams, also 1.000 g of homogenised wet tissue was subjected to the digestion procedure in triplicate (three carpet shells from each tank and exposure condition). Therefore, total Ag and Ti concentrations were referred to nine replicates for sea bass and sea bream muscle-skin, and for Japanese carpet shell (three subsamples from each specimen, and three specimens – three tanks) and to three replicates for sea bass and sea bream liver and kidney (one subsample from each specimen, and three specimens – three tanks). Digestion was performed with 4.0 mL of ultrapure water, 3.0 mL of 69% (w/v) HNO_3 and 1.0 mL of 33% (w/v) H_2O_2, and with a microwave program of four stages operating at 1800 W: a first heating ramp from room temperature to 100°C for 5 min, a second heating ramp from 100 to 170°C for 10 min, a third heating ramp from 170 to 220°C for 10 min, and a final heating stage at 220°C for 10 min. Two blanks were obtained in each microwave set of samples. After cold-down, acid digests were made up to 25 mL with ultrapure water, and they were kept in clean plastic tubes at room temperature prior to ICP-MS measurements.

4.3.5 Enzymatic hydrolysis for Ag and TiO_2 NPs extraction

Enzymatic hydrolysis procedures were based on previously developments [34][35] with slight modifications. The procedure consists of weighting approximately 1.00 g of homogenized seafood tissue and adding 7.5 mL of a daily prepared pancreatin-lipase solution (3.0 g L^{-1} each one for Ag NPs isolation, and 8.0 g L^{-1} each one for TiO_2 NPs isolation, dissolved in 0.2 M NaH_2PO_4/0.2 M NaOH, pH 7.4). The mixtures were then stirred (orbital- horizontal shaking) at 37°C and 150 rpm (Ag NPs isolation) and 200 rpm (TiO_2 NPs isolation) for 12 h. After enzymatic hydrolysis, the mixtures were passed through 5.0 µm pore size filters and the filtrate were made up to 10 mL with water. Three blanks were performed for each set of sample preparation. The enzymatic extracts were stored at 4°C and they analysed in the same day.

4.3.6 Culinary treatments: grilling and boiling

Sea bream tissues from the specimens exposed to the highest TiO_2 NPs concentration and Japanese carpet shell tissues which offered the highest TiO_2 NPs and Ag NPs concentrations (bioaccumulation trials) were selected to study the impact of culinary methods on the amount of bioaccumulated NPs in the seafood tissues and on the NPs bio-accessibility/bioavailability. Grilling and boiling were selected as the most common procedures to cook seafood products and both culinary treatments were carried out without using oil and spices. In accordance with the literature [36], grilling treatment was done for 5.0 min, maintaining the heat until the samples (sea bream's muscle-skin and pooled Japanese carpet shell) were completely cooked. Then the grilled samples were left to cool at room temperature before being stored at -20^{o}C. Boiling procedure for sea bream's flesh was carried out by applying heat to 300 mL of ultrapure water inside a cooking pot. Temperature (boiling temperature within the 90-100^{o}C range) was controlled with a thermometer, and once the boiling temperature was achieved, the fish tissues were immersed a cooked for 10 min. Then, samples were placed onto Petri dishes and left to cool at room temperature and then at 30- 40^{o}C in an oven to dry the cooked sample.

4.3.7 *In-vitro* digestion procedure: bio-accessibility assays

An *in vitro* digestion approach that replicated the environment of the stomach and intestines in two phases was used to model the human gastrointestinal process [37]. The homogenized seafood tissue (0.50 g of raw or cocked sample) was mixed with 20 mL of ultrapure water in an Erlenmeyer flask and after a few minutes of stabilization the pH was adjusted at 2.0 (gastric pH) by adding dropwise 0.1 M hydrochloric acid. Then, 0.15 g of gastric solution (16 g of pepsin in 100 mL of 0.1 M hydrochloric acid) was added, and the flask was covered with Parafilm® and placed in the Boxcult temperature-controlled chamber for gastric digestion (37 °C and orbital-horizontal shaking at 150 rpm for 2.0 h).

The enzymatic activity in the gastric digest was stopped by immersing the flask in an ice-water bath, and the pH of the mixture was then adjusted at 7.0. (0.1 M sodium hydroxide dropwise)

followed by adding the intestinal solution (4.0 g pancreatin and 25 g bile salts in 1.0 L of 0.1 M sodium dihydrogen carbonate). The intestinal digestion was then performed at 37 °C and orbital-horizontal shaking at 150 rpm for 2.0 h. The enzymatic digests were allowed to cold-down in an ice bath. The bio-accessible fraction was obtained after enzymatic digest filtration (5.0 µm filters) and they were stored in polyethylene tubes at -20 °C until analysis. Each fish sample was subjected to the enzymatic procedure in duplicate and at one reagent blank was also prepared.

4.3.8 Caco-2 cellular transport assays

4.3.8.1 Caco-2 cell monolayer development

Caco-2 cells were maintained in DMEM containing 10% (v/v) fetal bovine serum, 2 mM L- glutamine, 1% (v/v) penicillin/streptomycin, 1 mM sodium pyruvate, and 1 mM non-essential amino acids (NEAA) at 37 °C in a controlled environment with 95% relative humidity and a 5% CO_2 flow. The medium was changed every two or three days until 80% confluence was reached. A trypsin solution (0.5 g L^{-1}) was then used to detach the cells before resuspension in DMEM. Caco-2 cells were seeded (7.5×10^4 cells cm^{-2}) on polyester membrane inserts in 6-well Transwell plates. The insert divides the well into two compartments: the bottom (basolateral chamber) which represents the serous cavity, and the top (apical chamber) which represents the intestinal lumen. Resuspended cells (1.5 mL) were introduced in the apical chamber whereas 2.0 mL of DMEM were placed in the basolateral chamber. The Transwell plates are then placed in a temperature-controlled environment (37 °C, 95% relative humidity, and 5% CO_2 flow, medium changing every three days) to generate a Caco-2 monolayer. A value of 250 Ω cm^2 of transepithelial electrical resistance (TEER) was required for a proper Caco-2 monolayer development.

4.3.8.2 Cellular transport

Before bio-accessible fraction loading on the developed Caco-2 monolayer, 7.5 mL of the bio- accessible fraction (section 2.7.) was heated at 100 °C for 10 min in a water bath to denature the

remaining gastrointestinal enzymes and the osmolarity of the solution was adjusted to 280-300 mΩ cm^2 by adding 1.0 g L^{-1} of glucose and 10 mM sodium chloride dropwise. A volume of 1.5 mL of treated bio-accessible fraction and Lucifer Yellow were added to the apical chamber and 2.0 mL of HBSS were added to the basolateral chamber for cellular transport assay. Identical temperature, humidity, and CO_2 conditions than those used for Caco-2 monolayer development were set, and cellular transport was performed for 2.0 h. The basolateral and apical solutions were carefully removed and kept for analysis. Each bio-accessible fraction was subjected to the cellular transport procedure in triplicate which allows six independent measurements (two bio-accessible fractions per sample). At least two blanks were subjected to the same process in each set of samples.

4.3.9 ICP-MS measurements

The determination of the total Ag and Ti contents in the acid digests, bio-accessible fractions and apical and basolateral were performed under the ICP-MS operating conditions detailed in the **Table 4.1**. Daily performance was assessed by monitoring and verifying intensities of Be, In, U, and Ce as well as a background (mass-to-charge ratio of 202), and Ce^{++}/Ce and CeO/Ce ratios. Rhodium was used as an internal standard for Ag determination under KED work-mode which used Helium 4.5mL min^{-1} as a collision gas, whereas scandium was the selected internal standard for Ti determination under Dynamic Reaction Cell technology by using ammonia (1.0 mL min^{-1}) as a reaction gas and recording the ammonia adduct $Ti(NH)(NH_3)_4$ (mass-charge ratio of 131). The standard addition method was used for determinations covering range concentrations from 0.1 to 10 µg L^{-1}. Several reagent blanks were also prepared and analysed throughout the work. The limit of detection and quantification of the method are listed in **Table S4.1** (ESI).

Table 4.1. Instrumental conditions and data acquisition used for ICP-MS

PARAMETER/COMPONENT (UNIT)	
Instrument	Nex Ion 2000
Spray Chamber Type	QuartzCyclonic
PC3x Peltier Cooler System	4ºC
Nebulizer Type	Concentric Meinhard™
RF power (W)	1600
Plasma Gas Flow rate (L min^{-1})	15
Auxiliary gas flow rate (L min^{-1})	1.2
Nebulizer Gas Flow (L min^{-1})	1.14
Sample loop (µL)	100
Dwell time (ms)	50
Analyte (m/z)	Ag (107)
Internal Standard (m/z)	Rh (103)
Mode	KED or collision mode
Helium flow rate (mL min^{-1})	4.5
Analyte (m/z)	Ti (131)
Internal Standard (m/z)	Sc (45)
Mode	Dynamic Reaction Cell Technology
Ammonia flow rate (mL min^{-1})	1.0
Ion-product registered	$^{48}Ti(NH)(NH_3)_4$
Rejection parameter q	0.20
Quadrupole ion deflector (V)	Set for maximum ion transmission

4.3.10 single-particle-ICP-MS measurements

The determinations for Ag NPs and TiO_2 NPs aiming particle number concentrations and size distributions were performed by ICP-MS operating in the single particle mode (spICP-MS) under operating conditions summarized in **Table 4.2**. Since an exact mass-to charge ratio is not isolated with the quadrupole ion deflector (axial field

voltage, AFT at 350 V), RPa (high-mass cut-off) and RPq (low-mass cut-off) rejection parameters must be fixed at optimized values previously studied for a better focusing of the mass-to-charge ratio of interest in DRC work-mode for titanium determination (ammonia cluster at m/z 131). Daily performance was assessed by monitoring Be, In, U, Ce (Ce^{++}/ Ce and CeO/Ce ratios) and background and verifying intensities as well as ICP-MS measurements. Transport efficiency (TE%) was assessed by the particle frequency method, which implies the assessment of the sample flow rate, an aqueous ionic Au calibration, and the measurement of an Au NPs certified reference material. Therefore, sample flow rate was established by aspirating ultrapure water and weighing the solution after and before aspiration at the selected pump conditions (sample flow rates were between 0.19 and 0.21 mL min^{-1}). Ionic Au calibration was performed within the 0.5–3.0 μg L^{-1} range, and a suspension at 1.0×10^5 particles mL^{-1}, prepared in ultrapure water from a 49.6 nm Au NPs certified reference material, was finally measured. Transport efficiency (TE%) values (close to 8.0%) were automatically calculated by Syngistix ™ Nano Application. Calibrations were performed using ultrapure water and 1.0% (v/v) glycerol covering ionic Ti and Ag concentrations within the 0.1–10 μg L^{-1} range. Several reagent blanks were also analysed throughout the work. The limit of detection (number concentration and size) and quantification (number concentration) of the method are listed in **Table S4.1** (ESI).

4.3.11 Statistical analysis

Fish and clam growth parameters were statistically analysed by one-way analysis of variance (ANOVA). A post hoc multiple comparison tests (Fisher's least significant difference (LSD)) was used to detect which pairwise differences among effect levels were statistically significant (STATGRAPHICS Centurion XVI). Differences were considered statistically significant with a P value of <0.05 (From **Table S4.3** to **S4.8**-ESI, included).

The mean fish parameters (weight gain (WG), feed conversion ratio (FCR), and specific growth rate (SGR) were calculated from the

three replicates and expressed with standard deviation (n = 3) (**Table S4.3** and **S4.4**-ESI). Total Ag and Ti, and Ag NPs and TiO_2 NPs after different cooking procedures were analysed by one-way analysis of variance (ANOVA) too. Differences were considered statistically significant with a P value of <0.05.

Table 4.2. Operating conditions for spICP-MS analysis.

PARAMETER (UNIT)	
Analyte (m/z)	Ti (131)
Density (g cm^{-3})	4.23
Mass Fraction	59.90 %
Sample Flow Rate (mL min^{-1})	≈ 0.18
Transport efficiency (%)	≈ 8%
Dwell time (µs)	100
Mode	Dynamic Reaction Cell Technology
Ammonia flow rate (mL min^{-1})	0.75
Ion-product registered	$^{48}Ti(NH)(NH_3)_4$
Rejection parameter q	0.20
Quadrupole ion deflector (V)	Set for maximum ion transmission
Analyte (m/z)	Ag (107)
Density (g cm^{-3})	10.49
Mass Fraction	100 %
Sample Flow Rate (mL min^{-1})	≈ 0.18
Transport efficiency (%)	≈ 8%
Dwell time (µs)	50
Mode	Standard
Quadrupole ion deflector (V)	Set for maximum ion transmission

4.4 RESULTS AND DISCUSSION

4.4.1 Bioaccumulation: total Ag and Ti

Tissues from sea bass (exposure to 100 nm Ag NPs), from sea bream (exposure to 45 nm TiO_2 NPs), and for Japanese carpet shell (exposure to 100 nm Ag NPs and 45 nm TiO_2 NPs) were subjected to microwave assisted acid digestion (section 2.4.) and ICP-MS measurement (section 2.9.) for assessing total Ag and Ti contents.

4.4.1.1 Sea bass and sea bream

Data concentrations, plotted in Figure 4.1 for sea bream and in Figure S4.1 (ESI) for sea bass, show lower total contents in muscle skin than in kidney and liver tissues. This is especially significant for sea bass (**Figure S4.1**, ESI) which shows very low bioaccumulation for total Ag (levels within the ng g^{-1} range), quite close to the limit of detection of the method. The highest total Ag contents in sea bass muscle skin were achieved when exposed to the highest exposure concentration (1.5 mg kg^{-1}) after 60 and 75 (26.1±1 and 72.6±50.8 ng g^{-1}, respectively). Total Ti levels in muscle-skin from sea bream are also low (**Figure 4.1**), and the assessed values were between the LOD (83.2 ng g^{-1}) and the LOQ (277 ng g^{-1}) of the method (highest Ag concentrations of 162.9 and 232.8 ng g^{-1} when exposing at 1.5 mg kg^{-1} for 45 and 75 days, respectively).

Regarding liver tissues, **Figure S4.1** (ESI) shows that Ag is bioaccumulated from the beginning of the experiment (sampling at 15 days) with maximum bioaccumulation in the middle of the exposure time (between 15 and 60 days) and decreasing at the end of the experiment (sampling at 75 and 90 days) when using the highest exposure doses (0.75 and 1.5 mg kg^{-1}). The maximum Ag bioaccumulation was observed after 30 days of exposure at 0.75 mg kg^{-1} (4.60 µg Ag g^{-1}, **Figure S4.1**, ESI). This trend is also observed for Ti bioaccumulation in sea bream's liver (**Figure 4.1**) although the maximum Ti bioaccumulation was observed after 60 days of exposure at 1.5 mg kg^{-1} (1.14±0.09 µg Ti g^{-1}). In general, higher Ag bioaccumulation in sea bass's liver (within the 2.0-4.5 µg Ag g^{-1} range, **Figure S4.1** - ESI) than Ti in sea bream's liver (within the 0.5-1.5 µg Ti g^{-1} range, **Figure 4.1**). In addition, there is not a clear trend

for Ag and Ti bioaccumulation in kidney tissues (**Figure S4.1** – ESI and **Figure 4.1**) and similar bioaccumulation concentrations has been found from the middle to the end of the experiments (within the 15-90 days range in the case of Ag, and between 45 and 90 days for Ti mainly when using the highest dose).

The lower Ag and Ti bioaccumulation at large exposure times is not because fish eat less feed, since, as shown in ESI, the weight of the fish increases according to the time of exposure and feeding (**Figure S4.6** and **S4.7**, ESI).

On the other hand, the evaluation of growth parameters (culture conditions) in fish growth (WG, FCR, and SGR) are similar in all cases (**Table S4.3** and **S4.4**-ESI). No significant differences were observed for any parameter, in both studies. Furthermore, any mortality and anomalous behaviour were registered.

Finally, Ag and Ti are not bioaccumulated in the edible parts (muscle-skin) of sea bass and sea bream (even after exposure to high Ag NPs and TiO_2 NPs doses for long times) which implies a high degree of food safety regarding these pollutants in these cultured products.

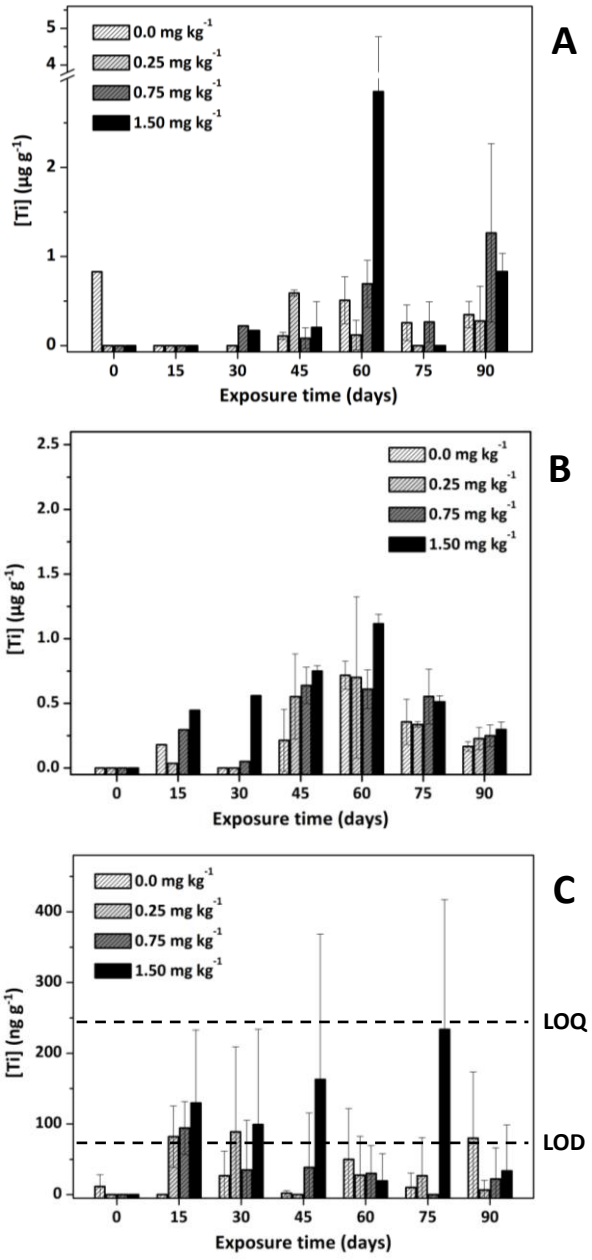

Figure 4.2. Titanium concentrations in sea bream kidney (A), liver (B), and muscle plus skin (C) after several exposure conditions.

4.4.1.2 Japanese carpet shell

Figure 4.2 shows the total Ag and total Ti concentrations in carpet shells after each exposure condition. In general, higher Ag and Ti bioaccumulation ratios than those measured for sea bass and sea bream were obtained, achieving maximum silver contents of 3.5±1.0 µg g^{-1} and total titanium contents of approximately 5.5±1.0 µg g^{-1}. Regarding silver bioaccumulation (**Figure 4.2A**), there were no found differences when using exposing to Ag NPs of different concentrations (0.1 and 1.0 mg kg^{-1}), and an increase in the total Ag contents is observed at the beginning of the experiment (sampling at the 7^{th} day) which remains constant until the end of trial (sampling at 28^{th} day). However, total Ti contents were found to gradually increase along the exposure trial, and higher bioaccumulation was also observed when exposed at the highest TiO_2 NPs dose (1.0 mg kg^{-1}).

The weight of the clams exposed to TiO_2 NPs were found be constant throughout the exposure trial, but shell length increased slightly (**Figure S4.8**, ESI). No significant differences were observed between the weight of clams fed with 0, 0.1 and 1 mg TiO_2 NPs L^{-1} at any time point (**Table S4.5**, ESI). However, regarding shell length (**Figure S4.9**, ESI), significant differences were observed between treated and control groups on days 7 and 14, although such differences disappear on days 21 and 28 (**Table S4.6**, ESI).

A decrease in weight (**Figure S4.10**, ESI) and no variation in shell length (**Figure S4.11**, ESI) were observed for specimens exposed to Ag NPs, where no significant differences were observed (**Table S4.7** and **S4.8**, ESI). Nevertheless, it is noteworthy that, the shell from the specimens exposed to the highest Ag NPs dose was found to be brittle.

No mortalities were observed in both clams assays.

In conclusion, results suggest that NPs bioaccumulation in Japanese carpet shells depends on the NPs type, and a greater concern is expected for TiO_2 NPs since, in addition to their higher bioaccumulation ratio, TiO_2 NPs tend to bioaccumulate in this mollusk over time.

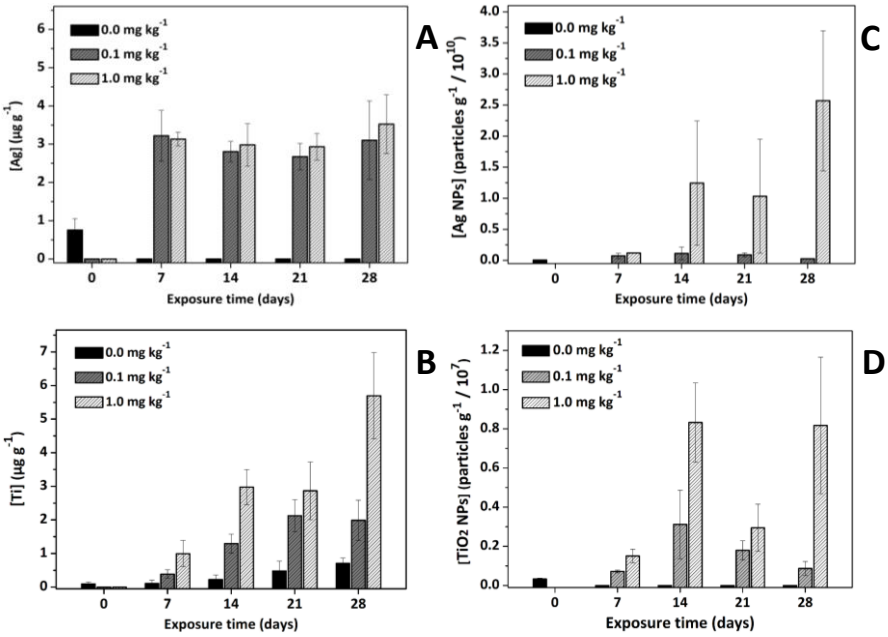

Figure 4.2. Titanium (A), silver (B), TiO_2 NPs (C), and Ag NPs (D) concentrations in Japanese carpet shell after several exposure conditions.

4.4.2 Bioaccumulation: Ag NPs and TiO_2 NPs

4.4.2.1 Sea bass and sea bream

The assessment of Ag NPs and TiO_2 NPs was performed in fish tissues which showed the highest total Ag and Ti concentrations. Therefore, sea bass's liver and kidney after Ag NPs exposure at 0.25, 0.75 and 1.5 mg kg^{-1} were analysed (**Figure S4.2**, ESI), whereas sea bream's muscle-skin, liver, and kidney after TiO_2 NPs exposure at 0.75 and 1.5 mg kg^{-1} were under investigation (**Figure 4.3**).

Ag NPs bioaccumulation in liver was found to be higher than in kidney, outcomes that agree with results obtained for total Ag in sea bass (**Figure S4.1**). Regarding sea bass's liver tissues, a rapid increase in Ag NPs levels (sampling within the 15-45 days) was again observed, followed by a clear Ag NPs concentration decrease. Hence, the highest level of Ag NPs concentration was measured for sea bass's liver tissues sampled after 15 days of exposure at 0.75 mg kg^{-1}

($2.27\times10^{9}\pm1.36\times10^{8}$ particles g^{-1}). Higher Ag NPs concentrations were also observed after 15 days of exposure at 0.25 mg kg^{-1} ($5.59\times10^{8}\pm1.20\times10^{8}$ particles g^{-1}), after 30 days exposure at 1.5 mg kg^{-1} ($7.15\times10^{8}\pm1.52\times10^{8}$ particles g^{-1}), and after 45 days exposure at 0.25 mg kg^{-1} ($1.39\times10^{9}\pm6.16\times10^{7}$ particles g^{-1}). Therefore, Ag NPs bioaccumulation in sea bass's liver appears to be higher at low Ag NPs concentrations and at small exposure times. However, results for sea bass's kidney are quite different, and the highest Ag NPs bioaccumulation was observed for long exposure time and also at the highest Ag NPs concentrations (0.75 and 1.5 mg kg^{-1}).

Regarding TiO_2 NPs bioaccumulation in sea bream, lower bioaccumulation than that found for Ag NPs bioaccumulation in sea bass was observed (in general values of 10^{6}-10^{7} vs 10^{9} particles per gram). Higher TiO_2 NPs concentrations were measured in sea bream's liver and muscle-skin than in kidney tissues (**Figure 4.3**), and the highest TiO_2 NPs levels in liver were noticed after 60- and 75-days exposure at the highest TiO_2 NPs concentrations (0.75 and 1.5 mg kg^{-1}). Similarly, the highest TiO_2 NPs levels in sea bream's kidney tissues was also observed at the end of the experiment (sampling at 90 days) also for exposure at 1.5 mg TiO_2 kg^{-1}. On the other hand, TiO_2 NPs assessment in muscle-skin from sea bream was also possible in sea bream specimens exposed to the largest TiO_2 NPs doses and results in **Figure 4.3** did not show a bioaccumulation trend since the quantified TiO_2 NPs number concentrations were close to the limit of detection of the method (6.97×10^{5} TiO_2 NPs g^{-1} as listed in **Table S4.1**, ESI)

4.4.2.2 Japanese carpet shell

Regarding Ag NPs and TiO_2 NPs bioaccumulation in Japanese carpet shell tissues, **Figure 4.2** shows a higher particles number for both Ag NPs and TiO_2 NPs when using the highest exposure dose (1.0 mg kg^{-1}), and also higher Ag NPs contents than TiO_2 NPs levels. This result would seem to be in opposition to that obtained for the total contents (higher Ti content than silver content) and it is due to TiO_2 NPs tend to agglomerate (higher TiO_2 NPs mean size and lower particle number concentration). In fact, the TiO_2 NPs

mean sizes assessed in Japanese carpet shell trials were within the 130-170 nm range, which is larger than the size of TiO_2 NPs used for the exposure experiments (45 nm).

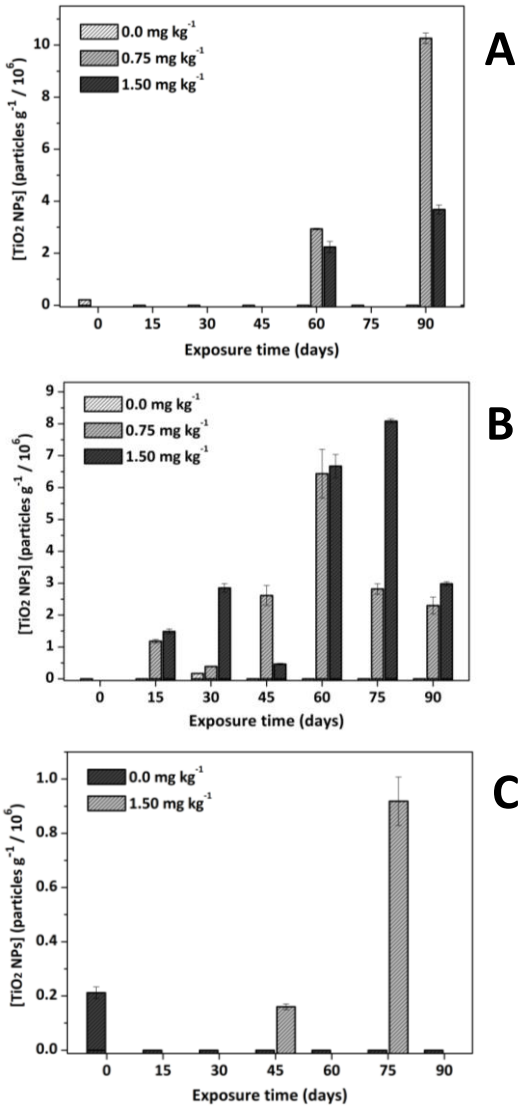

Figure 4.3. TiO_2 NPs concentrations in sea bream kidney (A), liver (B), and muscle plus skin (C)

4.4.3 Effect of the cooking procedure

Currently, fish's muscle is the edible part of fish, and fish's kidney/liver do not offer nutritional interest. For this reason, both liver and kidney tissues were discarded to study the impact of cooking on the total Ag and Ti, and Ag NPs and TiO_2 NPs bioaccumulation. In addition, since the low Ag bioaccumulation in sea bass's muscle-skin (values close to the LOD of the method) and the moderate-low Ti bioaccumulation in sea bream's muscle-skin (values within the LOD-LOQ range of the method), the effect of the culinary treatment was only carried out for muscle-skin from sea bream specimens exposed to 1.5 mg TiO_2 NPs kg^{-1} for 75 days. In addition, sea bream's muscle-skin from specimens unexposed (control at 90 days) were also used in the study. Therefore, two sample pools (muscle-skin from unexposed and exposed sea breams) were prepared, and total Ti contents (microwave assisted acid digestion and ICP-MS) and TiO_2 NPs concentrations (enzymatic hydrolysis and spICP-MS) in raw samples were obtained. Similarly, subsamples from the pooled samples were subjected to grilling and boiling (culinary treatments) in duplicate, and the remaining pooled samples were kept for further bio-accessible and bioavailable experiments.

Regarding Japanese carpet shell, the effect of the culinary process (grilling) was only tested in pooled samples obtained after 28-day exposure to Ag NPs (0.1 and 1.0 mg kg^{-1}), and in pooled samples from experiments with the maximum TiO_2 NPs dose (1.0 mg kg^{-1}) after 21-day and 28-day exposure.

Results for total Ti contents (**Table 4.3** and **Figure S3A**-ESI) and TiO_2 NPs concentrations (**Table 4.3** and **Figure S4.3B**, ESI) in sea bream reveals an increase of Ti and TiO_2 levels in the cooked samples, findings which can explain taking into account the pre-concentration effect of the culinary treatments especially when grilling (moisture has been reported to decrease from 78-80% in raw sea bass and sea bream to 73-76% when steaming cooking and to 51-59% when grilling) [36].

Similarly, results for Japanese carpet shell (**Table 4.3** and **Figure S4.4**-ESI) show an increase of total Ag and total Ti contents in grilled samples. However, the TiO_2 NPs number concentration in raw and cooked Japanese carpet shell were found to be similar in both tested pooled samples (TiO_2 NPs number concentrations were statistically compared at a 95% significance level by ANOVA obtaining p-values of 0.8235 and 0.7278 > 0.05, which implies that there are not statistically significant differences). Regarding Ag NPs number concentrations (**Table 4.3**) there were not statistically significant differences (95% confidence interval) in one pooled (raw and grilled) Japanese carpet shell (p-value after ANOVA of 0.7680 > 0.05). However, statistically significant differences (95% confidence interval) were found in the other sample (p-value after ANOVA of 0.0041 < 0.05).

Table 4.3. Results for total contents and Ag and TiO_2 NPs concentrations for sea bream and Japanese carpet shell. (R=ratio)

ID sample	MW digestion	Bioacc. fraction	R	Enzymatic extracion	Bioacc. fraction	R
	µg g^{-1} ±SD	µg g^{-1} ±SD	%	particles g^{-1} ±SD	particles g^{-1} ±SD	%
Clams (Ag)						
0.1 mg kg^{-1} (28 days) Raw tissue	3.17±0.74	2.4±0.24	75	$7.23±1.66×10^{8}$	$1.28±0.95×10^{8}$	17.6
0.1 mg kg^{-1} (28 days) Grilled	11.94±1.90	9.27±1.39	77	$4.55±0.57×10^{8}$	$9.59±1.10×10^{8}$	>100
1.0 mg kg^{-1} (28 days) Raw tissue	1.58±0.77	1.22±0.53	75	$3.28±0.82×10^{9}$	$9.12±0.09×10^{7}$	2.8
1.0 mg kg^{-1} (28 days) Grilled	10.48±4.84	9.56±2.43	90	$4.74±0.51×10^{8}$	$1.77±0.14×10^{9}$	>100
Clams (Ti)						
1.0 mg kg^{-1} (21 days) Raw tissue	1.02±0.16	0.21±0.04	20	$5.14±1.20×10^{6}$	$9.30±0.77×10^{6}$	>100
1.0 mg kg^{-1} (21 days) Grilled	2.95±0.23	0.80±0.16	27	$4.97±0.3×10^{6}$	$6.29±0.46×10^{6}$	>100
1.0 mg kg^{-1} (28 days) Raw tissue	1.71±0.25	0.26±0.02	15	$3.06±0.91×10^{7}$	$5.13±0.47×10^{6}$	16.6
1.0 mg kg^{-1} (28 days) Grilled	4.18±0.96	0.59±0.11	14	$1.11±0.90×10^{7}$	$8.14±0.40×10^{7}$	>100
Sea bream (Ti)						
1.5 mg kg^{-1} (90 days) Raw tissue	0.13±0.00	0.10±0.02	76	$1.52±0.11×10^{6}$	$1.05±0.07×10^{7}$	>100
1.5 mg kg^{-1} (90 days) Grilled	0.86±0.40	0.23±0.04	27	$2.80±1.27×10^{6}$	$8.80±0.14×10^{7}$	>100
1.5 mg kg^{-1} (90 days) Boiled	0.22±0.03	0.09±0.01	41	$5.51±0.98×10^{6}$	$9.71±0.50×10^{7}$	>100

4.4.4 Bio-accessibility in sea bream and Japanese carpet shell

The impact of the presence of TiO_2 NPs in sea bream, and Ag NPs and TiO_2 NPs in Japanese carpet shell on humans by sea bream's flesh and Japanese carpet shell consumption was evaluated by an *in vitro* bio-accessibility approach (section 2.7). The bio-accessibility ratio was calculated according to **Equation 4.1**:

$$\%\ \text{Bio} - \text{accessibility} = \frac{[\ ]_{Bio-accessible}}{[\ ]_{Total}} \times 100 \quad (\mathbf{Eq.4.1})$$

where $[]_{Total}$ is the total Ti /Ag concentration after microwave assisted acid digestion and ICP-MS assessment or the TiO_2 NPs / Ag NPs number concentration after enzymatic hydrolysis and spICP- MS in sea bream's muscle-skin (raw, grilled and boiled) and Japanese carpet shell (raw and grilled); and $[]_{Bio\text{-}accessible}$ is the total Ti / Ag concentration in the bio-accessible fraction after *in vitro* bio-accessibility and ICP-MS assessment or the TiO_2 NPs / Ag NPs number concentration after *in vitro* bio-accessibility and spICP-MS in sea bream's muscle-skin (raw, grilled and boiled) and Japanese carpet shell (raw and grilled).

The total Ti contents in the bio-accessible fractions (**Figure S4.3A**, ESI) are lower than those found in sea bream's muscle-skin sample (**Table 4.3**), which implies bio-accessibility ratio of 76% in raw sea bream flesh, and lower bio-accessibility ratios (41% and 27%) for cooked sea bream flesh. In general, we can conclude that the fraction of Ti that can be released from the matrix sample under gastro-intestinal conditions is moderate, which is a positive issue regarding human risk assessment. However, results are quite different for TiO_2 NPs, and therefore the TiO_2 NPs number concentrations in the bio-accessible fractions from cooked sea bream's flesh ($8.90\times10^7\pm1.45\times10^6$ and $9.71\times10^7\pm5.02\times10^6$ particles g^{-1} after grilling and boiling, respectively) are ten times higher than those measured in raw sea bream's flesh ($1.05\times10^7\pm7.0\times10^5$ particles g^{-1}). In addition, the bio- accessibility ratios for raw and cooked sea bream's flesh are higher than 100% when considering the TiO_2 NPs number

concentrations instead of total Ti contents. These false bio-accessibility ratios are explained considering the agglomeration tendency of TiO_2 NPs at different environments. The found TiO_2 NPs mean sizes in the enzymatic digests from raw, grilled, and boiled sea's bream flesh were 112±3, 113±3, and 114±4 nm, respectively, whereas the mean TiO_2 NPs mean sizes in the bio- accessible fractions were 101±3, 104±3, and 104±2 nm for raw, grilled, and boiled sea's bream flesh, respectively (**Table S4.2**, ESI).

Regarding Japanese carpet shell (**Table 4.3** and **Figure S4.4**-ESI), moderate bio-accessibility ratios (within the 15-20% and 14-27% ranges for raw and grilled shellfish, respectively) were observed for Ti, whereas higher bio-accessibilities ratios were obtained for Ag (75% for raw shellfish and 77 and 90% for grilled pooled samples). In the same way as the results found for sea bream, TiO_2 NPs and Ag NPs bio-accessibility ratios (**Table 4.3** and **Figure S4.4**-ESI) were found to be higher than 100% in some cases, mainly for TiO_2 NPs, due to the NPs agglomeration/dispersion phenomena depending on the environment (mean size data listed in **Table S4.2**, ESI). Raw Japanese carpet shell showed TiO_2 NPs bio-accessibilities ratios of 17% and higher than 100%, whereas calculated bio- accessibility in grilled shellfish was higher than 100%. Similarly, Ag NPs bio-accessibility ratios were low for raw Japanese carpet shell (2.8 – 18 %) and higher than 100% for grilled shellfish.

4.4.5 Bioavailability (transcellular transport) in sea bream and Japanese carpet shell

To evaluate the bioavailability of total Ti and TiO_2 NPs in sea bream's muscle-skin, an intestinal epithelium model (Caco-2 cells monolayer) was used for assessing the transcellular transport across the intestinal epithelium (section 2.8.). **Equation 4.2** was applied to determine the transport ratio where $[]_{Basal}$ is the total Ti concentration or TiO_2 NPs number concentration in the basolateral solution, and $[]_{Bio\text{-}accessible}$ is the total Ti concentration or TiO_2 NPs number concentration in the bio- accessible fraction (section 2.7.).

$$\% \text{ Transport} = \frac{[\ ]_{Basal}}{[\ ]_{Bio-accessible}} \times 100 \quad (\mathbf{Eq.4.2})$$

As shown in **Figure S4.4** (ESI), TiO_2 NPs transcellular transport ratios (bioavailability ratios) were lower than 15% (15±1.5, 2.7±0.70 and 4.8±1.6 % for raw, grilled, and boiled samples, respectively), whereas total Ti transcellular transport ratios were quite higher (67±13 and 74±9.2 % for after grilling and boiling treatments, respectively, and close to 100% for raw samples). The different transcellular transport when considering total Ti and TiO_2 NPs could be attributed to the TiO_2 NPs agglomeration/dispersion phenomena which depends on the TiO_2 NPs environment (pH, presence of large molecules and chloride ions) (Taboada-López et al. 2021). As shown in **Figure 4.4**, TiO_2 NPs mean sizes in the basal fraction are higher than in the bio-accessible fraction, which implies a lower TiO_2 NPs number concentration and hence, a lower transport ratio. In regard with clams tissues exposed to TiO_2 NPs, 1.0 mg kg^{-1} and 21-day exposure was defined as Ti(1) and 1.0 mg kg^{-1} and 28-day exposure was defined as Ti(2). By other side, clams exposed to Ag NPs were defined in **Figure 4.4** as Ag(1) (0.1 mg kg^{-1} and 28-day exposure) and as Ag(2) (1.0 mg kg^{-1} and 28-day exposure).

Finally, **Figure S4.4** (ESI) also shows that transcellular transports for cooked (grilling and boiling) sea bream muscle are lower than those obtained for raw samples. Again, agglomeration/dispersion phenomena when changing the TiO_2 NPs environment can explain these findings since as shown in **Figure 4.4**, TiO_2 NPs in the basal and apical fractions exhibit a lower mean size than in the bio- accessible fraction, which implies dispersion (higher TiO_2 NPs number concentration and higher transcellular transport).

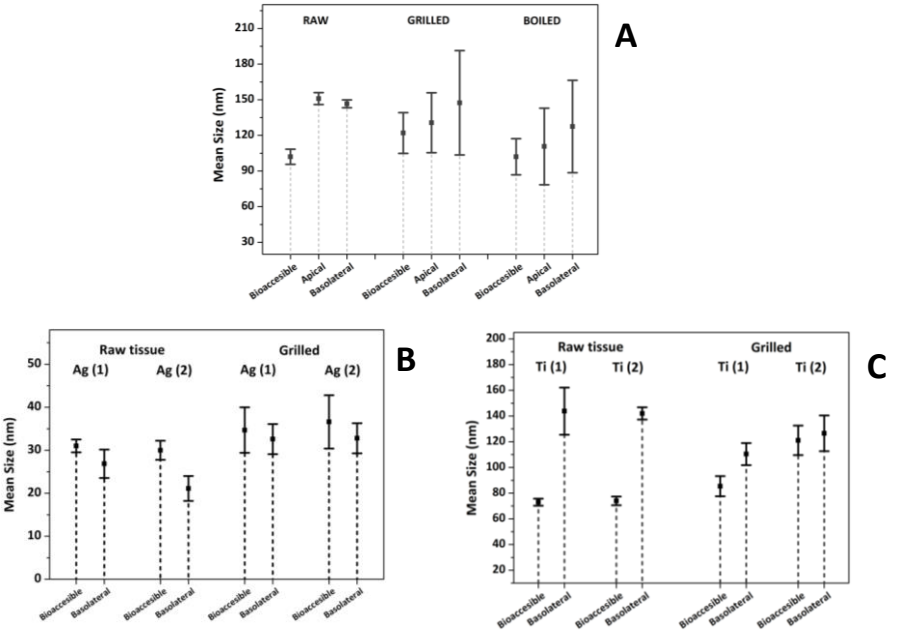

Figure 4.4. Mean sizes in the bio-accessible, apical, and basolateral fractions for transcellular transport assays of TiO_2 NPs in raw and cooked sea bream (A), and in the bio-accessible, and basolateral fractions for transcellular transport assays of Ag NPs (B) and TiO_2 NPs (C) in raw and cooked Japanese carpet shell.

Silver and Ag NPs transcellular transport ratios for raw Japanese carpet shell (**Figure 4.5**) were lower than 10 and 15%, respectively, whereas the ratios were found to be increased for grilled shellfish (within 40-60% range for total Ag and within 15-20% for Ag NPs). Similarly, Ti transcellular transport ratios were moderate (within the 35-75% range) and low for TiO_2 NPs (within the 5-30% range) for raw shellfish. Transcellular transport ratios for grilled Japanese carpet shell were lower than those found for total Ti (20-35%) and similar for TiO_2 NPs (25-30%). Mean sizes of Ag NPs and TiO_2 NPs in the bio-accessible and basolateral fractions must be considered for interpretating NPs transcellular transport (**Equation 4.2**) since the NPs agglomeration/dispersion phenomena (**Figure 4.4**).

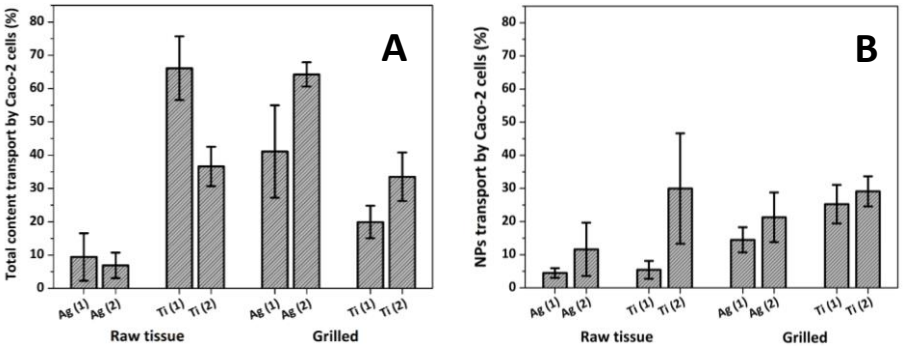

Figure 4.5. Total Ag and Ti (A) and Ag NPs and TiO_2 NPs (B) transcellular transport ratios in raw and cooked Japanese carpet shell.

4.5 CONCLUSIONS

Ag NPs and TiO_2 NPs bioaccumulation in aquaculture species (sea bass and sea bream) has been found low since only moderate bioaccumulation was observed in kidney and liver (non-edible parts of these species), whereas the presence of Ag NPs and TiO_2 NPs (ionic Ag and Ti) in fish's flesh was negligible even after exposure at high NPs doses and for long times (up 90 days). However, Japanese carpet shell species can bioaccumulate Ag NPs and TiO_2 NPs in the soft tissues, which could represent a health problem if the shellfish species were in contact with the high NPs doses tested in the trial (Ag NPs and TiO_2 NPs background are considerably lower than the used doses in the current study).

Regarding human risk assessment, Ag NPs and TiO_2 NPs human bioavailability (*in vitro* transcellular transport) from aquaculture species was found to be lower than 70% and 5% regarding total Ti and TiO_2 NPs, respectively, in cooked sea bream. Bioavailability ratios for total Ag and Ti in Japanese carpet shell were lower than 65 and 35%, respectively, whereas the bioavailability ratios for Ag NPs were even lower (lower than 20%) in cooked shellfish. However, similar TiO_2 NPs bioavailability ratios than those obtained for total Ti (lower than 30%) were found for cooked Japanese carpet shell species.

SUPPLEMENTARY INFORMATION

Table S4.1. Sensitivity: Limits of detection obtained for aquaculture species measurements.

analyte	spICP-MS (NPs assessment)			ICP-MS (total Ag/Ti assessment)	
	LOD_{size} (nm)	$LOD_{number\ concentration}$ (particles g^{-1})	$LOQ_{number\ concentration}$ (particles g^{-1})	LOD (ng g^{-1})	LOQ (ng g^{-1})
Ag	6	2.27×10^{6}	7.57×10^{6}	7.60	25.3
Ti	27	2.09×10^{5}	6.97×10^{5}	83.2	277

Table S4.2. Most frequent sizes and mean sizes of Ag NPs and TiO_2 NPs in the enzymatic digests and bio-accessible fractions from selected sea bream and Japanese carpet shell samples.

Sample description	Most Freq. size ±SD	Mean size ±SD
Clams (Ag) 0.1 mg kg^{-1} (28 days)		
Grilled - enzymatic extraction	29±1	34±1
Grilled- bioaccesible fraction	25±2	29±2
Clams (Ag) 1.0 mg kg^{-1} (28 days)		
Grilled - enzymatic extraction	31±2	37±2
Grilled - bioaccesible fraction	22±4	30±3
Clams (Ti) 1.0 mg kg^{-1} (21 days)		
Raw tissue - enzymatic extraction	70±4	102±4
Raw tissue - bioaccesible fraction	59±4	95±3
Grilled - enzymatic extraction	69±3	107±3
Grilled - bioaccesible fraction	62±2	98±4
Clams (Ti) 1.0 mg kg^{-1} (28 days)		
Raw tissue - enzymatic extraction	65±3	96±3
Raw tissue - bioaccesible fraction	57±4	74±2
Grilled - enzymatic extraction	71±3	104±3
Grilled - bioaccesible fraction	60±2	93±3
Sea bream (Ti) 1.5 mg kg^{-1} (90 days)		
Raw tissue - enzymatic extraction	87±2	112±3
Raw tissue - bioaccesible fraction	61±2	101±3
Grilled - enzymatic extraction	78±4	113±3
Grilled - bioaccesible fraction	70±2	104±3
Boiled - enzymatic extraction	75±3	114±4
Boiled - bioaccesible fraction	66±3	104±2

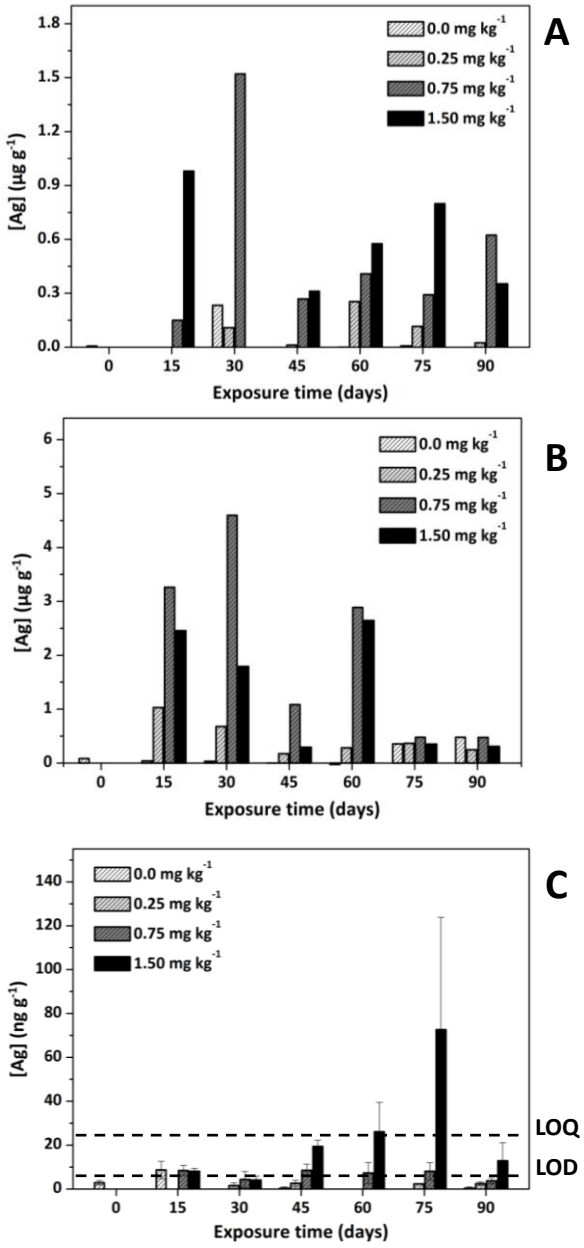

Figure S4.1. Silver concentrations in sea bass kidney (A), liver (B), and muscle plus skin (C) after several exposure conditions.

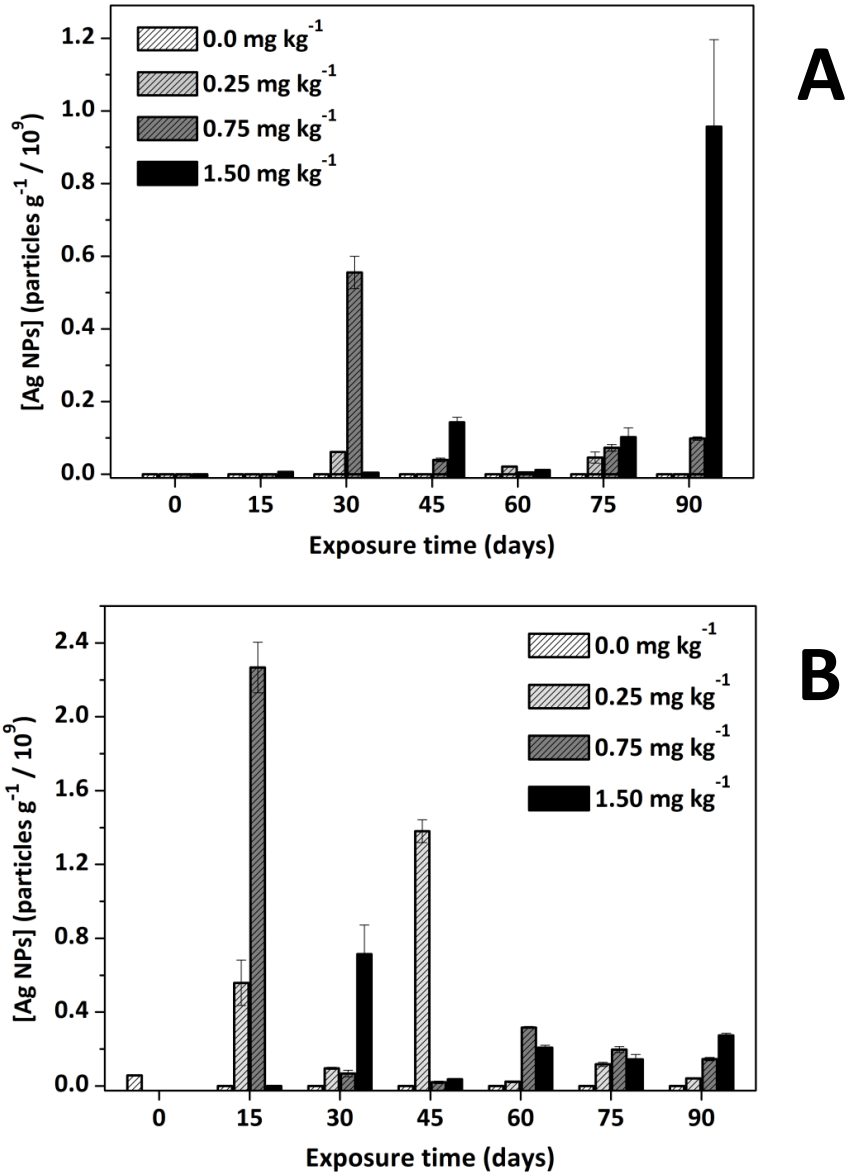

Figure S4.2. Ag NPs concentrations in sea bass kidney (A), and liver (B) after several exposure conditions.

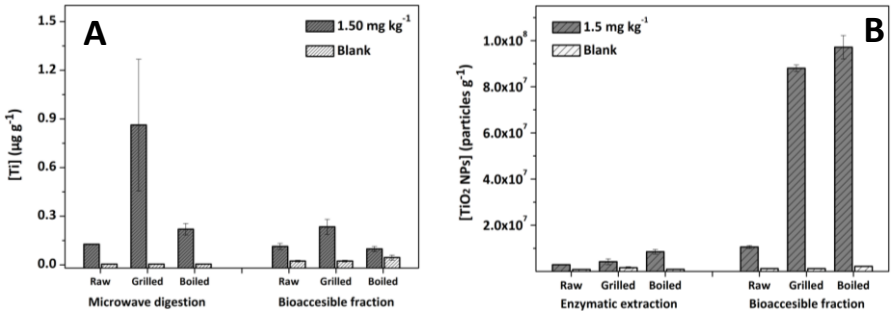

Figure S4.3. Titanium (A) and TiO_2 NPs (B) contents in raw and cooked (grilling and boiling) pooled sea bream's flesh, and Ti (A) and TiO_2 NPs (B) contents in the bio-accessible fractions from raw and cooked (grilling and boiling) sea bream's flesh.

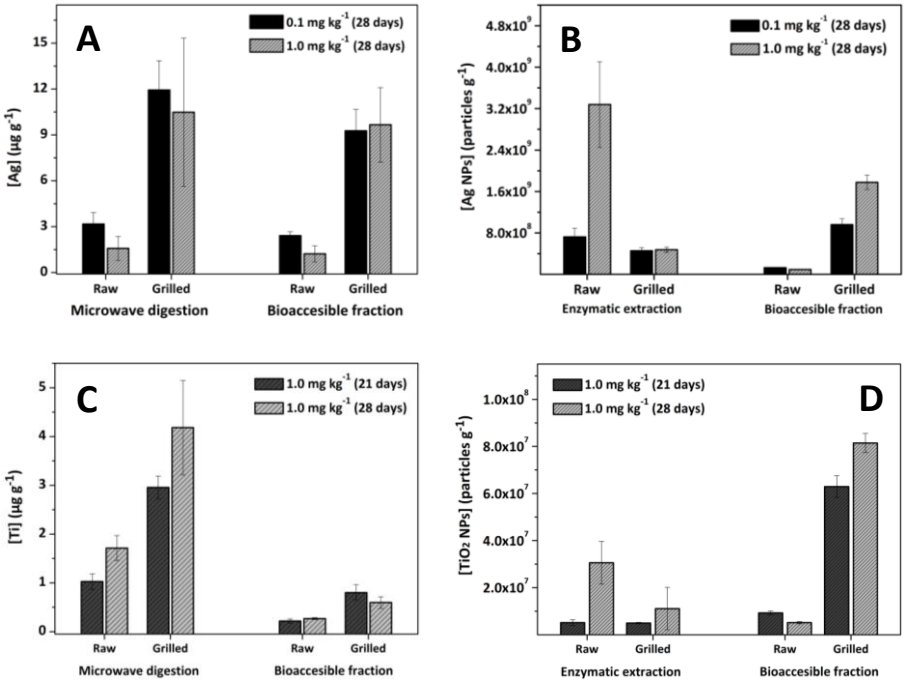

Figure S4.4. Silver (A), Ag NPs (B), Ti (C), and TiO_2 NPs (D) contents in a raw and grilled pooled Japanese carpet shell tissues, and Ag (A), Ag NPs (B), Ti (C), and TiO_2 NPs (D) contents in the bio-accessible fractions from raw and grilled Japanese carpet shell tissues.

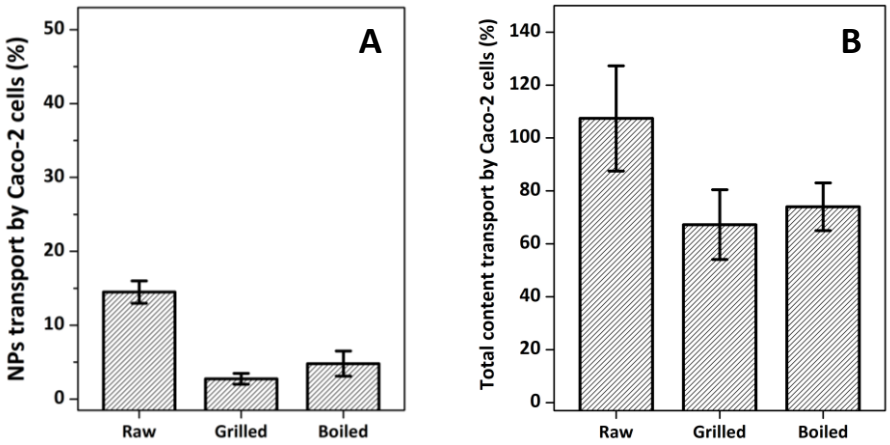

Figure S4.5. TiO_2 NPs (A) and Ti (B) transcellular transport (%) for raw and cooked sea bream's flesh.

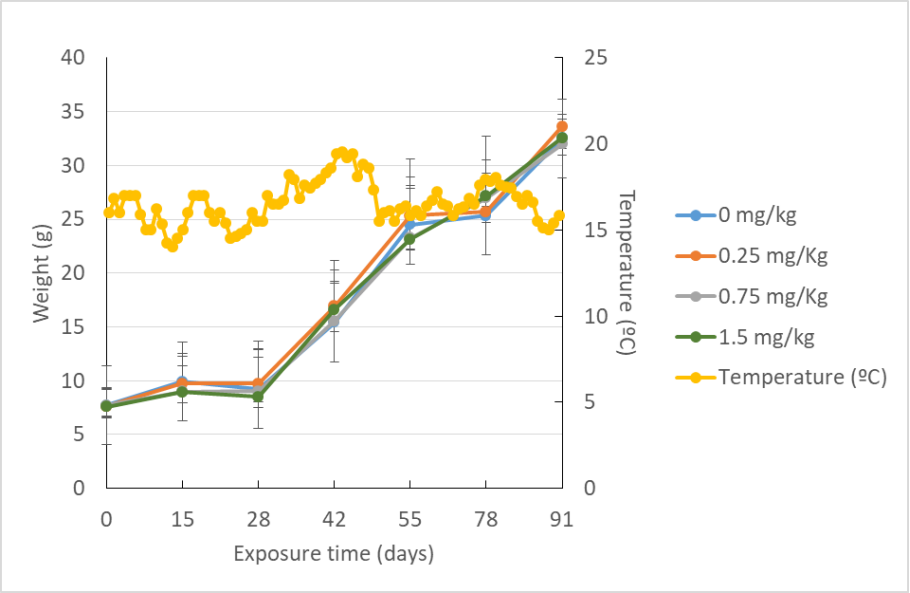

Figure S4.6. Evolution of weight and temperature in sea bream throughout 45 nm TiO_2 NPs bioaccumulation assay.

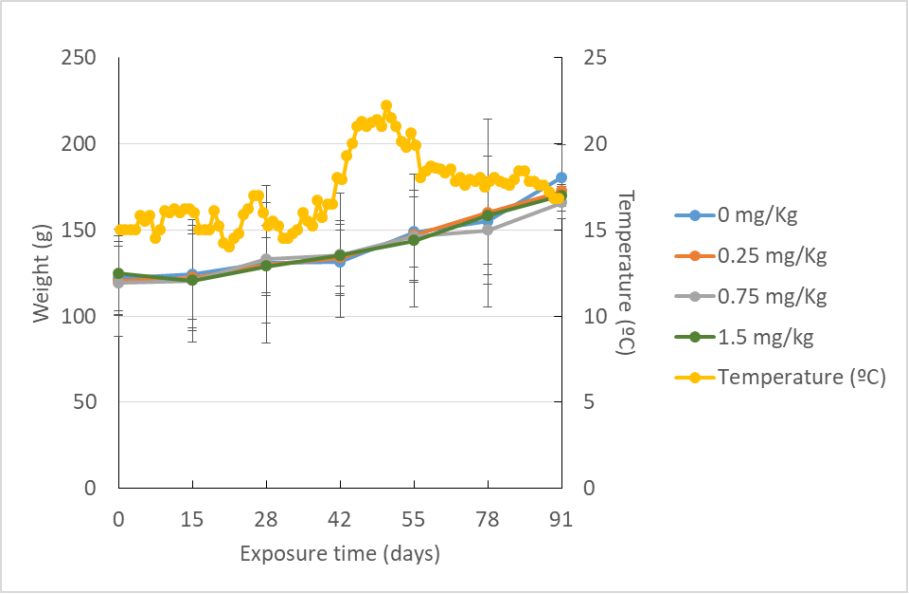

Figure S4.7. Evolution of weight and temperature in sea bass throughout 100 nm Ag NPs bioaccumulation assay.

Table S4.3. Growth parameters for sea bream trial after 90 days of TiO_2 NPs bioaccumulation assay.

Sea bream Parameters	TiO_2 nanoparticle dose (mg kg^{-1})			
	0.0	0.25	0.75	1.5
IBW (g)	7.7±1.5	7.16±1.81	7.61±1.3	7.31±1.1
FBW (g)	28.4±3.1	28.7±2.1	28.5±3.2	29.3±3.7
WG%)	73±2.8	73±1.2	73±1.5	74±1.9
FCR	1.9±0.3	1.9±0.2	2±0.2	2.1±0.2
SGR (%)	1.4±0.1	1.5±0.1	1.5±0.1	1.5±0.1

- Results are presented as mean ± SD (Initial and final weight: n=12; WG (%), FCR and SGR (%): n = 3). No significant differences between any parameter within the same row were observed.
- IBW (Initial body weight, g) = body weight at start of experiment (t=0 day); FBW (Final body weight, g) = Body weight at end of experiment (t=90 day); WG (Weight gain, %) = ((FBG (g) – IBW (g))/FBW (g)) x 100. Feed conversion ratio (FCR) = dry feed intake (g)/Weight gain (g); SGR (Specific growth rate/day, %) = 100x (ln FBW - ln IBW/ number of days).

Table S4.4. Growth parameters for sea bass trial after 90 days of Ag NPs bioaccumulation assay.

Sea bass Parameters	Ag nanoparticle dose (mg kg^{-1})			
	0.0	0.25	0.75	1.5
IBW (g)	118.5±21.3	127.9±27.1	118.2±22.7	117.5±27.8
FBW (g)	180.0±20.8	180.9±20.1	192.37±21.1	197.3±27.5
WG%)	32.6±4.0	32.8±2.1	36.76±2.6	38.3±5.0
FCR	2.4±0.3	2.4±0.3	2.9±0.3	2.8±0.5
SGR (%)	0.44±0.1	0.44±0.1	0.51±0.1	0.54±0.1

- Results are presented as mean ± SD (Initial and final weight: n=12; WG (%), FCR and SGR (%): n = 3). No significant differences, between any parameter within the same row were observed.
- IBW (Initial body weight, g) = body weight at start of experiment (t=0 day); FBW (Final body weight, g) = Body weight at end of experiment (t=90 day); WG (Weight gain, %) = ((FBG (g) – IBW (g))/FBW (g)) x 100. Feed conversion ratio (FCR) = dry feed intake (g)/Weight gain (g); SGR (Specific growth rate/day, %) = 100x (ln FBW - ln IBW/ number of days).

Table S4.5. Weight evolution in Japanese carpet shell throughout 45 nm TiO_2 NPs bioaccumulation assay.

Time (days)	TiO_2 nanoparticle dose (mg L^{-1})		
	0.0	0.1	1.0
0	19.9±2.3	19.9±2.3	19.9±2.3
7	18.2±1.8	18.5±2.2	18.5±1.7
14	18.2±1.2	19.3±2.0	19.1±2.4
21	18.8±1.0	18.8±2.5	19.7±1.7
28	19.1±1.8	18.8±2.3	18.8±3.4

Results are presented as mean ± SD (n = 12). No significant differences between any weight within the same row were observed.

Table S4.6. Shell length evolution in Japanese carpet shell throughout 45 nm TiO_2 NPs bioaccumulation assay.

Time (days)	TiO_2 nanoparticle dose (mg L^{-1})		
	0.0	0.1	1.0
0	$4.2±0.3^{a}$	$4.2±0.3^{a}$	$4.2±0.3^{a}$
7	$4.2±0.3^{a}$	$4.3±0.2^{ab}$	$4.0±0.2^{b}$
14	$4.4±0.2^{a}$	$4.5±0.3^{b}$	$4.2±0.2^{b}$
21	$4.5±0.2^{a}$	$4.5±0.3^{a}$	$4.4±0.3^{a}$
28	$4.6±0.3^{a}$	$4.7±0.3^{a}$	$4.7±0.3^{a}$

Results are presented as mean ± SD (n = 12). Values within the same row not sharing a common superscript letter are significantly different ($P < 0.05$).

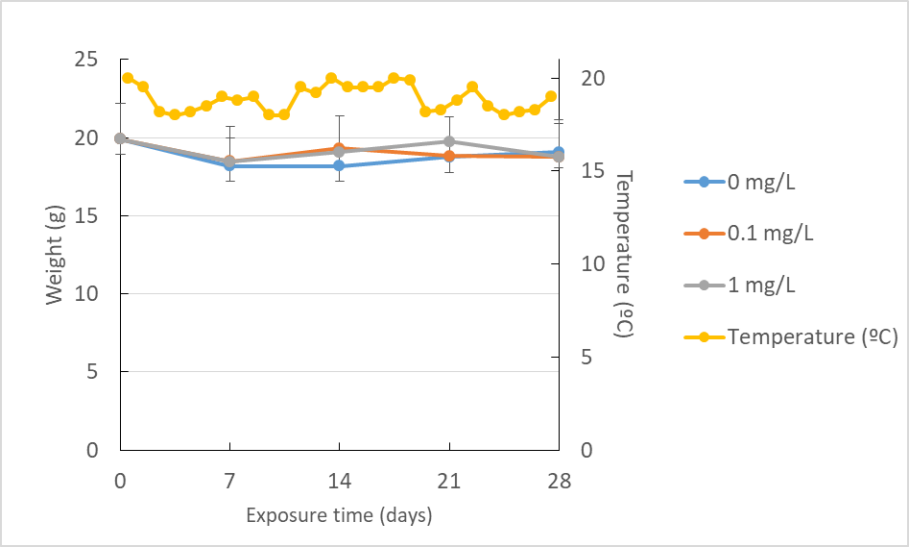

Figure S4.8. Evolution of weight and temperature in Japanese carpet shell throughout 45 nm TiO_2 NPs bioaccumulation assay.

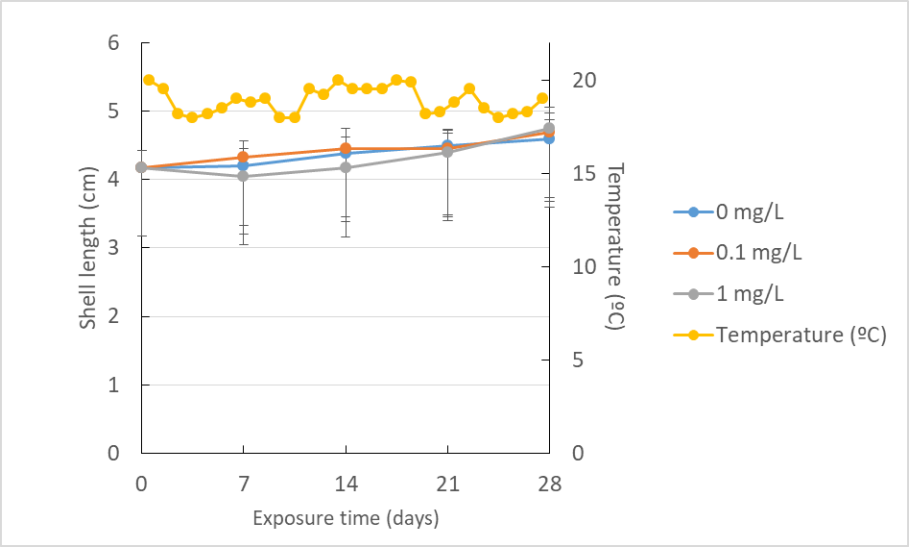

Figure S4.9. Evolution of shell length and temperature in Japanese carpet shell throughout 45 nm TiO_2 NPs bioaccumulation assay.

Table S4.7. Weight evolution in Japanese carpet shell throughout 100 nm Ag NPs bioaccumulation assay.

Time (days)	Ag nanoparticle dose (mg L^{-1})		
	0.0	0.1	1.0
0	23.3±3.4	23.3±3.3	23.3±3.3
7	24.0±5.2	22.0±6.5	21.6±4.5
14	22.4±3.8	20.1±2.4	20.8±1.9
21	20.6±4.5	21.1±3.9	20.2±3.0
28	18.3±3.3	18.3±3.3	19.4±3.8

Results are presented as mean ± SD (n = 12). No significant differences between any weight within the same row were observed.

Table S4.8. Shell length evolution in Japanese carpet shell throughout 100 nm Ag NPs bioaccumulation assay.

Time (days)	Ag nanoparticle dose (mg L^{-1})		
	0.0	0.1	1.0
0	4.7±0.2	4.7±0.2	4.7±0.2
7	4.8±0.3	4.7±0.5	4.5±0.4
14	4.5±0.3	4.3±0.2	4.5±0.2
21	4.6±0.3	4.6±0.4	4.7±0.3
28	4.5±0.3	4.8±0.4	4.6±0.3

Results are presented as mean ± SD (n = 12). No significant differences, between any shell length within the same row were observed.

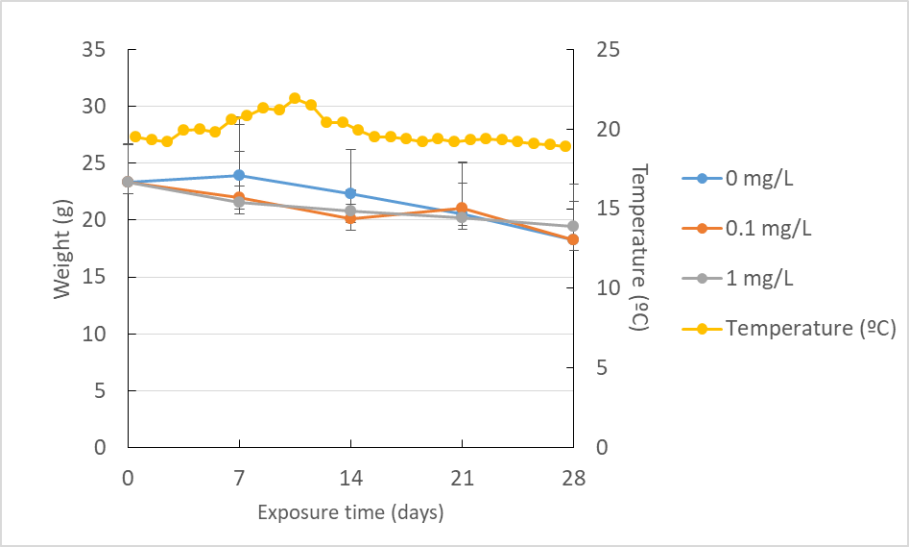

Figure S4.10. Evolution of weight and temperature in Japanese carpet shell throughout 100 nm Ag NPs bioaccumulation assay.

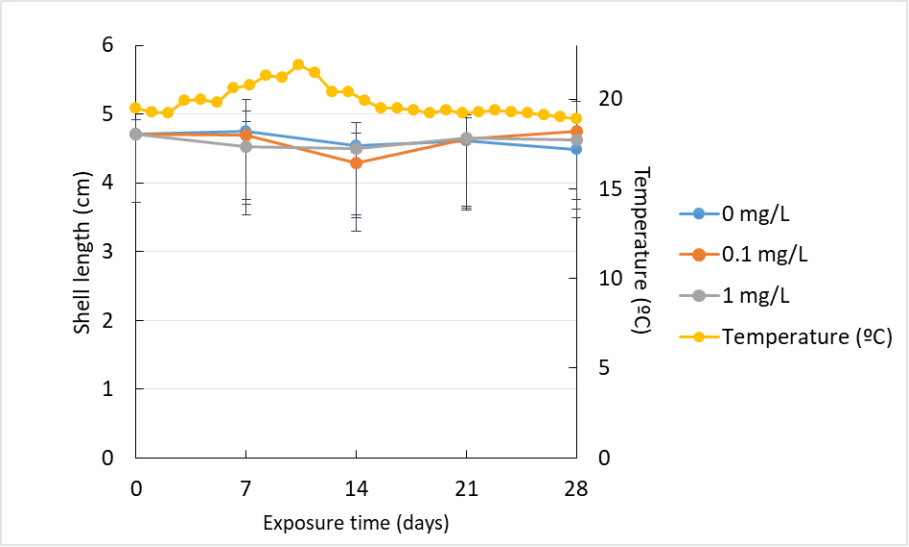

Figure S4.11. Evolution of shell length and temperature in Japanese carpet shell throughout 100 nm Ag NPs bioaccumulation assay.

REFERENCES

[1] E.C. (2022/C229/01), Commission Recommendation of 14 June 2021 on the definition of nanomaterial (2022/C229/01), Official Journal of the European Union, C229 (14 June 2021) 1–5.

[2] K.M. Tyner, A.M. Wokovich, D.E. Godar, W.H. Doub, N. Sadrieh, The state of nano-sized titanium dioxide (TiO2) may affect sunscreen performance, Int. J. Cosmet. Sci. 33 (2011) 234–244. https://doi.org/10.1111/j.1468- 2494.2010.00622.x.

[3] K. Kowal, P. Cronin, E. Dworniczek, J. Zeglinski, P. Tiernan, M. Wawrzynska, H. Podbielska, S.A.M. Tofail, Biocidal effect and durability of nano-TiO2 coated textiles to combat hospital acquired infections, RSC Adv. 4 (2014) 19945–19952. https://doi.org/10.1039/c4ra02759k.

[4] S. Josset, N. Keller, M.C. Lett, M.J. Ledoux, V. Keller, Numeration methods for targeting photoactive materials in the UV-A photocatalytic removal of microorganisms, Chem. Soc. Rev. 37 (2008) 744–755. https://doi.org/10.1039/b711748p.

[5] W.R. Li, X.B. Xie, Q.S. Shi, H.Y. Zeng, Y.S. Ou-Yang, Y. Ben Chen, Antibacterial activity and mechanism of silver nanoparticles on Escherichia coli, Appl. Microbiol. Biotechnol. 85 (2010) 1115–1122. https://doi.org/10.1007/s00253-009-2159-5.

[6] L.J. Wilkinson, R.J. White, J.K. Chipman, Silver and nanoparticles efficacy and safety, J. Wound Care. 20 (2011) 543–549. https://doi.org/10.12968/jowc.2011.20.11.543

[7] M. Larguinho, P. V. Baptista, Gold and silver nanoparticles for clinical diagnostics - From genomics to proteomics, J. Proteomics. 75 (2012) 2811– 2823. https://doi.org/10.1016/j.jprot.2011.11.007.

[8] B. Reidy, A. Haase, A. Luch, K.A. Dawson, I. Lynch, Mechanisms of silver nanoparticle release, transformation and toxicity: a critical review of current knowledge and recommendations for future studies

and applications, Materials (Basel). 6 (2013) 2295–2350. https://doi.org/10.3390/ma6062295.

[9] H. Shi, R. Magaye, V. Castranova, J. Zhao, Titanium dioxide nanoparticles: a review of current toxicological data. Part. Fibre Toxicol. 10 (2013) 15.

[10] A. Kazimirova, N. El Yamani, L. Rubio, A. García-Rodríguez, M. Barancokova, R. Marcos, M. Dusinska, Effects of titanium dioxide nanoparticles on the Hprt gene mutations in V79 hamster cells, Nanomaterials. 10 (2020) 465. https://doi.org/10.3390/nano10030465.

[11] I.L. Hsiao, F.S. Bierkandt, P. Reichardt, A. Luch, Y.J. Huang, N. Jakubowski, J. Tentschert, A. Haase, Quantification and visualization of cellular uptake of TiO2 and Ag nanoparticles: comparison of different ICP-MS techniques, J. Nanobiotechnology. 14 (2016) 1–13. https://doi.org/10.1186/s12951-016-0203- z.

[12] G.C. Renzi M, Ecotoxicity of nanoparticles in aquatic environments: a review based on multivariate statistics of meta-data, J. Environ. Anal. Chem. 2 (2015) 2–7. https://doi.org/10.4172/2380-2391.

[13] L. Truong, T. Zaikova, B.L. Baldock, M. Balik-Meisner, K. To, D.M. Reif, Z.C. Kennedy, J.E. Hutchison, R.L. Tanguay, Systematic determination of the relationship between nanoparticle core diameter and toxicity for a series of structurally analogous gold nanoparticles in zebrafish, Nanotoxicology. 13 (2019) 879–893. https://doi.org/10.1080/17435390.2019.1592259.

[14] X. Liu, E. Dumitrescu, A. Kumar, D. Austin, D. Goia, K.N. Wallace, S. Andreescu, Differential lethal and sublethal effects in embryonic zebrafish exposed to different sizes of silver nanoparticles, Environ. Pollut. 248 (2019) 627–634. https://doi.org/10.1016/j.envpol.2019.02.085.

[15] E. Fröhlich, E. Roblegg, Oral uptake of nanoparticles: human relevance and the role of in vitro systems, Arch. Toxicol. 90 (2016) 2297–2314. https://doi.org/10.1007/s00204-016-1765-0.

[16] M. Saez-Tenorio, J. Domenech, A. García-Rodríguez, A. Velázquez, A. Hernández, R. Marcos, C. Cortés, Assessing the relevance of exposure time in differentiated Caco-2/HT29 cocultures. Effects of silver nanoparticles, Food Chem. Toxicol. 123 (2019) 258–267. https://doi.org/10.1016/j.fct.2018.11.009.

[17] C. Gitrowski, A.R. Al-Jubory, R.D. Handy, Uptake of different crystal structures of TiO2 nanoparticles by Caco-2 intestinal cells, Toxicol. Lett. 226 (2014) 264–276. https://doi.org/10.1016/j.toxlet.2014.02.014.

[18] A. Abdelkhaliq, M. van der Zande, A.K. Undas, R.J.B. Peters, H. Bouwmeester, Impact of in vitro digestion on gastrointestinal fate and uptake of silver nanoparticles with different surface modifications, Nanotoxicology. 14 (2020) 111–126. https://doi.org/10.1080/17435390.2019.1675794.

[19] Z.M. Song, N. Chen, J.H. Liu, H. Tang, X. Deng, W.S. Xi, K. Han, A. Cao, Y. Liu, H. Wang, Biological effect of food additive titanium dioxide nanoparticles on intestine: An in vitro study, J. Appl. Toxicol. 35 (2015) 1169–1178. https://doi.org/10.1002/jat.3171.

[20] C. Bai, M. Tang, Toxicological study of metal and metal oxide nanoparticles in zebrafish, J. Appl. Toxicol. 40 (2020) 37–63. https://doi.org/10.1002/jat.3910.

[21] C.S. Ramsden, T.J. Smith, B.J. Shaw, R.D. Handy, Dietary exposure to titanium dioxide nanoparticles in rainbow trout, (Oncorhynchus mykiss): no effect on growth, but subtle biochemical disturbances in the brain, Ecotoxicology. 18 (2009) 939–951. https://doi.org/10.1007/s10646-009-0357-7.

[22] F. Ribeiro, C. Pinheiro, M. Monteiro, C.A.M. Van Gestel, A.M.V.M. Soares, S. Loureiro, Toxicokinetics of silver in the goldfish Carassius auratus under simultaneous waterborne and diet-borne exposures to silver nanoparticles, Environ. Sci. Pollut. Res. 29 (2022) 56079–56089. https://doi.org/10.1007/s11356-022-19717-7.

[23] M. Ates, V. Demir, R. Adiguzel, Z. Arslan, Bioaccumulation, subacute toxicity, and tissue distribution of engineered titanium dioxide nanoparticles in goldfish (Carassius auratus), J. Nanomater. 2013 (2013) 460518. https://doi.org/10.1155/2013/460518.

[24] M. Asztemborska, M. Jakubiak, R. Stęborowski, E. Chajduk, G. Bystrzejewska- Piotrowska, Titanium dioxide nanoparticle circulation in an aquatic ecosystem, Water. Air. Soil Pollut. 229 (2018) 208. https://doi.org/10.1007/s11270-018-3852-8.

[25] B.J. Shaw, R.D. Handy, Physiological effects of nanoparticles on fish: A comparison of nanometals versus metal ions, Environ. Int. 37 (2011) 1083– 1097. https://doi.org/10.1016/j.envint.2011.03.009.

[26] R.L. Naylor, R.W. Hardy, A.H. Buschmann, S.R. Bush, L. Cao, D.H. Klinger, D.C. Little, J. Lubchenco, S.E. Shumway, M. Troell, A 20-year retrospective review of global aquaculture, Nature. 591 (2021) 551–563. https://doi.org/10.1038/s41586-021-03308-6.

[27] C.E. Boyd, L.R. D'Abramo, B.D. Glencross, D.C. Huyben, L.M. Juarez, G.S. Lockwood, A.A. McNevin, A.G.J. Tacon, F. Teletchea, J.R. Tomasso, C.S. Tucker, W.C. Valenti, Achieving sustainable aquaculture: historical and current perspectives and future needs and challenges, J. World Aquac. Soc. 51 (2020) 578–633. https://doi.org/10.1111/jwas.12714.

[28] F. Teletchea, Fish domestication in aquaculture: Reassessment and emerging questions, Cybium. 43 (2019) 7–15. https://doi.org/10.26028/cybium/2019-431- 001.

[29] T. Fabrice, Fish domestication: an overview, Anim. Domest. 43 (2019) 7-15. https://doi.org/10.5772/intechopen.79628.

[30] F. Teletchea, Domestication of marine fish species: update and perspectives, J. Mar. Sci. Eng. 3 (2015) 1227–1243. https://doi.org/10.3390/jmse3041227.

[31] C. Suárez-Oubiña, P. Herbello-Hermelo, P. Bermejo-Barrera, A. Moreda- Piñeiro, Single-particle inductively coupled plasma mass spectrometry using ammonia reaction gas as a reliable and free-interference determination of metallic nanoparticles, Talanta. 242 (2022) 123286. https://doi.org/10.1016/j.talanta.2022.123286.

[32] C. Suárez-Oubiña, P. Herbello-Hermelo, P. Bermejo-Barrera, A. Moreda- Piñeiro, Exploiting dynamic reaction cell technology for removal of spectral interferences in the assessment of Ag, Cu, Ti, and Zn by inductively coupled plasma mass spectrometry, Spectrochim. Acta - Part B At. Spectrosc. 187 (2022) 106330. https://doi.org/10.1016/j.sab.2021.106330.

[33] M.J. Araújo, M.L. Sousa, E. Fonseca, A.B. Felpeto, J.C. Martins, M. Vázquez, N. Mallo, L. Rodriguez-Lorenzo, M. Quarato, I. Pinheiro, M. V. Turkina, J.J. López-Mayán, E. Peña-Vázquez, M.C. Barciela-Alonso, M. Spuch-Calvar, M. Oliveira, P. Bermejo-Barrera, S. Cabaleiro, B. Espiña, V. Vasconcelos, A. Campos, Proteomics reveals multiple effects of titanium dioxide and silver nanoparticles in the metabolism of turbot, Scophthalmus maximus, Chemosphere. 308 (2022) 136110. https://doi.org/10.1016/j.chemosphere.2022.136110.

[34] M.V. Taboada-López, N. Alonso-Seijo, P. Herbello-Hermelo, P. Bermejo- Barrera, A. Moreda-Piñeiro, Determination and characterization of silver nanoparticles in bivalve molluscs by ultrasound assisted enzymatic hydrolysis and sp-ICP-MS, Microchem. J. 148 (2019) 652–660. https://doi.org/10.1016/j.microc.2019.05.023.

[35] M.V. Taboada-López, P. Herbello-Hermelo, R. Domínguez-González, P. Bermejo-Barrera, A. Moreda-Piñeiro, Enzymatic

hydrolysis as a sample pre- treatment for titanium dioxide nanoparticles assessment in surimi (crab sticks) by single particle ICP-MS, Talanta. 195 (2019) 23–32. https://doi.org/10.1016/j.talanta.2018.11.023.

[36] G.D.T.M. Jayasinghe, P. Herbello-Hermelo, R. Domínguez-González, P.Bermejo-Barrera, A. Moreda-Piñeiro, Bioavailability of aflatoxins in cultured fish and animal livers using an in vitro dialyzability approach, J. Agric. Food Chem. 69 (2021) 11451–11460. https://doi.org/10.1021/acs.jafc.1c03643.

[37] M.V. Taboada-López, B.H. Leal-Martínez, R. Domínguez-González, P. Bermejo-Barrera, P. Taboada-Antelo, A. Moreda-Piñeiro, Caco-2 in vitro model of human gastrointestinal tract for studying the absorption of titanium dioxide and silver nanoparticles from seafood, Talanta. 233 (2021) 1–32. https://doi.org/10.1016/j.talanta.2021.122494.

CHAPTER 5

QUANTITATIVE IMAGING IN FISH TISSUES EXPOSED TO TITANIUM DIOXIDE NANOPARTICLES BY LASER ABLATION – INDUCTIVELY COUPLED PLASMA - MASS SPECTROMETRY

CHAPTER 5. QUANTITATIVE IMAGING IN FISH TISSUES EXPOSED TO TITANIUM DIOXIDE NANOPARTICLES BY LASER ABLATION – INDUCTIVELY COUPLED PLASMA - MASS SPECTROMETRY

5.1 ABSTRACT

Biodistribution of metals in biological tissues has emerged in life sciences as a useful tool to address biological questions regarding toxicity of metals. Nanomaterials, mainly inorganic nanoparticles (NPs), are emerging pollutants with a widespread use and impact on the marine environment, and new analytical methodologies are required for their assessment and monitoring. In the current research, imaging studies by laser ablation inductively coupled plasma mass spectrometry (LA-ICP-MS) have been successfully developed to obtain qualitative and quantitative information in fish tissues (kidney, liver and muscle) from sea bream specimens previously exposed to titanium dioxide nanoparticles (TiO_2 NPs) and which had already shown bioaccumulation of titanium (ionic and nanoparticulate titanium). Laboratory-produced gelatine standards containing titanium were used as a calibration strategy for obtaining LA-based images using quantitative (titanium concentrations) data. This strategy allowed to locate prominent areas of TiO_2 NPs in the tissues as well as to quantify the bioaccumulated titanium and a better understanding of the TiO_2 NPs spatial distribution in tissues.

5.2 INTRODUCTION

Downscaling materials to the nanometre range significantly alters their properties and give rise to interesting new features that allow new and outstanding applications. Nanomaterials, mainly inorganic nanoparticles (NPs), are widely used in various industries [1,2], and the determination and characterisation of NPs is one of the most challenging and demanded scientific research fields. However, due to

the massive use of NPs and their large discharges into the environment, concerns have arisen about their possible effects, especially on the marine environment and, consequently, on human health [3]. Therefore, there is a need for developing efficient and reliable analytical methodologies to improve the information on the presence of NPs in environmental matrices and for a better understanding of their distribution.

Current established analytical techniques provide various types of analytical information on NPs including size, shape, elemental composition, particle number and mass concentrations among others. Inductively coupled plasma - mass spectrometry (ICP-MS), mainly the time-resolved ICP- MS mode, also known as single particle ICP-MS (spICP-MS), has proven to be one of the most useful instrumental techniques for the determination and characterisation of NPs. Additionally, elemental distribution assays applied to soft biological tissues has emerged in various scientific fields to address questions regarding toxicity of pollutants. Hence, NPs as emerging pollutants require new analytical approaches, and the development of image-based techniques can help for a better understanding and monitoring of NPs in biological tissues. Numerous analytical techniques have attracted great interest for biological tissue imaging and elemental bioimaging, such as laser- induced breakdown spectroscopy (LIBS) [4], secondary ion mass spectrometry (SIMS) [5], X-ray fluorescence (XRF) [6], and matrix-assisted laser desorption with time of flight as a mass spectrometer (MALDI-TOF) [7]. These techniques are generally challenging to implement due to the expensive instrumentation and the tedious sample preparation required for imaging trace levels of analytes in biological tissues. On the contrary, laser ablation – inductively coupled plasma – mass spectrometry (LA-ICP-MS) can be also used for tissue imaging since it provides high quality features, such as a wide dynamic range, multi-element detection capabilities, and high spatial resolution; moreover sample preparation is less laborious and time consuming [8,9]. In addition, major, minor, and trace elements can be simultaneously imaged since the high sensitivity

inherent to ICP-MS (μg g^{-1} or even lower) [10–12]. Imaging studies based on LA-ICP-MS could be a breakthrough aiming the visualisation of metal distribution in biological tissues by using not only qualitative information (relative elemental intensities) but also quantitative data (elemental concentrations). Besides, mapping experiments can offer crucial information to understand how NPs can be bioaccumulated in soft tissues, and results can complement those obtained with other well-established techniques such as spICP-MS.

Applications of LA-ICP-MS in biological tissues have been mainly focused on bioimaging elements in cells [13,14], tumour tissues [15,16], brain sections [17], and tissues from several organs [18–20]. Developments for NPs imaging by LA-ICP-MS are however scarce [21,22], mainly when the studies are focused on biodistribution investigations [23–25]. By other side, the heterogeneity of biological samples and the absence of appropriate reference materials for calibration give rise to several difficulties derived from LA-ICP-MS analysis such as the signal drift over time as well as problems of transport and ionisation at the ICP source [26]. Also, the absence of adequate reference materials or standard matrix-matched materials hinder LA-ICP-MS analysis to obtain quantitative imaging studies. Regarding this barrier, some strategies have been proposed, although there are still disagreements to establish a universal calibration or protocol for an efficient quantification strategy [8,27]. Some proposals for quantitative analysis by LA-ICP-MS include isotope dilution analysis [28] and internal standardization [29]. As an alternative, lab-produced standards based on gel substances are gradually spreading, especially standards made of porcine gelatine [26,30], which results adequate for imaging of biological tissues.

The current research has been focused on novel quantitative imaging studies by LA-ICP-MS for assessing the biodistribution of titanium levels in sea bream tissues (kidney, liver, and muscle) from specimens previously exposed to TiO_2 NPs. Sea bream tissues were subjected to paraffin polymer embedding and thin slice cutting by microtome as a sample pre-treatment. Additionally, a calibration

technique was studied using lab-produced porcine gelatine standards, step that allowed producing not only qualitative, but also quantitative data based- images. Since the multi-element capabilities of ICP-MS, several isotopes of titanium were simultaneously recorded to verify the accurate titanium biodistribution the tissues. Furthermore, several control isotopes were included to verify the sample location (presence of magnesium and calcium, phosphorus) as well as the presence or absence of different sources of contamination (presence of aluminium derived from the glass holders).

5.3 EXPERIMENTAL

5.3.1 Instrumentation

A NexION 2000 Inductively Coupled Plasma Mass Spectrometry (Perkin Elmer, Waltham, MA, USA) equipped with an ESI NWR 213 laser ablation system (ESI New Wave Research Co., Cambridge, UK) was used. The instrument is equipped with triple nickel cone interface and a quartz torch with a quartz injector tube (2.5 mm i.d.). Data acquisition and management was performed with the Syngistix™ Application 2.5 version software (PerkinElmer), which allows data visualization as it is being acquired in real-time. Laser ablation equipment control and management was also performed with ActiveView2 4.1.2 version and data reduction software Iolite4 from Elemental Scientific (Nebraska, USA). An USC-TH ultrasound water bath (45 Hz, 80 W) from VWR International Eurolab S.L (Barcelona, Spain) was used for dispersing NPs before analysis. UV lamp was from Vilber Lourmat™ (Marne-la-Vallee, France) was used to visualise fixed fish tissues, whereas ARE heating and magnetic stirrer from Velp Scientifica (MB, Italy) was used for preparing gelatine standards. A pH-meter model Instruments XS (Carpi Mo, Italy) was used.

5.3.2 Material and reagents

All solutions were prepared with ultrapure water (18.2 MΩ cm of resistivity) obtained from a Milli- Q® IQ 7003 purification device system (Millipore, Bedford, MA, USA). Argon (99.998%) and Helium (99,999%) were from Nippon Gases (Madrid, Spain). Mono-

elemental 1000 mg L^{-1} standard of titanium [$(NH_4)_2TiF_6$] was from PerkinElmer. Other reagents as sodium hydroxide, sodium hydrogen carbonate, hyperpure nitric acid 69% (w/v), and absolute ethanol were from Panreac (Barcelona, Spain). Porcine-skin gelatine, type A, bloom strength 300, and formaldehyde solution (36.5-38% in water) were from Sigma-Aldrich (Osterode, Germany). Glass sample-holders were from Labbox (Barcelona, Spain). To avoid metal contamination, all glassware and plastic ware were washed with ultrapure water and kept in 10% (v/v) nitric acid for 48 h, and then rinsed several times with ultrapure water before use.

5.3.3 Aquaculture exposure experiments

Sea bream (*Sparus aurata*) exposure assays with 45 nm TiO_2 NPs were carried out at the facilities of the Aquaculture Cluster Technology Centre CETGA (Ribeira – A Coruña, Spain). Fish specimens were exposed to 45 nm TiO_2 NPs for 90 days and samplings were performed each 15 days establishing six different exposure times (0, 15, 30, 45, 60, 75 and 90 days). Exposure assays were performed at three 45 nm TiO_2 NPs concentration levels (0.25, 0.75 and 1.5 mg kg^{-1}, concentrations expressed as mg of TiO_2 NPs per fish feed mass in kg) and the specimens (15 sea breams) were daily fed with fish feed doped with TiO_2 NPs at several concentrations. Sea breams followed the standard aquaculture procedure for their growth under controlled conditions and were fasted for one day before being killed with an overdose of anaesthetic. Different sections (muscle-skin, liver, and kidney) from three fishes under each exposure conditions (TiO_2 NPs concentration and exposure time) were obtained. The samples were frozen and preserved at -20^{o}C until analysis.

5.3.4 Fish tissue preparation

Kidney, liver, and muscle tissues were from sea bream specimens exposed to 45 nm TiO_2 NPs at different times (up to 90 days) and from unexposed sea bream (control samples). Sample preparation consisted of immersing the fish tissues (kidney, liver, and muscle) in 4% paraformaldehyde at pH 7.0 overnight and 4^{o}C to harden the tissue (fixation process). The tissues were then subjected to a three-stage

washing step (dehydration process) with distilled water, 50% ethanol and 70% ethanol (the tissues were soaked in each solvent for 15 min), and then, the tissues were kept in 70% ethanol indefinitely before being embedded in blocks of paraffin polymer. The paraffin blocks were cut into 5.0 µm thin slides using a standard microtome, obtaining at least 5 replicates per sample to have enough samples to test and optimise the developed methodology as well as for the final application for quantitative imaging. Finally, the 5.0 µm slices were individually placed on microscope glass sample-holders. Additionally, paraffin blocks with no- embedded sample were also prepared and slices were also cut as used as blanks. All paraffin slides (Figure S1, ESI) were covered with glass sample-holders and kept at room temperature before analysis.

5.3.5 Gelatine standards preparation

Lab-produced gelatine standards were prepared by dissolving gelatine porcine skin (500 mg) in 5.0 mL of ultrapure water (gelatine concentration at 10% (m/v)). Porcine gelatine mixtures were then heated at 70^{o}C (use of a magnetic heater) until complete liquefaction of the mixture, followed by homogenization under continuous and soft stirring for 10 min. Liquid paraffin-based titanium standards from 0.1 to 2.0 µg g^{-1} (drops of 5.0 µL) were carefully pipetted (avoiding bubble formation) and displayed onto microscope glass sample-holders. Standards were covered and left to dry at room temperature. The titanium-based gelatine standards were analysed in triplicated by LA- ICP-MS.

5.3.6 LA-ICP-MS measurements

The assessment of Ti spatial distribution concentrations in fish tissues was performed by LA-ICP- MS under optimized operating conditions summarized in **Table 5.1**. The instrument was daily-tuned following the standard procedure based on ablating a NIST SRM 612 standard (50 µm diameter spot, repetition rate of 20 Hz, scan speed of 20 µm s^{-1}, and laser energy of 10.0 J cm^{-2} in line - scanning mode). Nebulization gas flow rate and ICP-MS parameters were also daily tuned by monitoring and verifying intensities as follows: ^{9}Be (≥ 15,000 counts), ^{24}Mg (≥ 270,000 counts), ^{115}In (≥ 400,000 counts),

^{208}Pb (≥ 235,000 counts), ^{238}U (≥ 400,000 counts), $^{232}Th^{16}O/^{232}Th$ (<0.02), $^{232}Th/^{238}U$ (>0.07) and Background (< 3.0). In addition to Ti isotopes (^{46}Ti, ^{47}Ti, ^{48}Ti, and ^{49}Ti), other isotopes such as ^{25}Mg, ^{26}Mg, ^{31}P, and ^{42}Ca were monitored to ensure fish tissue ablation, and ^{27}Al to ensure non-ablation of the glass slide.

Table 5.1. LA-ICP-MS operating conditions.

ICP-MS parameter (units)	Value
Instrument	Nex Ion 2000
Nebulizer gas flow (L min^{-1})	0.90 - 1.00 (daily optimised)
Auxiliary gas flow rate (L min^{-1})	1.2
Plasma gas flow (L min^{-1})	15
ICP RF power (W)	1600
Isotopes monitored	^{25}Mg, ^{26}Mg, ^{27}Al, ^{31}P, ^{42}Ca ^{46}Ti, ^{47}Ti, ^{48}Ti, ^{49}Ti
Dwell time (ms)	50 (^{25}Mg, ^{26}Mg, ^{27}Al, ^{31}P, ^{42}Ca) 10 (^{46}Ti, ^{47}Ti, ^{48}Ti, ^{49}Ti)

LA-ICP-MS parameter (units)	Value
Laser	Nd:YAG (213 nm)
Tygon® interface tube	3.5 m length – 1/16 inch i.d.
Ablation mode	Scan line
He flow rate (mL min^{-1})	900
Spot Size (μm)	110
Fluence (J cm^{-2})	0.40
Scan speed (μm s^{-1})	50
Repetition rate (Hz)	20
Ablation Depth (μm)	0
Laser warm-up (s)	10
Laser wash-out (s)	15

5.3.7 Data treatment

Spectra, data analysis and quantitative images were obtained using the data reduction software Iolite4. NetCDF files from ICP-MS and Laser Log files from laser ablation equipment were exported from the instrumentation software and attached to Iolite4 aiming optimum results after performing some steps: baseline subtraction, quantification using gelatine standards, assessment of the obtained spectra channels (elements selected in the developed methodology), and image construction selecting CellSpace as a map type. Data tables were also exported as Excel files.

5.4 RESULTS AND DISCUSSION

5.4.1 Methodology development

5.4.1.1 Preliminary studies

Based on the available literature, low laser energy conditions and a relatively high scanning rates are recommended for LA-ICP-MS when analysing thin slides of biological tissues polymer- embedded [15,19,22,31,32]. The use of soft ablation conditions by scan line as an ablation work- mode are specially needed when analytes such as NPs must be imaged since longer periods of time laser incidence and too high laser energy would lead to NPs ionisation resulting in a continuous signal (smoother discrete signals) [22] instead of well-defined and recognised peaks in the continuous LA-ICP-MS record. However, there are many discrepancies in the published literature regarding the influence of other parameters (spot size, frequency, dwell time, and helium flow) on metal imaging by LA-ICP-MS and the significant differences can be attributed to the different capabilities of the laser instrumentation.

Several titanium isotopes (^{46}Ti, ^{47}Ti, ^{48}Ti, and ^{49}Ti) were monitored but only ^{48}Ti (most abundant isotope) was used for quantification (other minor isotopes were used as qualifier isotopes to verify the presence of titanium). In addition, a preliminary selection of other elements, as control isotopes, was performed for establishing the borders between paraffin-embedded tissue and paraffin-free tissue, and also to control the avoidance of glass slide ablation. Minor isotopes such as ^{25}Mg and ^{26}Mg, ^{31}P, and ^{42}Ca (**Table 5.1**) were

selected as controls to ensure the ablation of the embedded fish tissue, whereas ^{27}Al was used to detect the ablation of the glass slide. The potential ablation of the glass holder can be also observed in the exported images (ActiveView™ software) such as those shown in **Figure S5.**2 (ESI) where a second black line appears in the scan line when ablating the glass slide in addition to the fish tissue polymer-embedded and paraffin polymer. Exported images from ActiveView™ software help also to visualise the borders between paraffin-embedded tissue / paraffin-free tissue and the glass holder (**Figure S5.3C**, ESI) and to show that the embedded biological tissue is not perfectly homogeneous (**Figure S5.3A-B**, ESI).

5.4.1.2 Laser ablation operating parameters

Experiments at high fluencies or laser energies (>0.50 J cm^{-2}) led to a partial ablation of the glass holder since the increase of the registered ^{30}Al intensities (ActiveView™ exported images in **Figure 5.1**), and the laser energy was therefore fixed at 0.40 J cm^{-2}, which is a rather low energy but enough to ablate the sample without a strong ablation of the paraffin in areas where there is no sample embedded.

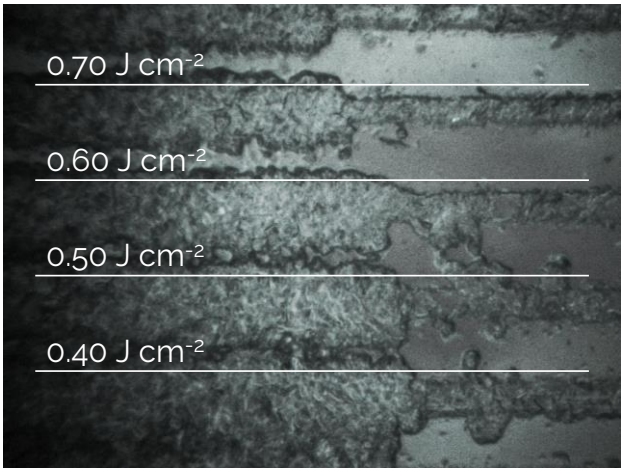

Figure 5.1. Exported image from ActiveView™ software illustrating the effect of the laser fluency on the ablation of the embedded fish tissue and embedded fish tissue plus paraffin.

The scanning rate should have been relatively high to avoid long laser incidence to NPs. Therefore, rates between 20 and 90 µm s^{-1} were investigated (LA-ICP-MS time vs intensity plots in **Figure S5.4**, ESI), and a rate of 50 µm s^{-1} was finally selected due to good stability of signal derived from the control isotopes and the well-defined peaks derived from TiO_2 NPs. This result is in good agreement with those previously reported which suggest the registration of discrete events minimising laser time incidence [22].

Remaining operating conditions are listed in **Table 5.1**. Regarding the dwell time, 50 ms were used for a proper acquisition of control isotopes (^{25}Mg, ^{26}Mg, ^{27}Al, ^{31}P and ^{42}Ca), whereas Ti isotopes were recorded at a dwell time of 10 ms for improving the discrimination between single peak- signals derived from TiO_2 NPs ablation and background (ionised titanium) as shown in **Figure S5.5**.

Finally, before proceeding to the imaging/mapping studies, experiments were carried out to check that 100% of the sample was ablated in a single ablation scan, and experiments based on two and three consecutive scans (two and three ablation lines over same location). Results showed that titanium records after two and three consecutive scans were negligible, and values were closed to those obtained when ablating the blanks (paraffin polymer). Therefore, we can affirm that under the optimised conditions the embedded sample is totally ablated in one single scan.

5.4.2 Calibration and limit of detection

Metals embedded in porcine gelatine standards are recommended for laser imaging of soft tissues although there are differences in the proposed procedures, mainly the heating temperature and the drop volumes used for metals embedding [21,22,33–35]. Before selecting the most suitable conditions to apply to the calibration strategy, the volume of added drop (from 2.5 µL to 20 µL) as well as the addition of two successive drops was studied. Better dispersion of the added titanium standard was found when using small drop sizes (2.5 and 5.0 µL), whereas large drop sizes led to heterogeneity and an oval shaped dispersion, factors that increase the occurrence of bubbles in the

embedded drop. Moreover, the addition of two successive drops of 2.5 µL, 5.0 µL and 10.0 µL also led to lack of homogeneity and stability of the dispersed drop and a higher occurrence of bubbles. Therefore, titanium-based gelatine calibration was prepared by dispersing only one 5.0 µL drop of the titanium standards. Each titanium standard solution was embedded in triplicate, covering titanium concentrations within the 0.1 – 2.0 µg g^{-1} range (**Table S5.1**).

Pure gelatine was used as a blank and as shown in **Table S5.1** titanium signals were close to those obtained when ablating the paraffin polymer used for soft tissue embedding. The titanium concentrations studied led signals clearly different from those obtained when ablating gelatine blanks (**Table S5.1**), which makes them suitable for application in the biological tissues under study. For all cases, titanium-based gelatine standards were completely ablated by covering the whole embedded droplet. **Figure 5.2** shows the registered signals from a calibration and good linearity was obtained for all cases. In addition, the titanium-based gelatine standard preparation procedure has been found to offer a homogeneous titanium distribution in the embedded droplet since the high stability of the recorded signal (**Figure 5.2B**).

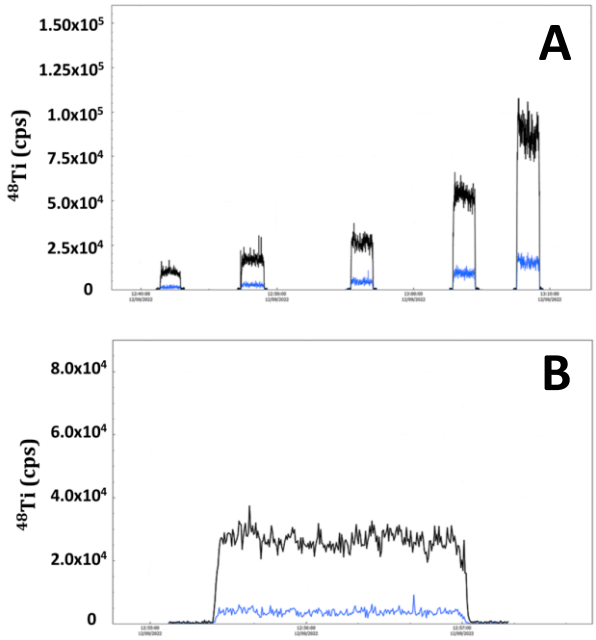

Figure 5.2. LA-ICP-MS spectra (time vs intensity) for ^{48}Ti (black) and ^{46}Ti (blue) in the gelatine standards displaying increasing Ti-doped concentrations: 0.1, 0.2, 0.4, 0.8 and 2.0 µg g^{-1} (from left to right in A). Good signal stability is observed in B for a standard at 0.4 µg g^{-1}.

A limit of detection (LOD) of 0.087 µg g^{-1} was obtained, and it was calculated using the 3σ criteria (three times standard deviation from eleven blank porcine gelatine measurements) and the slope of the titanium-based gelatine calibration curve ($4.21\times10^4 \pm 0.39\times10^4$, the mean value of three different calibration as shown in **Table S5.1** [10,11,36,37]. In addition, the LOD was also established by ablating paraffin polymer blanks (paraffin polymer used for embedding the fish soft tissue), and the 3σ criteria (mean slope of the titanium-based gelatine calibration curve) gave a value of 0.036 µg g^{-1}, a two times lower value that the obtained when using the gelatine blanks.

5.4.3 Imaging studies and spatial biodistribution of titanium

Soft tissues embedded in paraffin slides cannot be distinguished from paraffin slides under natural light, and 365 nm UV light

irradiation was used to obtain clear images for distinguishing soft tissues embedded in paraffin (**Figure S5.1**, ESI). These images were uploaded in the Iolite software, and they will be useful to correlate the sample tissue areas with the variations and recorded intensities in the LA-ICP-MS tests (verification of sample ablation when monitoring control elements such as ^{26}Mg). The area of interest in the embedded samples was delimited to be close to 6×6 mm (length×width) which are similar to those reported in other applications [13,15,16,18,19,36]. In order to avoid large ablation times that could drift the recorded signal, the selected areas were ablated in two separate analyses (an y-axis space of 75µm between the two ablated areas), and both images were then attached in a final image.

5.4.3.1 Kidney tissues

Figure 5.3 shows a set of 5.4×7.9 mm images of a kidney tissue from a sea bream previously exposed to TiO_2 NPs, whereas Figure 5.4 displays 6.0×3.6 mm images for a kidney tissue from an un-exposed sea bream specimen (a complete set of images can be found in ESI as **Figure S5.6** and **S5.7**). The selected control isotope (^{26}Mg in **Figure 5.3B** and **5.4B**) allows to distinguish the areas of the sample and to correlate this data to the UV-light images (**Figure 5.3A** and **5.4A**) and to the Ti distribution maps (**Figure 5.3C** and **5.4C**). ^{26}Mg signals (**Figure 5.3B**) were found to vary within the 1.0×10^5 - 2.0×10^5 counts per second range, whereas the images corresponding to titanium reflect some hot-spot areas, involving intense and discrete peaks which implies TiO_2 NPs bioaccumulation (**Figure 5.3C** for ^{48}Ti, and **Figure S5.6E**,**F** for ^{46}Ti). The recorded discrete signals have offered different intensities that could be attributed to several TiO_2 NPs agglomerates (typical TiO_2 NPs behaviour). The presence of TiO_2 NPs agglomerates led to higher titanium concentrations than the highest gelatine-based standard (2.0 µg g^{-1}) and therefore to define/discriminate the hotspots from the homogeneous ionic Ti a value of 0.8 µg g^{-1} (green colour in the images) was established. In addition to the hotspots, the presence of blue-colour regions corresponded to continuous signals derived from ionic titanium, which

occur in the analysed tissue at low concentrations (always below 0.20 $\mu g\ g^{-1}$).

Images for kidney tissues from an un-exposed sea bream (**Figure 5.4** and **Figure S5.7**) show clearly a lower amount of ionic titanium throughout the tissue, and hotspots derived from TiO_2 NPs were only observed in a small region of the ablated sample when monitoring ^{48}Ti and ^{46}Ti (**Figure 5.4C** and **Figure S5.7E**,**F**). The presence of TiO_2 NPs in unexposed specimens may be attributed to the background TiO_2 NPs in sea bream and/or contamination during the exposure trials.

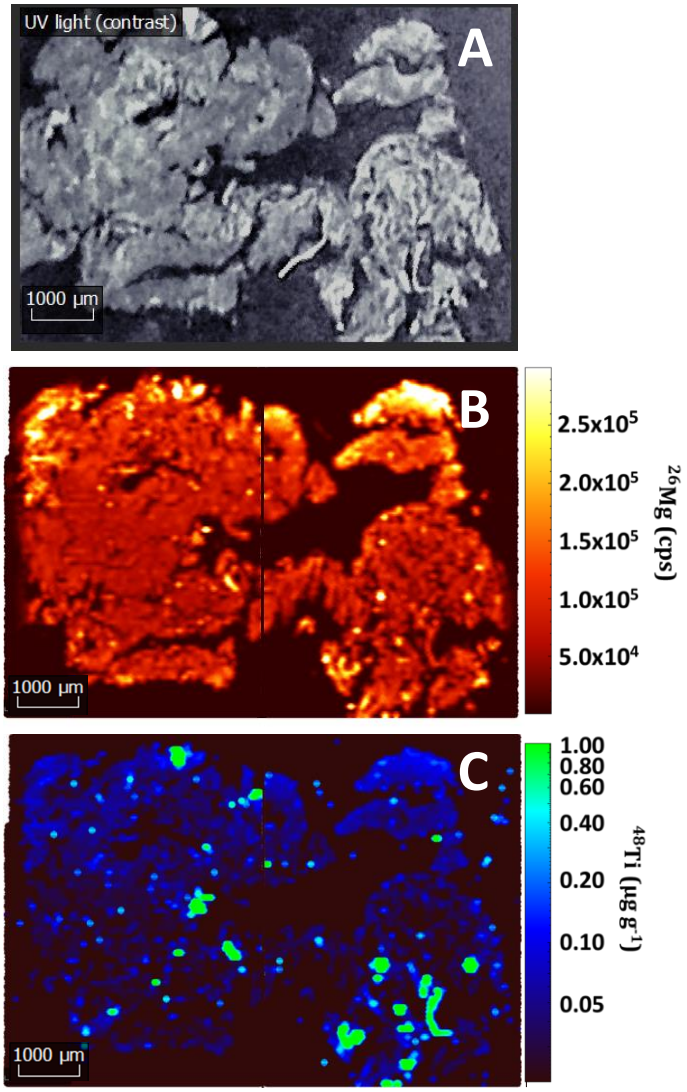

Figure 5.3. Images for a kidney tissue from a sea bream specimen exposed to 45 nm TiO_2 NPs (dietary exposure at 1.5 mg kg^{-1}) for 90 days tissues: sample image under UV light (A), ^{26}Mg map intensities (B), and ^{48}Ti map concentrations (C).

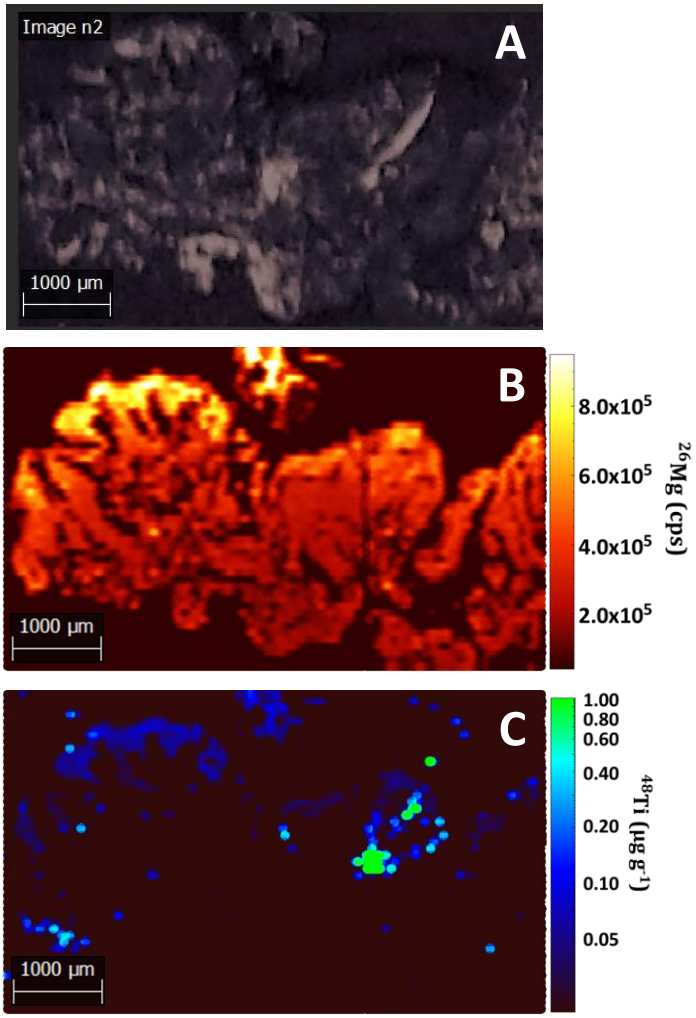

Figure 5.4. Images for a kidney tissue from an un-exposed sea bream specimen (sampling at 75 days): sample image under UV light (A), ^{26}Mg map intensities (B), and ^{48}Ti map concentrations (C).

5.4.3.2 Liver tissues

Ablation areas for embedded liver tissues were 5.8×5.4 mm (exposed sea bream) and 8.6×4.6 mm (un-exposed sea bream) and images are given in **Figure S5.8** and **S5.9** (ESI). Good homogeneity of the embedded tissues was observed since the ^{26}Mg intensities are

constant (from 2.0×10^5 to 3.0×10^5 cps) throughout the tissue. Different hotspots were observed in liver from TiO_2 NPs exposed sea bream (**Figure S5.8**) although in a lower proportion than those measured in kidney tissues. The lower bioaccumulation of titanium in liver than in kidney was verified by ICP-MS after microwave acid digestion (total Ti) and by spICP-MS after enzymatic hydrolysis (TiO_2 NPs) [38] as shown in **Table S5.2** (ESI). Likewise, the Ti biodistribution maps, especially the hotspots, are confirmed with the use of two isotopes (quantifier and qualifier). For this case (**Figure S5.8C**,**E**, ESI) a value of 0.25 µg g^{-1} was used as an upper limit (the limit of detection limit was 0.10 µg g^{-1} as given in **Table S5.1**). Results for un-exposed sea bream (**Figure S5.9**, ESI) show few colour-clear spots which do not follow a cluster (agglomerated) and which match with a lower titanium concentration.

5.4.3.3 Muscle tissues

Despite the difficulties for obtaining homogeneous clean cuts (slides) when using the histological sample pre-treatment for muscle tissues, the paraffin regions and the regions embedding the sample [4.4×5.5 mm (exposed sea bream) and 4.4×5.9 mm (un-exposed sea bream)] can be clearly distinguished when recording the ^{26}Mg a control isotope (**Figure S5.10B** and **S5.11B**, ESI). However, Ti-based maps for muscle tissues from exposed and un-exposed sea breams (**Figure S5.10** and **S5.11**), have been found to be less homogeneous than those obtained for kidney and liver tissues, which is directly attributed to a less efficient muscle embedding and microtome cuts. LA-ICP-MS time vs intensity plots for certain scans when mapping a kidney tissue (**Figure 5.5A**) and a muscle tissue (**Figure 5.5B**) show intense peak signals only when ablating areas with embedded kidney, whereas embedded muscle shows intense signals when ablating the tissue and the sample-free paraffin. As expected, based on TiO_2 NPs and total Ti determinations (**Table S5.2**), low Ti concentrations were mapped in sea bream muscle (titanium concentrations around 0.10 µg g^{-1}).

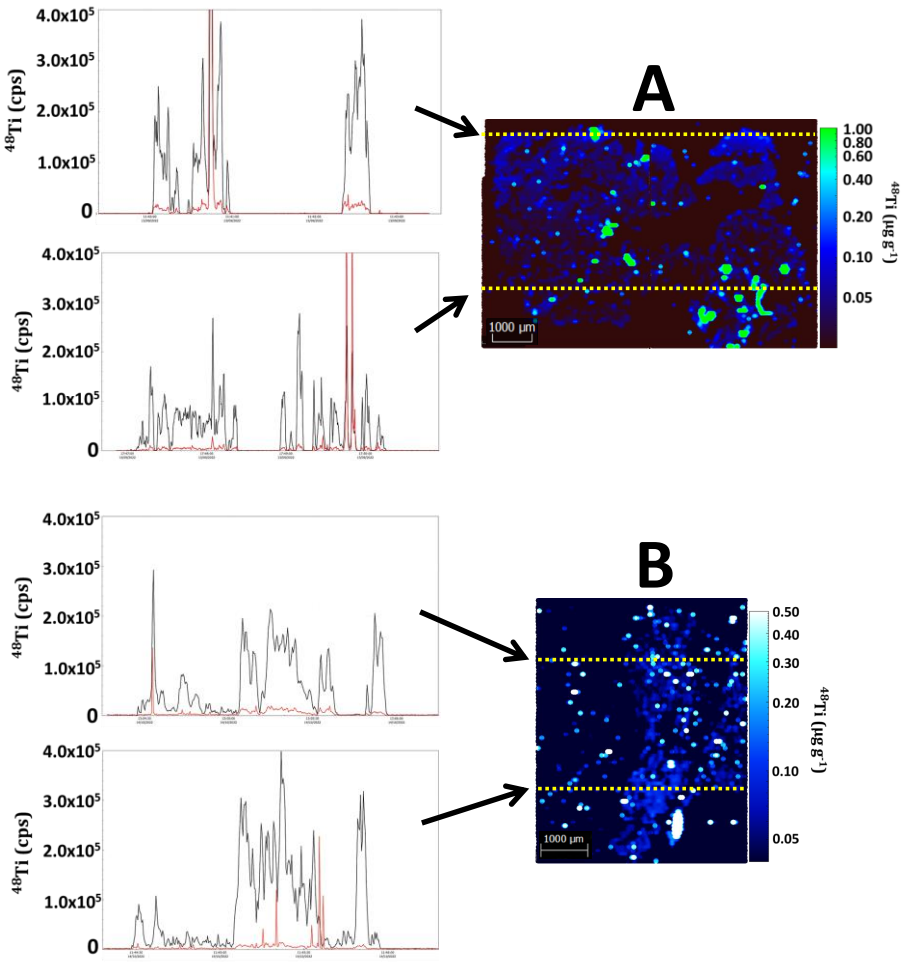

Figure 5.5. LA-ICP-MS image for a kidney tissue from a sea bream specimen exposed to 45 nm TiO_2 NPs (dietary exposure at 1.5 mg kg^{-1}) for 90 days (A) and for a muscle tissue from a sea bream specimen exposed to 45 nm TiO_2 NPs (dietary exposure at 1.5 mg kg^{-1}) for 75 days (B) showing LA-ICP-MS time vs intensity plots by recording ^{48}Ti (red) and ^{26}Mg (black).

5.5 CONCLUSIONS

The optimised LA-ICP-MS methodology by using high-rate scanning and low laser energy allowed sensitive and quantitative bioimaging studies with high spatial resolution. Lab-produced porcine gelatine

standards have been demonstrated to offer reliable capabilities for quantification and images based on concentrations rather than signal have been novelty and successfully obtained. LA-ICP-MS biodistribution maps from sea bream tissues have revealed the presence of Ti homogeneous distributed in the tissues, and as hot-spots derived from TiO_2 NPs in kidney and liver from TiO_2 NPs exposed sea bream specimens. Improvements, however, are required when imaging fish muscle tissues since the difficulties when embedding takes place. There are not applications for this type of tissues and the use of slides with large thickness could improve the homogeneity of the embedded tissue. Further LA-ICP-MS adjustments will be required such as the use of slightly higher energy to ablate the tissue in a single ablation scan and the use of longer washing times for an efficient removal of the ablated material.

Moreover, results show a potential of LA-ICP-MS for complementing the results obtained by other analytical techniques for distinguishing the presence of ionic and nanoparticulated species of an element since the local distribution of nanoparticles, in addition to the ionic element, can be mapped. Further potential applications are therefore expected for assessing the distribution of other nanoparticles in conventional and un-conventional tissues by quantitative LA-ICP-MS imaging.

SUPPLEMENTARY INFORMATION

Table S5.1. Gelatine standards as a calibration strategy: description, analytical performance and sensitivity obtained. (^{48}Ti intensities from 5 gelatine-droplets).

Concentration (μg g^{-1})	^{48}Ti Mean Intensity (cps)	RSD (%)	^{46}Ti Mean Intensity (cps)	RSD (%)
Paraffin polymer	9.70×10^{2}	3	2.46×10^{2}	10
Porcine gelatine	4.66×10^{3}	6	6.67×10^{2}	8
0.10	1.03×10^{4}	5	1.07×10^{3}	14
0.20	1.48×10^{4}	1	1.39×10^{3}	4
0.40	2.42×10^{4}	1	2.31×10^{3}	3
0.80	4.39×10^{4}	2	4.33×10^{3}	2
2.00	8.95×10^{4}	1	8.72×10^{3}	1
	Sensitivity			
Slope ^{48}Ti (n=3)	$4.21\times10^{4} \pm 0.39\times10^{4}$		($r^2 \geq 0.990$)	
Paraffin polymer	LOD (μg g^{-1})		0.036	
Porcine gelatine matrix	LOD (μg g^{-1})		0.087	

Table S5.2. Total titanium and TiO_2 NPs in fish tissues from exposed sea bream (N1) and unexposed sea bream (N2).

Sample tissue	sp-ICP-MS (particles g^{-1})	SD	ICP-MS (μg g^{-1})	SD
Kidney N1	3.88×10^{6}	1.78×10^{5}	0.83	0.20
Kidney N2	---	---	0.12	0.04
Liver N1	6.67×10^{6}	3.65×10^{5}	0.51	0.05
Liver N2	---	---	0.21	0.17
Muscle N1	8.14×10^{5}	8.90×10^{4}	0.23	0.15
Muscle N2	---	---	< LOD	---

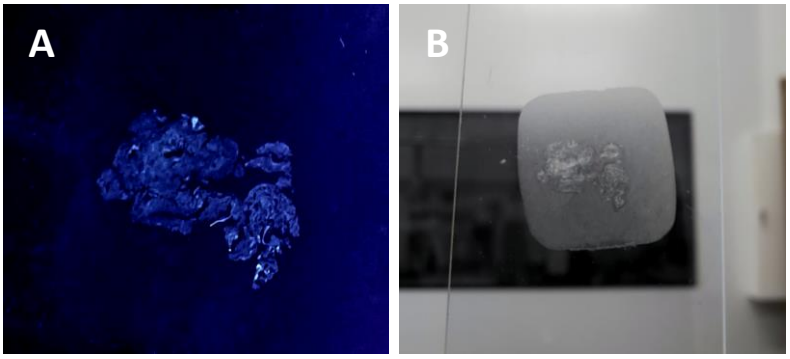

Figure S5.1. Thick paraffin slides (5.0 µm) of fish tissues obtained after sample pre-treatment: (A) under UV light and (B) natural light. Sample description: kidney tissue from sea bream exposed at 1.5 mg kg^{-1} TiO_2 NPs (45 nm) for 90 days.

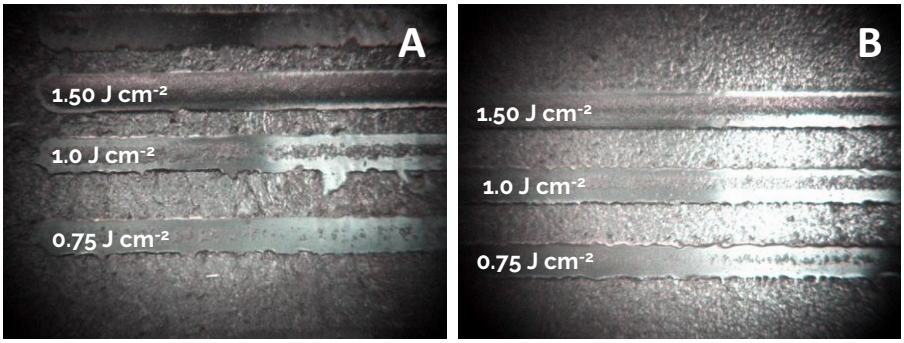

Figure S5.2. Exported images from ActiveView™ software (dark line under sample tissue) using laser energies for (A) sample fish tissue and (B) paraffin polymer under several laser fluencies.

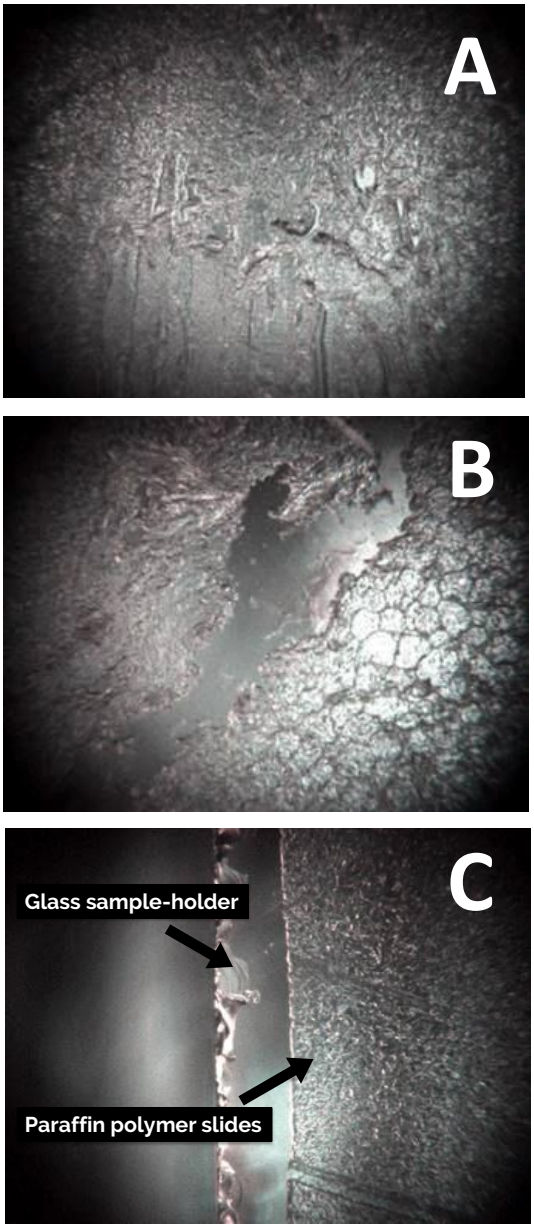

Figure S5.3. Exported images from ActiveView™ software illustrating the heterogeneity of the embedded samples (A,B) and the borders between paraffin-embedded tissue / paraffin-free tissue and the glass holder (C).

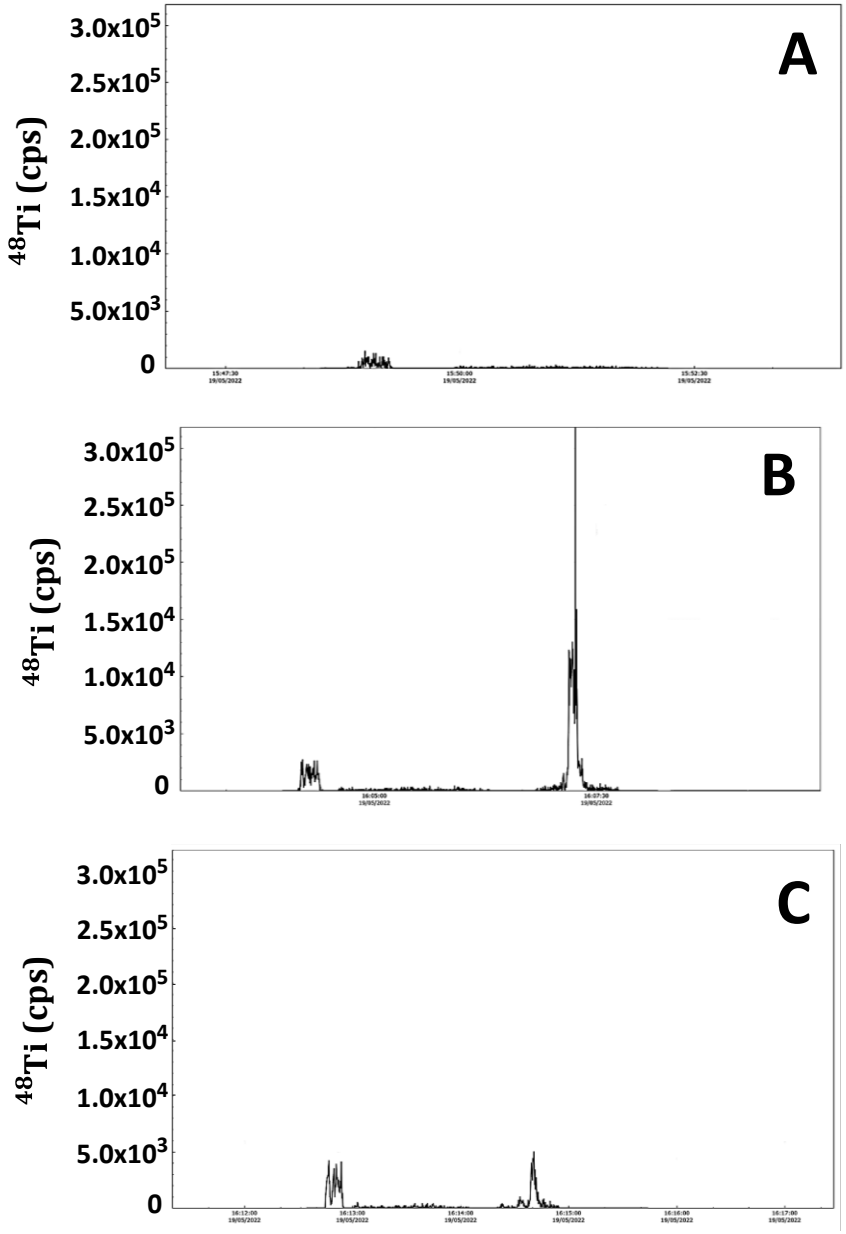

Figure S5.4. LA-ICP-MS time vs intensity plots for a kidney tissue obtained at scanning rates of 30 µm s^{-1} (A), 60 µm s^{-1} (B), and 90 µm s^{-1} (C).

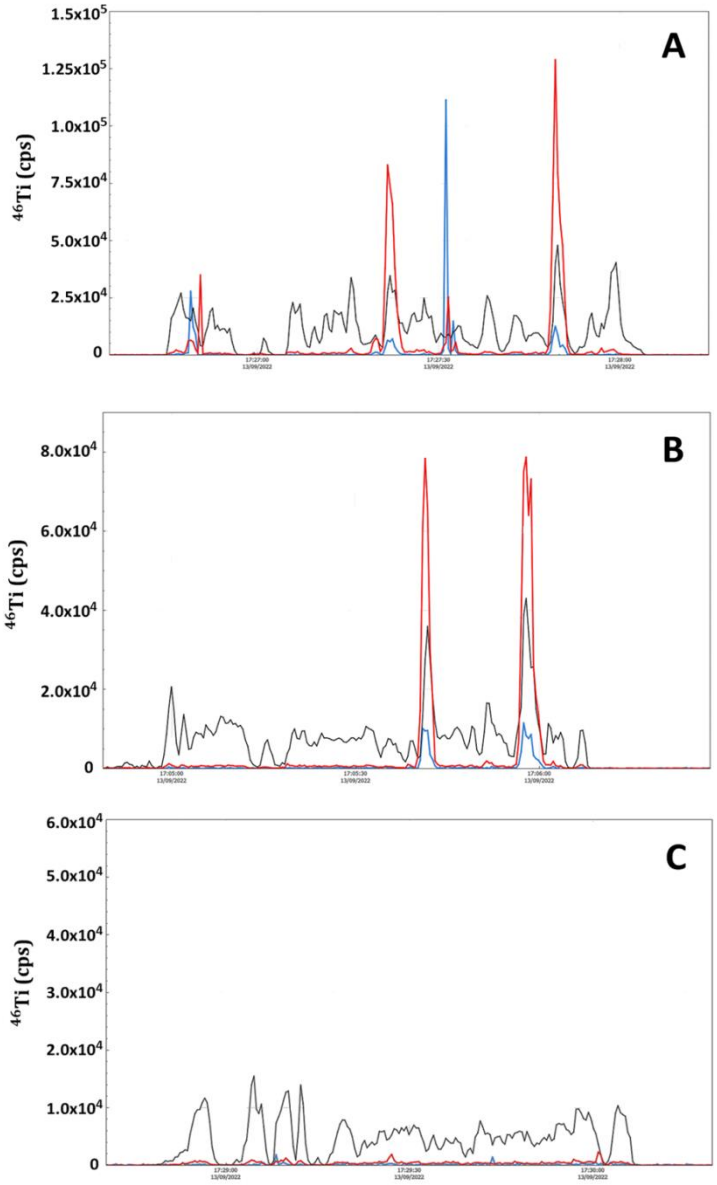

Figure S5.5. LA-ICP-MS time vs intensity plots for a kidney tissue by recording ^{48}Ti (red), ^{46}Ti (blue), and ^{26}Mg (black). Scale referred only to ^{46}Ti intensities: scan implying the presence of TiO_2 NPs (A and B) and the absence of TiO_2 NPs (C) in tissues from exposed sea bream.

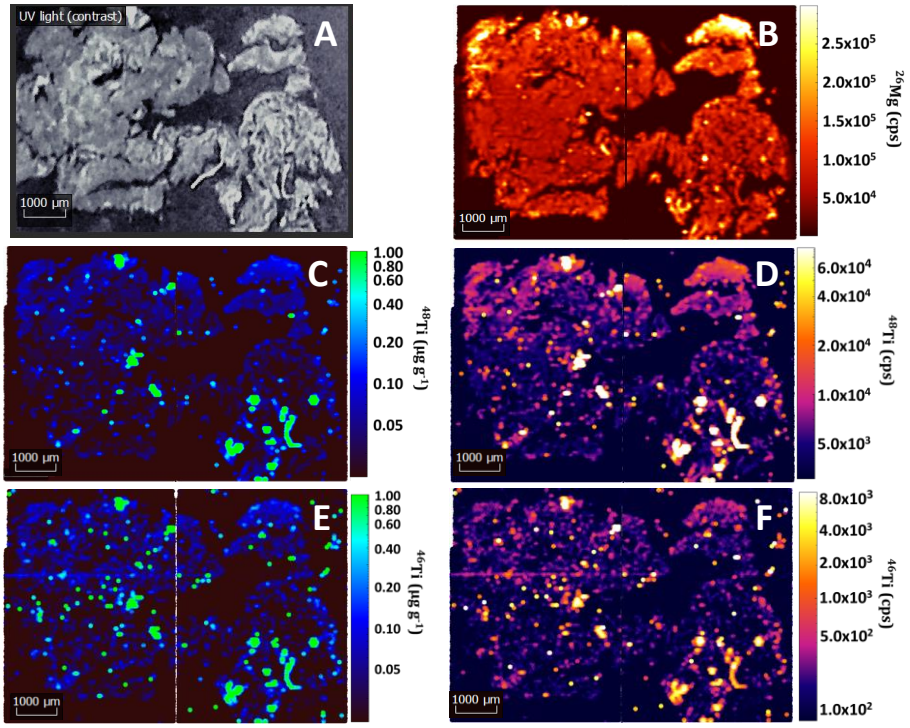

Figure S5.6. Images for a kidney tissue from a sea bream specimen exposed to 45 nm TiO_2 NPs (dietary exposure at 1.5 mg kg^{-1}) for 90 days tissues: sample image under UV light (A), ^{26}Mg map intensities (B), ^{48}Ti map concentrations (C), ^{48}Ti map intensities (D), ^{46}Ti map concentrations (E), ^{46}Ti map intensities (F).

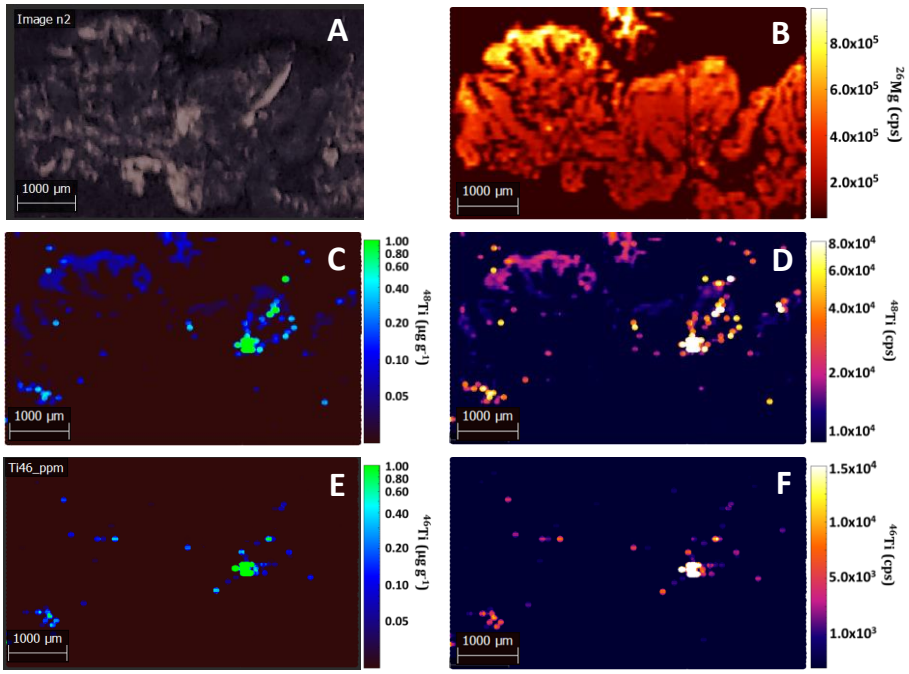

Figure S5.7. Images for a kidney tissue from an un-exposed sea bream specimen (sampling at 75 days): sample image under UV light (A), ^{26}Mg map intensities (B), ^{48}Ti map concentrations (C), ^{48}Ti map intensities (D), ^{46}Ti map concentrations (E), ^{46}Ti map intensities (F).

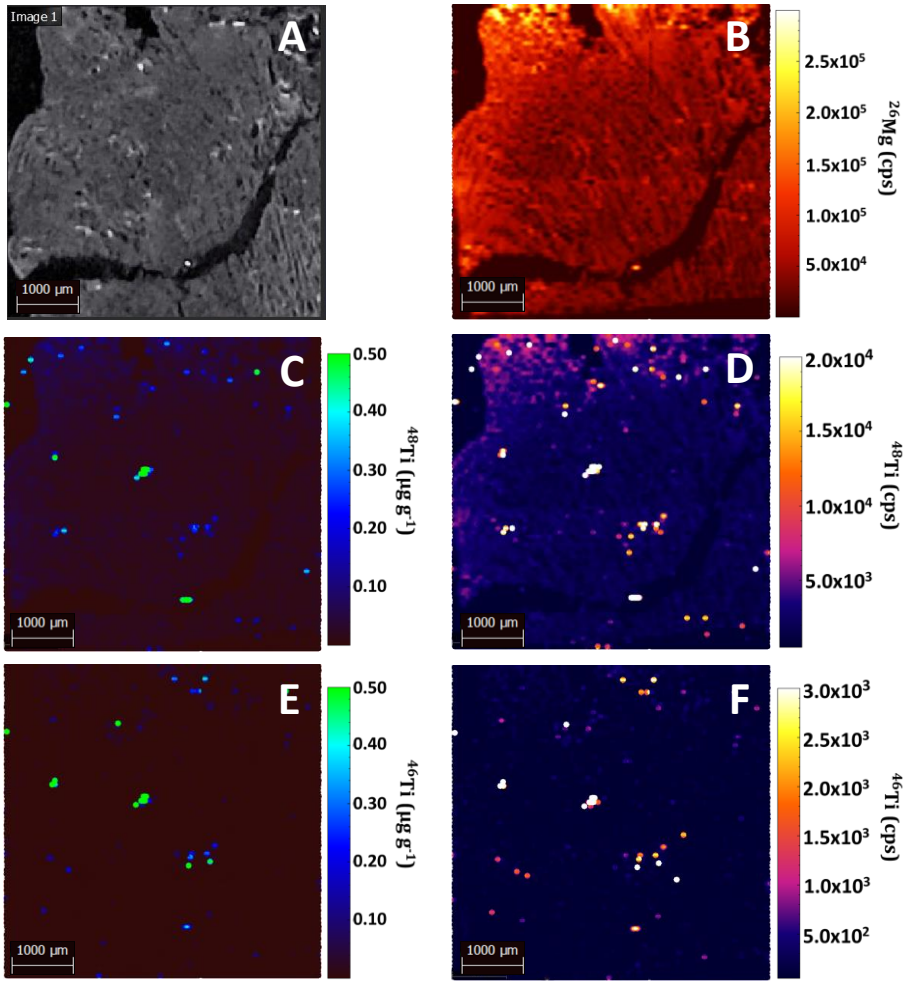

Figure S5.8. Images for a liver tissue from a sea bream specimen exposed to 45 nm TiO_2 NPs (dietary exposure at 1.5 mg kg^{-1}) for 75 days tissues: sample image under UV light (A), ^{26}Mg map intensities (B), ^{48}Ti map concentrations (C), ^{48}Ti map intensities (D), ^{46}Ti map concentrations (E), ^{46}Ti map intensities (F).

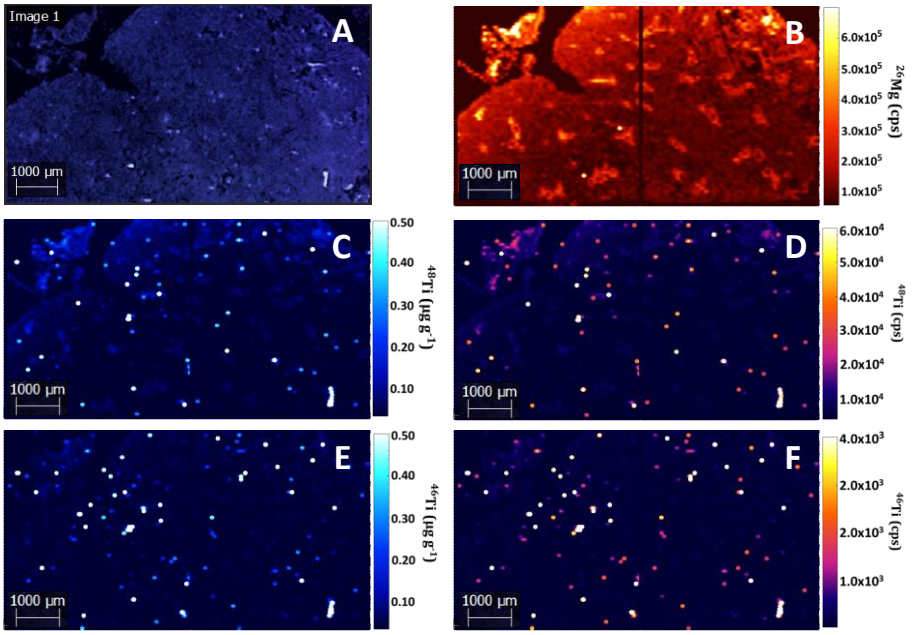

Figure S5.9. Images for a liver tissue from an un-exposed sea bream specimen (sampling at 45 days): sample image under UV light (A), ^{26}Mg map intensities (B), ^{48}Ti map concentrations (C), ^{48}Ti map intensities (D), ^{46}Ti map concentrations (E), ^{46}Ti map intensities (F).

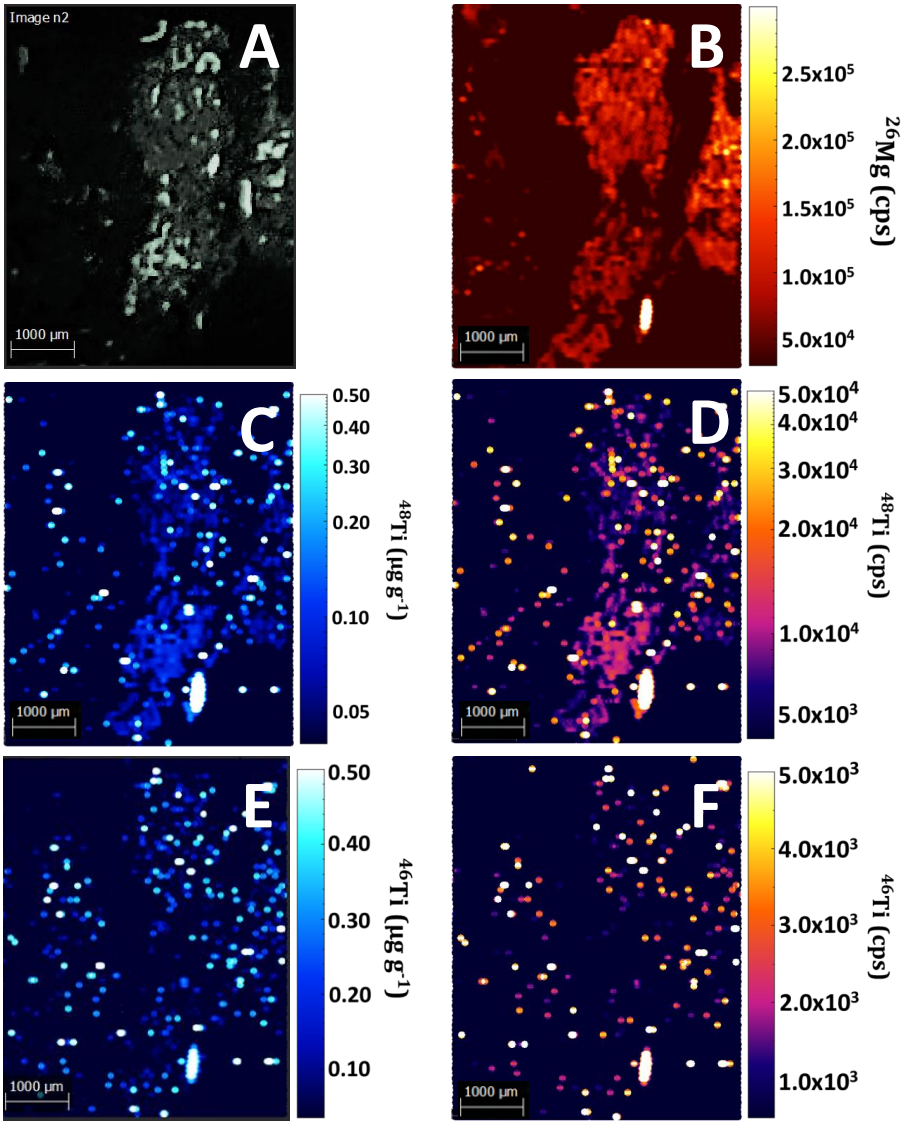

Figure S5.10. Images for a muscle tissue from a sea bream specimen exposed to 45 nm TiO_2 NPs (dietary exposure at 1.5 mg kg^{-1}) for 75 days tissues: sample image under UV light (A), ^{26}Mg map intensities (B), ^{48}Ti map concentrations (C), ^{48}Ti map intensities (D), ^{46}Ti map concentrations (E), ^{46}Ti map intensities (F).

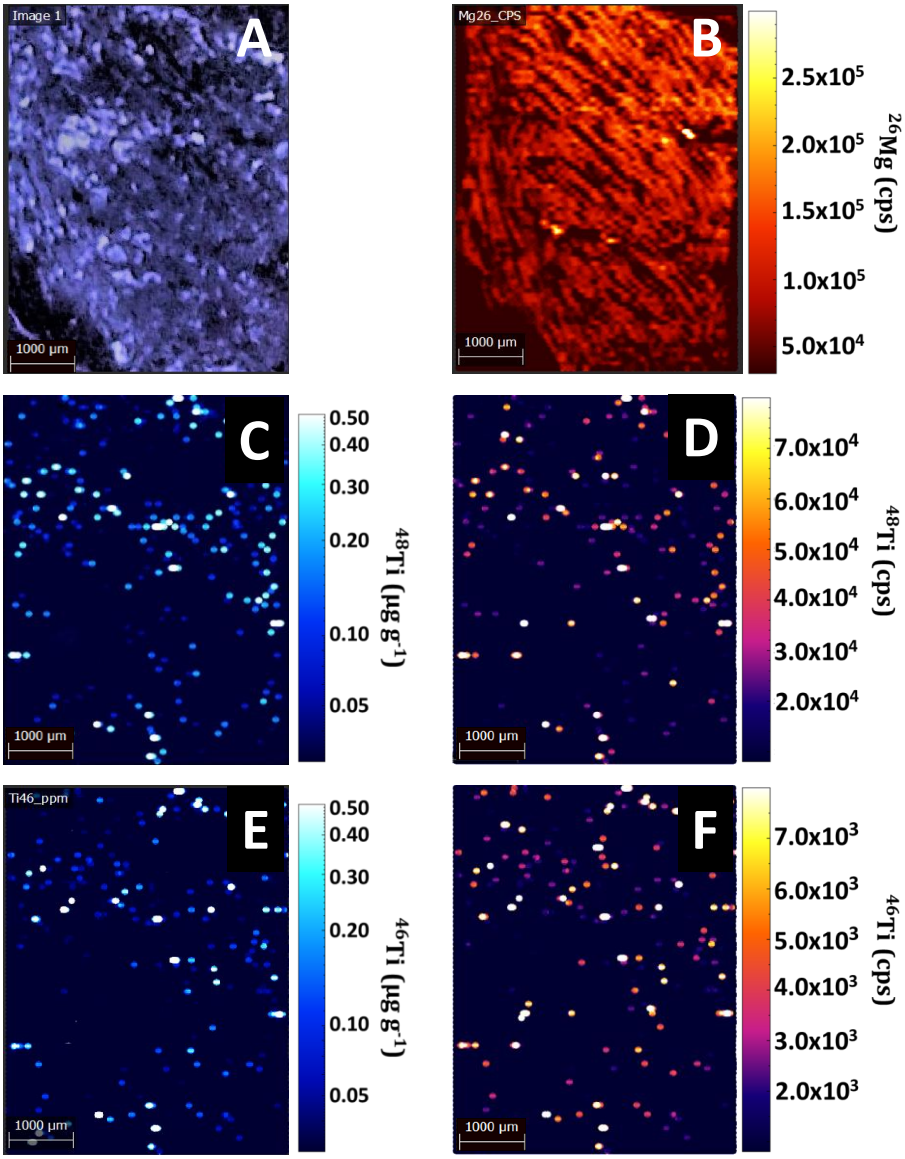

Figure S5.11. Images for a liver tissue from an un-exposed sea bream specimen (sampling at 45 days): sample image under UV light (A), ^{26}Mg map intensities (B), ^{48}Ti map concentrations (C), ^{48}Ti map intensities (D), ^{46}Ti map concentrations (E), ^{46}Ti map intensities (F).

REFERENCES

[1] J.R. Peralta-Videa, L. Zhao, M.L. Lopez-Moreno, G. de la Rosa, J. Hong, J.L. Gardea- Torresdey, Nanomaterials and the environment: a review for the biennium 2008–2010, J. Hazard. Mater. 186 (2011) 1–15. https://doi.org/10.1016/j.jhazmat.2010.11.020.

[2] L. Calzolai, D. Gilliland, F. Rossi, Measuring nanoparticles size distribution in food and consumer products: a review, Food Addit. Contam. Part A. 29 (2012) 1183–1193. https://doi.org/10.1080/19440049.2012.689777.

[3] M. Hassellöv, J.W. Readman, A.E. James, F.R. Ae, K. Tiede, Nanoparticle analysis and characterization methodologies in environmental risk assessment of engineered nanoparticles, Ecotoxicology. 17 (2008) 344–361. https://doi.org/10.1007/s10646-008-0225- x.

[4] M. Bonta, J.J. Gonzalez, C. Derrick Quarles, R.E. Russo, B. Hegedus, A. Limbeck, Elemental mapping of biological samples by the combined use of LIBS and LA-ICP-MS, J. Anal. At. Spectrom. 31 (2015) 252–258. https://doi.org/10.1039/c5ja00287g.

[5] H. Tian, L.J. Sparvero, P. Blenkinsopp, A.A. Amoscato, S.C. Watkins, H. Bayır, V.E. Kagan, N. Winograd, Secondary-ion mass spectrometry images cardiolipins and phosphatidylethanolamines at the subcellular level, Angew. Chemie Int. Ed. 58 (2019) 3156–3161. https://doi.org/10.1002/anie.201814256.

[6] F. Blaske, O. Reifschneider, G. Gosheger, C.A. Wehe, M. Sperling, U. Karst, G. Hauschild, S. Höll, Elemental bioimaging of nanosilver-coated prostheses using X-ray fluorescence spectroscopy and laser ablation-inductively coupled plasma-mass spectrometry, Anal. Chem. 86 (2014) 615–620. https://doi.org/10.1021/ac4028577.

[7] P.M. Angel, H.S. Baldwin, D. Gottlieb Sen, Y.R. Su, J.E. Mayer, D. Bichell, R.R. Drake, Advances in MALDI imaging mass spectrometry of proteins in cardiac tissue, including the heart valve,

Biochim. Biophys. Acta. Proteins Proteomics. 1865 (2017) 927–935. https://doi.org/10.1016/j.bbapap.2017.03.009.

[8] A. Limbeck, P. Galler, M. Bonta, G. Bauer, W. Nischkauer, F. Vanhaecke, Recent advances in quantitative LA-ICP-MS analysis: challenges and solutions in the life sciences and environmental chemistry, Anal. Bioanal. Chem. 407 (2015) 6593–6617. https://doi.org/10.1007/s00216-015-8858-0.

[9] J. Liu, J. Cui, X. Wei, W. Li, C. Liu, X. Li, M. Chen, Y. Fan, J. Wang, Investigation on selenium and mercury interactions and the distribution patterns in mice organs with LA-ICP- MS imaging, Anal. Chim. Acta. 1182 (2021) 338941. https://doi.org/10.1016/j.aca.2021.338941.

[10] Z. Yang, S.E. Jackson, L.J. Cabri, P. Wee, H.P. Longerich, M. Pawlak, Quantitative determination of trace level (ng g-1) contents of rhodium and palladium in copper-rich minerals using LA-ICP-MS, J. Anal. At. Spectrom. 35 (2020) 534–547. https://doi.org/10.1039/c9ja00285e.

[11] C. Arnaudguilhem, M. Larroque, O. Sgarbura, D. Michau, F. Quenet, S. Carrère, B. Bouyssière, S. Mounicou, Toward a comprehensive study for multielemental quantitative LA-ICP MS bioimaging in soft tissues, Talanta. 222 (2021) 121537. https://doi.org/10.1016/j.talanta.2020.121537.

[12] A.E. Egger, S. Theiner, C. Kornauth, P. Heffeter, W. Berger, B.K. Keppler, C.G. Hartinger, Quantitative bioimaging by LA-ICP-MS: a methodological study on the distribution of Pt and Ru in viscera originating from cisplatin- and KP1339-treated mice, Metallomics. 6 (2014) 1616–1625. https://doi.org/10.1039/c4mt00072b.

[13] A. Schoeberl, M. Gutmann, S. Theiner, M. Schaier, A. Schweikert, W. Berger, G. Koellensperger, Cisplatin uptake in macrophage subtypes at the single-cell level by LA-ICP-TOFMS Imaging, Anal. Chem. 93 (2021) 16456–16465. https://doi.org/10.1021/acs.analchem.1c03442.

[14] I.L. Hsiao, F.S. Bierkandt, P. Reichardt, A. Luch, Y.J. Huang, N. Jakubowski, J. Tentschert, A. Haase, Quantification and visualization of cellular uptake of TiO2 and Ag nanoparticles: Comparison of different ICP-MS techniques, J. Nanobiotechnology. 14 (2016) 1–13. https://doi.org/10.1186/s12951-016-0203-z.

[15] S. Theiner, A. Schweikert, C. Haberler, A. Peyrl, G. Koellensperger, Laser ablation – ICP - TOFMS imaging of germ cell tumors of patients undergoing platinum-based chemotherapy, Metallomics. 12 (2020) 1246–1252. https://doi.org/10.1039/d0mt00080a.

[16] C.J. Greenhalgh, E. Karekla, G.J. Miles, I.R. Powley, C. Costa, J. De Jesus, M.J. Bailey, C. Pritchard, M. MacFarlane, J.H. Pringle, A.J. Managh, Exploration of matrix effects in laser ablation inductively coupled plasma mass spectrometry imaging of cisplatin-treated tumors, Anal. Chem. 92 (2020) 9847–9855. https://doi.org/10.1021/acs.analchem.0c01347.

[17] K.N. Sikora, J.M. Hardie, L.J. Castellanos-García, Y. Liu, B.M. Reinhardt, M.E. Farkas, V.M. Rotello, R.W. Vachet, Dual mass spectrometric tissue imaging of nanocarrier distributions and their biochemical effects, Anal. Chem. 92 (2020) 2011. https://doi.org/10.1021/acs.analchem.9b04398.

[18] M. Togao, S.M.M. Nakayama, Y. Ikenaka, H. Mizukawa, Y. Makino, A. Kubota, T. Matsukawa, K. Yokoyama, T. Hirata, M. Ishizuka, Bioimaging of Pb and STIM1 in mice liver, kidney and brain using laser ablation inductively coupled plasma mass spectrometry (LA-ICP-MS) and immunohistochemistry, Chemosphere. 238 (2020) 124581. https://doi.org/10.1016/j.chemosphere.2019.124581.

[19] O. Reifschneider, C.A. Wehe, I. Raj, J. Ehmcke, G. Ciarimboli, M. Sperling, U. Karst, Quantitative bioimaging of platinum in polymer embedded mouse organs using laser ablation ICP-MS, Metallomics. 5 (2013) 1440–1447. https://doi.org/10.1039/c3mt00147d.

[20] N.M. Ralbovsky, L. Zou, B. Chen, N.R. Zhang, C.D.G. Hines, M. Vavrek, W. Zhong, J.P. Smith, X. Bu, Simultaneous multielement imaging of liver tissue using laser ablation inductively coupled plasma mass spectrometry, Talanta. 235 (2021) 122725. https://doi.org/10.1016/j.talanta.2021.122725.

[21] L.N. Zheng, Y.B. Sang, R.P. Luo, B. Wang, F.T. Yi, M. Wang, W.Y. Feng, Determination of silver nanoparticles in single cells by microwell trapping and laser ablation ICP-MS determination, J. Anal. At. Spectrom. 34 (2019) 915–921. https://doi.org/10.1039/c8ja00438b.

[22] D. Metarapi, M. Šala, K. Vogel-Mikuš, V.S. Šelih, J.T. Van Elteren, Nanoparticle analysis in biomaterials using laser ablation-single particle-inductively coupled plasma mass spectrometry, Anal. Chem. 91 (2019) 6200–6205. https://doi.org/10.1021/acs.analchem.9b00853.

[23] O. Reifschneider, A. Vennemann, G. Buzanich, M. Radtke, U. Reinholz, H. Riesemeier, J. Hogeback, C. Köppen, M. Großgarten, M. Sperling, M. Wiemann, U. Karst, Revealing silver nanoparticle uptake by macrophages using SR-μXRF and LA-ICP-MS, Chem. Res. Toxicol. 33 (2020) 1250–1255. https://doi.org/10.1021/acs.chemrestox.9b00507.

[24] S. Zarco-Fernández, A.M. Coto-García, R. Muñoz-Olivas, J. Sanz-Landaluze, S. Rainieri, C. Cámara, Bioconcentration of ionic cadmium and cadmium selenide quantum dots in zebrafish larvae, Chemosphere. 148 (2016) 328–335. https://doi.org/10.1016/j.chemosphere.2015.12.077.

[25] J. Wang, Y. Nie, H. Dai, M. Wang, L. Cheng, Z. Yang, S. Chen, G. Zhao, L. Wu, S. Guang, A. Xu, Parental exposure to TiO2 NPs promotes the multigenerational reproductive toxicity of Cd in Caenorhabditis elegans via bioaccumulation of Cd in germ cells, Environ. Sci. Nano. 6 (2019) 1332–1342. https://doi.org/10.1039/c8en01042k.

[26] P.A. Doble, R.G. de Vega, D.P. Bishop, D.J. Hare, D. Clases, Laser ablation-inductively coupled plasma-mass spectrometry imaging in biology, Chem. Rev. 121 (2021) 11769– 11822. https://doi.org/10.1021/acs.chemrev.0c01219.

[27] D.J. Hare, E.J. New, M.D. De Jonge, G. McColl, Imaging metals in biology: balancing sensitivity, selectivity and spatial resolution, Chem. Soc. Rev. 44 (2015) 5941–5958. https://doi.org/10.1039/c5cs00055f.

[28] L.N. Zheng, L.X. Feng, J.W. Shi, H.Q. Chen, B. Wang, M. Wang, H.F. Wang, W.Y. Feng, Single-cell isotope dilution analysis with LA-ICP-MS: a new approach for quantification of nanoparticles in single cells, Anal. Chem. 92 (2020) 14339–14345. https://doi.org/10.1021/acs.analchem.0c01775.

[29] J.S. Becker, R.C. Dietrich, A. Matusch, D. Pozebon, V.L. Dressler, Quantitative images of metals in plant tissues measured by laser ablation inductively coupled plasma mass spectrometry, Spectrochim. Acta Part B At. Spectrosc. 63 (2008) 1248–1252. https://doi.org/10.1016/j.sab.2008.08.001.

[30] M. Šala, V.S. Šelih, J.T. Van Elteren, Gelatin gels as multi-element calibration standards in LA-ICP-MS bioimaging: fabrication of homogeneous standards and microhomogeneity testing, Analyst. 142 (2017) 3356–3359. https://doi.org/10.1039/c7an01361b.

[31] D.J. Hare, E.P. Raven, B.R. Roberts, M. Bogeski, S.D. Portbury, C.A. McLean, C.L. Masters, J.R. Connor, A.I. Bush, P.J. Crouch, P.A. Doble, Laser ablation-inductively coupled plasma-mass spectrometry imaging of white and gray matter iron distribution in Alzheimer's disease frontal cortex, Neuroimage. 137 (2016) 124–131. https://doi.org/10.1016/j.neuroimage.2016.05.057.

[32] R. Torimoto, C. Ishii, H. Sato, K. Saito, Y. Watanabe, K. Ogasawara, A. Kubota, T. Matsukawa, K. Yokoyama, A. Kobayashi, Kimura, S.M.M. Nakayama, Y. Ikenaka, M. Ishizuka, Analysis of lead distribution in avian organs by LA-ICP-MS: study of experimentally

lead-exposed ducks and kites, Environ. Pollut. 283 (2021) 117086. https://doi.org/10.1016/j.envpol.2021.117086.

[33] S. Marković, K. Uršič, M. Cemazar, G. Sersa, B. Starešinič, R. Milačič, J. Ščančar, High spatial resolution imaging of cisplatin and Texas Red cisplatin in tumour spheroids using laser ablation isotope dilution inductively coupled plasma mass spectrometry and confocal fluorescence microscopy, Anal. Chim. Acta. 1162 (2021) 338424. https://doi.org/10.1016/j.aca.2021.338424.

[34] J. Müller, M. Horstmann, L. Traeger, A.U. Steinbicker, μXRF and LA-ICP-TQMS for quantitative bioimaging of iron in organ samples of a hemochromatosis model, J. Trace Elem. Med. Biol. 52 (2019) 166–175. https://doi.org/10.1016/j.jtemb.2018.12.012.

[35] N. Grijalba, A. Legrand, V. Holler, C. Bouvier-Capely, A novel calibration strategy based on internal standard–spiked gelatine for quantitative bio-imaging by LA-ICP-MS: application to renal localization and quantification of uranium, Anal. Bioanal. Chem. 412 (2020) 3113– 3122. https://doi.org/10.1007/s00216-020-02561-4.

[36] Y. Wang, X. Wei, J.H. Liu, C.X. Wu, X. Zhang, M.L. Chen, J.H. Wang, Cryogenic laser ablation in a rapid cooling chamber ensures excellent elemental imaging in fresh biological tissues, Anal. Chem. 94 (2022) 8547–8553. https://doi.org/10.1021/acs.analchem.2c01736

[37] J. Liu, L. Zheng, X. Wei, B. Wang, H. Chen, M. Chen, M. Wang, W. Feng, J. Wang, Quantitative imaging of trace elements in brain sections of Alzheimer's disease mice with laser ablation inductively coupled plasma-mass spectrometry, Microchem. J. 172 (2022) 106912. https://doi.org/10.1016/j.microc.2021.106912.

[38] M.V. Taboada-López, S. Iglesias-López, P. Herbello-Hermelo, P. Bermejo-Barrera, A. Moreda-Piñeiro, Ultrasound assisted enzymatic hydrolysis for isolating titanium dioxide nanoparticles from bivalve mollusk before sp-ICP-MS, Anal. Chim. Acta. 1018 (2018) 16– 25. https://doi.org/10.1016/j.aca.2018.02.075.

V. CONCLUSIONS

Chapter 1: Exploiting dynamic reaction cell technology for removal of spectral interferences in the assessment of Ag, Cu, Ti, and Zn by inductively coupled plasma mass spectrometry.

Ammonia (NH_3) was proven to be an excellent reaction gas for the development of ICP-MS methodologies capable to overcome polyatomic and isobaric interferences. Optimised methodologies have been obtained under several DRC work-modes: on-mass and mass-shift approach. The impact of the use of NH_3 on the sensitivity and selectivity has been studied and compared to the standard or "vented" mode analysis. Free-interference Ti determination can be performed using the mass-shift method due to the high selectivity and moderate sensitivity allowed by $^{48}Ti(NH)(NH_3)_4$ ion product. In the case of Zn determinations, the formation of Zn ammonia clusters is not as advantageous as Ti or Cu ion products, hence on-mass approach allowed the higher analytical performance. By contrast, Cu determinations demonstrated similar results both for on-mass and mass-shift work-modes in terms of selectivity and sensitivity. Similarly, the influence of the rejection parameters (RPq values) on the measurements has been carefully studied, being especially important for the sensitivity improvements in the on-mass approach due to collisional focusing phenomena.

Chapter 2: Single-particle inductively coupled plasma mass spectrometry using ammonia reaction gas as a reliable and free-interference determination of metallic nanoparticles.

The application of reaction gases in the study of NPs has been proven. It has been observed that the use of NH_3 can have a strong impact on the signal duration of a single NP event leading a pronounced peak broadening. According to these effects, the DRC conditions applied to spICP-MS were carefully established, especially the reaction gas flow rate. The analytical performance of the different work-modes (on-mass and mass-shift approach) was assessed and compared. Throughout the work, it was illustrated a strong dependence of the operating conditions on the size or nature of NPs. Furthermore, mass-shift measurements were proved as the most advantageous technique for TiO_2 NPs working at 100 µs of dwell time and a flow rate of 0.75 mL min^{-1}. Although on-mass mode was discarded for TiO_2 NPs, it represented a high analytical performance for Cu, CuO and ZnO NPs using low ammonia flow rates (0.5 mL min^{-1} for Cu and CuO; 0.25 mL min^{-1} for ZnO). Also, mass-shift approach has proven useful for CuO and Cu NPs measurements using the ion product $^{63}Cu(NH_3)_2$. Due to the abundance of the minority isotopes ^{65}Cu and ^{66}Zn, the generation of the adducts also represents an interesting alternative.

Chapter 3: Single-cell-ICP-MS for studying the association of inorganic nanoparticles with cell lines derived from aquaculture species.

After Ag NPs (15 and 100 nm) and TiO_2 NPs (5 and 25 nm) exposure trials, a scICP-MS approach was found to be an innovative technique for quantifying dissolved metals and NPs associated with cells. In order to obtain a reliable methodology, factors such as dwell time, cell concentration, and presence of NPs and other interferent compounds in the extracellular medium were carefully studied. Centrifugation cycles were required to avoid overestimation by counting NPs that are not interacting with cells and the registration of multi-cell events. As a result, limits of detection at attograms per cell were obtained. Furthermore, the use of DRC technology in scICP-MS measurement has been found to lead free-interference titanium determinations. The developed procedure has a wide range of possibilities for studying NPs interactions with cells and several correlations were established between association-internalisation degree and the exposure conditions and the cultured species under study. The results from this investigation show that the interaction is primarily determined by the cell type and the NP type, and the influence of NP concentration and size distribution was found to be less important.

Chapter 4: Bioaccumulation and human risk assessment of inorganic nanoparticles in aquaculture species

Several aquaculture products were subjected to exposure trials involving different concentrations, exposure times, and Ag NPs and TiO_2 NPs sizes. Regarding sea bass and sea bream species, muscle tissue revealed significantly lower bioaccumulation ratios than those found in kidney and liver tissues, even after exposure at high Ag NPs and TiO_2 NPs doses and long exposure times. However, Japanese carpet shell species may bioaccumulate Ag NPs and TiO_2 NPs in the soft tissues, which implies a health concern if the shellfish were exposed to the high Ag NPs and TiO_2 NPs levels. Human bioavailability was found to be low-moderate depending on the type of NPs: less than 70% and 5% for total Ti and TiO_2 NPs, respectively, for cooked sea bream. Regarding Japanese carpet shell, total Ag and Ti bioavailability ratios were less than 65 and 35%, but Ag NP bioavailability ratios in cooked shellfish were much lower (less than 20%). Also, Japanese carpet shell showed similar TiO_2 NPs and total Ti bioavailability ratios. In view of the data obtained, valuable information on food safety and the potential impact of NPs were achieved.

Chapter 5: Quantitative imaging in fish tissues exposed to titanium dioxide nanoparticles by laser ablation-inductively coupled plasma-mass spectrometry.

The optimized LA-ICP-MS technology, mainly by using high-rate scanning and low laser energy (50 µm s^{-1} and 0.4 J cm^{-2}), allowed sensitive and quantitative bioimaging experiments with great spatial resolution in tissues from cultured sea bream previously exposed to 45 nm TiO_2 NPs. Laboratory-produced porcine gelatin standards exhibited efficient and reliable quantification capacities for imaging studies. LA-ICP-MS biodistribution maps from sea bream tissues demonstrated the existence of Ti homogeneously distributed in the tissues, as well as hotspots formed from TiO_2 NPs in kidney and liver organs. Nevertheless, improvements are necessary for imaging fish muscle tissues due to challenges encountered during embedding and because of the low Ti and/or TiO_2 NPs concentrations in the tissues. Improvements could imply the use of thicker slides which might increase the uniformity of the embedded tissue as well as the implementation of soft LA-ICP-MS conditions. Therefore, LA-ICP-MS can be an alternative analytical technique which can distinguish and mapping the presence of ionic and nanoparticulated species.

ANNEX I: RESUMO

Esta tese doutoral céntrase no desenvolvemento de métodos analíticos novos para o estudo de nanopartículas inorgánicas (NPs). A investigación proposta expón un serio reto para a mellora da detección e caracterización destas NPs mediante o uso de ferramentas analíticas cun enorme potencial, como son o uso de novos gases de reacción, a detección de células individualizada así como a xeración de mapas de biodistribución. Todas estas aplicacións centraranse na crecente industria da acuicultura, evaluando a influencia que as NPs poden ter en diversas especies mariñas e deseñando diversas investigacións sobre nanotoxicidad. Nas últimas décadas, os nanomateriais (NMs) e a nanotecnoloxía revolucionaron o panorama científico, implicando aplicacións en diversos campos como a química, a bioloxía e a medicina, entre outros tantos. Debido ás súas excepcionais propiedades fisicoquímicas, este tipo de NPs espertou un gran interese. Esta tese céntrase principalmente nas NPs de prata e de dióxido de titanio (Ag NPs e TiO_2 NPs), dúas das máis estendidas na actualidade. As propiedades antimicrobianas son o uso máis importante das Ag NPs. Grazas ás súas propiedades fotocatalíticas e fotooxidantes, o TiO_2 e as TiO_2 NPs tamén se utilizan como axentes antibacterianos, entre outros usos. Sen embargo, as excepcionais calidades das NPs provocaron un aumento masivo do seu uso e vertedura no medio ambiente, o que suscitou preocupación polo seu posible impacto no medio ambiente, especialmente no medio mariño. Dada a falta de estudios toxicolóxicos, unido ao comportamento cambiante das NPs e a ausencia de plataformas nanométrolóxicas robustas e fiables para a súa caracterización, estes perigos seguen sendo todavía incertos. Todas estas cuestións abórdanse nesta tese doutoral a través de diversas investigacións sobre toxicidade e o desenvolvemento de varios procedementos analíticos baseados en distintos enfoques. Ademais todas estas actividades centráronse na investigación da influencia sobre matrices biolóxicas como as diversas especies acuícolas investigadas. As especies investigadas foron a

robaliza (*Dicentrachus labrax*), a dourada (*Sparus aurata*) e a ameixa (*Ruditapes philippinarum*), tres das especies máis importantes na produción acuícola a nivel global.

A acuicultura representa o cultivo de organismos acuáticos en circunstancias controladas, e para o consumo humano na súa maior parte. A principal responsabilidade da acuicultura é complementar eficazmente a pesca de captura convencional no medio mariño e satisfacer a futura demanda de alimentos ante o aumento da poboación e do consumo de peixe. Na actualidade, os produtos da acuicultura representan máis do cincuenta por cento do peixe e os alimentos de orixe acuática que se consumen no mundo. Ademais, o sector da acuicultura debe promover unha produción acuícola sostible e garantir a seguridade alimentaria dos consumidores, á vez que se enfronta a obstáculos como a aparición de novas enfermidades, o cambio climático e o uso indebido de antibióticos. Aínda que non cabe dúbida de que a acuicultura se está expandindo a nivel mundial, o seu desenvolvemento na Unión Europea (UE) foi máis ben gradual e lento; por iso, a Comisión Europea (CE) estableceu unha estratexia para fomentar a acuicultura. Os Estados membros están altamente cualificados e dotados dos recursos tecnolóxicos e os coñecementos técnicos adecuados para fomentar este sector de forma ecolóxica e sostible. Ademais, os estritos requisitos normativos da UE garanten a seguridade dos alimentos para os consumidores. A diferenza doutras rexións, especialmente no continente asiático, estas mesmas limitacións dificultan o crecemento e a promoción destas actividades. En termos de produción acuícola, España sitúase á cabeza da UE pola súa vantaxosa situación xeográfica e a recursos naturais. A produción acuícola do país está diversificada en toda a súa rexión, coa robaliza, a dourada, a troita arco iris, o rodaballo ou os mexillóns como especies dominantes. En particular, Galicia destaca como potencia acuícola en España, liderando a produción de especies como o rodaballo e o mexillón. Galicia é un territorio idóneo para o fomento deste tipo de

actividade pola súa localización, calidades xeográficas e climáticas, así como polos seus máis de 1.500 quilómetros de costa.

En vista do importante aumento do uso de NMs e da industria acuícola, é esencial examinar o impacto que a descarga destes materiais pode ter no medio mariño e as posibles repercusións para as criaturas acuáticas e tamén para os seres humanos. En consecuencia, esta influencia constitúe o núcleo desta tese doutoral, que pode achegar á comunidade científica información e metodoloxías avanzadas dende varias perspectivas. As NPs son fundamentalmente inestables e, se se liberan en o medio ambiente, son susceptibles de sufrir unha ampla gama de procesos físicos, químicos e biolóxicos que dependen non só das propiedades das NPs, senón tamén das condicións ambientais acuáticas. Demostrouse que múltiples tipos de NPs teñen efectos nocivos nunha serie de criaturas mariñas, como bacterias, algas, moluscos e peces. Ademais, existe un amplo consenso en que os principais mecanismos de toxicidade polos que actúan as NPs son a liberación de ións ou a formación de especies reactivas de osíxeno (ROS) e a tensión física orixinado polo tamaño, a forma e as propiedades superficiais das NPs. Ademais das dificultades inherentes ás NPs como consecuencia do seu comportamento cambiante e complexo, carécese dun marco normativo normalizado para a súa utilización e de información fiable sobre as súas consecuencias toxicolóxicas. Un claro exemplo desta complexidade é a controversia en torno ao uso e a toxicidade do aditivo alimentario E-171, que contén unha fracción de NPs de TiO_2. En resposta á demanda de estudos e información fiables e nun intento de fomentar a acuicultura, a UE nos últimos anos apoiou varios proxectos de investigación para garantir a seguridade alimentaria e a alta calidade dos produtos acuícolas.

A pesar de que a espectrometría de masas por plasma acoplado inductivamente en modo de detección de partícula única (single particle inductively coupled plasma mass spectrometry; spICP-MS)

considérase a técnica máis dominante e amplamente utilizada para a análise de NPs, é necesario empregar metodoloxías complementarias que melloren e fortifiquen os datos obtidos a partir destas NPs. Nos diferentes capítulos desta tese doutoral discutiranse estes novos procedementos avanzados desde numerosas perspectivas. As interferencias espectrais isobáricas son unha das limitacións máis significativas de spICP-MS. Esta limitación pode superarse empregando Dynamic Reaction Cell Technology (DRC technology) descrita neste proxecto para analitos iónicos (capítulo 1) e NPs de distinta natureza (capítulo 2), que implica o uso dun gas de reacción para eliminar interferencias ou desprazar os analitos a rexións libres de interferencias e que permite dous modos de operación: on-mass e mass-shift. Nestes capítulos utilízase o amoníaco (NH_3) como gas de reacción, xa que a súa gran selectividade permite xerar numerosos aductos ou ións producto que permiten realizar a análise nunha relación masa-carga (m/z) libre de interferencias. Doutra banda, a análise cuantitativa de oligoelementos e NPs en células biolóxicas individuais e os seus efectos está a desempeñar un papel cada vez máis importante. Single cell-ICP-MS (scICP-MS) xurdiu recentemente como unha das metodoloxías en desenvolvemento máis prometedoras para abordar estas cuestións, xa que permite límites de detección máis baixos, revela a heteroxeneidade celular e distingue entre células individuais. Deste xeito, foi posibles deseñar un estudio de gran interés para analizar a internalización de NPs en cultivos celulares de especies acuícolas e obter resultados de gran importancia para respaldar as probas toxicolóxicas llevadas a cabo ao longo do proxecto. Por outra banda, durante os anos de tese doutoral desenvolvéronse longos e completos estudos de bioacumulación en especies de ameixas, robalizas e douradas para observar o impacto e os efectos das NPs de Ag e TiO_2 en diferentes condicións de tempo de exposición e concentración, así como o uso de NPs de distintos tamaños. Ademais, investigouse a influencia de diversas técnicas

culinarias e obtivéronse datos sobre biodisponibilidade. Tamén, identificáronse algúns patróns ao longo do ciclo de acuicultura e relacionáronse coa exposición ás NPs, nos que as NPs de Ag sufriron procesos de ionización e as NPs de TiO_2 agregáronse. Utilizáronse con éxito diversos pretratamentos de mostra, como o illamento encimático das NPs, experimentos *in-vitro* e procedementos culinarios, para alcanzar os obxectivos expostos. Ademais, proporcionouse importante información sobre seguridade alimentaria ao demostrar que o tecido muscular do peixe contiña concentracións substancialmente máis baixas destas sustancias químicas. Un enfoque completamente distinto foi a creación de mapas de biodistribución elemental, estudos que espertaron un gran interese na comunidade científica nos últimos anos. A pesar das súas extraordinarias capacidades, a técnica de laser ablation inductively coupled plasma mass spectrometry (LA-ICP-MS) vese limitada por unha serie de factores, o máis significativo dos cales é a falta de materiais de referencia adecuados, o que dificulta a análise cuantitativa e os estudos de imaxe. A utilización de estándares producidos en laboratorio derivados de xelatina porcina, cuxa popularidade vai en aumento, permitiu superar este obstáculo. Ademais, a investigación empregando LA-ICP-MS, tan pouco común para a análise de NPs, especialmente para experimentos cualitativos ou cuantitativos de obtención de imaxes, logrouse obter, como se describe no capítulo final.

Esta tese doutoral divídese en cinco capítulos que se titulan como a súa publicación en inglés como segue: exploiting dynamic reaction cell technology for removal of spectral interferences in the assessment of Ag, Cu, Ti, and Zn by inductively coupled plasma mass spectrometry (capítulo 1), single-particle inductively coupled plasma mass spectrometry using ammonia reaction gas as a reliable and free-interference determination of metallic nanoparticles (capítulo 2), ultra-sensitive single-cell-ICP-MS for studying the association of inorganic

nanoparticles with cell lines derived from aquaculture species (capítulo 3), bioaccumulation and human risk assessment of inorganic nanoparticles in aquaculture species (capítulo 4), and quantitative imaging in fish tissues exposed to titanium dioxide nanoparticles by laser ablation-inductively coupled plasma-mass spectrometry (capítulo 5). Para facilitar a comprensión, nesta sección descríbese brevemente cada capítulo, incluíndo a motivación da investigación, os resultados obtidos ou as conclusións extraídas.

Capítulo 1: Exploiting dynamic reaction cell technology for removal of spectral interferences in the assessment of Ag, Cu, Ti, and Zn by inductively coupled plasma mass spectrometry. Para a medición de ultratrazas de Ti, Zn, Cu e Ag mediante inductively coupled plasma-mass spectrometry (ICP-MS), desenvolvéronse técnicas analíticas baseadas na tecnoloxía de cela de reacción dinámica (DRC) que utilizan amoníaco como gas de reacción. Demostrouse que a DRC permite superar as difíciles interferencias espectrais de matrices complicadas, e avaliáronse e compararon DRC nos seus modos de traballo (on-mass e mass-shift mode) empregando NH_3 como gas de reacción con respecto ao análisis en modo convencional ou vented mode. Para Ti, Cu, Zn e Ag, xeráronse ións producto de amonio (modo de traballo mass-shift). Tamén se investigou o modo de traballo on-mass para aproveitar os fenómenos de focalización colisional como resultado do confinamento dos ións (traxecto de viaxe máis longa na guía de iones) causado polas perdas de enerxía das colisións sucesivas na celda de reacción. Ademais, axustáronse as condicións de funcionamento do DRC alterando o caudal de gas NH_3 e o parámetro de rexeitamento q (RPq). As condicións optimizadas aplicáronse para demostrar a utilidade das estratexias de on-mass e mass-shift para eliminar as interferencias de Ca e P a concentracións de até 50 mg L^{-1} . Por último, se investigouse a sensibilidade de todas

as técnicas de medición e determináronse límites de detección mellorados (a valores duns poucos ng L^{-1}).

Capítulo 2: Single-particle inductively coupled plasma mass spectrometry using ammonia reaction gas as a reliable and free-interference determination of metallic nanoparticles. En resposta ás ameazas potenciais que supoñen as NPs para o medio ambiente requírense estratexias analíticas máis potentes e versátiles para a monitorización e caracterización destes novos contaminantes. Así spICP-MS é o método máis prometedor para analizar NPs metálicas como foi comentado anteriormente. Con todo, a súa aplicación vese ocasionalmente obstaculizada por interferencias espectrais causadas por isótopos isobáricos ou especies poliatómicas en matrices difíciles, como as matrices biolóxicas utilizadas nesta tese doutoral. Existen diversas opcións para superar estes obstáculos, pero a tecnoloxía DRC ofrece os resultados máis prometedores. En referencia ás NPs inorgánicas, até a data só existen unhas poucas aplicacións da tecnoloxía DRC, xa que o comportamento das NPs na célula é considerablemente diferente ao dos analitos disoltos, debido principalmente a unha explosión de ións moito maior que a dos analitos iónicos convencionais. Ademais, entre os gases de reacción investigados, a utilización de NH_3 promete unha reactividade variada e impredicible, xa que ofrece a vantaxe de producir múltiples aductos ou ións producto e, por tanto, unha maior selectividade en ICP-MS/MS para a eliminación de interferencias mediante o emprego de dous modos de traballo: on-mass e mass-shift. Por tanto, no capítulo 2, desenvolvéronse métodos spICP-MS baseados en DRC utilizando NH_3 como gas de reacción (tanto para on-mass como mass-shift) para determinar NPs de dióxido de titanio (TiO_2 NPs), NPs de óxido de cobre (CuO NPs), NPs de cobre (Cu NPs) e NPs de óxido de zinc (ZnO NPs). Levouse a cabo unha ampla investigación sobre os efectos do caudal de NH_3 e a duración do dwell time para a anchura do pico

(sinal transitorio de NP en spICP-MS). Tamén se estudou o impacto do tamaño e a composición das NPs. Os procedementos on-mass e mass-shift mostráronse eficaces para avaliar as NPs de Cu e CuO (empregando a relación masa-carga orixinal de 63 e o produto iónico $Cu(NH_3)_2$). Con todo, preferiuse o modo en-masa para avaliar as NPs de ZnO (relación masa-carga orixinal de 64 utilizando un fluxo de gas de 0,25 mL min^{-1}). Ademais, o método de desprazamento de masas (mass-shift) é o máis eficaz para facer fronte ás interferencias do Ti nas medicións de NPs de TiO_2 (relación masa-carga de 131 para $Ti(NH)(NH_3)_4$ a 0,75 mL min^{-1}).

Capítulo 3. Single-cell-ICP-MS for studying the association of inorganic nanoparticles with cell lines derived from aquaculture species. A fabricación a gran escala, a vertedura e os riscos potenciais asociados ás NPs inorgánicas esixen datos para avaliar o dano potencial destes novos contaminantes, concretamente datos que aborden a absorción de NPs inorgánicas en organismos mariños e as súas consecuencias a nivel biolóxico. Os experimentos *in-vitro* para avaliar a absorción das NPs polas células resultan atractivas como estudos de toxicidade, pero na actualidade non existe ningún procedemento consensuado para determinar como as células internalizan as NPs. Abriuse un novo campo de investigación grazas á scICP-MS, que permite a cuantificación a nivel realmente baixos de metais disoltos e NPs inorgánicas en células individuais operando a unha taxa mínima de absorción da mostra e distinguindo entre células individuais nun estado celular próximo ao nativo. Así, o terceiro capítulo desta tese doutoral desenvolveu novas investigacións sobre a avaliación de NPs de TiO_2 e Ag tanto asociadas como internalizadas en liñas celulares obtidas de especies de acuicultura como robaliza, dourada e ameixas mediante scICP-MS. O elevado fondo ou background, a coincidencia de picos entre múltiples células e as interferencias espectrais son factores que se tiveron en conta ao longo

dos estudos de optimización. Os tempos de permanencia ou dwell time de 50 µs para as NPs de Ag e de 100 µs para as NPs de TiO_2 demostraron ser óptimos nestas circunstancias. Aplicando a tecnoloxía DRC cun caudal de 0,75 mL min^{-1} de NH_3 e monitorizando o aducto $^{48}Ti(NH)(NH_3)_4$ (m/z de 131), lográronse medicións de titanio sen interferencias. Tamén se examinou a fondo o efecto doutros factores na precisión da scICP-MS, incluídos os ciclos de lavado e a concentración de células por mostra. Se alcanzaron límites de detección de attogramos por célula en determinacións ultrasensibles (5±1,4 para medicións de Ag e 95±11 para medicións de Ti), que non proporcionan outras técnicas instrumentais a día de hoxe. O método desenvolvido aplicouse a células renais de lubina e dourada, así como a células do manto de ameixa, e revelou que o grao de internalización das NPs nas células estaba significativamente influído pola distribución do tamaño das NPs, a concentración de TiO_2 NPs ou Ag NPs expostas e a especie cultivada obxecto de estudo.

Capítulo 4. Bioaccumulation and human risk assessment of inorganic nanoparticles in aquaculture species. Para obter estudos que avalíen a toxicidade potencial das NPs inorgánicas e o seu impacto no medio mariño, é esencial realizar estudos nanotoxicolóxicos fiables que permitan coñecer mellor o impacto das NPs nos organismos mariños, tal e como se describe neste capítulo. Por desgraza, esta tarefa é complexa, xa que as propiedades das NPs no medio acuático varían, e os verdadeiros efectos da súa presenza aínda non están claros e son difíciles de estudar. Ademais, hai que tener en conta numerosas características das NPs, xa que inflúen considerablemente na súa toxicidade. En relación coa toxicidade mencionada, no cuarto capítulo desta tese doutoral se levaron a cabo un conxunto de experimentos con varias especies e órganos de peixes para demostrar a toxicidade potencial e a bioacumulación efectiva tras a exposición ás NPs, incluíndo investigacións sobre a mencionada bioacumulación,

ademais do estudo da biodisponibilidade e bioaccesibilidade. Estas probas de exposición realizáronse en produtos acuícolas mediante a exposición dietética a NPs variando os períodos de exposición e as concentracións de NPs de Ag e TiO_2, revelando os órganos diana onde se concentran as NPs para dar e obter resultados exhaustivos de bioacumulación. Ademais, achegouse información sobre a seguridade alimentaria e a biodisponibilidade humana dos produtos acuícolas ao demostrar que o tecido muscular dos peixes presentaba concentracións moito máis baixas destas sustancias químicas. Tamén identificáronse varios patróns asociados á exposición das NPs, nos que as NPs de Ag experimentaron procesos de ionización e as NPs de TiO_2 agregáronse. Para alcanzar os obxectivos fixados utilizáronse diversos tratamentos previos, como o pretratamiento de mostras mediante dixestión aceda asistida por microondas, o illamento encimático das NPs, ensaios *in-vitro* con células caco-2 e distintos procedementos culinarios. Empregouse a spICP-MS como potente ferramenta para analizar as NPs, aplicando unha nova metodoloxía DRC en base a desenvolvido no capítulo 2.

Capítulo 5. Quantitative imaging in fish tissues exposed to titanium dioxide nanoparticles by laser ablation-inductively coupled plasma-mass spectrometry. Para comprender como se comportan as NPs nas mostras biolóxicas e no medio ambiente é preciso avalialas utilizando e desenvolvendo metodoloxías analíticas confiables e eficientes. Por iso as NPs, como contaminantes emerxentes, requiran novos enfoques para a súa mellor comprensión, control e seguimento mediante o desenvolvemento de imaxes cuantitativas. En diversos campos científicos, xurdiu gran interese nestes ensaios de biodistribución elemental dos metais nos tecidos biolóxicos para abordar os retos relativos ás investigacións sobre toxicidade. Este campo podería complementar técnicas ben establecidas como a spICP-MS ao proporcionar información esencial sobre a bioacumulación de metais

nunha ampla variedade de tecidos brandos. A pesar de que este tipo de estudo está a popularizarse cada vez máis nunha diversa gama de tecidos biolóxicos, como células, tumores e algúns outros órganos, os traballos publicados até a data son máis ben escasos sobre a análise de NPs. LA-ICP-MS proporciona capacidades prometedoras para realizar imaxes de tecidos biolóxicos. No quinto capítulo desta tese doutoral descríbense os procesos de pretratamento de mostras, como a inclusión en polímeros en parafina e o corte de láminas finas mediante micrótomo, utilizados para preparar diferentes tecidos de peixes para a análise por LA-ICP-MS. Ademais, optimizouse coidadosamente unha metodoloxía nova para LA-ICP-MS, utilizando un varrido de alta velocidade e baixa enerxía láser que permitiu realizar estudos de bioimaxe sensibles e cuantitativos con alta resolución espacial. Comparáronse conxuntos de datos de imaxes correspondentes a tecidos de especies acuícolas, o que revelou o impacto cando os tecidos proceden de experimentos de exposición a NPs en comparación cos que non foron expostos. Os datos recolleitos utilizáronse para localizar zonas prominentes de NPs vinculadas á exposición ás NPs de TiO_2 , así como unha mellor comprensión do patrón de distribución. Os estándares de xelatina porcina fabricados en laboratorio permitiron producir imaxes non só cualitativas senón tamén cuantitativas, demostrando a idoneidade do seu emprego para cuantificar estudos de imaxe, a pesar dos desacordos existentes para establecer unha calibración ou protocolo universal co fin de cuantificar eficientemente por LA-ICP-MS. Estes resultados iniciais demostraron o potencial dos estudos de imaxe por LA-ICP-MS para proporcionar información esencial sobre a distribución das NPs no interior de mostras biolóxicas de tecidos de peixes, co apoio dun alto rendemento analítico.

ANNEX II: LIST OF PUBLICATIONS

- Cristian Suárez Oubiña, Paloma Herbello Hermelo, Pilar Bermejo Barrera, Antonio Moreda Piñeiro, Exploiting dynamic reaction cell technology for removal of spectral interferences in the assessment of Ag, Cu, Ti, and Zn by inductively coupled plasma mass spectrometry, *Spectrochim. Acta B: At. Spectrosc*, 187 (2022), 944.

  DOI: 10.1016/j.sab.2021.106330
  Journal Impact Factor: **JCR**: 3.66
  JCR-Q1: Spectroscopy (8/43)
  Contribution: Formal analysis, Investigation, Validation, Visualization, Writing-original draft preparation.

- Cristian Suárez Oubiña, Paloma Herbello Hermelo, Pilar Bermejo Barrera, Antonio Moreda Piñeiro, Single-particle inductively coupled plasma mass spectrometry using ammonia reaction gas as a reliable and free-interference determination of metallic nanoparticles, *Talanta*, 242 (2022), 123286.

  DOI: 10.1016/j.talanta.2022.123286.
  Journal Impact Factor: **JCR**: 6.56
  JCR-Q1: Analytical Chemistry (11/87)
  Contribution: Formal analysis, Investigation, Validation, Visualization, Writing-original draft preparation.

ANNEX III: JOURNAL PERMISSIONS

- **FIGURE 12 (I. INTRODUCTION)**

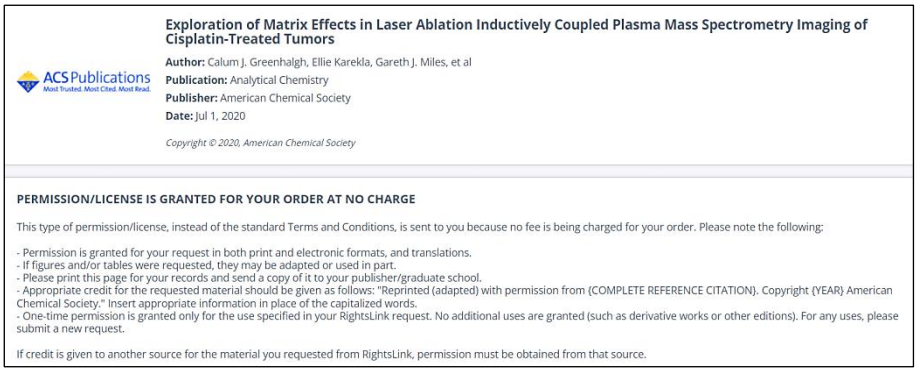

Exploration of Matrix Effects in Laser Ablation Inductively Coupled Plasma Mass Spectrometry Imaging of Cisplatin-Treated Tumors

Author: Calum J. Greenhalgh, Ellie Karekla, Gareth J. Miles, et al
Publication: Analytical Chemistry
Publisher: American Chemical Society
Date: Jul 1, 2020

Copyright © 2020, American Chemical Society

PERMISSION/LICENSE IS GRANTED FOR YOUR ORDER AT NO CHARGE

This type of permission/license, instead of the standard Terms and Conditions, is sent to you because no fee is being charged for your order. Please note the following:

- Permission is granted for your request in both print and electronic formats, and translations.
- If figures and/or tables were requested, they may be adapted or used in part.
- Please print this page for your records and send a copy of it to your publisher/graduate school.
- Appropriate credit for the requested material should be given as follows: "Reprinted (adapted) with permission from {COMPLETE REFERENCE CITATION}. Copyright {YEAR} American Chemical Society." Insert appropriate information in place of the capitalized words.
- One-time permission is granted only for the use specified in your RightsLink request. No additional uses are granted (such as derivative works or other editions). For any uses, please submit a new request.

If credit is given to another source for the material you requested from RightsLink, permission must be obtained from that source.

- **CHAPTER 1 (IV. RESULTS AND DISCUSSION)**

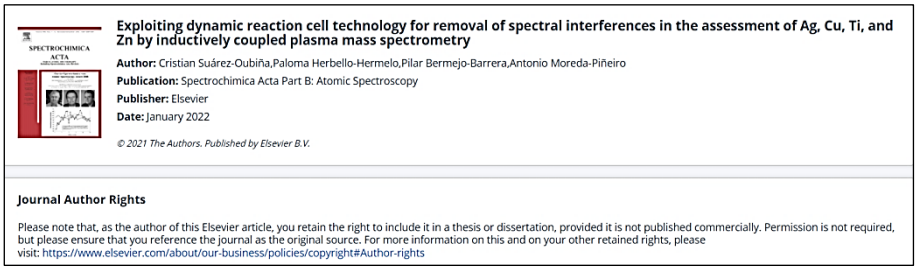

Exploiting dynamic reaction cell technology for removal of spectral interferences in the assessment of Ag, Cu, Ti, and Zn by inductively coupled plasma mass spectrometry

Author: Cristian Suárez-Oubiña,Paloma Herbello-Hermelo,Pilar Bermejo-Barrera,Antonio Moreda-Piñeiro
Publication: Spectrochimica Acta Part B: Atomic Spectroscopy
Publisher: Elsevier
Date: January 2022

© 2021 The Authors. Published by Elsevier B.V.

Journal Author Rights

Please note that, as the author of this Elsevier article, you retain the right to include it in a thesis or dissertation, provided it is not published commercially. Permission is not required, but please ensure that you reference the journal as the original source. For more information on this and on your other retained rights, please visit: https://www.elsevier.com/about/our-business/policies/copyright#Author-rights

- **CHAPTER 2 (IV. RESULTS AND DISCUSSION)**

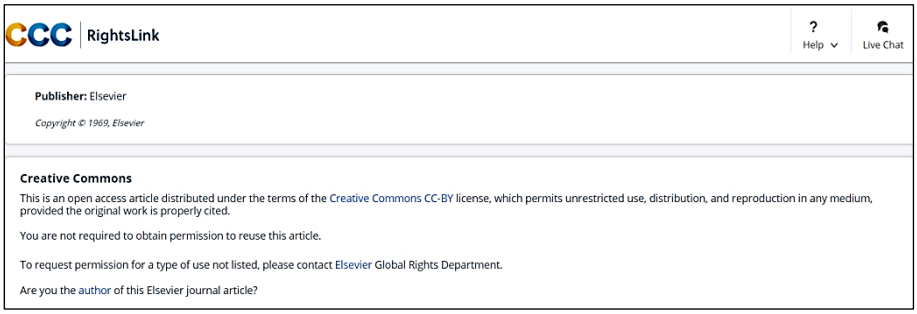

RightsLink

Help Live Chat

Publisher: Elsevier

Copyright © 1969, Elsevier

Creative Commons

This is an open access article distributed under the terms of the Creative Commons CC-BY license, which permits unrestricted use, distribution, and reproduction in any medium, provided the original work is properly cited.

You are not required to obtain permission to reuse this article.

To request permission for a type of use not listed, please contact Elsevier Global Rights Department.

Are you the author of this Elsevier journal article?

Nanomaterials, mainly inorganic nanoparticles (NPs), have brought about a revolution at the scientific and industrial level due to their outstanding physicochemical properties. The widespread use of NPs has raised concerns about their potential impact into the environment and, consequently, the risk to humans. Toxicological studies are therefore required to assess the threats associated to these emerging pollutants.

This doctoral thesis presents several nanometrological tools to face the challenge of improving the detection, characterization, and quantification of NPs in complex samples. The developed applications were focused on aquaculture products by assessing the potential effects from NPs on the cultured fish and shellfish species.